Coupling of oceanic and atmospheric heat transport in the tropics

Clare Helen Heaviside

April 2009

Space and Atmospheric Physics group, Department of Physics,
Imperial College, London, SW7 2AZ

A thesis submitted for the degree
of Doctor of Philosophy of the University of London
and for the Diploma of Imperial College

Abstract

A global thermal equilibrium on earth requires that heat is transported from the tropics towards the poles. In the tropics, the ocean and atmosphere are strongly coupled, and the amount of heat transported in each is influenced by the other. The focus of this thesis is the mechanisms controlling the meridional transport of heat in the tropical ocean and atmosphere.

Using reanalysis data, we investigate the seasonal and interannual, as well as spatial variability of moist static energy and meridional mass transport in the atmosphere. We then introduce a framework to sort the mass transport of the atmosphere as a function of low level moist static energy, which reflects underlying sea surface temperature (SST). The framework enables us to identify differences in the mass transport between convective regions (which correspond to high SST and surface moist static energy) and non-convective regions (where SSTs are lower, as is surface moist static energy).

Next we focus on the convective regions of the tropics, where the circulation reflects the shape of the overturning Hadley Cell, and quantify the amount of heat transported here. We find that the convective regions contribute significantly to the total heat transport, and that convective heat transport is largely controlled by mass transport, with smaller variations in moist static energy.

Finally, we use a coupled aquaplanet model to calculate the ocean and atmosphere heat transport associated with the surface wind stress to test the theory that annual variations in ocean and atmosphere heat transport are positively correlated in the tropics. We find there is a strong relationship between the trade winds and ocean heat transport out of the tropics. There is a similar relationship in the atmosphere, although with a smaller correlation, highlighting the important role of atmospheric eddies in the tropics of the aquaplanet model.

Acknowledgements

Firstly, I would like to thank my supervisor, Arnaud Czaja, for his great enthusiasm and attentiveness throughout my PhD. I would also like to thank the staff of the Space and Atmospheric Physics group, especially Jo Haigh and Ralf Toumi. The students in the group have really made my time here a joy, and I especially thank Isla Simpson for helpful discussions as well as our social outings. I thank my soon-to-be husband, Stu, for help and support throughout my time at Imperial, and throughout the writing up period.

My work was funded by the Natural Environmental Research Council and the data used in chapters 2 and 3 was ERA40 data from the European Centre for Medium Range Weather Forecasts, supplied through the British Atmospheric Data Centre. I would like to thank Robin Smith, Bablu Sinha and Adam Blaker for help with FORTE details.

Abbreviations

APE	Aquaplanet Experiment
C_p	specific heat capacity
DJF	December-January-February
ECMWF	European Centre for Medium-Range Weather Forecasts
ENSO	El Niño Southern Oscillation
ERA40	ECMWF Reanalysis dataset for 40 years
ERBE	Earth Radiation Budget Experiment
FORTE	Fast Ocean, Rapid Troposphere Experiment
F_s	Heat Flux into ocean surface
F_t	Heat Flux from top of atmosphere
GCM	Global Circulation Model
HA	Heat transport by the atmosphere
HA_{axisym}	Axisymmetric component of atmospheric heat transport
HO	Heat transport by the ocean
HO_{Ek}	Ekman heat transport in the ocean
hPa	hecto pascals
ICGCM	Intermediate Complexity General Circulation Model
ITCZ	Inter-tropical Convergence Zone
JJA	June-July-August
LH	Latent Heat
L_v	Latent heat of vapourisation
LW	Longwave
MAM	March-April-May
M_{Ek}	Ekman mass transport
MMC	Mean meridional circulation
MOMA	Modular Ocean Model Array
MTM	Multitaper method
NCEP	National Centre for Earth system prediction?
OAGCM	Ocean-Atmosphere Global Circulation Model
PW	Petawatts (10^{15} Watts)
RH	Relative humidity
SH	Sensible Heat
SO	Ocean heat storage

SON	September-October-November
SST	Sea surface temperature
SV	Sverdrups (used throughout the thesis as a mass rather than volume transport, where 1 Sv is defined as 10^9 kg s^{-1})
SW	Shortwave
TOA	Top of Atmosphere
WOCE	World Ocean Circulation Experiment

Table of figures

Figure 1.1. The radiation balance of the earth averaged over a 4 year period. Upper solid curve shows the average flux of solar energy reaching the outer atmosphere and lower solid curve shows the amount of solar energy absorbed. The dashed line shows the average amount of outgoing radiation. From Gill (1982). 19

Figure 1.2. General circulation of the atmosphere. From online Encyclopaedia Britannica (Britannica 2008) 21

Figure 1.3. Composite image of instantaneous infrared imagery from geostationary satellites (1200 UTC 29th March 2004). From SATMOS, © METEO-FRANCE and Japan Meteorological Agency. From Bony *et al*. (2006). 22

Figure 1.4. Sea surface temperatures (degrees Celsius) for El Niño and La Niña. From Philander & Federov (2003). 23

Figure 1.5. The annual mean meridional streamfunction. Contour interval 20 x 10^9 kg s^{-1}. Shading shows zonal winds greater than 20 m s^{-1}, based on 20 years of ECMWF analysis. From James (2003).. 25

Figure 1.6. Monthly variation of the climatological-mean streamfunction in the NCEP-NCAR reanalysis. Contour interval is 20 x 10^9 kg s^{-1}, solid positive, dashed negative. From Dima & Wallace (2003). 26

Figure 1.7. Mean meridional circulation for A) DJF and B) JJA. Other details as for Figure 1.5. From James (2003). 28

Figure 1.8. Ocean state and atmospheric circulation in the Pacific for normal conditions (upper) and El Niño conditions (lower). Colours represent SST and the thermocline is shown below the surface. The atmospheric circulation is represented by arrows and convective clouds. From the National Oceanic and Atmospheric Administration website (NOAA 2009).. 30

Figure 1.9. Difference in streamfunction between the five warmest and five coldest DJF (upper) and JJA (lower) seasons. Contour intervals 10^{10} kg s^{-1}. The difference is a measure of the range in values between El Niño and La Niña conditions. From Oort & Yienger (1996). 31

Figure 1.10. Climatology of the summer and winter Asian monsoon circulation over the Arabain Sea. Arrows represent surface winds velocity. From NASA Earth Observatory (NASA 2006).. 32

Figure 1.11. Total gain and loss of radiative heat in the northern hemisphere, total heat flux (sensible + latent) across latitude bands and meridional heat flux in ocean and

atmosphere. Units on the right are 10^{19} calories per day ~ 0.5 PW (10^{15} Watts). From (Bjerknes 1964), using radiation data (Houghton 1954) and flux data (Sverdrup 1957). . 34

Figure 1.12. Northward transport of sensible heat plus potential energy plus kinetic energy by the atmosphere (solid line), latent heat by the atmosphere (dashed) and sensible heat by the oceans (dotted), units are 10^{14} Watts. From Lorenz (1967). 35

Figure 1.13. Total flux of energy across latitude circles in the northern hemisphere (left) and southern hemisphere (right) for earth with no latitudinal structure or axial tilt (dashed), no latitudinal structure but with an axial tilt (solid), for the actual earth (circles) and an approximation with ocean and atmosphere structure included (crosses), from Stone (1978). 36

Figure 1.14. Annual transport of energy (left) for a) total, b) atmosphere and c) ocean. In c), 3 curves for T_o are based on different corrections. Oceanic annual poleward transport of heat (right). Y axis values are in PW. From Carissimo *et al*. (1985). 37

Figure 1.15. The fraction of poleward energy transport contributed by ocean and atmosphere (left), and the predicted shape of energy transports (right) from Held (2001). Latitude is normalized by the latitude of the subtropical boundary of the Hadley Cell. 38

Figure 1.16. Total heat transport implied from the TOA radiation (RT), derived estimate of adjusted ocean heat transport as a residual (OT) and atmospheric transport (AT) from reanalyses in PW. From Trenberth & Caron (2001). 39

Figure 1.17. Solid lines as for Figure 1.11 in section 1.2.1 pertaining to present climatic conditions. Dashed lines refer to a model of the conditions around 1800 A.D. with decreased Atlantic and total oceanic heat flux and increased heat flux by atmospheric circulation. From Bjerknes (1964). 40

Figure 1.18. θ_E and θ_M as a function of latitude for the Held and Hou model (Held & Hou 1980). From James (1994). 43

Figure 1.19. The vertical distribution of potential energy (PE), sensible heat (SH), latent heat (LH) and total moist static energy near the equator for January (upper left). Mean meridional mass streamfunction for January in pressure latitude cross-section (upper right). The northward fluxes of various energies by the MMC (lower right). From Hartmann (1994) using data from Oort (1971). 46

Figure 1.20. The Ekman spiral at the ocean surface. From Ekman (1905). 47

Figure 1.21. Directions (northern hemisphere) of steady Ekman mass transports in the oceanic and atmospheric boundary layers when the stress at the surface has the

direction shown. In this figure, the wind is blowing from the west to the east (left to right), hence equatorward flow in upper ocean layers and poleward flow in lower atmospheric layers. From Gill (1982). 48

Figure 1.22. Section through a cyclone over the ocean. The geostrophic wind gives a cyclonic rotation around the low pressure centre. Ekman transport in the atmosphere is inward and associated pumping velocity is upward. The Ekman mass transport in the oceanic boundary layer is equal and opposite, so there is an outward mass transport and upward pumping velocity in the ocean. This tends to raise the thermocline. From Gill (1982). 51

Figure 1.23. Representation of the coupling of ocean and atmosphere heat transport, as envisioned by Held (2001), where h represents moist static energy in the atmosphere, and theta is ocean temperature. Grey curved lines represent constant h and theta in the atmosphere and ocean respectively. Horizontal and vertical gradients in h (Δh) are indicated in the atmosphere (similar gradients in temperature are present in the ocean). 53

Figure 2.1. Schematic meridional-vertical diagram illustrating deep convection (dashed lines) and observed shallow (solid) meridional circulations in the tropical eastern Pacific. There is southerly flow in the boundary layer, the top of which is represented by the thin dashed line. Deep clouds indicate the location of the ITCZ and depths of the shallow and deep meridional circulations are marked on the left. From Zhang *et al*. (2004) 56

Figure 2.2. 1000 hPa winds (contours) and SST (colours) for a) JJA and b) DJF. Black contours show southerly winds and white show northerly winds. Contour interval is 1 ms^{-1}. Produced using ERA40 reanalysis data. 59

Figure 2.3. Moist static energy (colours) in K and meridional winds (contours) in m s^{-1} at the equator for 1992-2001 JJA. Positive (black) contours show northward winds and negative (white) contours show southward winds. Contour interval is 0.5 m s^{-1} 63

Figure 2.4. Moist static energy (colours) in K and meridional winds (contours) in m s^{-1} as for Figure 2.3, for El Niño seasons: DJF 1998 (upper) and JJA 1997 (lower). 65

Figure 2.5. Relative humidity (colours) and mass transport (contours) at the equator for 1992-2001 JJA. Positive (black) contours are northward mass transport and negative (dashed) contours are southward mass transport, contour interval is 0.5 Sv. 70

Figure 2.6. As for Figure 2.5 but for DJF 70

Figure 2.7. As for Figure 2.5 but for MAM. 72

Figure 2.8. As for Figure 2.5 but for SON. 72

Figure 2.9. Estimates of summed positive and negative mass transport for each season, produced from data shown in Table 2.1. 76

Figure 2.10. Atmospheric meridional mass transport streamfunction within moist static energy layers (C.I. = 25 Sv), positive clockwise, for May-September 2003, y axis is moist static energy. Upper grey curve is the zonally averaged moist static energy at the tropopause and lower curve is at the ground. From Czaja & Marshall (2006). 77

Figure 2.11. Positive and negative mass transport and relative humidity (as for Figure 2.5) for the region 44^o to 58^o at the equator, corresponding to the region of the Somali Jet during JJA. 78

Figure 2.12. Schematic to represent features of mass transport over the Indian and Pacific Oceans at the equator in JJA. Circles represent centres of mass transport, crosses show circulation into the page (northward), dots represent transport out of the page (southward). The central region over the western Pacific is deeply convecting........ 79

Figure 3.1. A schematic of the interaction of convection with a large scale circulation driven by a) small and b) large surface temperature gradients. The dashed lines indicate contours of constant saturation entropy, while the thick arrows depict the large scale circulation and thin arrows represent convection. From Emanuel *et al.* (1994)........ 85

Figure 3.2. Horizontal and vertical standard deviation of moist static energy throughout the region enclosed by a given column averaged RH, divided by C_p, as a function of (mass weighted) vertical mean RH (left). Mean moist static energy profiles (right) for the convective region (solid line) and non-convective region (dashed line) based on a threshold between convective and non-convective regions of 60% vertically averaged RH........ 86

Figure 3.3. Vertical mean mass weighted relative humidity between the surface and 100 hPa in the tropics for DJF (top) and JJA (bottom). The thick black line represents 60% relative humidity, and hence areas within the thick black line represent the convective region. 87

Figure 3.4. Percentage of total equatorial data points classed as convective (vertically averaged relative humidity > 60%) for a) seasonal means over the 22 year period and b) monthly means for the 22 years. Year markers on axis in a) refer to JJA in each case. The dashed lines in a) and b) represent the long term mean value. c) Variation of mean SST (Kelvin) with vertical mean RH (%). 88

Figure 3.5. Total zonally integrated poleward heat transport and the contribution from the convective region in Petawatts (1 PW = 10^{15} Watts) for seasonal data. The diagonal

line represents a 1:1 ratio of convective region heat transport to total heat transport. Each point represents a season from the years 1980 to 2001. Seasons are: DJF (green circles), MAM (blue squares), JJA (red triangles), SON (yellow stars) and mean values for each season are represented by crosses. 91

Figure 3.6. Poleward heat transport by the convective region H_* in PW and the extent of the convective region L_* represented by the number of degrees longitude at the equator which are classed as convective, out of a maximum 360 degrees. A linear fit has been added to the data for each season. Each point represents a year from 1980 to 2001, seasons are: DJF (green circles) and JJA (red triangles). 94

Figure 3.7. Seasonal cross equatorial convective region mass transport ψ_* in Sverdrups (where 1 Sv = 1×10^9 kg s^{-1}) and convective region heat transport H_* in PW. Each point represents a year from 1980 to 2001, seasons are: DJF (green circles) and JJA (red triangles)... 96

Figure 3.8. Deviation of convective region mass transport from the mean $d\psi_{ovr}/\psi_{ovr}$ against the fractional deviation of convective region extent from the mean dL_*/L_* (crosses) and fractional deviation of mean overturning wind below P_{mid} from the mean dv_{ovr}/v_{ovr} (squares). Each point represents a deviation from the long term mean for either a DJF or JJA in the 22 year period. The line represents a 1:1 ratio between the axes...... 99

Figure 3.9. Seasonal variation of gross moist static stability Δh from annual mean. Δh_{ovr} was calculated using H_{ovr}/M_{ovr}, and *Δh 2 layer* was calculated using the difference between h averaged over an upper layer and h averaged over a lower layer. Δq is the contribution to Δh from humidity using the 2 layer model, *Δq using fixed R* used a fixed annual mean value of relative humidity, and *ΔDSE* (dry static energy) is the contribution to the gross moist static stability anomaly from temperature and geopotential terms only. See text for details of calculations. 100

Figure 4.1. The aquaplanet geographies used by Smith *et al.* (2006): left: WaterWorld, middle: RidgeWorld, and right: DrakeWorld. From Smith (2004). 106

Figure 4.2. Annual mean zonally averaged meridional heat transport in PW for 3 coupled equilibria. Hemispherically symmetric solution based on thermal buoyancy (solid), asymmetric pole to pole forcing (dotted) and symmetric solution based on freshwater forcing (dashed). Panels represent atmosphere component, ocean component and total atmosphere plus ocean component. From Saravanan & McWilliams (1995)............... 107

Figure 4.3. Relative contribution of ocean (grey) and atmosphere (black) to the total energy transport for an aquaplanet (continuous curves), and observed ratios using NCEP and ECMWF heat transports (broken curves). From Czaja & Marshall (2006). 108

Figure 4.4. a) Correlation of decadal atmospheric and Atlantic Ocean energy transports and b) Time series of decadal anomalies in extratropical atmospheric energy transport (bold), Atlantic energy transport (solid) and Atlantic Meridional Overturning Index (dashed). Units in b) are PW (left) and Sverdrups (right) and time in years (x axis). From Shaffrey & Sutton (2006). 110

Figure 4.5. Potential temperature (colours) and zonal wind (contours) for atmosphere (upper) and theta (colours) and zonal current (contours) for ocean (lower). Black contours show eastward flow and white contours show westward flow. Units are K for potential temperature and meridional velocity contour interval is 2 m s^{-1} (upper) and 0.1 m s^{-1} (lower) for zonal flow. 112

Figure 4.6. Atmospheric surface temperature in ^{o}C, against latitude, mean for years 980-1020. 113

Figure 4.7. Zonal mean precipitation in mm day^{-1} for waterworld. Mean for years 980 - 1020. 114

Figure 4.8. Zonal mean meridional wind in ms^{-1} (colours) and potential temperature in Kelvin (contours) versus latitude, annual mean for years 980-1020. Arrows show direction of circulation. 115

Figure 4.9. Zonal mean net TOA radiation (blue) and surface heat flux into the ocean (green) in Wm^{-2} versus latitude, mean for years 980-1020 of the FORTE model waterworld run. 116

Figure 4.10. Total northward heat transport (red), ocean heat transport (green) and atmospheric heat transport (blue), in petawatts, mean for years 980-1020. 117

Figure 4.11. Schematic showing direction of energy fluxes in the ocean and atmosphere in a 20^{o} latitude band. Vertical red arrows represent heat fluxes from the TOA and flux between atmosphere and ocean, and horizontal arrows show heat transport out of the latitude band by the ocean and atmosphere. There is storage of heat in the ocean, but this is assumed to be negligible in the atmosphere. 118

Figure 4.12. Ocean heat transport (*HO*) and atmospheric heat transport (*HA*) out of 20^{o} band in PW, for years 500-1020, calculated from TOA and surface fluxes and ocean heat storage. 121

Figure 4.13. Timeseries of annual mean *HA*, *HO*, F_t, F_s and *storage* for years 500 to 1020, in PW. 121

Figure 4.14. Difference from mean *HO* and difference from mean *storage* for annual means, from year 500 to 1020, in PW. 122

Figure 4.15. Zonal mean wind stress 40 annual means (left), years 980 to 1020 and zonal mean wind stress in the tropics (right) in Nm^{-2} 123

Figure 4.16. zonal mean wind stress from model output windstress field, τ_x (black), windstress calculated using low level atmospheric wind for monthly output (blue) and daily output (red) using equation (4.6). Differences between τ_x and the monthly calculation (blue dashed) and τ_x and the daily field (red dashed) are included. 125

Figure 4.17. Ocean heat transport out of 20 degree latitude band (*HO*) and the Ekman heat transport in the ocean (HO_{Ek}) in petawatts shown with blue markers. HO_{Ek} calculated using fixed Δθ is shown with red markers. 127

Figure 4.18. Contribution to moist static energy of (a) internal energy, (b) latent heat, (c) geopotential and (d) their total, in Kelvin. 129

Figure 4.19. Zonal mean moist static energy profiles at various latitudes (divided by C_p to give units in Kelvin). Mean for years 980-1020. 130

Figure 4.20. Meridional wind profiles for 40 years of annual means (980-1020yrs of the model run) at 20^oN, 20^oS (left) and the equator (right), in ms^{-1} 131

Figure 4.21. Atmospheric heat transport from radiative fluxes, *HA*, and axisymmetric atmospheric heat transport, HA_{axisym} in PW at 20^o latitude. 133

Figure 4.22. Ekman heat transport in the ocean, HO_{Ek}, and axisymmetric heat transport in the atmosphere, HA_{axisym} in PW. 134

Figure 4.23. Timeseries of main components of heat transport for years 500 to 1020 in PW. See text for explanation. 134

Figure 4.24. Eddy heat flux versus latitude for years 585 to 600. (Data kindly donated by Jacob Cheung, Imperial College.) 136

Figure 4.25. The transient eddies showing the contributions to the total of latent heat, sensible heat and potential energy for a) model results and b) observations (Oort & Peixoto 1983). From Colman *et al*. (1994). 137

Figure 4.26. Annual average northward energy flux versus latitude in Northern Hemisphere for real world. MMC indicates mean meridional circulation. Data from Oort (1971), figure from Hartmann (1994). 138

Figure 4.27. Zonal-mean cross sections of the mass stream function in 10^{10} kg s^{-1} for annual, DJF and JJA mean conditions. Vertical profiles of the hemispheric and global mean values are shown on the right. From Peixoto & Oort (1992)............................. 139

Figure 4.28. Detrended timeseries of *HO*, *HA*, F_t and *storage* (top), and 10, 20 and 50 year running means (2nd, 3rd and 4th panels). 140

Figure 4.29. Power spectra for *HO*, *HA*, F_t, *SO*, H_t, HO_{Ek} and HA_{axisym} using Thomson multitaper method.. 141

Figure 5.1. Mass transport as a function of surface moist static energy for JJA. Colours represent relative humidity and contours are mass transport, solid northward and dashed southward. On the right hand side, high relative humidity represents the convective regions, where heat transport takes a dipolar form. The low-level Somali jet is visible centred around 342 K, with little return flow at upper levels. Below 336 K is the region associated with low relative humidity and low surface moist static energy, where the mass transport is more complicated. Figure repeated from section 2.5.3. 145

Figure 5.2. Convective region heat transport and total poleward heat transport at the equator, showing that the convective region contributes significantly to the total heat transport. Figure repeated from section 3.3.1. 146

Figure 5.3. The relation between atmospheric and oceanic heat transport out of the tropics in the FORTE aquaplanet calculated using radiative fluxes and ocean heat storage. The figure shows there is no correlation between *HO* and *HA* at 20° in FORTE. Figure repeated from section 4.4.2. 148

List of tables

Table 2.1. Estimates of summed positive mass transport (Mpos) and summed negative transport (Mneg) for each season. The estimates have been broken down into total mass transport, transport only over the ocean, over low h_{sfc} and high h_{sfc}, and the mass transport associated with the Somali Jet in JJA. All mass transports are in Sv. Included is the difference between the magnitude of Mpos and Mneg (Diff) and estimates of the mean moist static energy in the lower and upper layers (h lower, h upper), and the difference between them: an estimate of the Δh in the vertical in Kelvin. 74

Table 2.2 Thresholds determining regions of high h_{sfc} and low h_{sfc} for each season (K) in order to calculate Mpos and Mneg 75

Table 3.1. Mean seasonal total cross equatorial heat transport (H_A) and convective heat transport (H_*) in PW using 3 different RH thresholds to define the convective regions (60% threshold is used throughout the chapter and shown in bold, other results are included for interest) over the 22 year period. Positive values represent northward transport and negative values represent southward transport. Numbers in brackets represent the ratio of H_* to H_A. 92

Table 3.2. The relationship between convective region heat transport and longitudinal extent of the convective region. Rate of change of convective region heat transport with growth of the convective region (dH_*/dL_*) is shown in the second column. The correlation is significant to the 99% level in DJF, although not statistically significant above 80% in JJA. 94

Table of Contents

Abstract 2

Acknowledgements 3

Abbreviations 4

Table of figures 6

List of tables 14

Table of Contents 15

Chapter 1 Introduction 19

1.1 Tropical dynamics and climatology 21

1.1.1 Regulation of the tropics 22

1.1.2 The Hadley Circulation 24

Hadley Cell seasonality 24

1.1.3 The El Niño Southern Oscillation (ENSO) and the Walker Cell. 28

1.1.4 The Asian monsoon circulation 31

1.2 Observations and estimates of meridional heat transport 32

1.2.1 Methods for calculating heat transport 32

1.2.2 Overview of heat transport estimates 34

1.2.3 Bjerknes Compensation 39

1.3 Poleward heat transport in the tropical ocean and atmosphere 41

1.3.1 The Held and Hou model of the Hadley Circulation 41

1.3.2 Moist static energy 44

1.3.3 Ekman transport 47

Ekman Dynamics 48

Ekman Pumping 50

1.4 Coupling of heat transport: An overview of a simple model of the tropics (Held 2001) 51

1.5 Key questions addressed in this thesis 54

Chapter 2 The distribution of moist static energy and meridional mass transport in the tropical atmosphere 55

2.1 Introduction 55

2.2 Data 57

2.3 Seasonal variability in meridional surface winds and SST in the tropics 58

2.3.1 SST and low level moist static energy in the tropics 59

2.4 The distribution of moist static energy and meridional flow at the equator 61

2.4.1 Overview of moist static energy in the tropics 61

2.4.2 Seasonal variability 62

June – August 63

December – February 64

2.4.3 Interannual variability 64

December to February 65

June - August 66

2.5 Mass transport as a function of low level moist static energy 67

2.5.1 Framework of analysis 67

2.5.2 Method 68

2.5.3 Seasonal results 69

June - August 71

December - February 73

March – May and September – November 73

2.6 Estimates of atmospheric mass transport in the tropics 74

2.6.1 Mass transported by the Somali Jet 77

2.7 Summary and conclusions 79

Chapter 3 Deconstructing the cross-equatorial Hadley Cell heat transport: the role of convective regions 82

3.1 Introduction 82

3.2 Framework and Methodology 84

3.2.1 Data 84

3.2.2 Definition of convective regions of the tropics 84

3.2.3 Calculating baroclinic wind in convective regions 88

3.2.4 Atmospheric heat transport calculation 89

a) Total heat transport 89

b) Convective region heat transport 89

3.3 Results 90

3.3.1 The contribution of the convective region to the total heat transport 90

3.3.2 Mechanisms controlling convective region heat transport 93

a) Convective region extent 93

b) Mass transport and heat transport 95

c) Variability of meridional wind strength and convective region extent 96

d) Seasonal variability of gross moist static stability 99

e) El Niño conditions 102

3.5. Summary and conclusions 103

Chapter 4 The coupling of ocean and atmosphere heat transport in the FORTE aquaplanet coupled model 105

4.1 Using an aquaplanet coupled model to study heat transport 105

4.1.1 Testing theories of ocean-atmosphere interaction using FORTE 109

4.2 Components and details of the FORTE model 110

4.3 Climate of the FORTE aquaplanet 111

4.4 Heat transport calculations 115

4.4.1 Heat transport calculated from radiative fluxes 115

4.4.2 Heat transport out of the tropics 118

4.5 Heat transport associated with surface winds 122

4.5.1 Wind stress calculations 122

4.5.2 Ekman mass transport 125

4.5.3 Ekman heat transport in the ocean 126

4.5.4 Axisymmetric atmospheric heat transport (HA_{axisym}) 128

4.6 Atmospheric Eddy heat transport in FORTE 135

4.7 Timeseries analysis 139

4.8 Summary and conclusions 142

Chapter 5 Summary and conclusions 144

5.1 Future work 148

Appendix – Isolating the convective region heat transport using a baroclinic framework 150

A.1 Description of the model 150

A.2 Validation of baroclinic decomposition model against previous results 154

Bibliography 156

Chapter 1 Introduction

The geometry of the earth is such that the tropics receive more incoming solar energy than the extra-tropics; hence there is a temperature gradient between the equator and the poles. In fact, the tropics receive more energy from the sun than they emit and the extra-tropics emit more energy than they receive. The curves in Figure 1.1 show the latitudinal variation in insolation and emitted radiation in W m^{-2}. The amount of emitted longwave energy has a flatter distribution than the absorbed radiation, indicating that there must be heat transport from the tropics towards the poles in order for a global thermal equilibrium to exist.

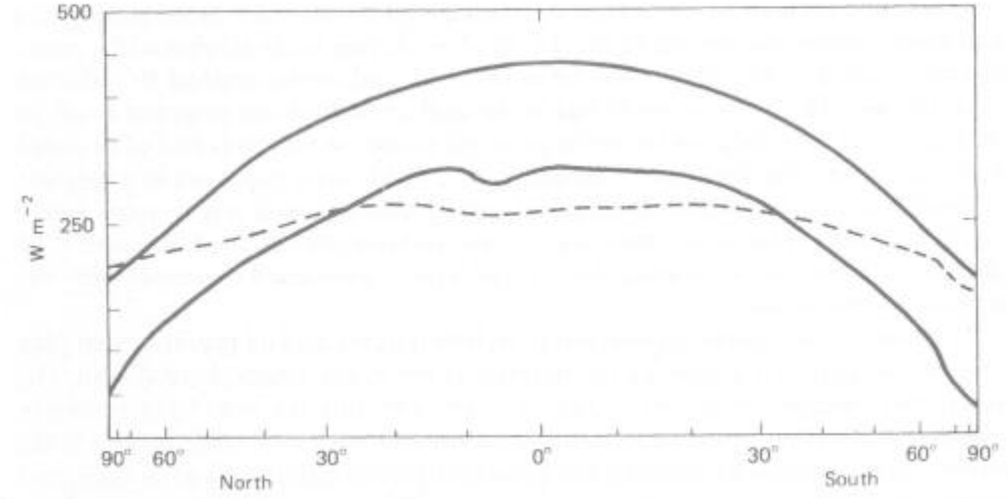

Figure 1.1. The radiation balance of the earth averaged over a 4 year period. Upper solid curve shows the average flux of solar energy reaching the outer atmosphere and lower solid curve shows the amount of solar energy absorbed. The dashed line shows the average amount of outgoing radiation. From Gill (1982).

In recent years, the aim of much research has been to discover the relative roles of the ocean and atmosphere in the poleward transport of heat (e.g. Held (2001), Trenberth & Caron (2001), Wunsch (2005), Czaja & Marshall (2006)). The complexity of the earth's system means that the way energy is transported around the planet, and indeed how energy transports may change under different conditions in the future, is an area which requires continuing investigation. In the past, a lack of observational data, especially in the oceans where data is often geographically confined (Wunsch 1997) has made estimates difficult, but recent observational campaigns, for example, the World Ocean Circulation Experiment (WOCE 2003), have provided more accurate and spatially diverse data, and more and more accurate estimates of the partitioning between ocean and atmosphere are being computed over time (Trenberth & Caron 2001; Wunsch 2005). As well as studying the proportion of the heat transport taking place in the ocean and atmosphere, we need to understand the basic mechanisms of heat transport in both. In the atmosphere, different circulation patterns, such as the Walker and Hadley Cells in the tropics, and the mid latitude westerlies and storm tracks (Figure 1.2) influence how heat it transported. In the ocean, heat transport takes place as a result of geostrophic flow driven by pressure differences and wind driven currents.

A strong coupling between the ocean and atmosphere means that each plays a role in determining how heat is transported by the other. For example, ocean circulation near the surface is largely driven by winds, and lower atmosphere moisture and temperature are heavily influenced by ocean conditions such as sea surface temperature (SST). This coupling means that a change in any part of the earth’s system, such as an increase in greenhouse gases resulting in changes in radiative conditions in the atmosphere, is likely to drive changes in both the ocean and atmosphere. This could lead to changes in regional temperatures, global circulation, precipitation patterns, storms and more (Solomon *et al.* 2007). All these factors can have catastrophic consequences for mankind, including increased flood and drought risk, increased storm occurrence or intensity, and difficulties for agriculture. It is important to discover how the ocean and atmosphere work together, for example do variations in heat transport in one media follow that of the other, e.g. Held (2001), or is there compensation between the ocean and atmosphere meaning that variations are anticorrelated, e.g. Bjerknes (1964)? A greater understanding of the mechanisms of ocean and atmosphere heat transport and the coupling between them will aid more accurate predictions of possible global and regional climate scenarios for the future.

This thesis focuses particularly on the tropics, where ocean and atmosphere play an approximately equal role in poleward heat transport (Trenberth & Caron 2001). We first use reanalysis data to investigate spatial variations in parameters such as SST, meridional mass transport and moist static energy, which play a role in poleward heat transport. After identifying the differences in mass transport in the atmosphere as a function of low level moist static energy, emphasis is given to determining the atmospheric heat transport associated with the Hadley Cell in the convective regions of the tropics. We also investigate ocean and atmosphere heat transport using a coupled aquaplanet GCM to enable us to try to determine the extent to which the ocean and atmosphere heat transport is coupled in the tropics.

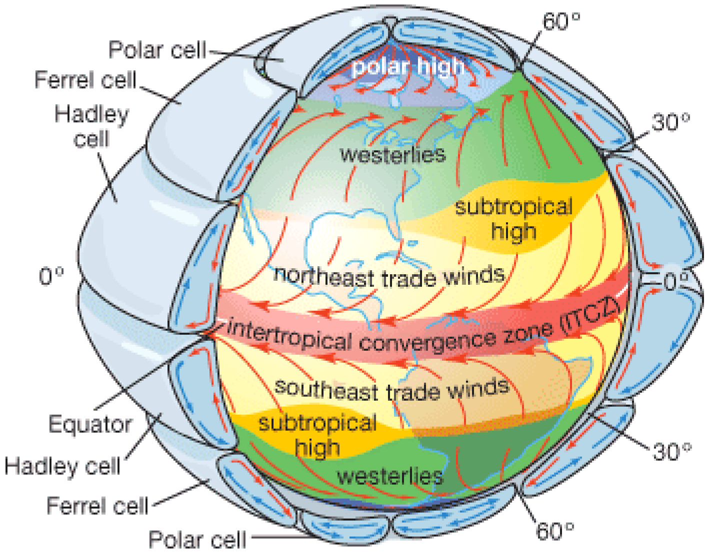

Figure 1.2. General circulation of the atmosphere. From online Encyclopaedia Britannica (Britannica 2008)

This chapter continues by providing a background to the analyses presented in the thesis. It begins with an overview of the main features of the tropical climate. We then provide a review of observations and estimates of meridional heat transport and look at meridional ocean and atmosphere heat transport in the tropics. The chapter concludes with an overview of the simple heat transport model of Held (2001), followed by some key questions addressed in the thesis.

1.1 Tropical dynamics and climatology

The tropics comprise half the surface of the planet, and motions in the tropics represent an important component of the dynamics of the whole planet through various teleconnections; the midlatitudes may also influence conditions in the tropics by means of propagating waves and heating anomalies (Tomas & Webster 2003). Figure 1.3 shows a global infrared image which highlights features in the tropics such as clusters of convective clouds aligned in narrow bands indicating the position of the inter-tropical convergence zone (ITCZ). There are also regions of subsidence in the subtropics with little cloud, for example over much of north Africa. In the extra-tropics, wave-like baroclinic disturbances dominate (Figure 1.3). Large scale circulations in the tropics include the Hadley circulation, the Walker Cell, monsoon circulations and those influenced by the El Niño Southern Oscillation (ENSO).

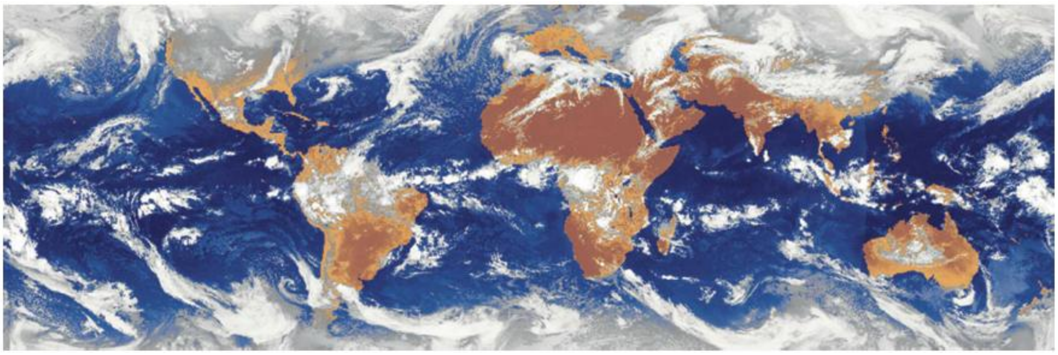

Figure 1.3. Composite image of instantaneous infrared imagery from geostationary satellites (1200 UTC 29th March 2004). From SATMOS, © METEO-FRANCE and Japan Meteorological Agency. From Bony *et al*. (2006).

For the rest of section 1.1, we focus on the climate of the tropics. We next discuss how the temperature of the tropics appears to be regulated. We then move on to describe the Hadley Circulation, which is the dominant mechanism in the meridional transport of heat in the tropical atmosphere. The section concludes after a discussion of the Walker Circulation, ENSO and the tropical monsoon circulation.

1.1.1 Regulation of the tropics

There is considerable interannual variability in the tropics. The El Niño Southern Oscillation (ENSO) is associated with large gradients in the temperature of the surface of the ocean, yet the maximum SSTs in the tropics are fixed at around 29^{o}C (Figure 1.4). Past paleoclimate data suggests a fixed upper limit on SST, although it is not clear how the tropics maintain this limit (Philander & Fedorov 2003). Ramanathan & Collins (1991) proposed that the tropical Pacific SST is mainly regulated by negative feedback from cirrus clouds, which they called the ‘thermostat hypothesis’. The theory was that feedbacks between SST, convection and cloud reflection of solar radiation prevents a runaway greenhouse effect and acts as a thermostat to limit the maximum SST. This implies that even an order of magnitude larger CO_2 forcing in the atmosphere would result in an increase in the maximum SSTs of only a few degrees, although there would be significant warming outside the deep tropics (Ramanathan & Collins 1991). This work sparked off alternative proposals as to how the tropics are regulated. Further theories included those where evaporation at the surface is thought to be more important in terms of limiting tropical SST (Hartmann & Michelsen 1993). Also there were those where it is the coupling between large scale circulation and the local environment which is thought to be the main mechanism for regulation, for example, heat is transported from convective regions to the dry subtropics, where it is radiatively cooled (Wallace 1992; Pierrehumbert 1995; Sun & Liu 1996).

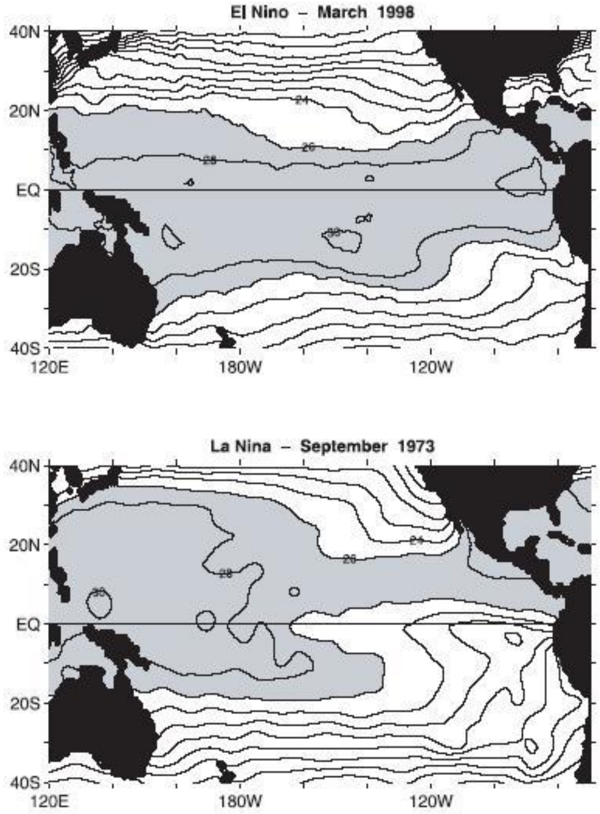

Figure 1.4. Sea surface temperatures (degrees Celsius) for El Niño and La Niña. From Philander & Federov (2003).

Wallace argued that heat transported by the large scale circulation regulated the tropical temperature and that feedback from cirrus clouds would be unable to reduce temperatures below 305 K in the face of extensive greenhouse warming (Wallace 1992). In reply, Ramanathan and Collins answered that Wallace's theory did not fit with observations and pointed out that extensive evaporation was suppressed in the western Pacific ocean due to the high humidity in the boundary layer while feedback from clouds was highly sensitive (Ramanathan & Collins 1992). Obviously, the complex nature of the regulation of temperatures in the tropics and the associated feedback mechanisms requires greater understanding.

By considering the coupled nature of the oceanic and atmospheric circulation, we may be able to address some fundamental climate questions. For example, what would happen to oceanic and atmospheric heat transport as tropospheric temperatures increase due to increased greenhouse gases? Also, how is the energy transport different during periods where surface temperatures are relatively spatially uniform (e.g. El Niño conditions) and conditions where there are strong surface temperature gradients (e.g. La Niña), (Figure 1.4)? Next we introduce the Hadley circulation, which dominates meridional heat transport in the tropical atmosphere.

1.1.2 The Hadley Circulation

The Hadley cells are thermally driven, direct circulations in the tropical atmosphere between 30^{o}N and 30^{o}S which conserve angular momentum (Held & Hou 1980). The circulation was proposed by both Edmond Halley and George Hadley over 250 years ago even though at that time, there was no way to discover the state of the winds at upper levels in order to verify the theory (Halley 1686; Hadley 1735). The cells consist of low level flow toward the equator (the north-easterly and south-easterly trades), ascending air near the equator, in the region of the intertopical convergence zone (ITCZ), poleward flow aloft, and descent in the subtropics (James 2003). The Hadley Cells are illustrated in the schematic of Figure 1.2 as part of the general circulation of the atmosphere.

The sinking of relatively cool air in the subtropics and the rising of lighter warm moist air at the equator means that potential energy is released by the circulation, and this is converted to kinetic energy to help drive the circulation (James 2003).

Hadley Cell seasonality

On an annual, zonal mean basis, the Hadley Circulation takes the form of two overturning cells, centred just north of the equator (Figure 1.5).

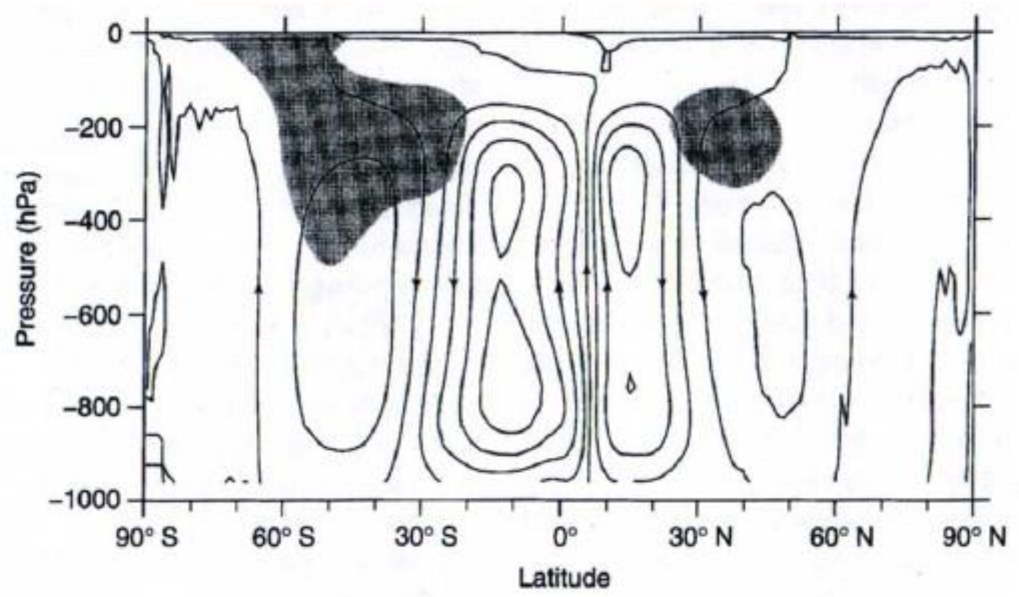

Figure 1.5. The annual mean meridional streamfunction. Contour interval 20 x 10^9 kg s^{-1}. Shading shows zonal winds greater than 20 m s^{-1}, based on 20 years of ECMWF analysis. From James (2003).

The streamfunction is defined as:

$$\psi = \iint_{P}^{P_s} v \frac{dP}{g} dx \tag{1.1}$$

where *v* is meridional wind, *P* is pressure (P_s is surface pressure) and *x* is longitude.

Rising motion near the equator and sinking motion around 30° in each hemisphere defines the two overturning cells. However, on shorter timescales, e.g. seasonal or monthly, the Hadley circulation differs from this almost symmetric picture, due to the change in the position of maximum insolation relative to the equator. A month by month view of the zonal mean circulation is shown in Figure 1.6.

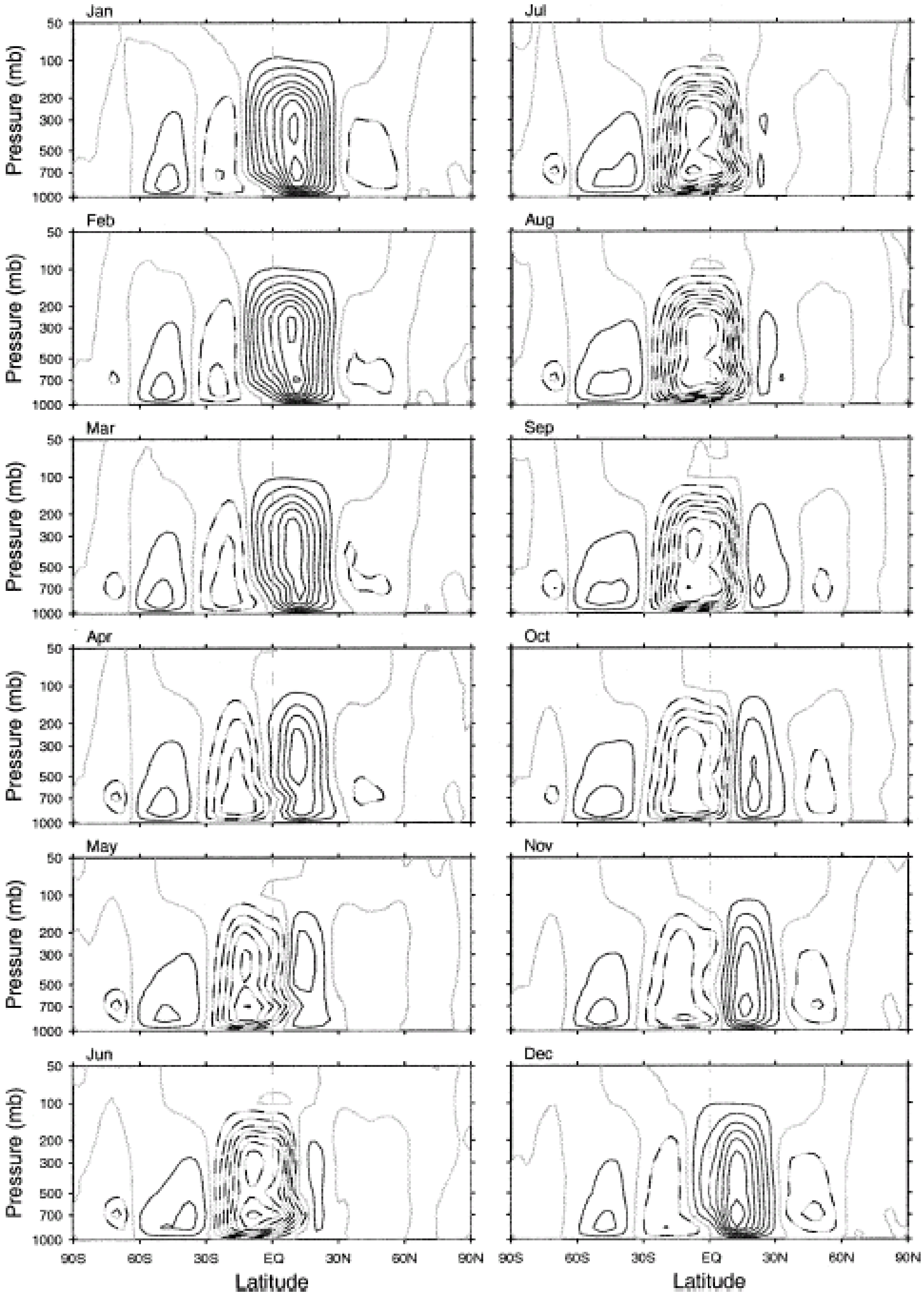

Figure 1.6. Monthly variation of the climatological-mean streamfunction in the NCEP-NCAR reanalysis. Contour interval is 20 x 10^9 kg s^{-1}, solid positive, dashed negative. From Dima & Wallace (2003).

Months where the latitude of maximum insolation is furthest from the equator (July, January) exhibit a circulatory pattern where the winter cell is greatly enhanced and the summer cell much decreased (Figure 1.6). During months where the position of the sun is over the equator, (April, October), the circulation appears more like the annual mean picture (Figure 1.5). It was suggested that the solsticial pattern would dominate the tropical mean meridional circulation throughout most of the year, with the equinoctial pattern only present fleetingly between single cell distributions (Lindzen & Hou 1988). Lindzen and Hou suggested that the idealized equinoctial pattern is “almost never realized” due to the sensitivity of the mean meridional circulation (MMC) to small equatorial asymmetries at the surface. Later it was suggested that the ‘square wave’ type transitions between solsticial patters were not as abrupt as thought (Fang & Tung 1999; Dima & Wallace 2003), although the theory that small displacements of the thermal equator might be responsible for driving the solsticial cell persists. An alternative view is that it is largely the regionally concentrated monsoon circulation which drives the solsticial cell. Dima and Wallace (2003) suggest that the equatorially symmetric and asymmetric components can be considered to be of roughly comparable importance, because of the smaller meridional scale of the slightly enhanced solsticial circulation. They support the theory that the monsoon circulation coincides closely with the maximum asymmetrical component and hence plays a large role in interhemispherical mass transport (Dima & Wallace 2003; Schulman 1973). Walker & Schneider (2005) also studied seasonal variability in the Hadley Circulation and their results were largely consistent with Dima & Wallace (2003). They postulated that the nonlinear amplification of the annual averaged Hadley Cell found in Held & Hou (1980) and Lindzen & Hou (1988) was largely due to the upper boundary condition of a nearly inviscid lid. They point out that different seasons approach the nearly inviscid limit at varying degrees and that baroclinic eddies at the poleward edge of the cell may influence the Hadley Cell strength (Walker & Schneider 2005). Chapters 2 and 3 of this thesis aim to investigate the relative roles of the Hadley Cell and the monsoon circulation in transporting heat. We also highlight the role of atmospheric eddies in the tropics, in chapter 4.

The Hadley Cell is at a maximum in the winter hemisphere during the solsticial seasons JJA (June to August) and DJF (December to February), (Figure 1.7). The cross-equatorial mass transport in these seasons is also at a maximum. It is for these reasons that we concentrate on the cross equatorial heat transport during the solsticial seasons in much of chapter 2 and 3. There is an asymmetry in the annual mean atmospheric heat transport at the equator due to the position of the ITCZ north of the equator for most of the year (Philander *et al.* 1996), meaning that the atmosphere has a net southward transport across the equator on annual timescales. Investigating atmospheric heat transport at the equator in all seasons of the year therefore goes towards understanding the mechanisms underlying this asymmetry.

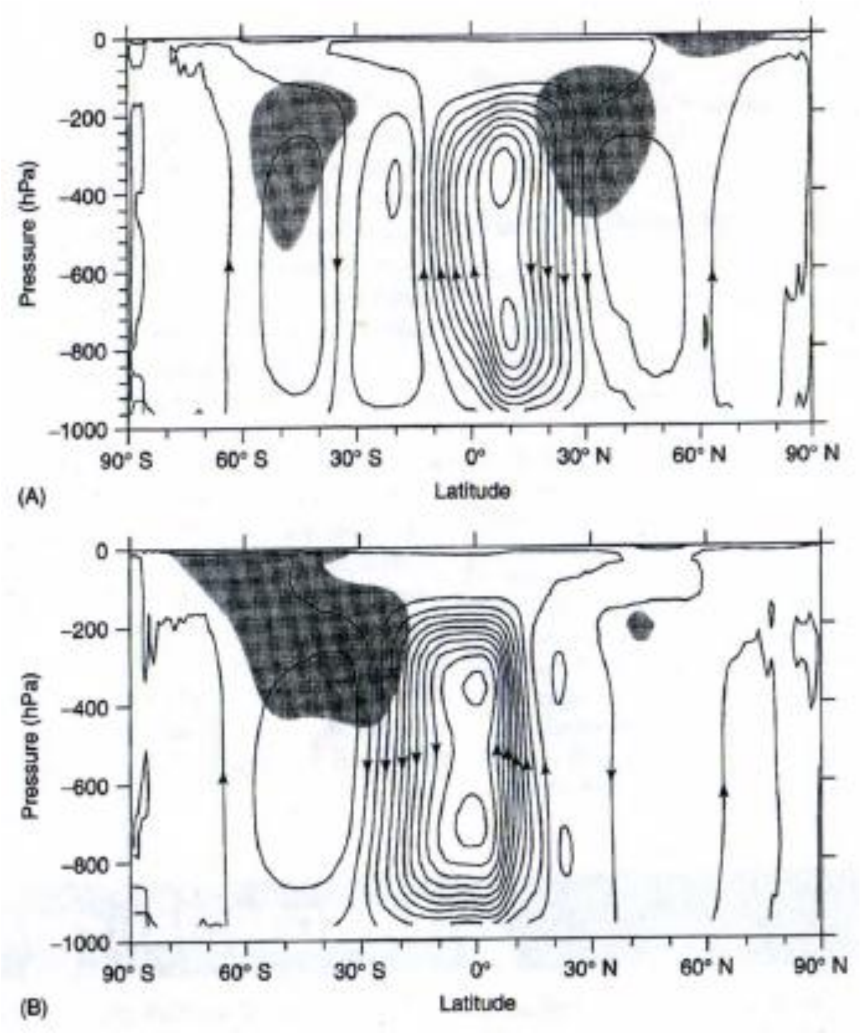

Figure 1.7. Mean meridional circulation for A) DJF and B) JJA. Other details as for Figure 1.5. From James (2003).

1.1.3 The El Niño Southern Oscillation (ENSO) and the Walker Cell.

In 1969, Bjerknes suggested a link between a circulation cell in the tropics, the Walker Cell, and the east-west SST contrast in the Pacific Ocean associated with the Southern Oscillation (Bjerknes 1969). The Walker Cell consists of rising air over the warm waters of the western Pacific Ocean, flow towards the east Pacific aloft, and sinking over the east Pacific. The Southern Oscillation is a large scale pressure difference with dipoles over the eastern South Pacific and Indonesia. The timescale of the anomalously low/high surface pressure at Tahiti/Darwin is 2 to 10 years (Tomas & Webster 2003). It was

Bjerknes who recognized that the Walker Cell was associated with the El Niño phenomenon on the west coast of South America (Bjerknes 1969).

The El Niño phenomenon concerns the anomalous warming of surface waters in the east Pacific. During an El Niño phase, the trade winds in the western and central equatorial Pacific weaken or reverse. The western Pacific warmpool migrates eastward as a result, and this means the equatorial cold 'tongue' of water which is usually present between the west coast of South America and the international dateline does not occur (McPhaden 1999). The cold tongue is usually present as a result of coastal upwelling to replace the surface waters which are advected westward by the trade winds. El Niño conditions are most pronounced during DJF. Figure 1.8 shows a schematic of normal conditions in the Pacific, and El Niño conditions.

During normal conditions, the Walker Cell is shown as as a convective loop (top). The thermocline, which represents a sharp vertical temperature gradient between the top 100 m or so of well mixed, relatively warm ocean and the rest of the ocean, can be seen below the surface in Figure 1.8. White arrows indicate that the surface waters are advected by the trade winds towards the west. The shallow thermocline in the east Pacific in normal conditions means that cold waters are outcropping at the surface. In the lower panel, El Niño conditions mean that the Walker Cell has been disrupted and the centre of convection that is usually near the western Pacific has migrated towards the central Pacific. Warm surface waters extend all across the tropical ocean and the thermocline is less tilted, meaning the cold deep waters do not reach the surface. The opposite phase of El Niño is La Niña, where the Walker Cell is strengthened (Philander 1990). SSTs in the tropics for March 1998, which was an El Niño year, and September 1973, a La Niña year, are shown in Figure 1.4. In the upper panel, the highest SSTs extend across the Pacific and there is no cold tongue in the east Pacific. The lower panel shows areas of lower SST, coinciding with upwelling of cold waters.

The phases of El Niño reflect changes in the circulation of the tropics, particularly for the Walker Cell. It is a good example of ocean-atmosphere coupling, since conditions in the top layers of the ocean influence atmospheric convection, which leads to large scale variations in circulation. In turn, the surface winds go some way to determining the distribution of warm surface waters in the Pacific Ocean. In other words, ENSO could not exist in the ocean or the atmosphere in isolation without the influence of the other.

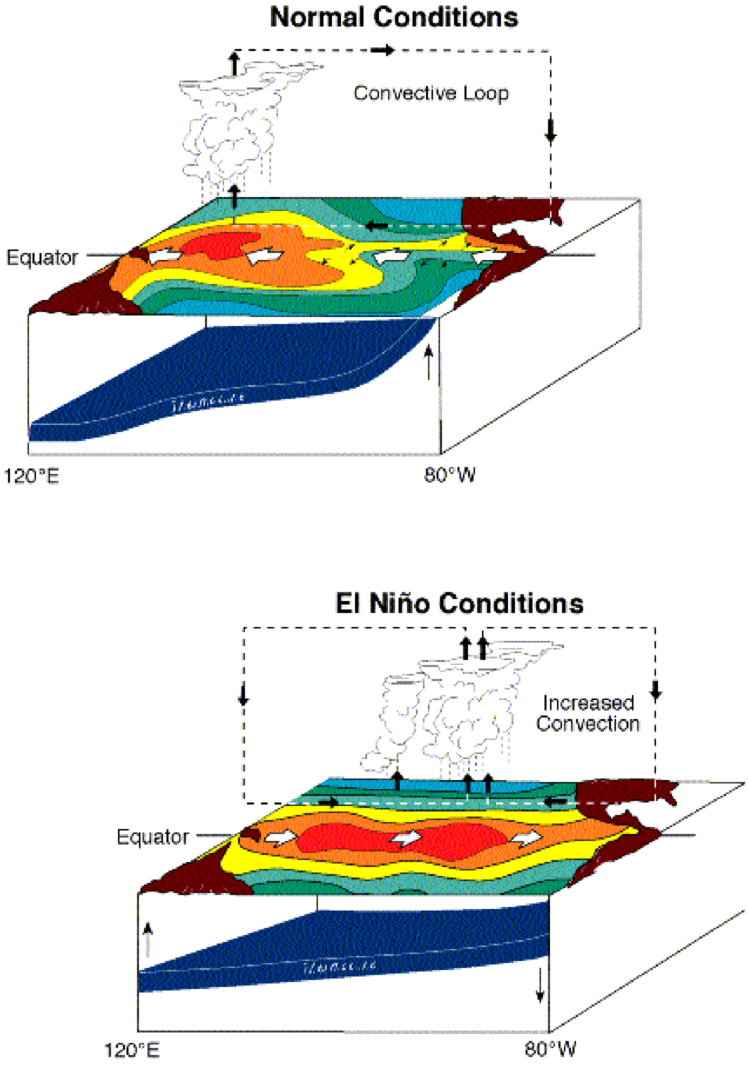

Figure 1.8. Ocean state and atmospheric circulation in the Pacific for normal conditions (upper) and El Niño conditions (lower). Colours represent SST and the thermocline is shown below the surface. The atmospheric circulation is represented by arrows and convective clouds. From the National Oceanic and Atmospheric Administration website (NOAA 2009).

In a study which concentrated on the interannual variability in the Hadley circulation, the connection between ENSO, the Walker circulation and Hadley Cell strength was measured based on observations (Oort & Yienger 1996). It was shown that anomalies in the strength of the Hadley Cell were strongly anticorrelated with the Walker circulation. The 2 symmetric Hadley Cells were enhanced during El Niño events where there were higher SSTs in the eastern Pacific, and suppressed when there were cold anomalies (Figure 1.9), (Oort & Yienger 1996). This means that we would expect the Hadley cell mass transport to increase during periods of enhanced SST and this motivates an investigation into the variation in the amount of heat transported by the Hadley Cell depending on SST. In chapter 2 we look into the distribution of moist static energy (introduced in section 1.3.2) throughout the tropical troposphere, and how this varies as a function of surface conditions. We demonstrate how the atmospheric energy differs in El Niño seasons. Also, when calculating the cross equatorial Hadley Cell heat transport in chapter 3, we investigate how heat transport varies as warm surface conditions extend throughout the tropics, as they do in an El Niño year.

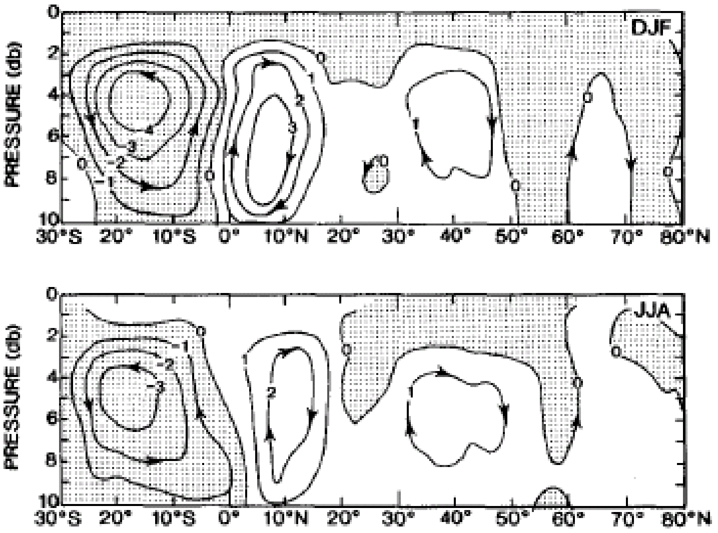

Figure 1.9. Difference in streamfunction between the five warmest and five coldest DJF (upper) and JJA (lower) seasons. Contour intervals 10^{10} kg s^{-1}. The difference is a measure of the range in values between El Niño and La Niña conditions. From Oort & Yienger (1996).

The monsoon circulation is another large scale feature of the tropical circulation, and hence has implications for heat transport. The following section offers a short introduction.

1.1.4 The Asian monsoon circulation

The tropical monsoons are seasonally reversing circulation systems driven by the contrast in thermal properties of land and sea surfaces. The temperature of land responds to seasonal changes more rapidly than the ocean. Warming of land relative to ocean can produce enhanced cumulus convection and latent heat release, leading to warm tropospheric temperatures and driving large-scale atmospheric circulations (Holton 2004).

In the Indian Ocean, the Indian Monsoon circulation results in a strong low level cross equatorial jet along the coast of Somalia towards the Indian subcontinent during northern hemisphere summer, known as the Somali Jet (Figure 1.10, right).

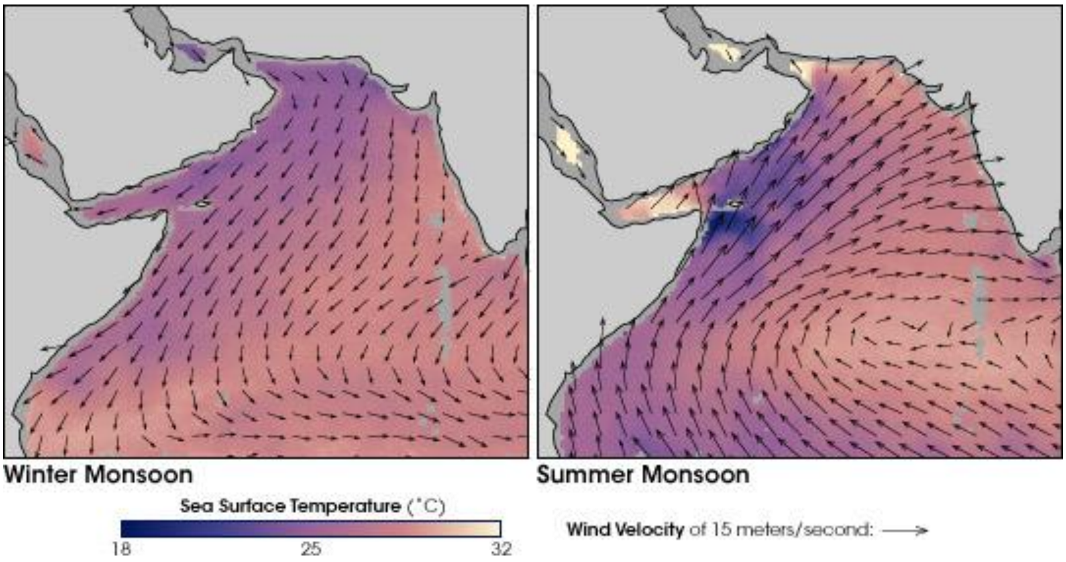

Figure 1.10. Climatology of the summer and winter Asian monsoon circulation over the Arabain Sea. Arrows represent surface winds velocity. From NASA Earth Observatory (NASA 2006).

The low level jet feeds into the convergence over the Indian subcontinent in July, and in January, when the maximum solar insolation has moved to the southern hemisphere, the direction of the circulation over the Indian Ocean is reversed. Clearly, the strong low level winds associated with the monsoon circulation play a role in the transport of atmospheric mass between hemispheres. Some consider the monsoon circulation contributes to the asymmetrical component of the Hadley Circulation (Schulman 1973; Dima & Wallace 2003), but in any case the monsoon circulation is an important feature of the meridional tropical circulation and we investigate the mass transport associated with the Somali Jet in chapter 2. Section 1.2 is a review of meridional heat transport estimates for ocean and atmosphere.

1.2 Observations and estimates of meridional heat transport

1.2.1 Methods for calculating heat transport

The ocean and atmosphere play a vital role in regulating the climate on earth by distributing heat around the globe, from the equatorial region, towards the poles. There have been many attempts to model or measure the oceanic and atmospheric heat transport over the years, and the complexity of the earth's system and a lack of global observations in the past have meant that estimates of meridional heat transport have varied, and these heat transport estimates are being refined over time.

The total heat transport consists of the contribution from atmosphere and ocean: $H_{tot} = H_A + H_O$, and these are defined as:

$$H_A = \iint \rho_A v \, h \, dxdz \tag{1.2}$$

$$H_O = \iint \rho_O v \, C_p \theta \, dxdz \tag{1.3}$$

where ρ is density, h represents moist static energy, which describes the energy of the atmosphere per mass and is fully introduced in section 1.3.2, θ is potential temperature, C_p is specific heat capacity of water and v is meridional velocity. The implied H_{tot} can be calculated by integrating the radiatiative flux at the top of the atmosphere (TOA), for example, using satellite measurements such as the Earth Radiation Budget Experiment (ERBE), (Bess & Smith 1993). Ocean heat transport can be calculated by integrating the flux into the ocean surface and taking ocean heat storage into account. In Chapter 3, we use a form of (1.2) to calculate atmospheric heat transport and in Chapter 4 we use radiative fluxes to calculate heat transport in the ocean and atmosphere of the FORTE aquaplanet model.

Heat transport estimates can be made using data from radiosondes and weather stations, or ocean sections such as that used in the World Ocean Circulation Experiment (WOCE 2003). There are also estimates which use model output such as the NCEP/NCAR (National Centres for Environmental Prediction/National Centre for Atmospheric Research) reanalysis (Kalnay *et al.* 1996) and the ECMWF (European Centre for Medium-Range Weather Forecasts) ERA40 reanalysis (Uppala *et al.* 2005). Indirect methods involve calculating implied heat transport estimates as a residual of other measured heat transport. For example, Trenberth and Caron (2001) use reanalysis data for the atmosphere and calculate the implied ocean heat transport, whereas Wunsch (2005) uses ERBE (Earth Radiation Budget Experiment) satellite data and in situ ocean data from WOCE (Ganachaud & Wunsch 2003) to calculate the atmospheric heat transport as a residual.

1.2.2 Overview of heat transport estimates

Early estimates include that of Bjerknes (1964) which includes the ocean and atmosphere contribution to poleward heat transport, and used flux data from Sverdrup (1957) and radiation data from Houghton (1954), (Figure 1.11). The estimates show a dominance of the atmosphere over the ocean in transporting heat at almost all latitudes apart from the deep tropics, where the ocean heat transport exceeds the atmosphere heat transport.

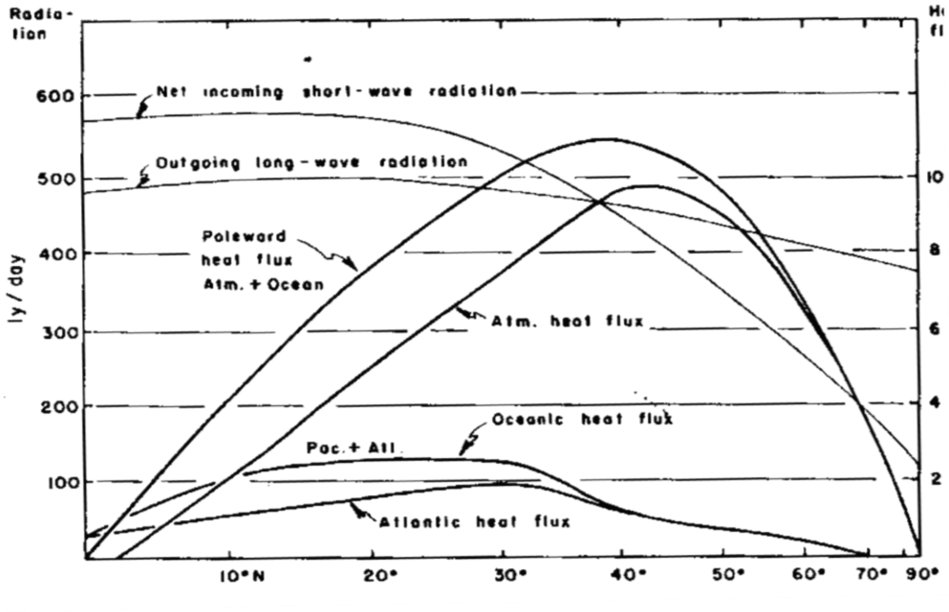

Figure 1.11. Total gain and loss of radiative heat in the northern hemisphere, total heat flux (sensible + latent) across latitude bands and meridional heat flux in ocean and atmosphere. Units on the right are 10^{19} calories per day ~ 0.5 PW (10^{15} Watts). From (Bjerknes 1964), using radiation data (Houghton 1954) and flux data (Sverdrup 1957).

A few years later, Lorenz made a similar estimate which made more of the contribution of the ocean to the total heat transport (Lorenz 1967). He based the estimates on the required energy transport from evaporation, precipitation and radiative fluxes. Lorenz splits the atmospheric component into a sensible heat component (sensible heat + potential energy + kinetic energy) and a latent heat component, represented by solid and dashed lines respectively in Figure 1.12. There is clearly compensation between these components, especially in the tropics. The ocean component of heat transport is larger than the one estimated by Bjerknes (1964). Unconventionally, Lorenz considers the latent heat transport could be thought of as being part of the ocean heat transport, if one assumes the vapour has no latent energy (Lorenz 1967). He also goes on to suggest that the compensation in the tropics is due to the equatorward transport of moist air to the Intertropical Convergence Zone (ITCZ) and the poleward transport of dry air with high potential energy away from the equator, which is indeed the case.

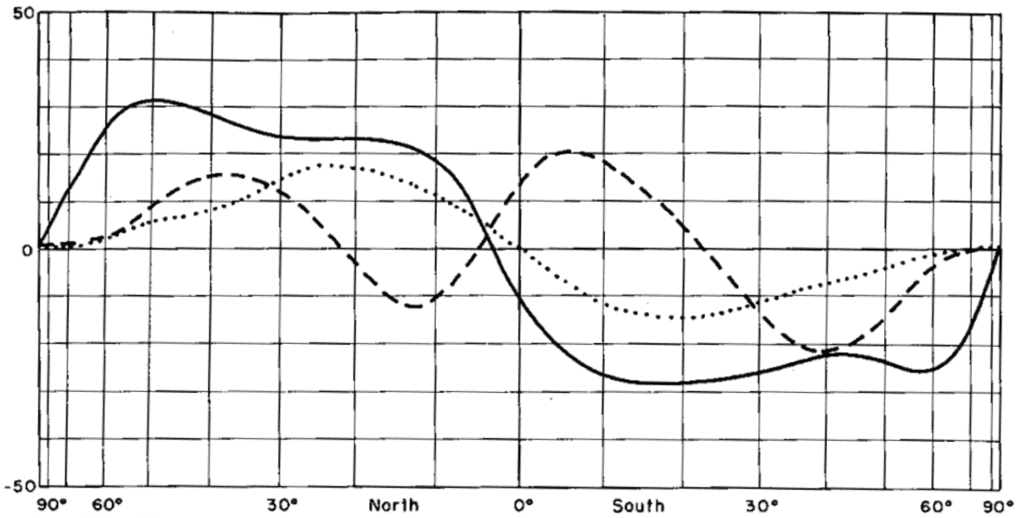

Figure 1.12. Northward transport of sensible heat plus potential energy plus kinetic energy by the atmosphere (solid line), latent heat by the atmosphere (dashed) and sensible heat by the oceans (dotted), units are 10^{14} Watts. From Lorenz (1967).

Stone (1978) was motivated by conclusions from previous work which found that the total meridional energy transport is insensitive to particular mechanisms such as the hydrological cycle (Manabe *et al.* 1965), stationary eddies (Manabe & Terpstra 1974) and ocean currents (Manabe *et al.* 1975). He examined the total meridional heat transport in the ocean and atmosphere system using a GCM, and concluded that the distribution (in particular, the latitude of maximum heat transport) is fixed and is not dependent on the structure, and hence the dynamics, of the ocean-atmosphere system (Figure 1.13). This independence is illustrated by the fact that the latitude of maximum heat transport is equal in each hemisphere, even though the structure of each hemisphere is different, with the northern hemisphere having substantially more land and less ocean than the southern hemisphere (Stone 1978). This further implies that variations in contributions from mechanisms such as ocean heat transport and stationary eddies caused by mountain ranges do not alter the distribution of the total meridional heat flux. Stone concluded that the important factors determining the distribution of heat flux are the solar constant, the axial tilt, the radius of the earth and the mean albedo (Stone 1978).

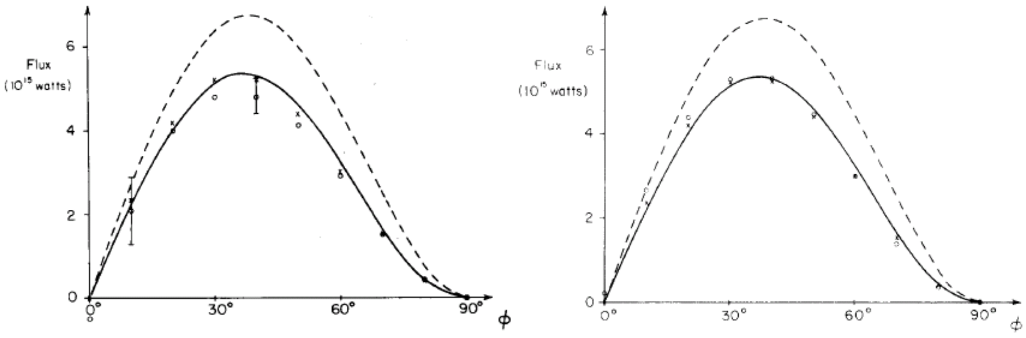

Figure 1.13. Total flux of energy across latitude circles in the northern hemisphere (left) and southern hemisphere (right) for earth with no latitudinal structure or axial tilt (dashed), no latitudinal structure but with an axial tilt (solid), for the actual earth (circles) and an approximation with ocean and atmosphere structure included (crosses), from Stone (1978).

A number of other estimates of ocean and atmosphere heat transport using various methods have been carried out, for example, Oort & Vonder Haar (1976) looked at the partitioning in the northern hemisphere. They used atmospheric observations and satellite data as well as ocean heat storage for their estimates. They highlighted the importance of the ocean heat storage in seasonal variation in total energy transport Oort & Vonder Haar (1976), and these estimates were then extended to the whole globe (Carissimo *et al.* 1985). Estimates of the total atmosphere and ocean energy transport by Carissimo *et al*. (1985) are qualitatively similar to previous estimates (Newell *et al.* 1972; Trenberth 1979), and these are illustrated in Figure 1.14, top left panel. However, the estimates of ocean heat transport by Carissimo *et al*. are much larger than previous estimates (Bryan & Lewis 1979; Hastenrath 1982; Meehl *et al.* 1982), (Figure 1.14, right hand side).

Carissimo *et al*. (1985) give approximately equal prominence to ocean and atmosphere heat transport at all latitudes; the ocean energy estimates are often more than twice that of previous estimates (Figure 1.14). This could be due to the fact that they did not properly resolve the seasonal cycle in ocean heat storage leading to errors in the annual cycle (Jayne & Marotzke 2001). Since these estimates were published, consequent work has leaned towards the dominance of atmospheric heat transport over oceanic heat transport at most latitudes, which is discussed shortly.

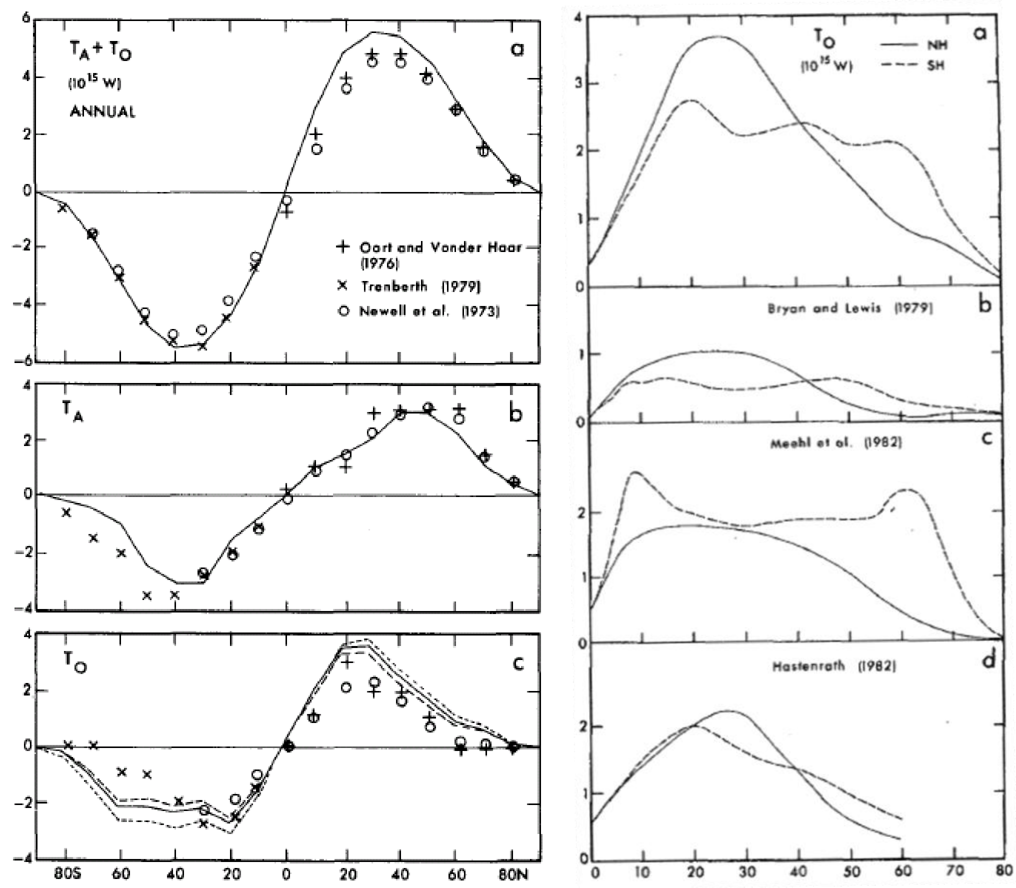

Figure 1.14. Annual transport of energy (left) for a) total, b) atmosphere and c) ocean. In c), 3 curves for T_o are based on different corrections. Oceanic annual poleward transport of heat (right). Y axis values are in PW. From Carissimo *et al.* (1985).

In 1982, Hall and Bryden provided estimates of ocean heat using hydrographic data at 25°N in the Atlantic Ocean. By using measurements across a section of the Atlantic from data collected by 38 stations in the International Geophysical Year (IGY) project in 1957 (Fuglister 1960), they were able to estimate the poleward heat transport, seasonal variability and the eddy contribution at 25°N (Hall & Bryden 1982).

In 2001, Held estimated the partitioning between ocean and atmosphere heat transport in the tropics, based on the idea that the ocean and atmosphere heat transport was closely coupled at low latitudes, and controlled by the surface trade winds such that an increase in transport in one of the media would lead to a similar change in the other (Figure 1.15). The idea is that in the tropics, heat is mainly transported as a result of overturning cells in the ocean and atmosphere, both as a result of the trade winds and each of the same magnitude. The partitioning of the heat transport depends on the energy contrasts across the overturning cells in the ocean and atmosphere, which are largely fixed. Since the mass transport in the ocean and atmosphere are strongly coupled, it would be difficult to change the partitioning of heat transport between them. The model proposed by Held is discussed more fully in section 1.4.

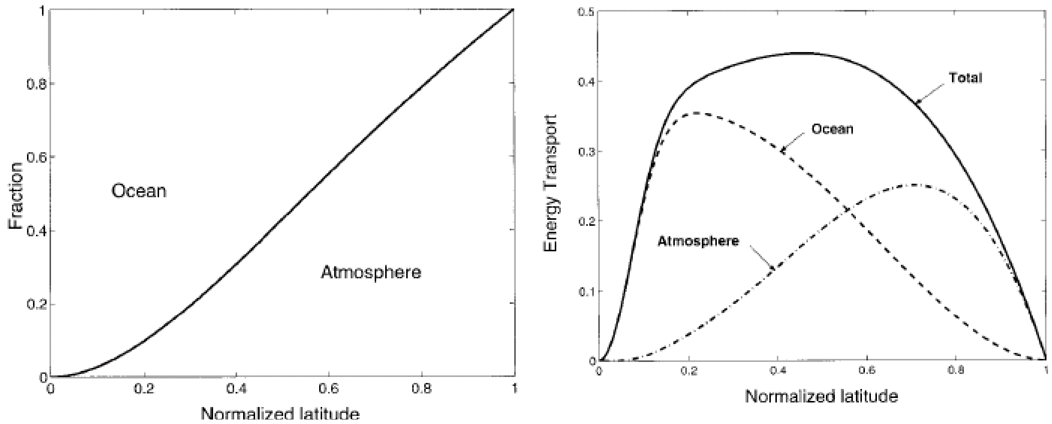

Figure 1.15. The fraction of poleward energy transport contributed by ocean and atmosphere (left), and the predicted shape of energy transports (right) from Held (2001). Latitude is normalized by the latitude of the subtropical boundary of the Hadley Cell.

More recently, Czaja & Marshall (2006) used reanalysis data and model runs with the idea that heat transport in the ocean and atmosphere can be expressed as the product of a meridional mass transport and the change in the energy across the circulation. They explained that the dominance of the ocean over atmosphere in transporting heat in the deep tropics is due to a greater stratification of the oceanic potential temperature compared to the atmospheric moist potential temperature at these latitudes, even given similar mass transport values. In the mid-to-high latitudes, atmospheric mass transport dominates over the ocean mass transport and the result is a greater atmospheric heat transport at these latitudes.

In 2008, Vallis and Farneti used a simply configured coupled primitive equation model to examine meridional energy transports and also noted the dominance of atmospheric heat transport over ocean heat transport at all but very low latitudes (Vallis & Farneti 2008a). In a second paper, they changed variables such as basin geometry and diapycnal diffusivity for the ocean, planetary rotation rate, distribution of incoming solar radiation, and presence or lack of moisture in the atmosphere (Vallis & Farneti 2008b). They note that the atmosphere and ocean gyre heat transport is strongly coupled, although atmosphere and deep ocean transport is less coupled and they note some compensation between atmosphere and deep ocean heat transport.

Trenberth and Caron (2001) provided a dataset of up to date estimates of ocean and atmosphere poleward heat transport based on corrected reanalysis data from NCEP and ECMWF, and ERBE data (Figure 1.16).

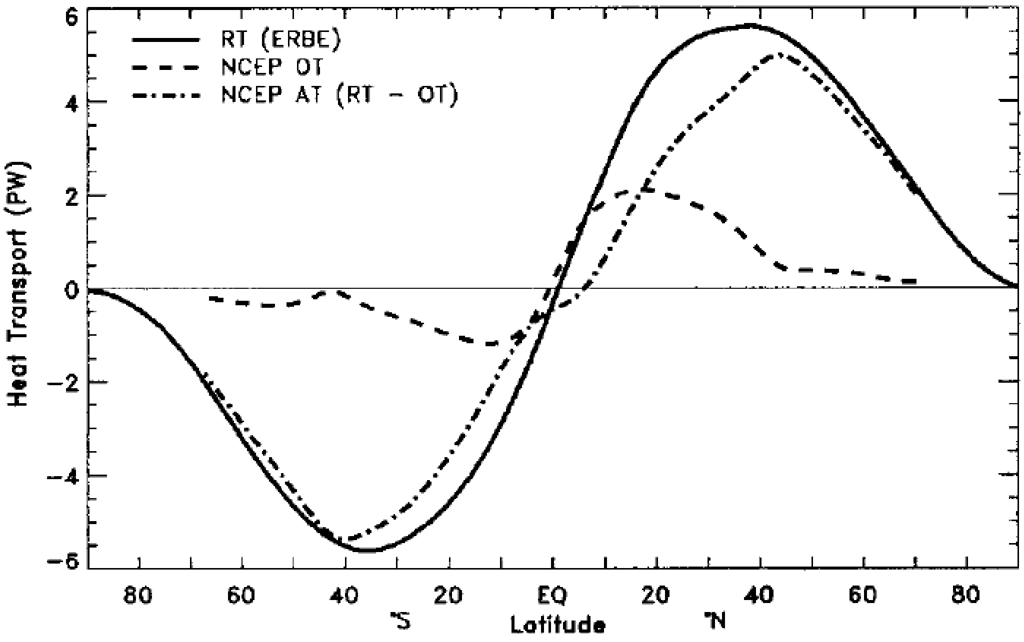

Figure 1.16. Total heat transport implied from the TOA radiation (RT), derived estimate of adjusted ocean heat transport as a residual (OT) and atmospheric transport (AT) from reanalyses in PW. From Trenberth & Caron (2001).

Error estimates were not given in the paper, although the errors in atmospheric heat transport based on ERBE uncertainty were calculated and presented in a later paper by Wunsch (2005). Comparisons with estimates by Bjerknes (1964) show that the qualitative shape of the earlier estimate (Figure 1.11), with dominance of ocean heat transport only in the deep tropics and dominance of atmosphere heat transport outside of the tropics is similar to the estimates of Trenberth and Caron (2001), (Figure 1.16). The most comprehensive and up to date data estimating the partitioning is given by Trenberth and Caron, so we use this for comparison throughout this thesis from now on.

1.2.3 Bjerknes Compensation

In 1964, Bjerknes first put across the theory that if the top of atmosphere fluxes and oceanic heat storage did not vary too much that the total energy transport by the climate system should not vary too much either, and in particular, anomalies of oceanic or atmospheric heat transport should be equal and opposite, in a scenario known as Bjerknes compensation (Bjerknes 1964). This is well illustrated by considering a situation where Atlantic heat transport was estimated to be different to the present day, such as the period around 1800 A.D. During this period, the North Atlantic is thought to have been weaker than the present day, which would have lowered the total oceanic heat flux, and Bjerknes illustrates this using Figure 1.17. With the total radiation curve kept the same as the curve in Figure 1.11, Bjerknes postulated that the reduction in oceanic heat transport would have been compensated by an increase in atmospheric heat transport, which is shown by the added dashed line at latitudes around 40°N in Figure 1.11.

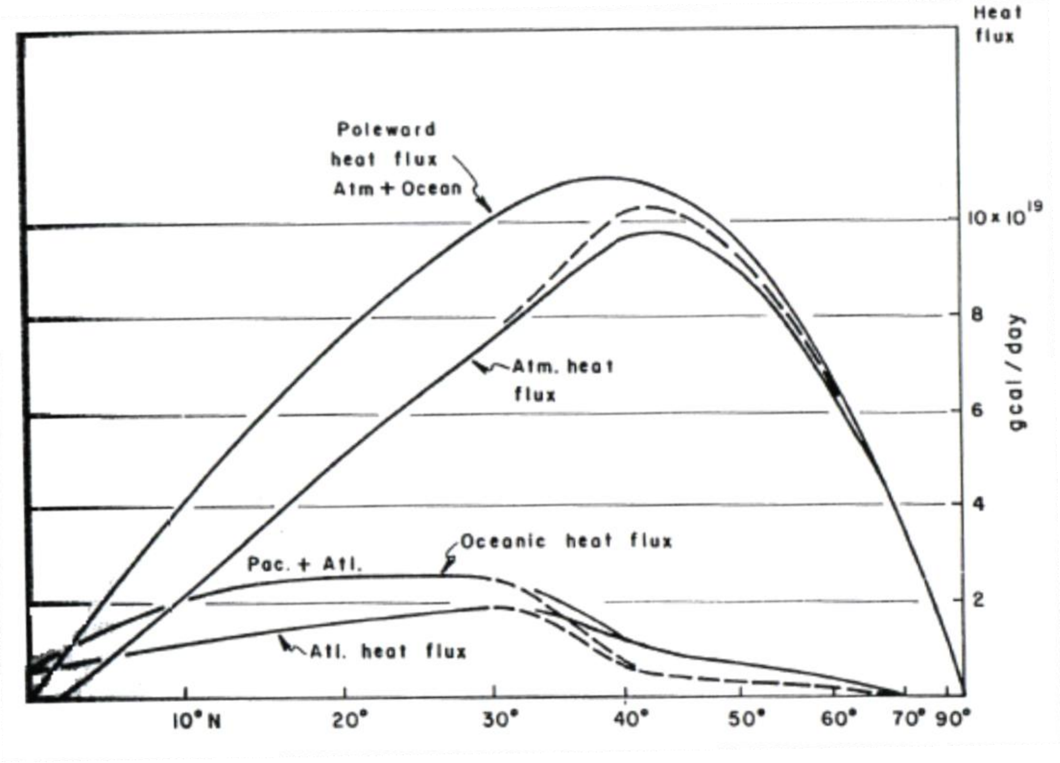

Figure 1.17. Solid lines as for Figure 1.11 in section 1.2.1 pertaining to present climatic conditions. Dashed lines refer to a model of the conditions around 1800 A.D. with decreased Atlantic and total oceanic heat flux and increased heat flux by atmospheric circulation. From Bjerknes (1964).

Bjerknes postulated that the anomalies of heat flux in the oceans and atmosphere would cancel, leaving the total heat flux and radiation budget unchanged. He suggests that some changes in the radiation budget were likely to have occurred, but that these are likely to have been small. The results of Bjerknes (1964) were consistent with results found by Stone (1978), (section 1.2.2).

Now that we have introduced some methods and estimates of heat transport, we look in more detail at oceanic and atmospheric transport in the tropics.

1.3 Poleward heat transport in the tropical ocean and atmosphere

In the tropics, the main mechanism of poleward heat transport in the atmosphere is the Hadley Circulation, which was introduced in section 1.1.2, and in the tropical oceans, the dominant mechanism is an overturning circulation associated with the surface winds known as Ekman transport (Gill 1982). In this section, we describe the Held and Hou model of the Hadley Circulation (Held & Hou 1980) and introduce the concept of moist static energy. We then introduce Ekman transport in order give background to the main mechanisms of heat transport in the tropics.

1.3.1 The Held and Hou model of the Hadley Circulation

In 1980, Held and Hou published a quantitative model describing the Hadley circulation together with the factors determining its extent (Held & Hou 1980). The model uses angular momentum and thermal wind balance for circulating air parcels to predict the latitudinal extent and strength of the Hadley Cell. The model consists of a lower layer with equatorward flow (reduced to negligible levels by friction at the surface) and an upper frictionless layer with poleward flow. The idea of the model is to compare a radiative equilibrium temperature distribution with the temperature distribution predicted from angular momentum balance considerations. Below we outline a simplified version of the Held and Hou model in Cartesian coordinates put forward by James (1994).

The circulation at low latitudes is driven by Newtonian cooling towards the radiative equilibrium distribution of potential temperature, θ_E, over a time τ_E as follows:

$$\frac{D\theta}{Dt} = \frac{(\theta_E - \theta)}{\tau_E} \tag{1.4}$$

Where $D\theta/Dt$ is the material or advective derivative and is defined as

$$\frac{D}{Dt} \equiv \frac{\partial}{\partial t} + \boldsymbol{u} \cdot \nabla \tag{1.5}$$

where $\boldsymbol{u} = (u,v,w)$. The radiative equilibrium temperature can be represented by

$$\theta_E(\phi) = \theta_{E0} - \frac{\Delta\theta}{a^2} y^2 \tag{1.6}$$

at low latitudes where y/a = ϕ is very small (the latitude is small compared with the radius of the earth). θ_E is the global mean radiative equilibrium potential temperature and Δθ is the equilibrium pole-equator temperature difference, *a* is the radius of the earth and *y* is latitude. The actual temperature profile differs from this distribution since the equilibrium distribution does not take into account the movement of air parcels to distribute heat. The actual temperature profile is predicted from angular momentum balance considerations. At low latitudes, we can assume that sin ϕ can be replaced by y/a since ϕ is so small, and cos ϕ ~ 1. The specific angular momentum of a ring of air at a latitude ϕ is ($\Omega a \cos\phi + [\bar{u}]$) $a \cos\phi$. Conservation of angular momentum for a ring of air with zero zonal velocity at the equator implies the zonal wind at other latitudes is given by:

$$[u] = \frac{\Omega a sin^2\phi}{cos\phi} \tag{1.7}$$

And this can be approximated by

$$U_M = \frac{\Omega y^2}{a} \tag{1.8}$$

which is the zonal wind derived on the basis of conservation of angular momentum. We assume low level wind is zero due to friction, so that:

$$\frac{\partial u}{\partial z} = \frac{U_M}{H} = \frac{\Omega y^2}{aH} \tag{1.9}$$

where *H* is the height of the Hadley Cell. We now use the thermal wind balance equation and use the Coriolis force, *f* = 2Ω *sin* ϕ to get:

$$2\Omega sin\,\phi \frac{\partial u}{\partial z} = -\frac{g}{\theta_0}\frac{\partial \theta}{\partial y} \tag{1.10}$$

Then substituting from the previous equation and integrating the result gives us the potential temperature distribution from thermal wind considerations:

$$\theta_M = \theta_{M0} - \frac{\Omega^2 \theta_0}{2a^2 gH} y^4 \,. \tag{1.11}$$

Here, θ_{M0} is an unknown constant of integration representing the equatorial temperature. Next we compare the radiative equilibrium temperature distribution, θ_E, with the actual temperature distribution, θ_M (Figure 1.18).

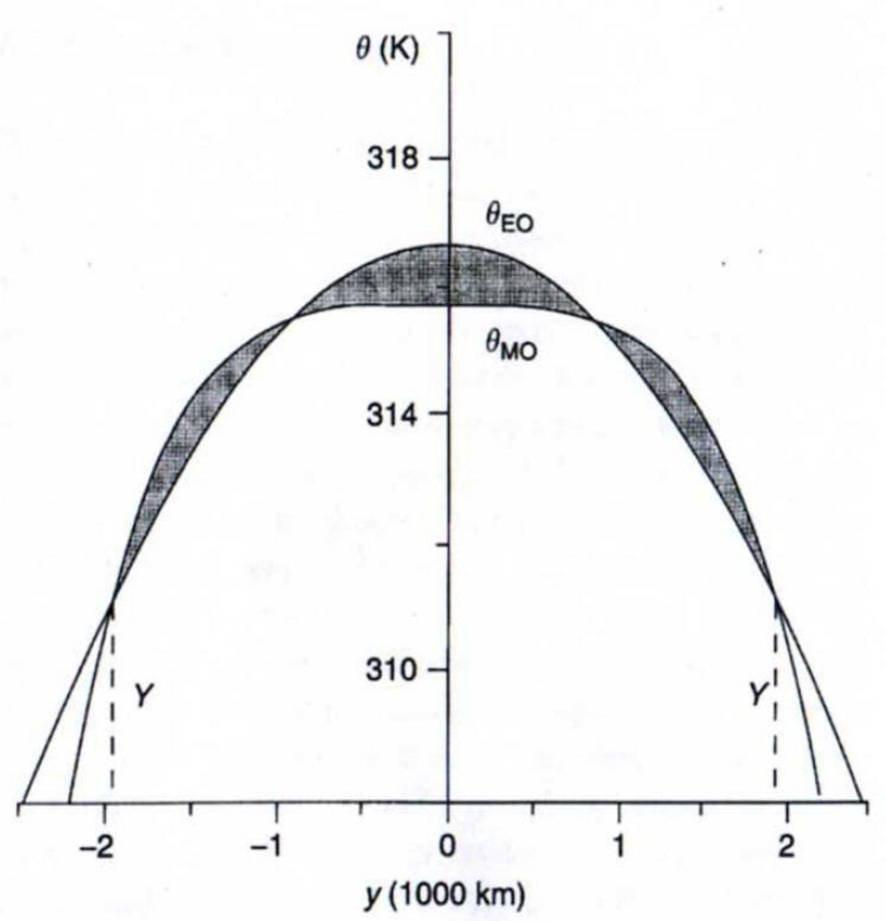

Figure 1.18. θ_E and θ_M as a function of latitude for the Held and Hou model (Held & Hou 1980). From James (1994).

Here, the value of θ_{M0} is chosen so that the shaded area at the equator equals the shaded areas outside the equator, otherwise there would be net heating of air parcels (Figure 1.18). In other words:

$$\int_0^Y \theta_M dy = \int_0^Y \theta_E dy \tag{1.12}$$

There is heating in the shaded area at the equator up to the first crossing point, and then cooling between the crossing points. The poleward limit of the Hadley Cells is represented by the second crossing point, denoted *Y*. By equating the equations for radiative equilibrium temperature and the actual temperature curve where $\theta_M = \theta_E$ at $y = Y$, we can calculate the poleward extent of the Hadley Cell:

$$Y = \left(\frac{5\Delta\theta^2 gH}{3\Omega^2\theta_0}\right)^{\frac{1}{2}} \tag{1.13}$$

and the temperature change between θ_M and θ_E at the equator:

$$\theta_{E0} - \theta_{M0} = \frac{5\Delta\theta^2 gH}{18a^2\Omega^2\theta_0} \tag{1.14}$$

Using typical temperature values, Y = 2200 km and $\theta_{E0} - \theta_{M0}$ = 0.8 K. The vertically integrated flux of potential temperature is given by:

$$\frac{1}{H}\int_0^H \frac{1}{acos\phi}\frac{\partial}{\partial\phi}(v\theta cos\phi)\,dz = \frac{\overline{\theta_E} - \bar{\theta}}{\tau} \tag{1.15}$$

The solution offered by Held and Hou (1980) implies that the heat budget is balanced within the tropics, whereas this is not the case (Figure 1.1), and it is the heat transport from the tropics to the poles that balances the heat gain in the tropics with the heat loss in the extratropics. The Held and Hou model of the Hadley Circulation predicts the extent of the Hadley Cell, along with the mass and heat transport, although the model does not include the effects of latent heat release by condensation. In the next section, we introduce moist static energy, which is used throughout the thesis as a parameter to calculate the heat transported by the Hadley Cell.

1.3.2 Moist static energy

In this thesis, we are concerned with quantifying the amount of meridional heat transport which takes place in the ocean and atmosphere and we mainly consider the mean meridional transport of energy which is dominated by the Hadley Cell in the tropical atmosphere. In the same way we would use potential temperature gradients in the ocean to calculate heat transported by an overturning circulation, in the atmosphere, we use moist static energy. In the atmosphere, 99.7% of the total energy can be broken down into the internal energy associated with temperature, the potential energy associated with the gravitational potential of the air above the earth, and the Latent energy associated with the atmospheric moisture (Hartmann 1994). Moist static energy is the sum of these energies:

$$h = C_pT + L_vq + gz \tag{1.16}$$

where C_p is the heat capacity of air at constant pressure, L_v is the latent heat of vapourisation, q is specific humidity, T is temperature and gz is geopotential.

The expression for moist static energy can be derived from Bernoulli's equation (Gill 1982) which is a statement of the conservation of energy for an inviscid fluid in steady motion:

$$\frac{D}{Dt}\left(E + \frac{\rho}{p} + \Phi + \frac{1}{2}u^2\right) = Q_{NF} \tag{1.17}$$

where Q_{NF} represents non-frictional heating and includes latent, sensible and radiative heating terms: $Q_{NF} = Q_{lat} + Q_{rad} + Q_{sens}$, and using the material derivative defined in (1.5), and where E is internal energy. The other terms on the left hand side represent the work done by pressure forces, the gravitational potential energy and the kinetic energy. The quantity of $E + p/\rho$ is the enthalpy per unit mass, which for a perfect gas is equal to C_PT. In atmospheric physics, the quantity $E + p/\rho + \Phi$ is known as the dry static energy per unit mass (Gill 1982). An approximation for the atmosphere is:

$$E + \frac{p}{\rho} + \Phi \simeq C_PT + gz \tag{1.18}$$

In order to include effects of latent heat release, we note that $Q_{lat} = - L_v\, dq/dt$, in which case, (1.17) becomes:

$$\frac{D}{Dt}\left(E + \frac{\rho}{p} + \Phi + L_vq + \frac{1}{2}u^2\right) = Q_{sens} + Q_{rad} \tag{1.19}$$

where the quantity

$$E + \frac{p}{\rho} + \Phi + L_vq \simeq C_PT + gz + L_vq \tag{1.20}$$

represents the moist static energy per unit mass.

The net fluxes of sensible and latent heat by the Hadley Cell are equatorward, as warm moist air converges in the ascending region of the circulation. The energy from the sensible heat and that released by latent heat drives upward motion and is converted to potential energy. The potential energy flows poleward in the upper branch of the Hadley Cell, and exceeds the equatorward energy slightly, to give a net poleward heat transport (Hartmann 1994). In the stably stratified tropics, moist static energy increases with height and the geopotential term dominates at upper levels, so that the energy transport is in the direction of the upper level flow in the Hadley Cells. A diagram to explain the transport of energy by the mean meridional circulation in January is shown in Figure 1.19.

The amount of heat transported by the overturning Hadley cell is dependent on the contrast in moist static energy between the upper and lower branches, known as the gross moist static stability (Δh), and the strength of the circulation (ψ):

$$H_A = \psi \Delta h \tag{1.21}$$

Equation (1.21) provides a method of calculating Δh based on calculations of H_A and ψ.

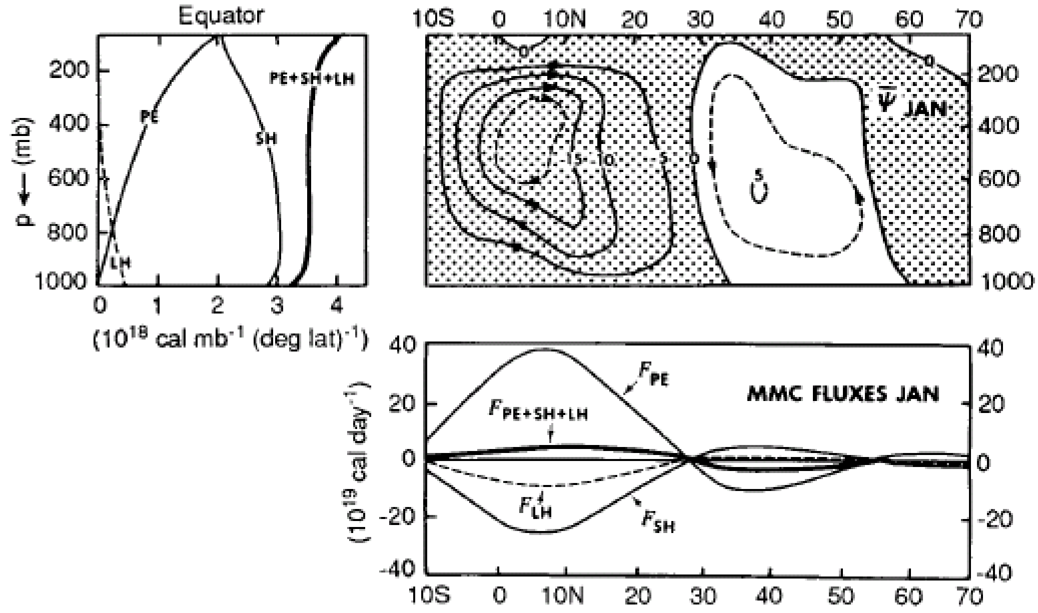

Figure 1.19. The vertical distribution of potential energy (PE), sensible heat (SH), latent heat (LH) and total moist static energy near the equator for January (upper left). Mean meridional mass streamfunction for January in pressure latitude cross-section (upper right). The northward fluxes of various energies by the MMC (lower right). From Hartmann (1994) using data from Oort (1971).

We investigate the distribution of moist static energy and mass transport in the tropical troposphere in chapter 2, and the Hadley Cell heat transport, along with variability in moist static energy and mass transport in chapter 3.

1.3.3 Ekman transport

Heat transport in the ocean associated with surface wind stress is known as Ekman transport, and here we provide an introduction. Ekman transport is particularly relevant for chapter 4, where a lack of zonal barriers in the aquaplanet model mean that Ekman transport plays a dominating role in meridional heat transport in the ocean.

The Ekman layers in the ocean and atmosphere occur at the ocean surface and the lowest part of the atmosphere and can be a few tens to several hundreds of metres. The depth of the layer is less than the depth of the whole fluid and is given as the level where frictional stresses effectively disappear (Vallis 2006). The Ekman spiral demonstrates the direction of movement of different layers of the Oceanic Ekman layer as a result of the stress exerted on the surface due to the wind (Figure 1.20).

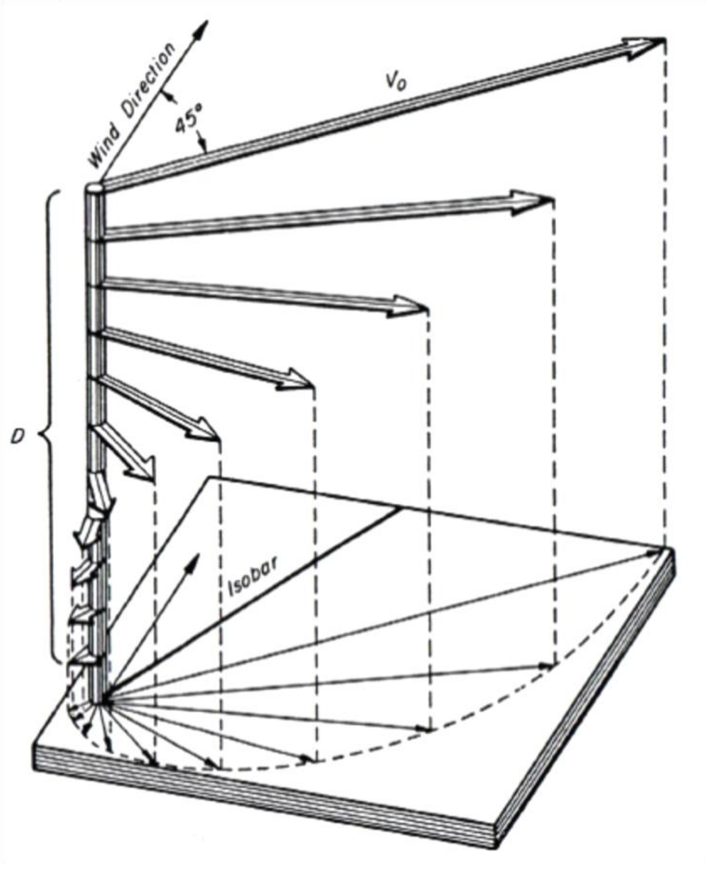

Figure 1.20. The Ekman spiral at the ocean surface. From Ekman (1905).

The surface layer is directed at 45° to the right of the wind direction (northern hemisphere), and each thin layer beneath the surface is deflected further to the right due to the added effect of frictional drag due to the neighbouring thin layers. The net, vertically intregrated Ekman mass transport is 90° to the right of the direction of the surface wind.

The wind stress at the boundary of the ocean and atmosphere acts equally and oppositely on each medium, leading to opposite sign and same magnitude Ekman mass transports (Figure 1.21). In the northern hemisphere, the Ekman transfer is to the left of the surface winds in the atmosphere, and to the right in the ocean. This means that the Easterly trade winds lead to equatorward atmospheric Ekman transport and poleward oceanic Ekman transport.

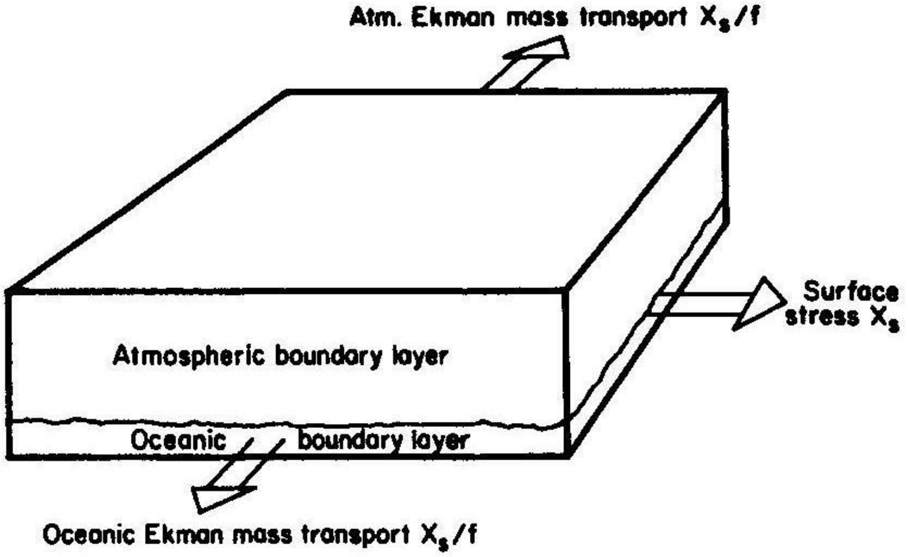

Figure 1.21. Directions (northern hemisphere) of steady Ekman mass transports in the oceanic and atmospheric boundary layers when the stress at the surface has the direction shown. In this figure, the wind is blowing from the west to the east (left to right), hence equatorward flow in upper ocean layers and poleward flow in lower atmospheric layers. From Gill (1982).

Ekman Dynamics

The equations of motion represent Newton's second Law of motion for a material volume element. In a frame of reference rotating with the earth

$$\frac{D\vec{u}}{Dt} + 2\vec{\Omega} \times \vec{u} = -\frac{\vec{\nabla} p}{\rho} + \vec{g} + \frac{\vec{F}}{\rho} \tag{1.22}$$

where $\vec{u}$ is velocity, $\vec{\Omega}$ is the angular velocity of the earth, p is pressure, ρ is density, $\vec{g}$ is the acceleration due to gravity and $\vec{F}$ represents turbulent momentum mixing effects which work to diffuse the momentum of the larger scale flow.

The first term of (1.22) is the rate of change of momentum of the element and the second term is the Coriolis force. On the right hand side, the terms are the pressure gradient force, the acceleration due to gravity, and the effect of friction.

The frictional force, $\vec{F}$, can be split into two parts:

$$\vec{F} = \frac{\partial \vec{\tau}}{\partial z} + \vec{F}_H \tag{1.23}$$

The second term on the right is defined as

$$\vec{F}_H = \rho \nu \nabla^2 \vec{u} \tag{1.24}$$

and represents horizontal momentum transfer by molecular viscosity. The turbulent viscosity coefficient v, is a constant, and represents the viscosity of the fluid.

The first term on the right hand side of (1.23) is the vertical divergence of the horizontal turbulent stress equal to the wind stress at the surface. The wind exerts a stress on the top layer of a thin fluid layer, which moves and exerts a stress on the layer below. The net force per unit area on the layer is the difference in stress between the top and bottom, where the thickness of the layer is δz:

$$\left(\frac{\partial \tau_x}{\partial z}, \frac{\partial \tau_y}{\partial z}\right) \delta z \tag{1.25}$$

Multiplying by the area and dividing by the mass gives the force per unit mass due to horizontal stresses (Gill 1982). This is a force which tends to accelerate the fluid, so is included in the horizontal momentum equations as the final term on the right hand side:

$$\frac{\partial u}{\partial t} - fv = -\frac{1}{\rho}\frac{\partial p}{\partial x} + \frac{1}{\rho}\frac{\partial \tau_x}{\partial z} \tag{1.26}$$

and

$$\frac{\partial v}{\partial t} + fu = -\frac{1}{\rho}\frac{\partial p}{dy} + \frac{1}{\rho}\frac{\partial \tau_y}{\partial z} \tag{1.27}$$

Over timescales greater than f^{-1}, the geostrophic component of velocity is driven by pressure gradients (first term on right hand side) and extends deep into the water column in the ocean (Hastenrath 1985). The velocity is at right angles to the pressure gradient, and the components of velocity due to the pressure gradient force are

$$-v_g = -\frac{1}{\rho f}\frac{\partial p}{\partial x} \tag{1.28}$$

$$+u_g = -\frac{1}{\rho f}\frac{\partial p}{\partial y} \tag{1.29}$$

The component driven by the windstress is the Ekman velocity, which is confined to the shallow frictional layer of the ocean and atmosphere:

$$v_E = -\frac{1}{\rho f}\frac{\partial \tau_x}{\partial z} \tag{1.30}$$

$$u_E = +\frac{1}{\rho f}\frac{\partial \tau_y}{\partial z} \tag{1.31}$$

The vertical integration of (1.30) and (1.31) gives the equations of Ekman mass transport, which represents the mass flux per unit length, since at the surface, $\tau_{(x,y)} = \tau_{(x,y)}^{wind}$ and at the bottom of the Ekman layer, $\tau_{(x,y)} = 0$.

$$M_{yE} = -\frac{\tau_x}{f} \tag{1.32}$$

$$M_{xE} = +\frac{\tau_y}{f} \tag{1.33}$$

The relationship breaks down very near the equator, where $1/f$ becomes very large.

Ekman Pumping

Since the windstress is not uniform over the planet, there are regions of convergence and divergence of mass in the boundary layer, which lead to fluid being expelled from the layer, or sucked into the layer, known as Ekman pumping (Figure 1.22), (Gill 1982). For example, water advected away from shorelines with alongshore winds can result in a divergence of water and pumping colder water into the surface layers from the deeper ocean which can have a large effect on local climate, ocean currents, fishing and agriculture. The easterly trade winds force the ocean surface northwards, and the midlatitudes westerlies force the ocean surface southwards so there is convergence of surface water in the region between. In Chapter 4, we estimate Ekman transport in the ocean and atmosphere of an aquaplanet in order to test the theory put forward in Held (2001), which is discussed in the next section.

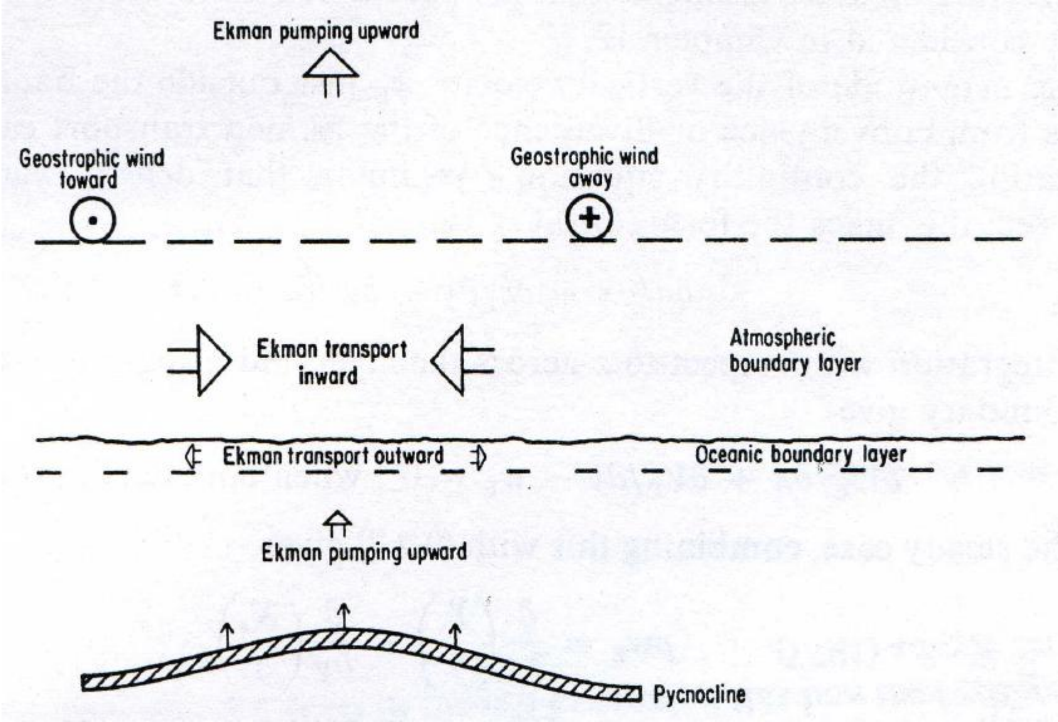

Figure 1.22. Section through a cyclone over the ocean. The geostrophic wind gives a cyclonic rotation around the low pressure centre. Ekman transport in the atmosphere is inward and associated pumping velocity is upward. The Ekman mass transport in the oceanic boundary layer is equal and opposite, so there is an outward mass transport and upward pumping velocity in the ocean. This tends to raise the thermocline. From Gill (1982).

1.4 Coupling of heat transport: An overview of a simple model of the tropics (Held 2001)

In 2001, Held proposed a simple model to estimate the partitioning of heat transport in the tropics (Held 2001). It was based on the idea that in the tropical atmosphere, the ageostrophic Hadley Cell dominates the heat transport, and in the ocean, shallow wind driven cells dominate. He suggested that the atmospheric and oceanic overturning mass transport is strongly coupled near the surface and both could be thought of as the Ekman drift associated with the same surface stress.

In formulating the model, Held made some simplifications. He considered the land surface to take up a modest fraction of the area in the tropics (~70% between 20°N and

20^{o}S) so that most of the wind stress acts on the ocean surface. He considers the Ekman transport in the ocean is equal and opposite to that in the atmosphere. For the atmosphere, he suggests winds are small in order to neglect nonlinear terms, and there are small frictional stresses, mountain torques and eddies. In the ocean, he considers the geostrophic component of circulation to be small compared to the Ekman drift in the tropics. On the whole, this is a long term picture of the partitioning of heat transport, so the focus is on annual mean surface stress and mass transport.

From estimates by Peixoto & Oort (1992), the annual atmospheric mass transport is roughly 60 Sv (where a Sverdrup in this case is defined as a unit of mass rather than volume transport: 1 Sv = 10^6 m^3 s^{-1} x 10^3 kg m^{-3} = 10^9 kg s^{-1}). Accounting for the presence of land gives an estimate of the required upwelling at the equator of around 85 Sv, which is consistent with an earlier estimate of 91 Sv (Klinger & Marotzke 2000).

Since the mass transport in the ocean and atmosphere is assumed to be of equal magnitude, the amount of heat transport in each media depends on the gross stability in each and the ratio of the heat transports (see section 1.2.1) can be given by

$$\frac{H_A}{H_O} = \frac{\psi_A \Delta h_A}{\psi_O \Delta h_O} \simeq \frac{\Delta h_A}{\Delta h_O} \tag{1.34}$$

where Δh represents the gross stability in each (Figure 1.23). In the ocean, Δh_O represents the difference in θ between poleward and return flow (see equation (1.3) in section 1.2.1) and Δh represents gross moist static stability (see equation (1.2) in section 1.2.1).

Since the ocean stability dominates over the atmospheric gross stability, the oceanic stability determines the total Hadley Cell heat transport in the deep tropics. Furthermore, since the flow in the subsurface layers can be assumed to be adiabatic and can be traced back to subduction in the subtropics, the temperature difference in the vertical can be determined by the difference at the surface across the tropics. Similarly, the vertical temperature difference in the atmosphere can be estimated by the difference between the equator and the subtropical boundary of the Hadley Cell, so that the vertical gross stability in the atmosphere can be approximated as:

$$\Delta_p \bar{h} \approx \bar{h}_{sfc}(eq) - \bar{h}_{sfc}(\phi_{HC}) \tag{1.35}$$

where $\Delta_p\bar{h}$ is the vertical variation in moist static energy, $\bar{h}_{sfc}$(eq) is surface moist static energy at the equator, $\bar{h}_{sfc}(\phi_{HC})$ is the surface moist static energy at the latitude coinciding with the poleward edge of the Hadley Cell and the overbar represents a zonal mean.

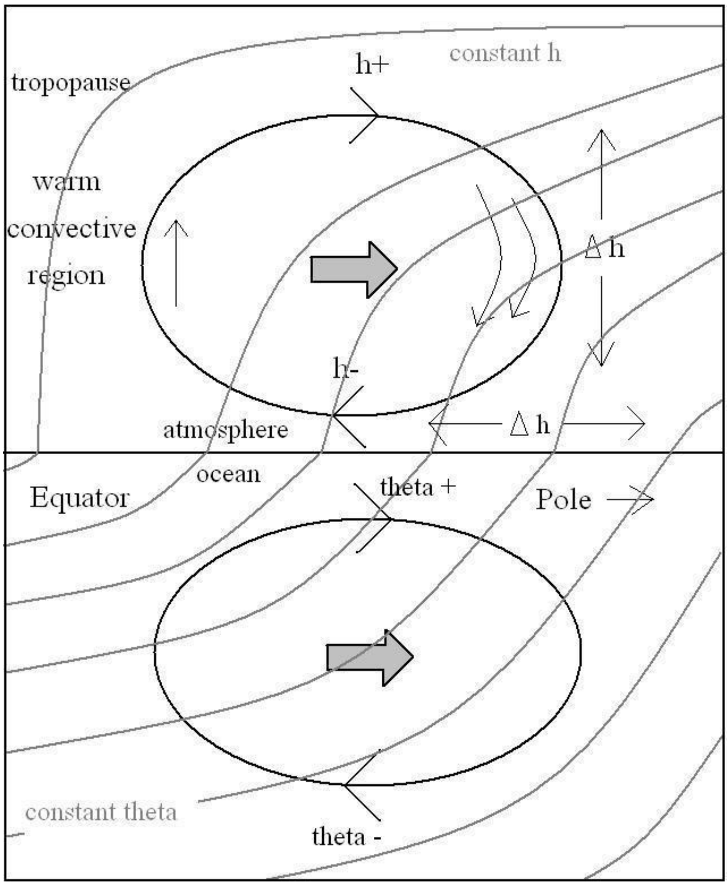

Figure 1.23. Representation of the coupling of ocean and atmosphere heat transport, as envisioned by Held (2001), where h represents moist static energy in the atmosphere, and theta is ocean temperature. Grey curved lines represent constant h and theta in the atmosphere and ocean respectively. Horizontal and vertical gradients in h (Δ*h*) are indicated in the atmosphere (similar gradients in temperature are present in the ocean).

The estimated partitioning between ocean and atmosphere heat transport is illustrated by Figure 1.15 in section 1.2.2. According to the model, at 10° latitude, the ocean transports 77% of the total heat transport and the atmosphere 23%. If we compare this with Trenberth and Caron (2001), Figure 1.16 in section 1.2.2, this seems like a reasonable estimate. The implication of the analysis is that it is difficult to change the partitioning of poleward heat transport in the tropics, and that we should expect the oceans to dominate poleward energy flux out of the deep tropics, but the atmosphere to catch up as we approach the latitude of maximum Hadley Cell energy flux. The idea that the partitioning of ocean and atmosphere heat transport is largely invariable was questioned by Hazeleger *et al*. (2004). They point out that the equatorward transport of heat by the equatorial ocean gyre compensates for variations in the subtropical ocean cell. This means that reductions in the heat transport by the overturning circulation in the ocean are accompanied by a reduction in the gyre heat transport toward the equator. They also point out that a reduction in Hadley cell mass transport does not necessarily mean a reduction in atmospheric meridional heat transport, since increases in moist static energy gradients between the tropics and subtropics may compensate for the decreased circulation (Hazeleger *et al.* 2004). In chapter 4, we test Held's model in an aquaplanet, to see if it can be applied to a situation when there are no ocean gyres and the tropical heat transport in the ocean is largely wind driven.

1.5 Key questions addressed in this thesis

Throughout this thesis we keep the simple model proposed by Held (2001) in mind. In chapter 2, we build on the idea that the tropics are not spatially uniform (as was seen by the various features described in section 1.1) and we use reanalysis data to answer key questions such as:

- How large are horizontal variations in moist static energy in the tropics?
- How does the atmospheric circulation vary depending on low level moist static energy in the tropics?

In chapter 3, we concentrate on the true overturning circulation which occurs mainly in the convective regions of the tropics, which correspond to areas with high SST, in order to answer the following questions:

- How much heat is transported by the true overturning Hadley circulation present in the convective regions of the atmosphere?
- What mechanisms control variations in Hadley Cell heat transport?
- Does convective region heat transport vary under El Niño conditions?

In chapter 4, we test Held's theory of strongly coupled heat transport in the tropics (section 1.4) using a coupled aquaplanet model to answer a key question:

- Are annual variations in ocean and atmosphere heat transport positively correlated in the tropics of an aquaplanet?

Chapter 2 The distribution of moist static energy and meridional mass transport in the tropical atmosphere

The observed spatial variability in the tropics (e.g. circulation patterns, SST, convection) motivates an analysis of the distribution of moist static energy and meridional mass transport in the tropical atmosphere, in particular the relationship between moist static energy at the surface, and the associated atmospheric circulation throughout the troposphere.

Using reanalysis data, we present horizontal and longitude-pressure maps of SST, meridional wind and moist static energy to investigate seasonal and interannual variability as well as spatial variability. We then introduce a framework to sort the mass transport of the atmosphere based on low level moist static energy, which reflects underlying SST. The framework enables us to identify differences in the mass transport between convective regions (which correspond to high SST and surface moist static energy) and non-convective regions (where SSTs are lower, as is surface moist static energy). We also identify the mass transport associated with the Somali Jet during JJA and put approximate values on this as well as mass transport which occurs in convective and non-convective regions of the tropics.

2.1 Introduction

Conditions in the tropics are not spatially uniform, as we have seen in chapter 1. The tropical atmosphere consists of convective regions, which tend to coincide with high SSTs and are characterized by high relative humidity, and drier regions, such as those found over the colder eastern Pacific Ocean, associated with shallower convection and colder SSTs. As well as the variations in convection, temperature and humidity across the tropics, there are also considerable differences in atmospheric circulation patterns in different regions: monsoons, Walker and Hadley cells, which were introduced in section 1.1.

Heat transported by the Hadley and Walker Cells is associated with deep convection over high SSTs, whereas the monsoon circulation is more associated with strong, low level jets, often over colder SSTs (Kumar & Schlussel 1998). In the drier regions of the tropics where SSTs are low, a deep overturning circulation is not often realized, as convection can be suppressed by descending air from other regions, and instead, a shallow overturning circulation just above the boundary layer has been observed in these regions (Zhang *et al.* 2004; Back & Bretherton 2006; Raymond *et al.* 2006). A schematic of the circulation over the eastern Pacific, as observed by Zhang *et al.* (2004), is illustrated in Figure 2.1. The more complex structure of the circulation in non-convective regions means that heat transport is realized in different ways in convective and non-convective regions.

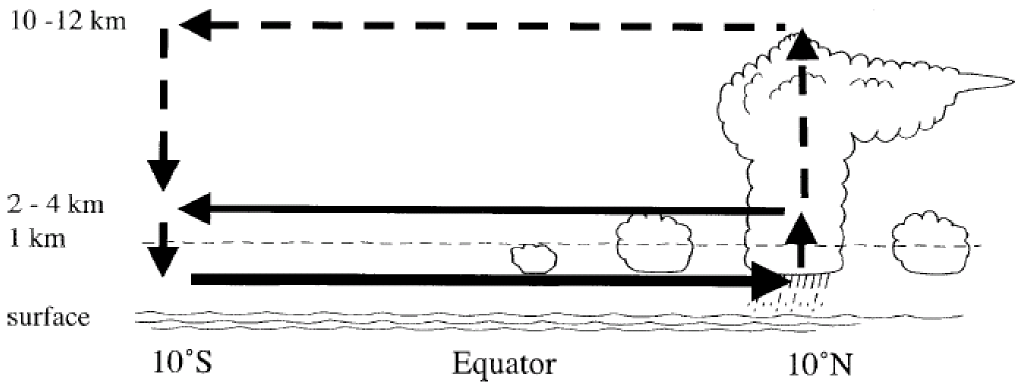

Figure 2.1. Schematic meridional-vertical diagram illustrating deep convection (dashed lines) and observed shallow (solid) meridional circulations in the tropical eastern Pacific. There is southerly flow in the boundary layer, the top of which is represented by the thin dashed line. Deep clouds indicate the location of the ITCZ and depths of the shallow and deep meridional circulations are marked on the left. From Zhang *et al.* (2004).

In section 1.3., we introduced the Hadley Cell as a mechanism of meridional atmospheric heat transport in the tropics where the amount of heat transport can be written as

$$H_A = \psi_A \Delta h \qquad (2.1)$$

This implies that both the strength of the overturning Hadley circulation of the atmosphere (ψ_A) and the difference in moist static energy between upper and lower troposphere (gross moist static stability, Δh) play a role in determining the amount of meridional heat transported by the Hadley Cell. Given the spatial variations in the tropical atmosphere mentioned above, it may seem surprising that the total meridional heat transported by the atmospheric circulation is well approximated using zonally averaged values of mass transport and Δh (Peixoto & Oort 1992). The fact that we can use (2.1) to give an approximation of the total Hadley cell heat transport when there is such spatial variability in tropical circulation suggests that the total heat transport is dominated by a true overturning circulation in one region of the tropics.

The heat transport model constructed by Held (2001) and discussed in section 1.4 assumed that moist static energy at the surface can be determined using zonally averaged surface temperatures. In this chapter we investigate the distribution of moist static energy and meridional mass transport throughout the tropics, rather than considering a zonal mean view in order to investigate the mechanisms of heat transport in the tropics. We concentrate on the heat transport at the equator; since ψ_A reaches a maximum here during the solsticial seasons, when the equator largely bisects the winter Hadley Cell (Figure 1.7) and seasonal variations in mass transport are most marked at the equator.

We start by introducing the reanalysis data used in the analysis, then show horizontal maps of surface meridional winds and SSTs in the tropics, since low level h, and hence Δh, is strongly influenced by SST. Next we introduce cross sections of moist static energy and meridional winds throughout the troposphere, at the equator, and introduce a framework whereby we sort mass transport in the atmosphere as a function of surface h, which gives a good indication of the relationship between the two quantities. Finally we perform some approximate calculations of mass transport in the various regions of the atmosphere identified using the framework.

2.2 Data

The data used for the analyses in chapters 2 and 3 of this thesis came from the ERA40 reanalysis dataset from the European Centre for Medium Range Weather Forecasting (Uppala *et al.* 2005). See Trenberth *et al.* (2001) for an overview of reanalysis data in the tropics. The ERA40 dataset describes the state of the atmosphere from 1957 to 2001 and combines a physical model with observations in order to create a global reanalysis product of various meteorological variables (Uppala *et al.* 2005). For the analysis in this chapter, 10 years (1992 to 2001) of monthly mean data were used to calculate seasonal means for each of the years (DJF, MAM, JJA and SON represent December to February, March to May, June to August and September to November, respectively). We used analysis data at 13 pressure levels: 1000, 925, 850, 725, 600, 500, 400, 300, 200 and 100 hPa. The horizontal resolution of the data was $1^{\circ} \times 1^{\circ}$. Variables used included meridional wind, temperature, relative humidity, geopotential height and surface pressure. The ERA40 reanalysis is similar to the NCEP/NCAR reanalysis dataset (Kalnay *et al.* 1996).

2.3 Seasonal variability in meridional surface winds and SST in the tropics

There is considerable variability in the distribution of SST in the tropics: on interannual timescales, ENSO is reflected in large gradients in SST, but there is also a pronounced seasonal cycle (Mitchell & Wallace 1992). The surface winds which flow into the region of convergence that marks the ascending branch of the Hadley Circulation reverse across the equator on seasonal timescales as the thermal equator moves north and south (Dima & Wallace 2003). Figure 2.2 shows the mean 1000 hPa meridional winds and SST for 10 years (1992-2001) in JJA (upper) and DJF (lower). Black contours show northward surface winds and white contours show southward. Colours represent SST. There is no data over land since surface pressure here is generally lower than 1000 hPa.

In JJA, the majority of the surface wind at the equator is from south to north, reflecting the position of the ascending branch of the Hadley Cell, and hence the ITCZ, to the north of the equator. In the Indian Ocean, the northward component of the monsoon circulation is visible, with the Somali Jet reaching maximum values of mean meridional windspeeds of 13 ms^{-1} along the east coast of Africa. The ITCZ is indicated at around 10^{o}N in the east Pacific and Atlantic oceans, where northerly and southerly surface winds converge. The strong northward wind along the west coast of South America results in Ekman pumping and upwelling of cold waters along the coastline (section 1.3.3), and this is reflected by low SST values (colours). In this season, the eastern Pacific cold tongue is relatively well developed (Mitchell & Wallace 1992) and there is a large temperature gradient between the east and west Pacific on the order of 10 K.

During DJF, the surface flow across the equator is generally, but not entirely southwards, although some northward flow persists, and this is due to the position of the ITCZ north of the equator in the east pacific throughout the year (Philander *et al.* 1996). Apart from the northward flow along the west coast of South America and some in the Atlantic, the rest is southward. In DJF, the highest SSTs have shifted south with the thermal equator. There is no strong northward Somali Jet during DJF since this is a feature of the northern hemisphere summer, but there is a reversal of the flow at the surface over the Indian Ocean, especially along the coast of Africa. The SST in the Indian Ocean varies greatly between the two seasons, especially in the western half. During JJA, the strong low level Somali Jet assists in the upwelling of cold waters offshore, and when the flow is reversed in DJF, the SST is higher as warm surface water is advected from the equator along the coast of Africa.

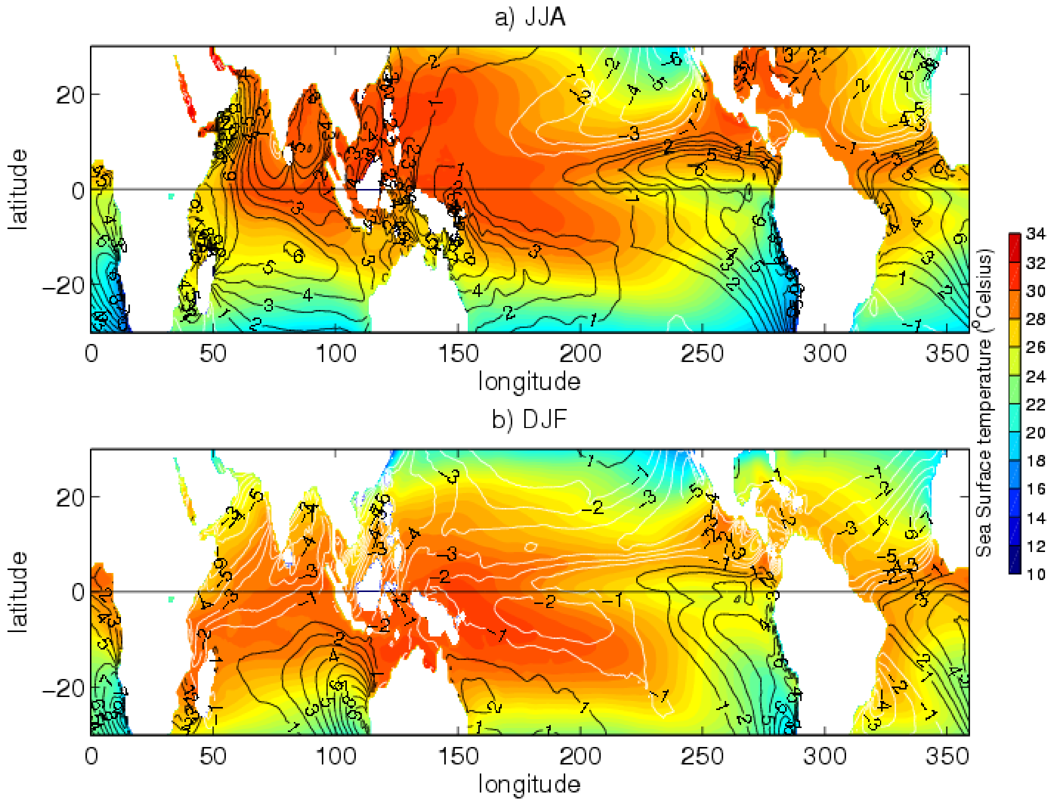

Figure 2.2. 1000 hPa winds (contours) and SST (colours) for a) JJA and b) DJF. Black contours show southerly winds and white show northerly winds. Contour interval is 1 ms^{-1}. Produced using ERA40 reanalysis data.

2.3.1 SST and low level moist static energy in the tropics

The horizontal maps of surface conditions in the tropics highlight the spatial variability in SST and winds within a season, as well as demonstrating the variation between seasons. There are some important observations to make from Figure 2.2.

Strong northward winds blow from south to north along the west coasts of Africa and South America all year round. These strong winds assist the upwelling of cold waters by Ekman pumping along the coast, which creates strong temperature gradients along the surface of the ocean. The result is that there is strong low level flow over relatively cold regions of the ocean throughout most of the year. The Somali jet associated with the monsoon circulation in the Indian Ocean also flows above relatively cold SST.

The creation of these regions of relatively cold surface temperatures also means that there are strong east-west gradients in SST in the deep tropics. In some regions these gradients can be as large as 10^{o} C along the equator, especially in months when the eastern Pacific cold tongue is most developed (March, April, May). There are some regions of the tropics where the SST is consistently high throughout the year, such as the Indo Pacific region and over the western Atlantic, which are characterized by deep convection throughout the year. The heat transport model constructed by Held (2001) and discussed in section 1.4 assumed that moist static energy at the surface can be determined using zonally averaged surface temperatures. However (Figure 2.2) would seem to suggest that there are large horizontal gradients in SST.

SSTs are strongly related to values of moist static energy in the atmospheric boundary layer (Neelin & Held 1987). At low levels, the geopotential term in (1.16) disappears, and moist static energy is given by:

$$h_{sfc} = C_P T_{sfc} + L_v q_{sfc} \tag{2.2}$$

In the tropics, RH is fairly uniform at around 80% at the surface and the dependence of q_{sat} on pressure is small, hence h_{sfc} tends to be largely a function of SST (Neelin & Held 1987).

Low level convergence of warm, moist air in the regions of the tropics with highest underlying SST leads to high values of h_{sfc}. Upper level moist static energy tends to be horizontally uniform (as we will see in the next section), so variations in Δh come mainly from the boundary layer and are largely set by SST (Neelin & Held 1987). It follows that we would expect regions such as the equatorial cold tongue in the eastern Pacific, where h_{sfc} is relatively low, to give rise to a large Δh. This is an important consideration in terms of atmospheric heat transport (2.1), although clearly the amount of heat transported where Δh is large is also dependent on the mass transport, ψ_A. The next section aims to introduce the vertical variations in Δh as well as horizontal ones, and to investigate the structure of the circulation related to regions of high and low h_{sfc}.

2.4 The distribution of moist static energy and meridional flow at the equator

2.4.1 Overview of moist static energy in the tropics

We introduced the concept of moist static energy, *h*, in section 1.3.2 and here we outline the expected distribution of *h* throughout the tropics, before showing various results of the data analysis in sections 2.4.2 and 2.4.3.

At the surface of the tropics, the geopotential term in the moist static energy equation ($h = C_pT + L_vq + gz$) is zero and moist static energy is simply represented by the temperature and moisture terms in the boundary layer ($C_pT_{sfc} + L_vq_{sfc}$). In the upper troposphere, the moisture term vanishes and we are left with the dry static energy ($C_pT + gz$). Overall, temperature and humidity decrease with height but the geopotential term increases, and in general the upper level *h* is greater than at lower levels. The gross stability, Δh is the difference between the upper and lower level *h.* In fact, most of the variation in Δh is a result of gradients in the planetary boundary layer, which are influenced by SST. This is because at upper levels in the tropics, temperature and geopotential vary little, and there is an absence of moisture, leading to horizontally uniform values of *h*.

In convective regions of the atmosphere, which usually coincide with high values of SST, the moist convection acts to maintain a moist adiabatic temperature profile throughout the troposphere and moisture is mixed upwards throughout (Emanuel *et al.* 1994). The stability in the upper troposphere is determined by the level of neutral buoyancy for air parcels in these convective regions. Weak spatial variations in saturation entropy, S_{sat} characterize the convective region, and in practice, since entropy, *S*, and moist static energy, *h*, are related as follows:

$$\frac{T}{M_d}dS = d(C_pT + L_vq + \phi) \qquad (2.3)$$

where M_d is the mass of dry air (Bohren & Albrecht 1998), it follows that there are also weak variations in *h* in convective regions, and that Δh should approach zero in these convective regions, as saturation entropy is approximately constant throughout the troposphere. If we move away from the deeply convecting regions, reductions in moist static energy in the boundary layer lead to a larger gross moist static stability in the troposphere. It is in these regions that subsidence occurs, as a result of sinking dry air, and the radiative cooling in these regions balances the heating in the deeply convecting regions.

From these considerations, we would expect *h* to be relatively horizontally uniform at upper levels and at lower levels to vary more in the horizontal as a result of variations in temperature and moisture in the boundary layer. In the vertical, we would expect strongly convecting regions, often over the warmest parts of the ocean, to have approximately constant *h* and relative humidity with height (such as the picture illustrating Held's model, Figure 1.23) as the convection acts to mix the moisture throughout the troposphere and the temperature profile follows that of a moist adiabat. Over cooler sea surfaces, we would expect less convection, and a larger Δh. In these drier regions, air is often descending from convective regions, and can lead to a minimum in *h* and relative humidity at mid troposphere (around 600 hPa) levels.

2.4.2 Seasonal variability

The distribution of *h* and meridional winds throughout the troposphere at the equator for the solsticial seasons is shown in Figure 2.3. We focus on the equator since this is where meridional mass transport is at a maximum during solsticial seasons, reflecting a cross section of the winter Hadley Cell. White areas at the surface represent the coincidence with land. Since the section is taken along the equator, Africa coincides with 10^{o} – 40 of longitude, Indonesia with 100^{o} – 135^{o} and South America with 280^{o} – 310^{o}. The value of *h* in Figure 2.3 has been divided by C_p in order to give units in Kelvin.

For both seasons, moist static energy (colours) shows little horizontal variation above around 300 hPa, whereas horizontal gradients are larger near the surface, which is expected from the considerations highlighted above. There is a minimum in *h* at around 600 hPa. Over the cooler SSTs, such as those in the eastern Pacific, the minimum in *h* extends down further towards the surface than in other regions. The Pacific warm pool has relatively high values of h_{sfc} compared with that of the eastern Pacific and Atlantic oceans. In fact, horizontal gradients in h_{sfc} between parts of the tropics at the equator are of the same order as vertical gradients. Between the regions with warmest and coldest sea surfaces, the difference in h_{sfc} can be as much as 15 K. There is also less of a pronounced minimum of *h* at mid-levels in places where h_{sfc} is high.

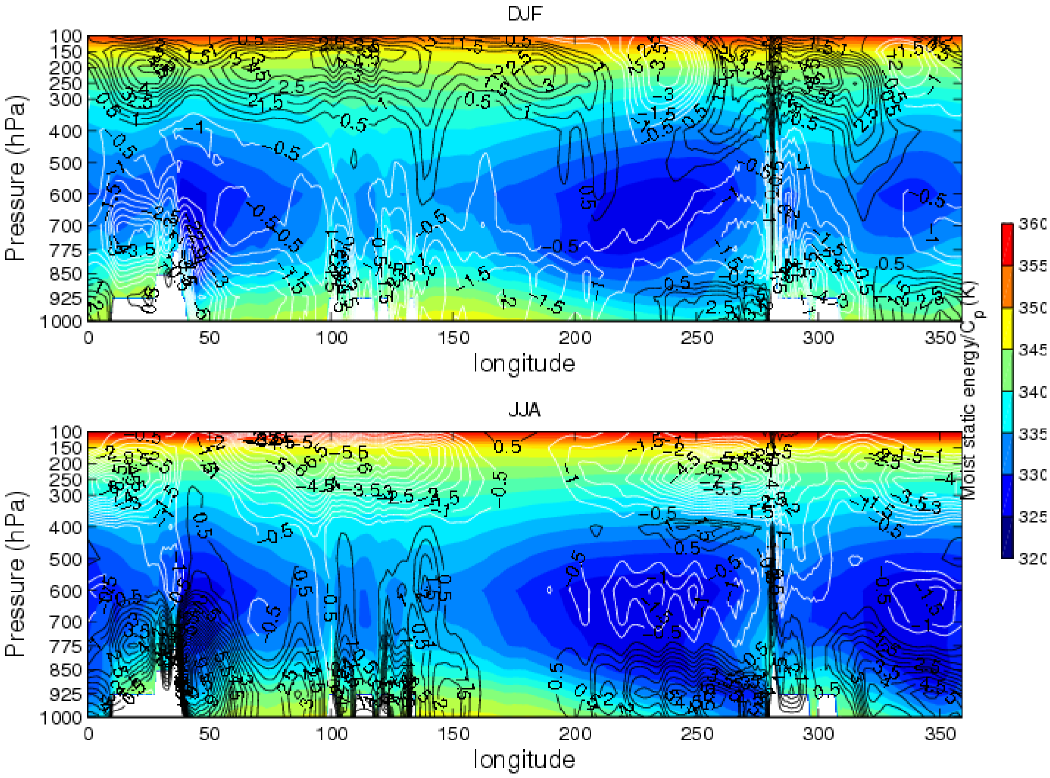

Figure 2.3. Moist static energy (colours) in K and meridional winds (contours) in m s^{-1} at the equator for 1992-2001 JJA. Positive (black) contours show northward winds and negative (white) contours show southward winds. Contour interval is 0.5 m s^{-1}

June – August

During JJA, the general structure of the flow is northward at low levels and southward at upper levels, consistent with a cross section through an overturning Hadley Cell with an ascending branch in the northern hemisphere (Figure 1.7), although there is some departure from this structure in regions where h_{sfc} is low. The southward flow is mainly confined to above 400 hPa, where h is higher than the lower level northward flow, resulting in a net southward transport of heat.

In the eastern Pacific and Atlantic oceans, the structure of the flow differs from that of other regions. The strong surface northward winds observed in Figure 2.2 can be seen here, below around 750 hPa. There is also a low level southward return flow centred at around 600 hPa, where moist static energy is at a minimum, reflecting descending dry air. Above this, is a small region of northward flow at around 400 hPa. The Hadley Cell is acting to transport heat from the northern to the southern hemisphere during JJA, although in the regions where h_{sfc} is low, the flow at 600 hPa acts to transport *low* energy air from north to south, which opposes the direction of the main Hadley Cell heat transport. Over the Indian Ocean, the flow is strongly northward flowing, with maximum mean winds reaching 13 ms^{-1} along the coast of Somalia. Over the western part of the Indian Ocean, there is little return flow at upper levels, with the main southward flow to the west and east of the region containing the Somali Jet.

December – February

The circulation in DJF is generally a reversal of JJA, since now the ascending branch of the Hadley Cell is in the southern hemisphere and the direction of the mean heat transport is from southern hemisphere to northern (Figure 2.3). The cold tongue is less well developed during DJF compared to JJA, and the minimum in h does not extend as far down to the surface. There is still northward flow at the surface over the eastern Pacific and Atlantic oceans, as was noted from Figure 2.2, although it is weaker than in JJA. In fact in some parts of these colder, drier regions, the direction of the flow reverses up to 3 times. Again it could be that this more complicated flow opposes the general direction of Hadley Cell heat transport. Aside from the more complicated regions, there is mainly southward flow below 500 hPa, with some just above the surface northward flowing winds in the eastern Pacific and Atlantic. The situation over the Indian Ocean shows a reversal in direction, reflecting the reversal in the direction of monsoon circulation, with surface winds now flowing southward during DJF, and a less intense flow along the western side. Due to the less pronounced low in h over the eastern Pacific and Atlantic during DJF compared to JJA, horizontal gradients in moist static energy at the surface are slightly reduced but can still be as large as 9 K.

Figure 2.3 demonstrates the vertical and horizontal gradients in h, as well as allowing us to observe the form of the circulation in various regions of the atmosphere. We have seen that there is a reflection of SST on the moist static energy in the atmosphere, so now we highlight an example where anomalously high SSTs covered most of the tropics: the El Niño seasons of DJF 1997-8 and JJA 1997. This will give us a view of the amount of variability which can occur in solsticial seasons, between years.

2.4.3 Interannual variability

The El Niño of 1997/1998 was one of the strongest on record (McPhaden 1999). During positive phases of ENSO, SSTs are anomalously high in the eastern Pacific (corresponding to around 250° to 280° longitude in Figure 2.3); see section 1.1.3 for an introduction to El Niño. SSTs throughout the tropics are more spatially uniform than during normal years, and this is reflected in an increase in boundary layer moist static energy (2.2). Figure 2.4 shows the distribution of *h* and meridional wind during the northern hemisphere winter and summer corresponding to the maximum phase of the 1997/8 El Niño.

December to February

The El Niño event of 1997/98 was most developed during DJF 1998, and this is reflected by the high values of *h* throughout the troposphere (Figure 2.4) compared to the climatological mean for DJF (Figure 2.3).

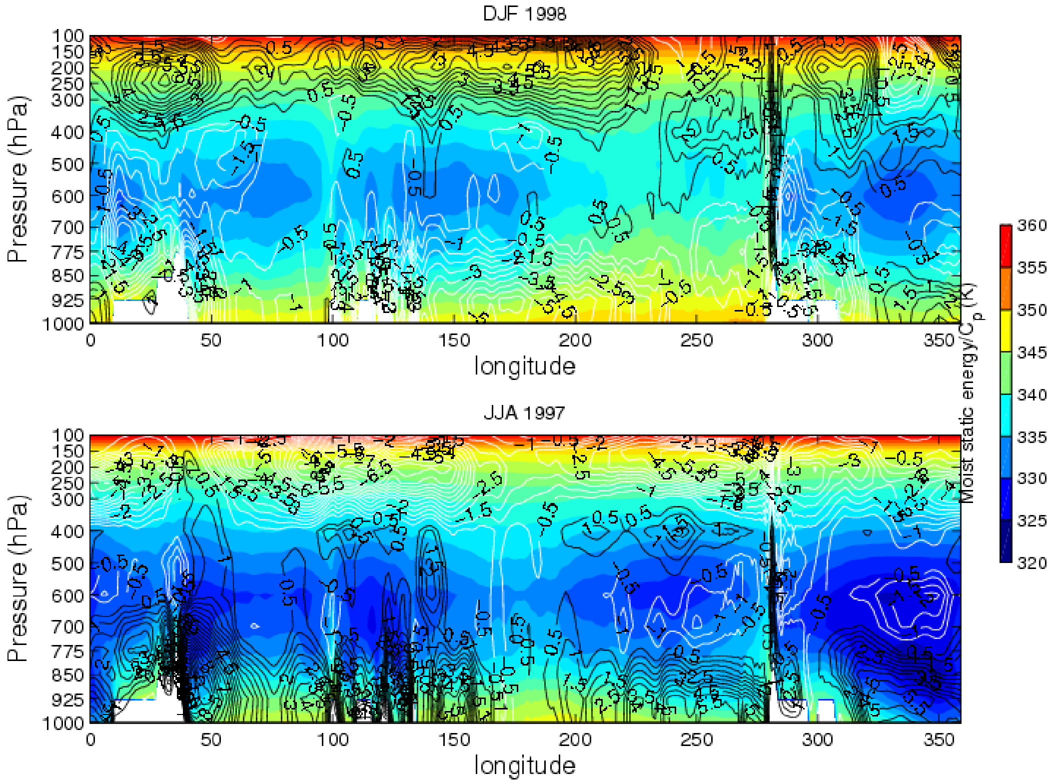

Figure 2.4. Moist static energy (colours) in K and meridional winds (contours) in m s^{-1} as for Figure 2.3, for El Niño seasons: DJF 1998 (upper) and JJA 1997 (lower).

The minimum in *h* at mid levels is much less pronounced and there are noticeably higher values of *h* in the atmospheric boundary layer. The general meridional circulation during DJF 1998 reflects a Hadley Cell which extends along the equator, with southward flow at low levels and northward flow at upper levels. The complicated structure of the circulation including the low level return flow usually present over the eastern Pacific is not present during this season, and h is markedly more uniform in the vertical than for normal years. Surface h is also higher than normal over the eastern Atlantic Ocean, although there is still some low level northward flow here.

The reduction of horizontal and vertical gradients in h in DJF 1998, means that although the overturning circulation is present throughout most of the tropics at the equator, the gross moist static stability is smaller than normal. This raises the question of how much the heat transport varies between normal seasons and El Niño seasons. We investigate heat transport during El Niño seasons in more detail in Chapter 3 and quantify this. In effect, there is a slight reduction in Δh during El Niño seasons, but an increase in ψ_A throughout the extended convective region of the tropics dominates over this, leading to an overall increased H_A (see section 3.4.5).

June - August

In JJA 1997, the El Niño event is not as well developed than in DJF 1998 (Figure 2.4), although again, there is a less pronounced minimum in h in mid levels than is seen in the climatological mean for JJA (Figure 2.3). The Atlantic Ocean still has a minimum, however, and this extends down close to the surface. The eastern Pacific Ocean has higher h than normal, reflecting the increased SST in this region compared with normal years. Again, the horizontal gradient in moist static energy at the surface is less than for normal years, throughout the Pacific. The circulation in JJA 1997 is similar to that of normal years, but with a less pronounced low level return flow in the eastern Pacific.

The figures in section 2.4 show that moist static energy varies with longitude throughout the deep tropics, especially near the surface, as is expected from the considerations introduced in section 2.4.1. There are also seasonal variations in moist static energy which reflect variations in SSTs in the ocean. We have seen how the distribution of moist static energy changes in a positive ENSO phase, which is a reflection of anomalously high equatorial SSTs. As well as the seasonally reversing Hadley Cell circulation which is mostly visible where low level h is at a maximum, a more complex circulation has been highlighted in regions of low moist static energy, such as the eastern Pacific and Atlantic. Finally, the strong, low level jet associated with the Asian monsoon has been noted, particularly during JJA. This jet often has a non-local upper level return flow.

In the next section, we build on these observations by sorting regions of the tropics depending on surface h, in order to more clearly study the circulation in various atmospheric regions.

2.5 Mass transport as a function of low level moist static energy

2.5.1 Framework of analysis

Here, we propose a framework which enables us to view the circulation of the atmosphere as a function of low level moist static energy (h_{sfc}) rather than latitude or longitude. Other recent work has sorted variables in ways other than by geography: one such example is that of Bony (2004), which uses a framework based on the large scale atmospheric circulation to define a series of dynamical regimes responding to different values of vertical velocity (ω). For example, ascending branches of the Hadley and Walker cells over the warmest parts of the tropics would correspond to negative values of ω, and large scale subsidence would correspond to positive values of ω. The idea was to investigate the relative roles of dynamic and thermodynamic effects in the variation of clouds, and the use of vertical velocity as a proxy to define a circulation regime was chosen because cloud types and their radiative properties are largely controlled by the large scale vertical motion of the atmosphere (Bony *et al.* 2004).

Historically, mass flux has been examined on pressure levels and as well within isentropic layers (surfaces of constant potential temperature), e.g. (Held & Schneider 1999). A recent paper uses potential temperature and equivalent potential temperature to sort meridional mass flux in order to investigate the discrepancy in mass transport on moist and dry isentropes (Pauluis *et al.* 2008). By viewing variables (cloud type or mass transport in the examples above) in terms of a closely related or controlling parameter gives a focused picture of the relationship between the quantities in question.

In the present work, motivations are the study of heat transport and atmospheric dynamics and the coupling of ocean and atmosphere. We are particularly interested in the mass transport of the atmosphere, ψ_A, and the contrast in moist static energy between the surface and upper troposphere, Δh, equation (2.1). Since we have established that variability in Δh is set by the surface (and largely by SST) because h at upper levels is relatively uniform (Neelin & Held 1987), we use the low level moist static energy, h_{sfc}, as a basis to sort the mass transport in the atmosphere.

In this way, we can see the form of the circulation present in various regions of the atmosphere which are determined by surface conditions. The dependence of mass transport on h_{sfc} means that we get an idea of gross moist static stability in the atmosphere, as well as being able to visualize the horizontal variations in moist static energy. Grouping regions of similar surface h together allows us to investigate the mean circulation present in each region of the atmosphere, without the complication of geographical distribution. Values of relative humidity in the troposphere give an indication of the amount of atmospheric convection, and we include these in our analysis to give an indication of which regions of the tropics are likely to be convective, and what form the vertical structure of the mass transport takes in these regions.

2.5.2 Method

The lowest pressure level included in the ERA40 dataset is 1000 hPa, and atmospheric variables are provided at this level at all locations. However, in some cases, data points coincide with land and it is possible to identify these areas as those where the corresponding surface pressure is lower than1000 hPa. Since in this analysis, we are interested in the coupling of ocean and atmosphere, data which are incident with land have been removed from the analysis. In fact, the whole atmospheric column present over land has been removed for the whole of section 2.5, leaving the mass transport over the oceans only. The reason to remove land areas is that the focus of the analysis is on the interaction between ocean and atmosphere. It also makes the results clearer and removes the complication of the low level datapoints which are coincident with land. In removing the land from the analysis, we retain around 80% of the data. We reintroduce land areas in section 2.6, where we make estimates of mass transport across the whole equatorial section.

Another consequence of the lowest pressure level being at 1000 hPa is that there is no allowance for regions where surface pressures are above 1000 hPa, as is the case for much of the ocean surface. A correction was made to the ERA40 data to include mass fluxes in these regions by interpolating the 1000 hPa data to the surface. This means that the lowest layer in the atmosphere extends from the surface pressure value to the pressure value halfway between 1000 hPa and the level above this, and the data used within this lowest level were those defined at the 1000 hPa level.

The positive (northward) and negative (southward) mass transport in kg s^{-1} at the equator, between 1000 and 150 hPa for each degree longitude and for each pressure interval, is calculated as follows:

$$\delta\psi_{+} = v_{+}\frac{\delta P}{g}\delta x \tag{2.4}$$

$$\delta\psi_{-} = v_{-}\frac{\delta P}{g}\delta x \tag{2.5}$$

where, v_+ is the northward meridional wind, v_- is the southward meridional wind and g is gravity. Next, the positive and negative mass transport as a function of longitude is binned depending on surface moist static energy, which is calculated as follows:

$$h_{sfc} = C_P T_{2m} + L_v q_{2m} \tag{2.6}$$

where T_{2m} and q_{2m} are values taken at 2m above the surface. Each h_{sfc} interval (bin) is equal to 1 K. The positive and negative mass transport in each bin of h_{sfc} is then summed for each pressure interval and plotted as contours against h_{sfc} and pressure. Filled contours of the corresponding tropospheric relative humidity are added.

2.5.3 Seasonal results

We investigated the seasonal variation in mass transport averaged for each season over the 10 year period. The mass transport as a function of h_{sfc} for each season is shown in Figure 2.5 to Figure 2.8 . These figures show the relationship between h_{sfc}, (determined by 2 m temperature and humidity) and the structure of mass transport in the atmosphere. The colours show relative humidity, solid contours are the sum of the positive (northward) mass transport and dashed contours are the sum of the negative (southward) mass transport. Again, the moist static energy (x axis) has been divided by C_p, so that the units are in Kelvin. Mass transport is in Sverdrups, and we use the Sverdrup as defined in section 1.4 and used by Held (2001) where it is equal to 10^9 kg s^{-1}. We discuss the following figures firstly in general, and then highlight the features of each season individually.

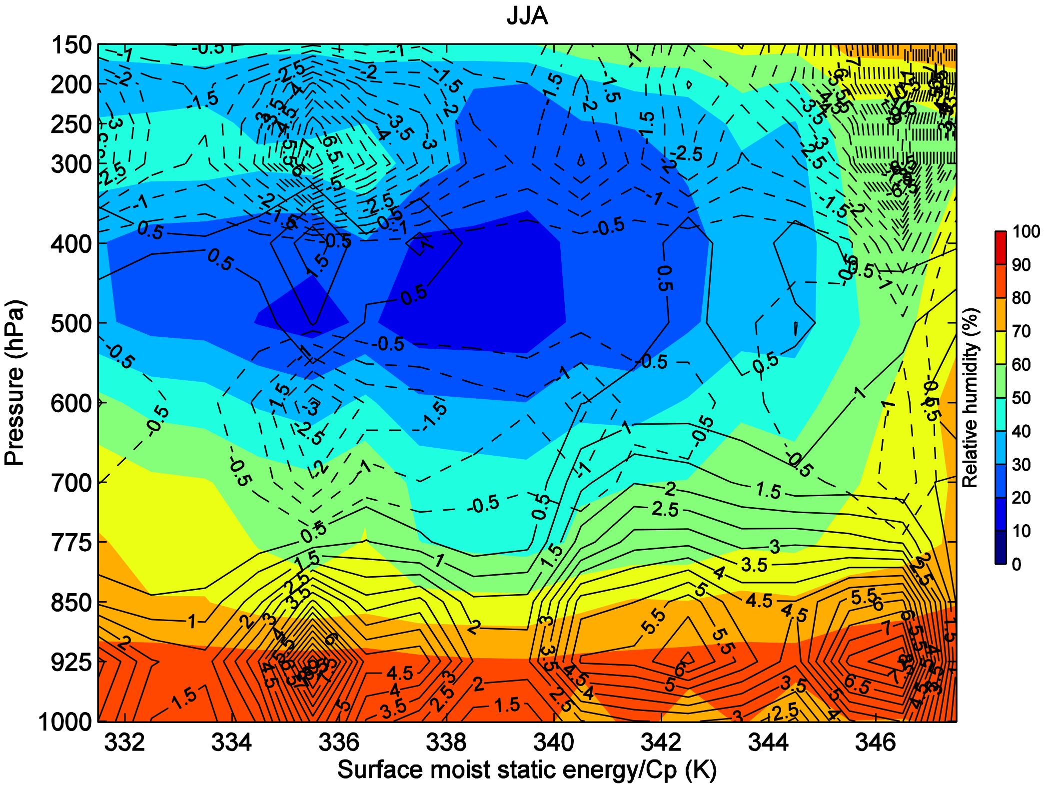

Figure 2.5. Relative humidity (colours) and mass transport (contours) at the equator for 1992-2001 JJA. Positive (black) contours are northward mass transport and negative (dashed) contours are southward mass transport, contour interval is 0.5 Sv.

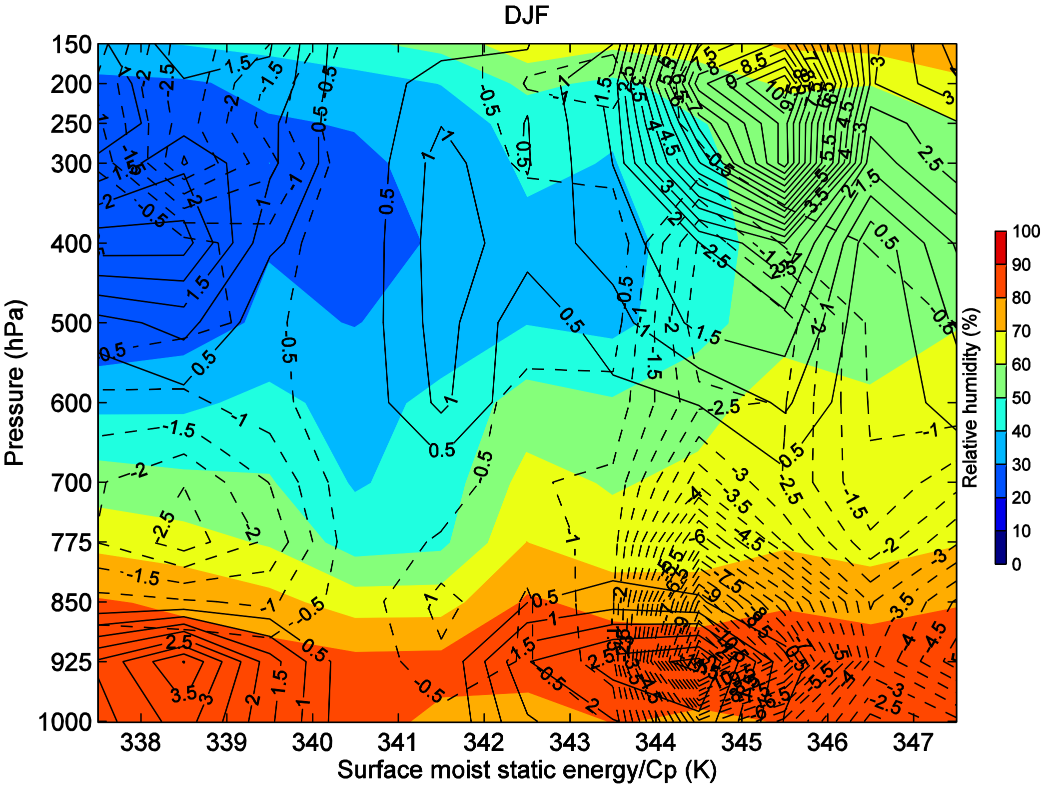

Figure 2.6. As for Figure 2.5 but for DJF

In the tropical oceans, the maximum SSTs do not vary greatly throughout the year, whereas the coldest SSTs (for example in the eastern Pacific) tend to vary much more from season to season (Peixoto & Oort 1992), and this is reflected in h_{sfc}. During each season in the analysis, the maximum value of h_{sfc} is fairly constant at around 348 K, but the minimum value varies from 328 K in SON to 341 K in MAM. For this reason, the minimum value on the x axis scale varies from season to season in Figure 2.5 to Figure 2.8. In each season, high values of h_{sfc} (x axis) correspond to high values of tropospheric relative humidity (colours), so that regions on the right hand side of the plots can be considered to be ‘convective’ regions. Towards the left hand side of the plots are regions where h_{sfc} is low, such as the atmosphere over the eastern Pacific Ocean. In these regions, relative humidity is reduced and there is often a minimum at mid tropospheric levels (Figure 2.5 to Figure 2.8).

June - August

During JJA, in general, there is a northward transport (into the page) of air across the equator at low levels, and a southward return flow at upper levels (Figure 2.5). The centres of northward mass transport at low levels are approximately concentrated in 3 regions, corresponding to where values of h_{sfc} are around 335K, 342K and 346K. These areas correspond to the atmosphere over oceanic ‘cold’ regions (eastern Pacific and Atlantic Ocean), the Somali Jet and the atmosphere over the Pacific and Indian warm pool (which we will refer to as the ‘convective’ region), respectively.

The structure of the mass transport in the convective region has a simple dipolar structure vertically, with most of the northward mass transport confined to below around 700 hPa and most of the southward mass transport confined to above around 500 hPa. This is a good representation of a simple overturning Hadley Circulation. In chapter 3 we focus on the overturning dipolar structure in the convective regions as a basis for calculating the overturning heat transport. Where this overturning circulation occurs, the relative humidity is high throughout the troposphere, implying weak vertical gradients in moist static energy and a small Δh due to the presence of convection. The low values of h_{sfc} over the cold tongues (around 335K, Figure 2.5) mean that there is a larger Δh between the upper level and the surface. However, the mass transport over the colder sea surfaces is not as simple as that of the warmest regions.

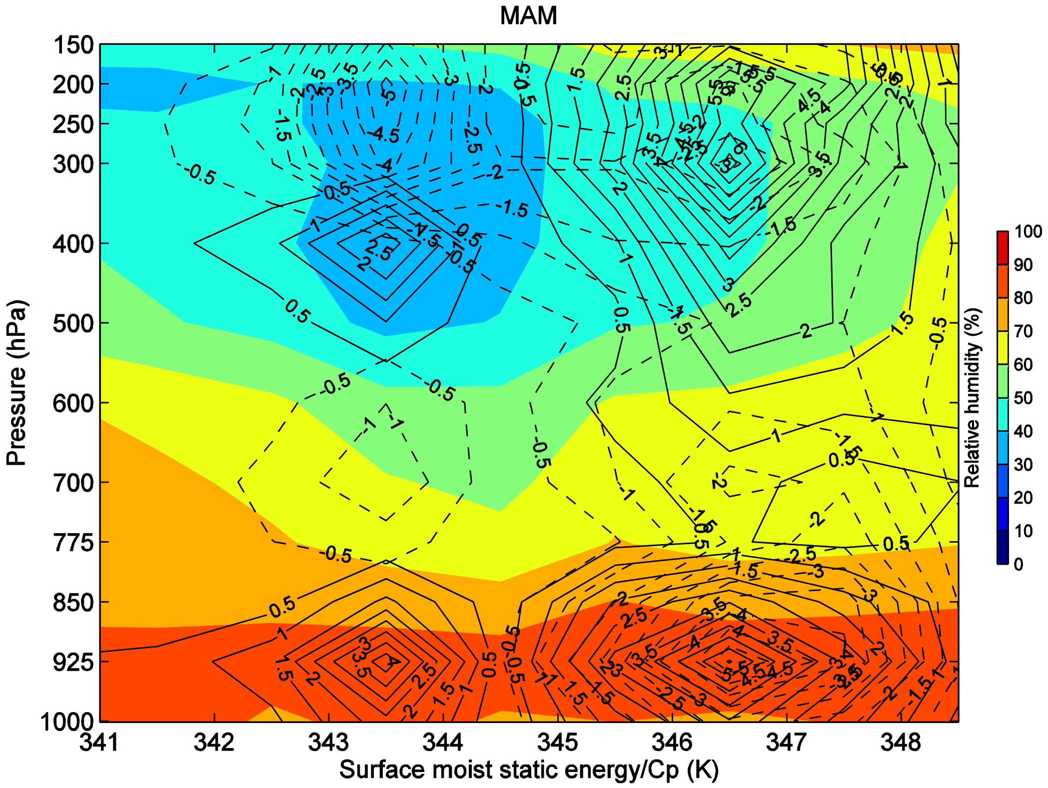

Figure 2.7. As for Figure 2.5 but for MAM.

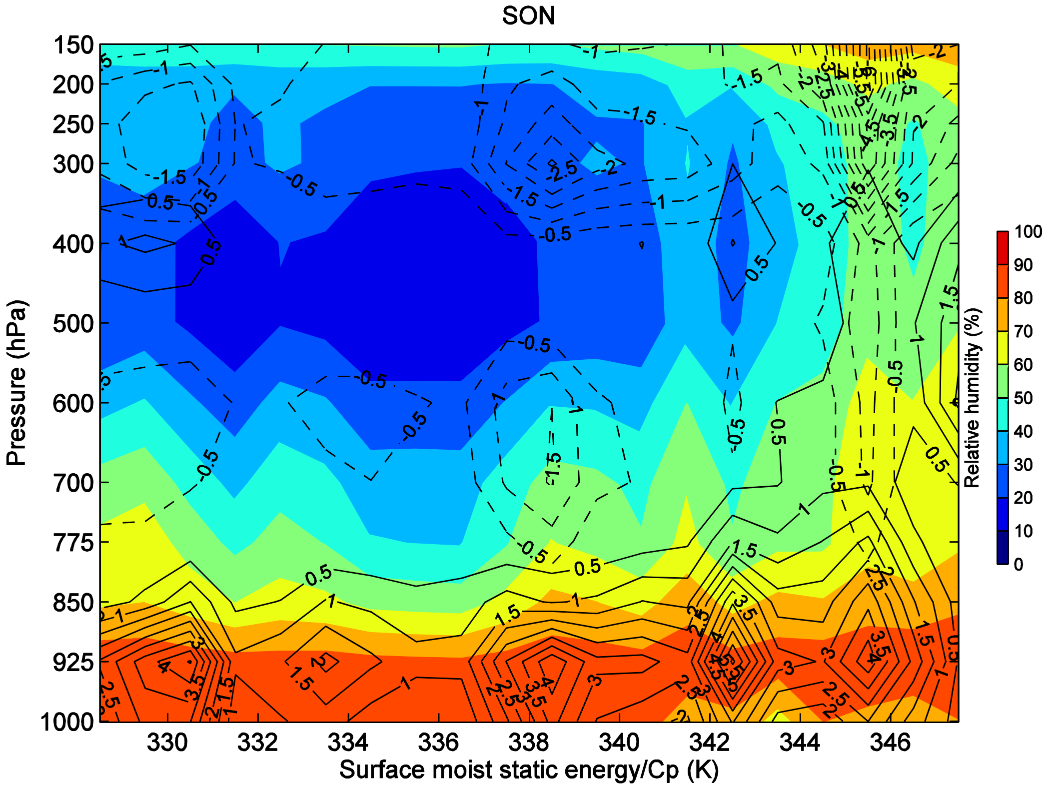

Figure 2.8. As for Figure 2.5 but for SON.

There is northward mass transport at low levels and southward at upper levels, as expected, but also some southward mass transport centered around 700 hPa. There is also some weak northward transport at around 450 hPa in the colder regions, such as noted from Figure 2.3. The low level return flow in these regions which is also noted by Raymond *et al*. (2006) and Zhang *et al*. (2004) could be due to suppressed convection. Since we are using monthly mean data, it is possible that in these regions, there is a combination of deep convection and shallow convection on different timescales, which are both reflected in the seasonal mean.

December - February

During DJF, the vertical structure of the mass transport in the convective regions is a similar shape to that of JJA, but reversed so that the low level flow is southward and the upper level flow is northwards, due to the position of the thermal equator and the ascending branch of the Hadley Cell in the southern hemisphere (Figure 2.6). Again, the relative humidity is high throughout the troposphere in this region. Where there are low values of h_{sfc}, there is some low level northward flow across the equator, which reflects the low level flow across the east Pacific (Figure 2.2). There is also southward flow below 600 hPa, and above this there is more positive and negative flow. There are 4 centres of flow in this region, compared with the 2 in the region with highest h_{sfc} (Figure 2.6).

March – May and September – November

Included for interest are the results of the analysis for MAM and SON although these are equinoctial seasons and so there is less of a clear cross equatorial flow. During MAM especially, the two symmetrical Hadley Cells are realized and there is little flow across the equator (Figure 1.6). SON has slightly more of a cross equatorial flow as the ITCZ is slightly north of the equator.

For MAM, the structure with 4 centres of mass transport over the colder region is very clear and similar in structure to DJF, although with a smaller amplitude (Figure 2.7). In the convective region, there is positive flow throughout the troposphere, and also two regions of negative flow, at around 900 hPa and 400 hPa. For SON, the picture is nearer to that of JJA, but with a slightly smaller magnitude of mass transport (Figure 2.8). In section 2.6 we present a quantification of mass transport in convective and non-convective regions of the tropics as well as the mass transport associated with the Somali Jet during JJA.

2.6 Estimates of atmospheric mass transport in the tropics

In this section, we present some approximate estimates of mass transport and gross moist static stability in the convective and non-convective regions of the atmosphere which were identified in the previous sections. For each season, estimates of positive and negative mass transport for the whole equatorial cross section have been calculated, along with mass transport solely over the oceanic regions, and mass transport associated with particularly low and high h_{sfc}. During JJA there is also an estimate of the mass transported by the Somali Jet, and this is discussed in section 2.6.1. These estimates represent the total summed positive mass transport and summed negative mass transport rather than the mean of positive and negative mass transport and are presented in Table 2.1 and Figure 2.9.

Table 2.1. Estimates of summed positive mass transport (Mpos) and summed negative transport (Mneg) for each season. The estimates have been broken down into total mass transport, transport only over the ocean, over low h_{sfc} and high h_{sfc}, and the mass transport associated with the Somali Jet in JJA. All mass transports are in Sv. Included is the difference between the magnitude of Mpos and Mneg (Diff) and estimates of the mean moist static energy in the lower and upper layers (h lower, h upper), and the difference between them: an estimate of the Δ*h* in the vertical in Kelvin.

		Mpos (Sv)	% of total	% of ocean	Mneg (Sv)	% of total	% of ocean	Diff (Sv)	h lower	h upper	delta h
DJF	Total	242.1	100.0		-247.8	100.0		-5.75			
	ocean only	177.9	73.5	100.0	-178.0	71.8	100.0	-0.17			
	low h_{sfc}	41.4		23.3	-43.4		24.4	-1.99	330.6	338.1	7.53
	high h_{sfc}	36.2		20.3	-41.7		23.4	-5.57	336.3	340.0	3.72
JJA	Total	293.5	100.0		-303.0	100.0		-9.47			
	ocean only	242.4	82.6	100.0	-238.0	78.6	100.0	4.31			
	low h_{sfc}	78.3		32.3	-93.4		39.3	-15.18	328.4	338.2	9.88
	high h_{sfc}	43.4		17.9	-72.0		30.2	-28.64	332.5	339.0	6.46
	Somali Jet	48.1		19.8	-3.8		1.6	44.28	331.5	338.1	6.66
MAM	Total	140.2	100.0		-144.8	100.0		-4.61			
	ocean only	118.1	84.2	100.0	-111.7	77.1	100.0	6.38			
	low h_{sfc}	18.8		16.0	-28.0		25.1	-9.18	334.7	339.4	4.75
	high h_{sfc}	24.6		20.9	-21.9		19.6	2.76	336.6	340.1	3.48
SON	Total	174.5	100.0		-180.8	100.0		-6.25			
	ocean only	153.9	88.2	100.0	-147.7	81.7	100.0	6.18			
	low h_{sfc}	52.1		33.8	-51.2		34.6	0.90	327.1	338.0	10.84
	high h_{sfc}	26.0		16.9	-30.9		20.9	-4.88	335.3	339.6	4.38

Mpos and Mneg are calculated as follows:

$$Mpos = \int_{P_{1000}}^{P_{150}} v_{+} \frac{dP}{g} dx \tag{2.7}$$

$$Mneg = \int_{P_{1000}}^{P_{150}} v_{-} \frac{dP}{g} dx \qquad (2.8)$$

As well as the total values of Mpos and Mneg, which are summed over the whole of the ocean and land at the equator, are calculations of 'ocean only' which refer to mass transport just over oceanic regions, so that (2.7) and (2.8) are integrated only over ocean regions. Further to this, estimates of mass transports over the highest and lowest h_{sfc} were calculated for each season. The thresholds used to define high and low h_{sfc} varied slightly depending on the season, and are shown in Table 2.2.

Table 2.2 Thresholds determining regions of high h_{sfc} and low h_{sfc} for each season (K) in order to calculate Mpos and Mneg

Season	Low h_{sfc} (K)	High h_{sfc} (K)
JJA	<337.5	>345.5
DJF	<341.5	>345.5
MAM	<344.0	>346.0
SON	<337.5	>345.0

In each season the threshold values were set so that the highest values of h_{sfc} coincided with the centres of mass transport which had a dipolar structure and the lowest values of h_{sfc} coincided with the centres of mass transport of the more complex circulation. (2.7) and (2.8) were then applied just over these regions. This gives estimates of the amount of mass transported by the circulations in each region.

These calculations provide an approximate estimate of the seasonal mass transport values. The 'Diff' column is the difference between positive and negative mass estimates and allows us to check to what extent the mass transport is balanced over the season. The difference values are small enough to suggest that mass transport is approximately balanced over this time period. The largest difference for the total transport is for JJA, where the difference between summed positive and negative transports is 9.5 Sv. This is only around 3% of the summed positive transport for JJA.

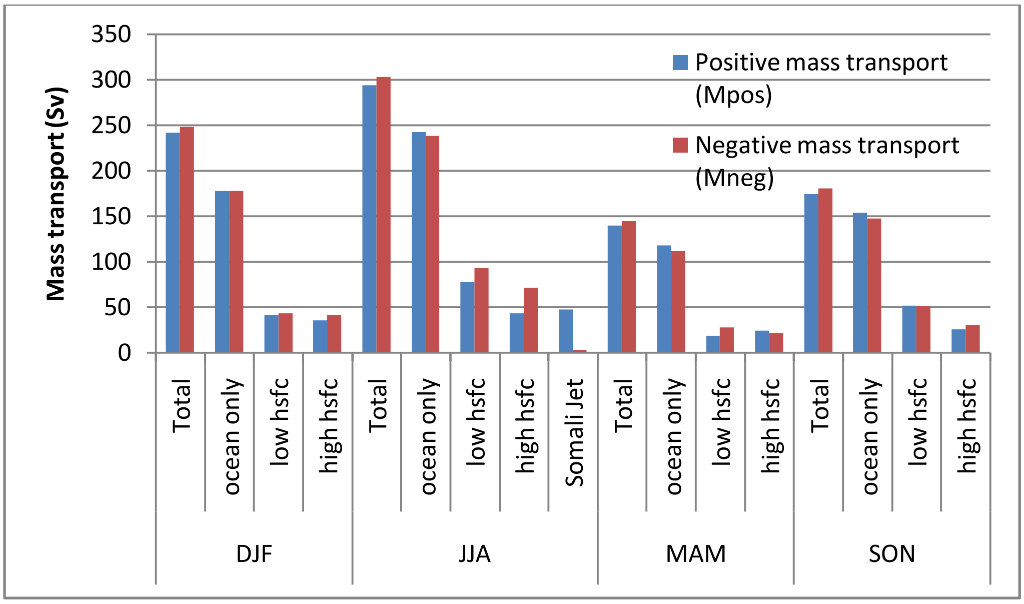

Figure 2.9. Estimates of summed positive and negative mass transport for each season, produced from data shown in Table 2.1.

The estimates of average moist static energy in the upper and lower layers of the atmosphere were calculated by calculating the mass weighted mean *h* above and below 600 hPa respectively. The difference between these values is an approximation of Δh, (final column in Table 2.1). Larger values of Δh imply more heat transport in the case where the atmosphere takes a shape of an overturning cell. Both the values of Δh and mass transport are larger in the regions with low h_{sfc} than high h_{sfc}. However, we have seen that the structure of the circulation in the non-convective regions does not take the form of a simple overturning cell, so it does not follow that more heat is transported in these regions. In chapter 3, we focus on quantifying the heat transport across the equator and especially look at the contribution of the convective regions (where h_{sfc} is highest) to the total.

Czaja and Marshall (2006) calculated the meridional atmospheric streamfunction within moist static energy layers (Figure 2.10). They note that the equatorward mass transport occurs within layers with temperatures colder than the mean, zonally averaged surface moist static energy. They explain this in the midlatitudes by the presence of cold air outbreaks, which are transient features of the general circulation (Held & Schneider 1999; Czaja & Marshall 2006). In the tropics, they attribute the mass transport at low values of surface moist static energy to zonal asymmetries in surface *h*, noting that low level equatorward flow often occurs at low levels over the cold tongues of the Atlantic and Pacific Oceans (as was noted in section 2.3.1). We also find that there is a significant amount of mass transport in regions with low h_{sfc} (Table 2.1 and Figure 2.9). It could be that mass transport over elevated land contributes to the equatorward mass transport at low levels of h_{sfc}.

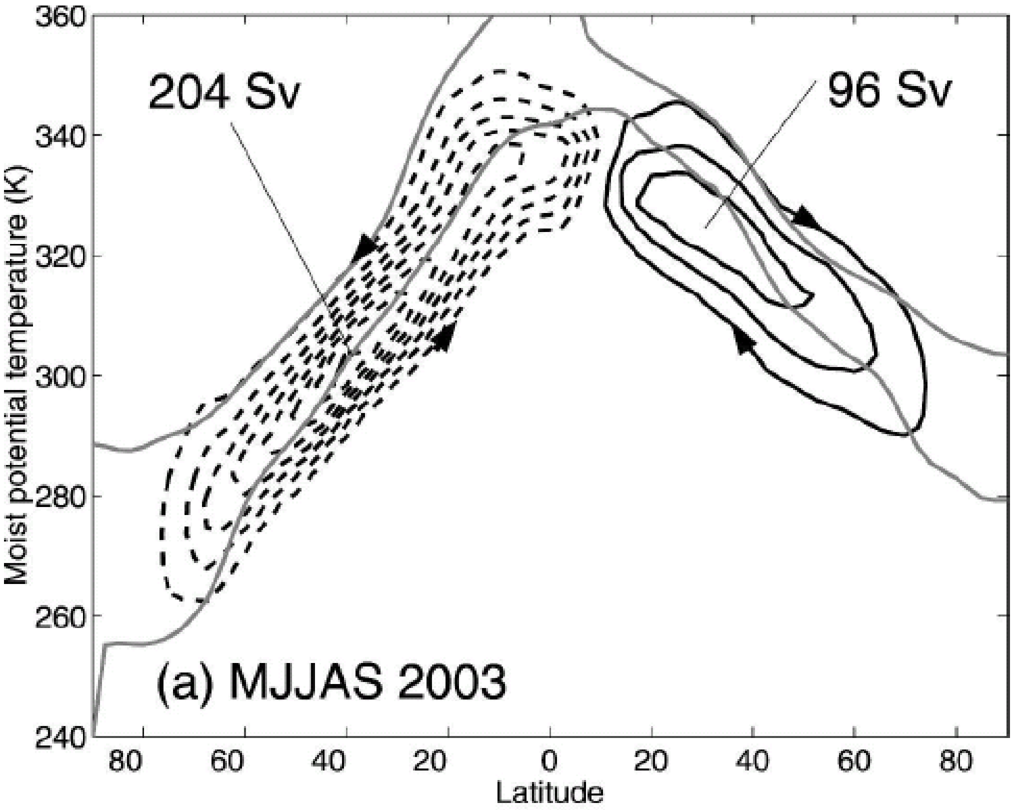

Figure 2.10. Atmospheric meridional mass transport streamfunction within moist static energy layers (C.I. = 25 Sv), positive clockwise, for May-September 2003, y axis is moist static energy. Upper grey curve is the zonally averaged moist static energy at the tropopause and lower curve is at the ground. From Czaja & Marshall (2006).

2.6.1 Mass transported by the Somali Jet

A special case in JJA was the amount of mass transported by the Somali Jet, which was calculated using geographic coordinates corresponding to the strong jet in the west Indian Ocean. The positive and negative mass transport in just this region (between 44° and 58°) is shown in Figure 2.11.

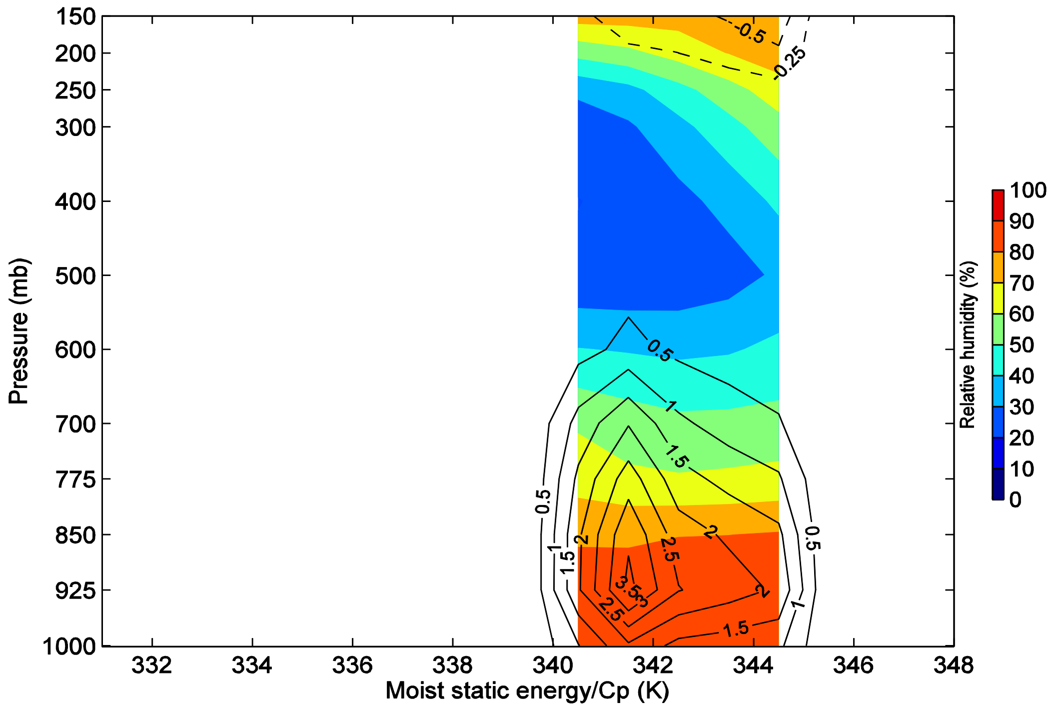

Figure 2.11. Positive and negative mass transport and relative humidity (as for Figure 2.5) for the region 44° to 58° at the equator, corresponding to the region of the Somali Jet during JJA.

The Somali Jet is centred at around 900 hPa and occurs where h_{sfc} is around341 K. This is slightly less than the region with high h_{sfc}, which was classed as being above 345.5 K during JJA. The Somali Jet also did not coincide with the region with low h_{sfc} meaning that the three mass transport estimates are from mutually exclusive areas of the tropics (Table 2.1, Figure 2.9). Relative humidity reaches a minimum at around 500 hPa, indicating that this is not a convective region. There is little southward flow in this region (Figure 2.11). The summed positive mass transport of the Somali Jet is 48 Sv, and the upper level negative flow is only -4 Sv.

During JJA, the positive mass transport for the region with low h_{sfc}, the region with high h_{sfc}, and the Somali Jet is 78 Sv, 43 Sv and 48 Sv respectively (Table 2.1, Figure 2.9). The corresponding negative mass transport in these regions is 93 Sv, 72 Sv and 4Sv. This shows that in each of the 3 regions in question, the positive and negative mass transport is unbalanced. However, the sum of the mass transports over the 3 regions is 169 Sv for the positive value and -169 Sv for the negative values. This is an indication that the northward mass transport at low levels, which is a feature of the Somali jet, gets returned southwards over different regions of the tropics, possibly over the regions with low and high h_{sfc}, to give a balance of mass transport between the three regions. This situation is illustrated in Figure 2.12, which is a schematic of the circulation over the Indian and Pacific oceans, and includes the circulation over the warmpool, the cooler eastern Pacific and the Somali Jet over the Indian Ocean.

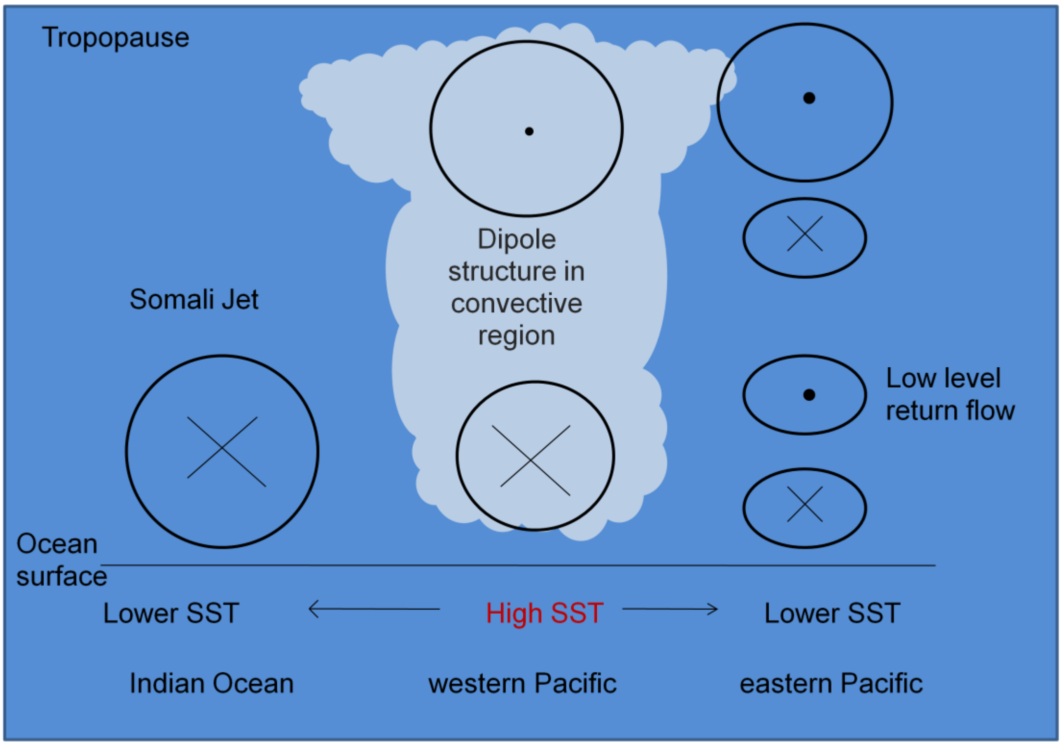

Figure 2.12. Schematic to represent features of mass transport over the Indian and Pacific Oceans at the equator in JJA. Circles represent centres of mass transport, crosses show circulation into the page (northward), dots represent transport out of the page (southward). The central region over the western Pacific is deeply convecting.

2.7 Summary and conclusions

We ended Chapter 1 with a discussion of the simple model proposed by Held (2001), in which the surface moist static energy was assumed to be a function of the zonally averaged surface temperature (section 1.4). We discussed at the beginning of Chapter 2 that although quantities such as meridional flow, low level moisture and SST in the tropics are not spatially uniform, zonally averaged values of mass transport and moist static energy give a good approximation of the total atmospheric heat transport in the tropics. The use of zonal mean values in heat transport calculations, e.g. Held (2001), was the motivation to investigate exactly how the circulation and the moist static energy varied spatially in order to understand the mechanisms of atmospheric heat transport in the tropics.

We identified that Δh is controlled by variations in h in the atmospheric boundary layer, and these are strongly related to SST. We also found that the mass transport in the atmosphere varies depending on whether or not the atmosphere is convective and has a high value of vertical mean h, or if it is non-convective, usually over cooler SSTs and with a lower value of tropospheric h. We identified that horizontal gradients in h in the tropics are of the same order as vertical gradients, and that variations along the equator are on the same order as gradients between the tropics and subtropics. This suggests that although a zonal mean surface value, such as that used by Held (2001) may be appropriate in a simple model to calculate heat transport, there are parts of the tropics which differ from the zonal mean view in terms of circulation and distribution of h, and the aim of section 2.5 was to introduce a framework to identify the different regimes throughout the tropics and investigate their characteristics.

We based our analysis at the equator, since this is where mass transport reaches a maximum during solsticial seasons, representing the middle of the winter hemisphere Hadley Cell during JJA and DJF. Heat transport in an overturning Hadley Cell is the product of an overturning mass transport and the difference in h between the surface and upper levels. We found that over the highest SSTs in the tropics, values of Δh may be small due to the moist, convective nature of the troposphere. However, although Δh may be larger in non-convective regions, it does not follow that the amount of heat transport will be greater in these regions since the circulation of the atmosphere does not often take the form of a deep overturning cell as convection is often suppressed due to subsidence in these regions. We can summarize the key findings in Chapter 2 as follows:

- Hoizontal variations in SST, and hence low level moist static energy and Δh are prominent throughout the tropics. In the horizontal, Δh can be of the same order as in the vertical in some regions.
- The structure of mass transport is different in various regions of the tropical atmosphere. Regions coinciding with high SST have high h throughout the troposphere and are characterized by a mass transport which is approximately equal and of opposite sign at lower and upper levels.
- Over lower SSTs, there is a minimum in tropospheric h, and the structure of mass transport in the atmosphere is more complicated. There is often a low level return flow over areas with low values of h_{sfc} which could be acting to

oppose the general direction of heat transport in the overturning Hadley Cell and could mean that the non-convective regions are less effective at distributing heat from summer to winter hemisphere.

- Seasons such as DJF 1998, where SSTs were anomalously high showed an increase in tropospheric h throughout the whole of the equatorial section. There was reduced Δh in the vertical and horizontal and the structure of the mass transport throughout most of the tropics took the form of the overturning Hadley Cell.
- The framework introduced in section 2.5 allowed us to group atmospheric mass transport by h_{sfc}. This means we were able to clearly identify overturning circulations in regions with high h_{sfc} and note that relative humidity is high throughout the troposphere in these regions, which is an indication of deep convection. We could also identify the minimum in relative humidity in regions with low surface h, indicating that convection was suppressed in these regions.
- Using the framework, we identified the low level Somali Jet which occurs during JJA in the Indian Ocean. We could put approximate values of mass transport on the various regions of the tropics, those with high h_{sfc}, those with low h_{sfc}, and the Somali Jet, although a more rigorous method is required to quantify heat transport in different regions of the tropics.

In chapter 3, we build on the findings of this chapter and investigate the convective region in more detail in order to quantify the amount of heat which is directly attributable to the overturning circulation in the regions where h_{sfc} is highest. We use a criterion based on vertically averaged relative humidity in order to identify the regions which are convective, and isolate and quantify the heat transport associated with a true overturning circulation within these regions.

Chapter 3 Deconstructing the cross-equatorial Hadley Cell heat transport: the role of convective regions

In an attempt to understand the mechanisms controlling the poleward atmospheric heat transport in the tropics, in this chapter we focus on convective regions, over which a simple overturning (Hadley Cell type) circulation is present. We isolate the overturning component of the meridional wind within the convective region using reanalysis data, and find that the associated heat transport is a significant fraction of the total cross-equatorial atmospheric heat transport (80% and 51% of the total during boreal winter and summer respectively).

Variations in convective heat transport are largely controlled by mass transport variations, and moist static energy within the convective regions tends to vary less. The north-south asymmetry resulting in a net annual southward atmospheric flow at the equator which is present in the total atmospheric cross-equatorial heat transport is not a feature of the convective region heat transport. This indicates that other mechanisms, such as the monsoon circulation, are responsible for the asymmetry at the equator.

Overall, our results suggest the presence of a 'true' overturning cell in the convective region is instrumental in explaining why, in the face of many zonal asymmetries in the tropics, the atmospheric heat transport at low latitudes can be successfully computed using only zonally averaged energy and wind fields. The overturning cell is not responsible for all the heat transport, so other mechanisms drive the remaining heat transport, especially the hemispherically asymmetric part.

3.1 Introduction

From the work in chapter 2, we have identified that there is a relationship between SST and moist static energy, h, in the tropics and that regions with high values of h_{sfc} tend to have circulations in the form of a dipole structure, as predicted by Emanuel (1994), and this is reviewed further in section 3.2. These regions are also associated with high relative humidity throughout the troposphere, which is characteristic of deep convection. The dipole structure in the convective regions reflects the Hadley

Circulation, so in this chapter we concentrate on regions with high relative humidity in order to quantify the heat transported by the overturning Hadley Circulation. In these convective regions, such as over the western Pacific warm pool, humidity and moist static energy are relatively high in the boundary layer and throughout the troposphere. In fact, if moist static energy was completely constant throughout the troposphere, no heat would be transported by the Hadley Cell (2.1). Clearly this is not the case, due to the presence of regions of subsidence which give rise to a positive Δh. Still, given the small Δh, in convective regions of the tropics, it would seem that the overturning circulation must be an effective transporter of heat.

We use a criterion based on vertical mean relative humidity to define convective regions of the tropics and isolate the overturning circulation within these regions. The idea is to test the theory that convective regions of the tropics contribute significantly to the total atmospheric heat transport, and to investigate the mechanisms controlling the Hadley Cell heat transport.

Another focus of this chapter is to discover whether or not the convective region contributes to the observed annual mean net southward atmospheric heat transport at the equator (Trenberth & Caron 2001; Wunsch 2005). A strong coupling of ocean and atmosphere heat transport in the deep tropics has been suggested (Chapter 1) and the distribution of convective and descending regions is largely set by SST, as we saw in chapter 2. In particular, at the equator there appears to be compensation between the ocean and atmosphere, where a net southward heat flow in the atmosphere is balanced by a net northward flow in the ocean (Trenberth & Caron 2001; Wunsch 2005). The ITCZ remains mainly north of the equator throughout the year, and heat is mainly transported from northern to southern hemisphere in the atmosphere (Philander *et al.* 1996). Here, we focus on atmospheric heat transport at the equator, and in looking at cross-equatorial convective region heat transport, we are able to address the question of whether or not the convective region contributes to the annual mean net southward atmospheric heat transport. As in chapter 2, the focus at the equator is because it is here that mass transport is at a maximum during solsticial seasons since it dissects the centre of the winter Hadley Cell.

We begin by describing the methodology in section 3.2, including the criterion used to define convective regions. We then go on to quantifying the convective region heat transport as a fraction of the total atmospheric heat transport at the equator using the reanalysis data, then look in more detail at the mechanisms which control the convective region heat transport in section 3.3 such as the variability of gross moist static stability, mass transport and convective heat transport during an El Niño year.

3.2 Framework and Methodology

3.2.1 Data

As in chapter 2, we use the ERA40 reanalysis dataset from the European Centre for Medium Range Weather Forecasting (Uppala *et al.* 2005). However, in this chapter we use 22 years of monthly mean data, (1980-2001) and calculate seasonal means for each of the years on 13 pressure levels from 1000 hPa to 100 hPa, at the equator. Variables include meridional wind, temperature, relative humidity, geopotential height and surface pressure.

Several corrections were applied to the data in order to account for conservation of mass and to adjust for surface pressure, and these are detailed as follows. To allow for atmospheric data points which were coincident with land, points given on fixed pressure levels of higher values than surface pressure were removed. This correction ensures that all land areas were removed from the atmospheric data set. To allow for regions where surface pressures were above 1000 hPa, such as over much of the ocean surface, again, a similar correction as was made in chapter 2 included mass fluxes in these regions by interpolating the 1000 hPa data to the surface. This means that the lowest layer in the atmosphere extends from the surface pressure value to the pressure value halfway between 1000 hPa and the level above this, and the data used within this lowest level were those defined at the 1000 hPa level. One further correction to the data was made in order to correct for conservation of mass: we enforced that over a season, the vertically integrated mass flux across the equator was zero as follows:

$$\int_{0}^{360} \int_{P_{100}}^{P_{sfc}} v \frac{dP}{g} dx = 0 \qquad (3.1)$$

3.2.2 Definition of convective regions of the tropics

We have identified that there are different regions of the tropical atmosphere which can be thought of as convective or non-convective, and we have seen that the circulation differs in each region (chapter 2). In order to be able to distinguish between these regions, we require a criterion, and here we use one which is based on vertical mean relative humidity. To motivate our analysis we use the framework put forward in Emanuel *et al.* (1994), and illustrate the basic physical picture in Figure 3.1.

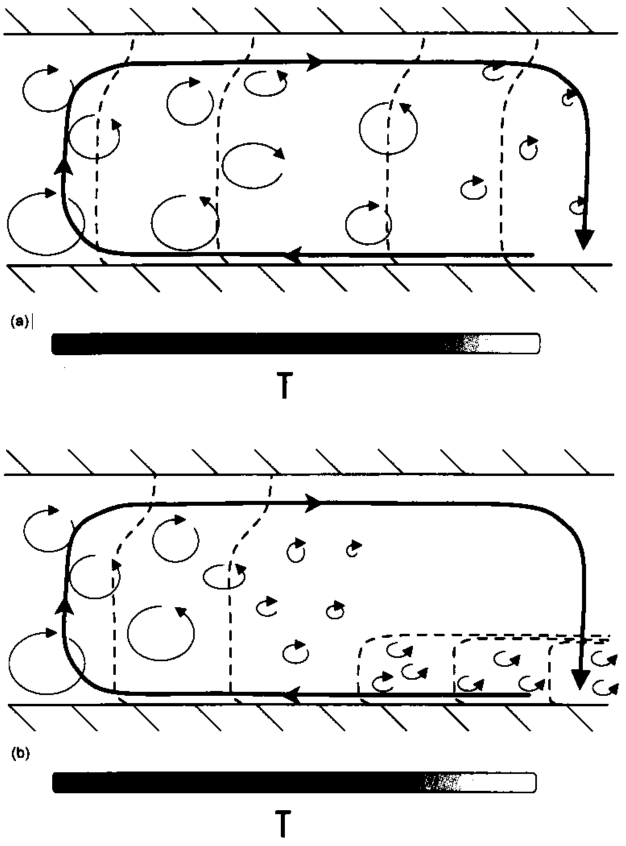

Figure 3.1. A schematic of the interaction of convection with a large scale circulation driven by a) small and b) large surface temperature gradients. The dashed lines indicate contours of constant saturation entropy, while the thick arrows depict the large scale circulation and thin arrows represent convection. From Emanuel *et al.* (1994).

The interaction between convection and large scale circulation can be schematized in two different regimes using an idealized forced convection problem with insulated upper boundary and prescribed temperature at the lower boundary (Figure 3.1). Where there are weak imposed variations in surface temperature, convection develops over the whole domain (Figure 3.1a) and saturation moist entropy (S_{sat}, contours in dashed lines) is almost constant in the vertical and horizontal. Where the surface temperature variations are stronger (Figure 3.1b), the resulting large scale circulation is strong enough to suppress convection in some regions, leading to sharp vertical gradients in S_{sat}.

This discussion suggests that weak spatial variations in S_{sat} characterize the convective region and we use this theory in the following. In practice, since we have seen that entropy, S, and moist static energy, h, are related by (2.3), (section 2.4.1), we can use h instead of S to distinguish between convective regions and non-convective regions. The spatial variability of moist static energy h is smaller for regions with high relative humidity (RH) than with low RH and this is illustrated by the relationship between the spatial standard deviation of h and the vertically averaged RH (Figure 3.2, left panel).

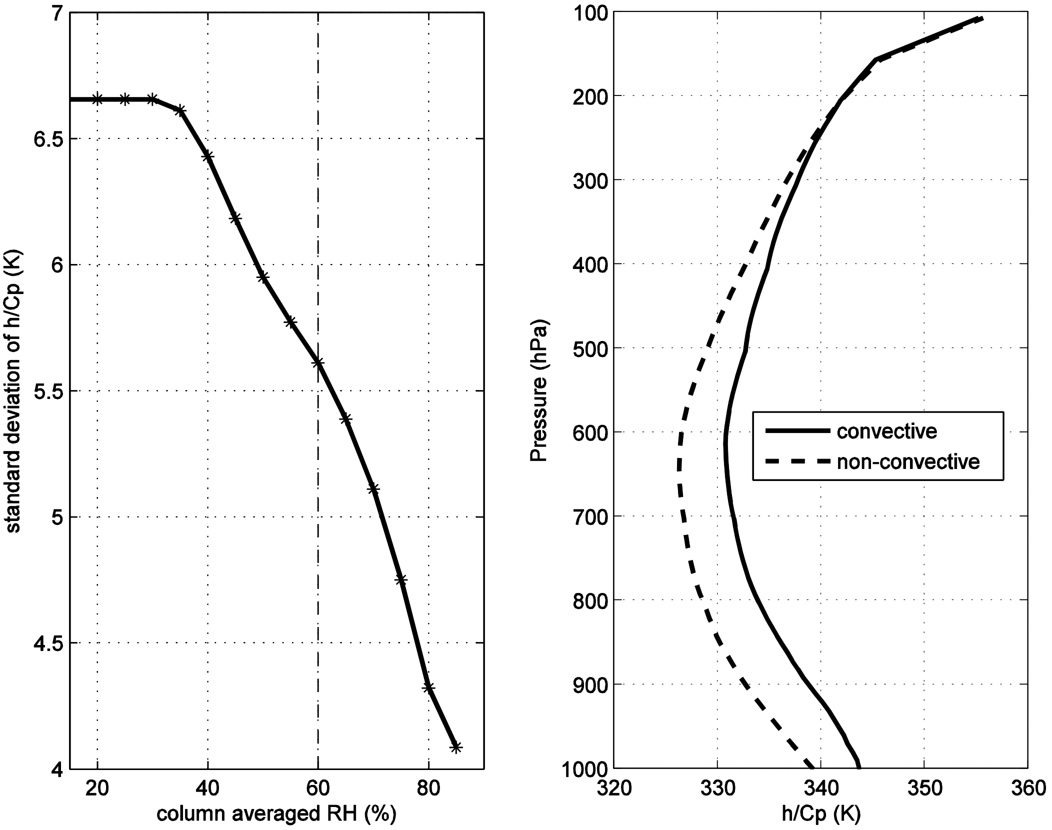

Figure 3.2. Horizontal and vertical standard deviation of moist static energy throughout the region enclosed by a given column averaged RH, divided by C_p, as a function of (mass weighted) vertical mean RH (left). Mean moist static energy profiles (right) for the convective region (solid line) and non-convective region (dashed line) based on a threshold between convective and non-convective regions of 60% vertically averaged RH.

Based on Figure 3.2, we have defined convective regions as those with vertically averaged mass weighted RH greater than 60%, and non-convective regions where it is less than 60%. Examples of moist static energy profiles in convective and non-convective regions based on this criterion are shown in Figure 3.2, (right panel).

The convective region extent, which we denote as L_*, is simply the sum of the number of degrees at the equator which are classed as convective (so the maximum extent would be 360). The value of L_* based on the RH > 60% criterion varies with season. For example, during JJA and SON, the convective region is further north of the equator than during DJF and MAM, and this is reflected on maps of vertical mean RH (Figure 3.3). To give a sense of scale, when taking all seasons of the 22 years into account, the mean extent of the convective region defined using the 60% relative humidity criterion represents approximately half of the all the data points along the equator (Figure 3.4a,b). The mean SST in a convective region which has a threshold of 60% is approximately 302 K (Figure 3.4c). There is an increase in mean SST as the column averaged RH increases from around 40%, but after 60%, there is little variation in the mean SST, indicating that the 60% threshold captures the regions with the highest SSTs (Figure 3.4c).

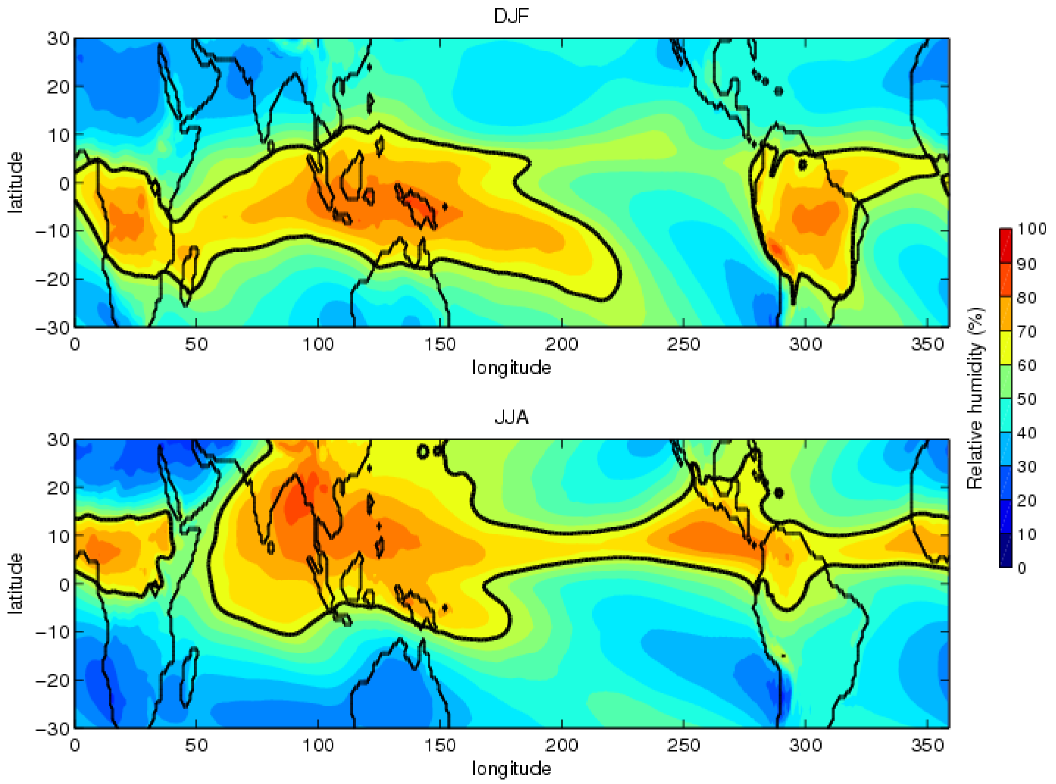

Figure 3.3. Vertical mean mass weighted relative humidity between the surface and 100 hPa in the tropics for DJF (top) and JJA (bottom). The thick black line represents 60% relative humidity, and hence areas within the thick black line represent the convective region.

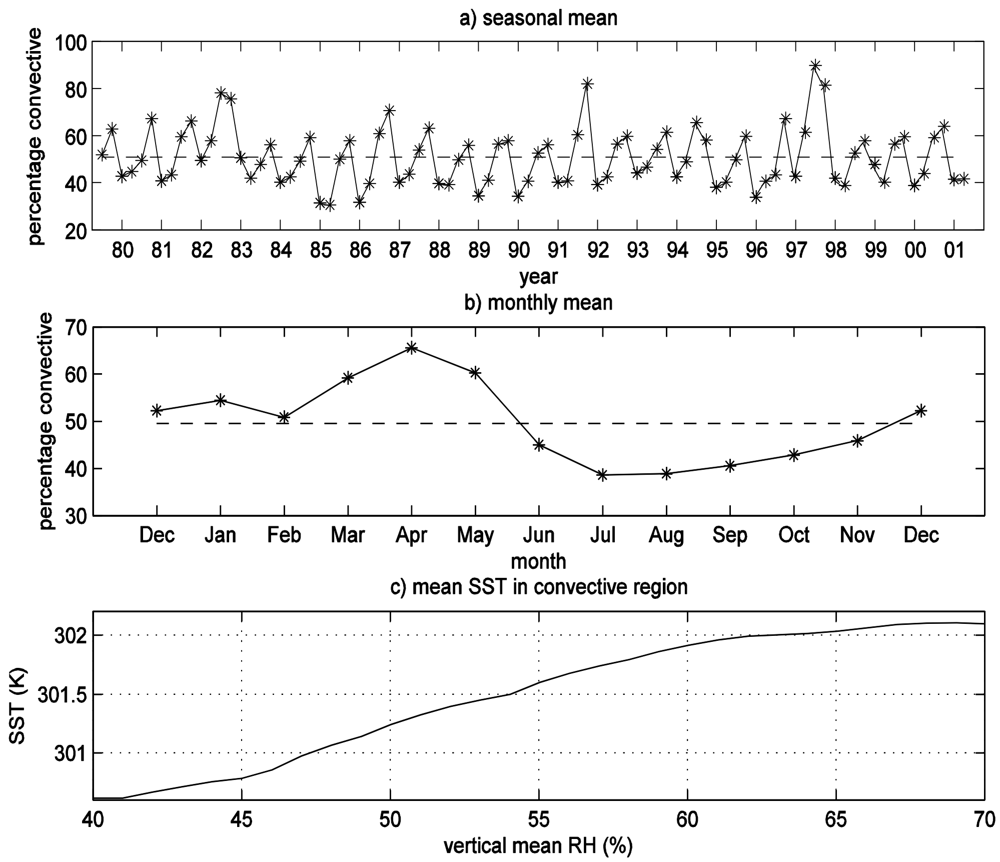

Figure 3.4. Percentage of total equatorial data points classed as convective (vertically averaged relative humidity > 60%) for a) seasonal means over the 22 year period and b) monthly means for the 22 years. Year markers on axis in a) refer to JJA in each case. The dashed lines in a) and b) represent the long term mean value. c) Variation of mean SST (Kelvin) with vertical mean RH (%).

3.2.3 Calculating baroclinic wind in convective regions

Here we define the barotropic component in the atmosphere as that which represents the circulation which does not sum to zero when mass transport is vertically integrated, and can represent lower or upper level jets. The baroclinic component defined here represents a closed overturning circulation, where mass transport at upper levels is equal and opposite to that at lower levels.

In this chapter, we remove the vertical mean (barotropic) wind profile from the total wind profile in order to obtain the baroclinc wind profile, which can be used to calculate the overturning heat transport in the convective regions, which are defined as those with vertical mean RH > 60% (previous section). Since the shape of the baroclinic component is based on the meridional wind profile minus the vertical mean wind profile, there is a zero crossing at mid levels and the vertical integral is zero. We call the baroclinic wind profile, calculated in this way and averaged over the whole convective region, v_*. The focus on the baroclinic profile in regions with high RH is consistent with the result from Emanuel (1994), which identified a baroclinic wind profile in deeply convecting regions of the atmosphere.

3.2.4 Atmospheric heat transport calculation

a) Total heat transport

Firstly we needed to calculate the total cross equatorial heat transport in all regions of the atmosphere, convective and non-convective together. We calculated the moist static energy, *h*, throughout the troposphere at the equator, using (1.16) and reanalysis temperature, relative humidity and geopotential height fields. The moist static energy and the meridional wind field, *v*, were used to calculate the total zonally integrated cross-equatorial heat transport, H_A, using

$$H_A = \int_0^{360} \int_{P_{100}}^{P_{sfc}} vh \frac{dP}{g} dx \tag{3.2}$$

integrated from the surface to 100 hPa. This analysis highlights an annual net southward total atmospheric heat transport at the equator in the ECMWF reanalysis data of -0.4 PW which is consistent with Wunsch (2005) and Trenberth and Caron (2001).

b) Convective region heat transport

When calculating the convective region heat transport, H_*, the *v* in (3.2) was replaced by the baroclinic wind profile, v_*, which was the mean wind profile with the barotropic component removed (section 3.2.2). The heat transport over the convective region was calculated as follows:

$$H_* = L_* \int_{P_{100hPa}}^{P_{sfc}} v_* h_* \frac{dP}{g} \tag{3.3}$$

where L_* is the longitudinal extent of the moist region and h_* is the mean moist static energy profile in the convective region. The convective region heat transport calculated in this way represents the transport associated with a closed overturning circulation within this region, since

$$\int_{P_{100hPa}}^{P_{sfc}} v_* \frac{dP}{g} = 0 \tag{3.4}$$

i.e. mass transport at low levels is equal and opposite to that at upper levels. We define the overturning mass transport ψ_* associated with the convective region as

$$\psi_* = L_* \int_{P_{mid}}^{P_{sfc}} v_* \frac{dP}{g} \tag{3.5}$$

where P_{mid} is defined as a point in the mid troposphere where the overturning meridional wind profile v_* is zero (around 500 hPa). The gross moist static stability in the convective region is then computed as

$$\Delta h_* = \frac{H_*}{\psi_*} \tag{3.6}$$

so that

$$H_* = \psi_* \Delta h_* \tag{3.7}$$

In the following, for short, we refer to the total cross-equatorial heat transport as H_A, and the convective region cross equatorial heat transport simply as H_*.

3.3 Results

3.3.1 The contribution of the convective region to the total heat transport

The convective region accounts for a significant portion of the total zonally integrated heat transport H_A (Figure 3.5). [Note that Figure 3.5 shows poleward heat transport so that all northward and southward heat transport values appear positive]. H_* on the x axis was calculated using (3.3) and H_A was calculated using (3.2). Table 3.1 summarises the total northward heat transport and the contribution of the convective region to the total. [Included are calculations for convective regions based on thresholds of 55% and 65% column averaged RH for illustration, although further results based on these thresholds are not included and all results from this point refer to convective regions based on >60% RH.] The mean convective region transport H_* in DJF is 0.80 of the total, and in JJA it is 0.51. In MAM and SON, the convective region transports 0.75 and 0.55 of the total heat transport respectively, based on the 60% RH threshold (Table 3.1). The greatest total poleward heat transport, H_A, at the equator occurs during the solsticial seasons (DJF and JJA), when the thermal equator is displaced furthest south and north of the geographical equator respectively and cross equatorial heat transport is enhanced.

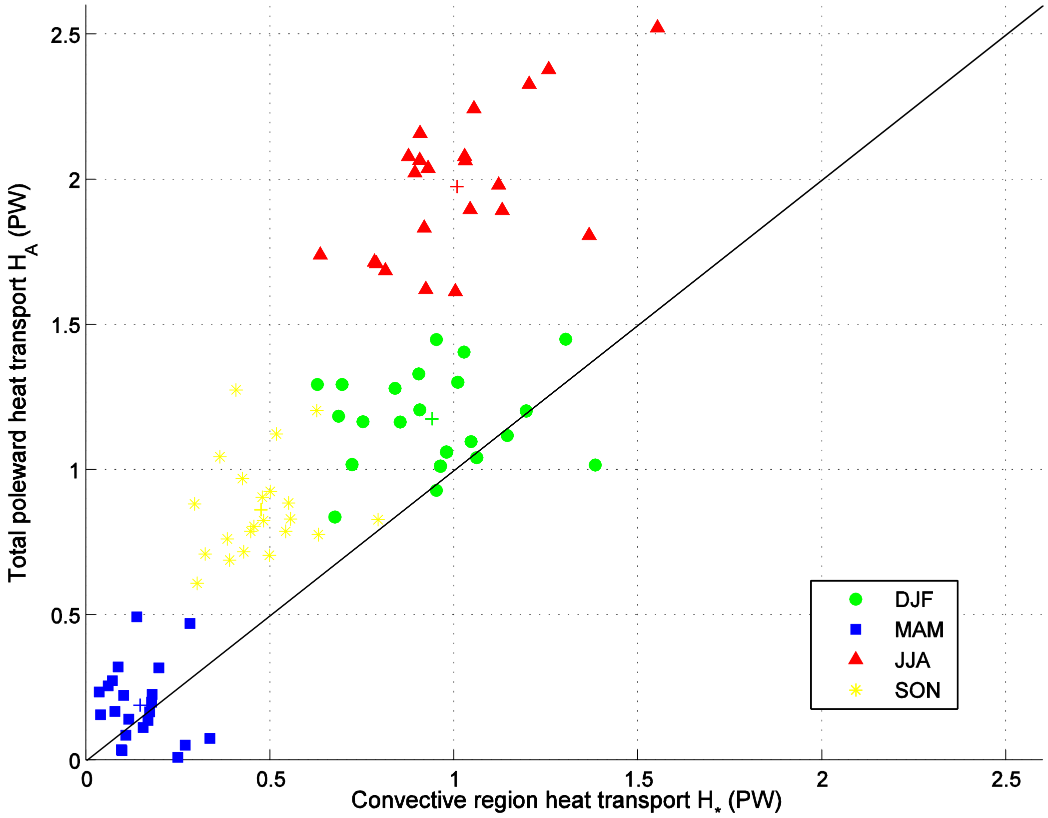

Figure 3.5. Total zonally integrated poleward heat transport and the contribution from the convective region in Petawatts (1 PW = 10^{15} Watts) for seasonal data. The diagonal line represents a 1:1 ratio of convective region heat transport to total heat transport. Each point represents a season from the years 1980 to 2001. Seasons are: DJF (green circles), MAM (blue squares), JJA (red triangles), SON (yellow stars) and mean values for each season are represented by crosses.

There is some north-south asymmetry in the zonally integrated total heat transport H_A: the mean JJA heat transport is -2.0 PW whereas the DJF mean is +1.2 PW. During MAM and SON, H_A is smaller at +0.2 PW and -0.9 PW respectively. The annual mean H_A over the 22 year period is -0.4 PW, showing a net southward heat transport across the equator. Although there is seasonal north-south asymmetry in H_A, the convective region heat transport is more symmetric, with the annual mean H_* at -0.1 PW.

Although convective region heat transport is significant, it does not account for the entire cross equatorial heat transport, indicating that other mechanisms, such as the seasonally reversing monsoon circulation play a role (the strength of the jet associated with the Indian monsoon was discussed in Chapter 2). Also, there is an indication that the net southward total heat transport is due to these mechanisms rather than the convective region heat transport.

Table 3.1. Mean seasonal total cross equatorial heat transport (H_A) and convective heat transport (H_*) in PW using 3 different RH thresholds to define the convective regions (60% threshold is used throughout the chapter and shown in bold, other results are included for interest) over the 22 year period. Positive values represent northward transport and negative values represent southward transport. Numbers in brackets represent the ratio of H_* to H_A.

		55% RH	**60% RH**	65% RH
Season	H_A	H_* (H_*/H_A)	**H_* (H_*/H_A)**	H_* (H_*/H_A)
DJF	1.18	1.08 (0.92)	**0.94 (0.80)**	0.66 (0.56)
MAM	0.18	0.13 (0.67)	**0.14 (0.75)**	0.14 (0.74)
JJA	-1.98	-1.25 (0.63)	**-1.00 (0.51)**	-0.66 (0.33)
SON	-0.86	-0.51 (0.59)	**-0.47 (0.55)**	-0.38 (0.44)

The results presented throughout this thesis are based on a RH threshold of 60%, although analyses were also carried out using different thresholds. The choice of 60% was motivated by the fact that it separates regions with high variance in *h* from those with low variance in *h* (motivated in section 3.2.2). Some results of convective region heat transport using different RH thresholds for the convective region are shown in Table 3.1. When setting the RH threshold values for defining the convective region, it is important not to set the threshold too low, as this means that regions may be classed as convective which are not consistent with the framework of section 2.4, which is based on the assumption of constant S_{sat} (Emanuel *et al.* 1994). Conversely, by setting the threshold too high, we reduce the amount of data points included in the convective region. For example, by choosing our threshold as 70% or above means that there is at least one season in the 22 year period with has no convective region since the threshold is too high.

With increased RH threshold there are fewer data points included in the convective region and H_* is reduced (Table 3.1). Increasing the threshold also has the effect of reducing the asymmetry between H_* in JJA and DJF, and at 65% RH, H_* is well balanced between JJA and DJF at -0.61 and 0.61 PW respectively. We mentioned previously that the monsoon circulation must be responsible for transporting heat across the equator, since the convective region does not explain all of the heat transport. It seems likely that it is responsible for most of the north-south asymmetry at the equator since the convective region does not contribute much to this. The heat transport by the monsoon is not generally included in the convective region heat transport since it usually takes place in regions where RH is low as a result of strong cross equatorial winds and cold waters due to coastal upwelling (Kumar & Schlussel 1998). By including regions with vertical mean RH lower than 60% potentially means that some monsoon associated heat transport is included in the convective region, which increases the north-south asymmetry. Section 3.3.2 looks in more detail at the mechanisms of convective region heat transport.

3.3.2 Mechanisms controlling convective region heat transport

a) Convective region extent

The size of the convective region L_* varies with season; in DJF and MAM, areas with high SSTs are more extensive at the equator than during JJA and SON (Figure 3.3). Although L_* is comparable in JJA and SON and also in DJF and MAM, H_* differs greatly in each season. For example, the magnitude of H_* in JJA is more than double that of SON, although L_* is approximately similar in each season. This is due to the dominance of cross equatorial mass transport in the solsticial season and a greater heat flow from the summer to winter hemisphere. The situation is also true for DJF compared to MAM, with a similar L_* but greater H_* in DJF. Since the solsticial seasons feature the strongest cross equatorial mass and heat transport, we concentrate on DJF and JJA to study the mechanisms controlling convective region heat transport.

Within both DJF and JJA there is a positive relationship between L_* and H_* (Table 3.2 and Figure 3.6). DJF 1983 and 1998 have been highlighted on the figure, as these were strong El Niño years and hence the convective region extent is enhanced, as was the convective heat transport.

Table 3.2. The relationship between convective region heat transport and longitudinal extent of the convective region. Rate of change of convective region heat transport with growth of the convective region (dH_*/dL_*) is shown in the second column. The correlation is significant to the 99% level in DJF, although not statistically significant above 80% in JJA.

Season	dH_*/dL_* (Tera watts or 10^{12} W per degrees longitude)	Correlation coefficient
DJF	3.3	0.60
JJA	3.4	0.30

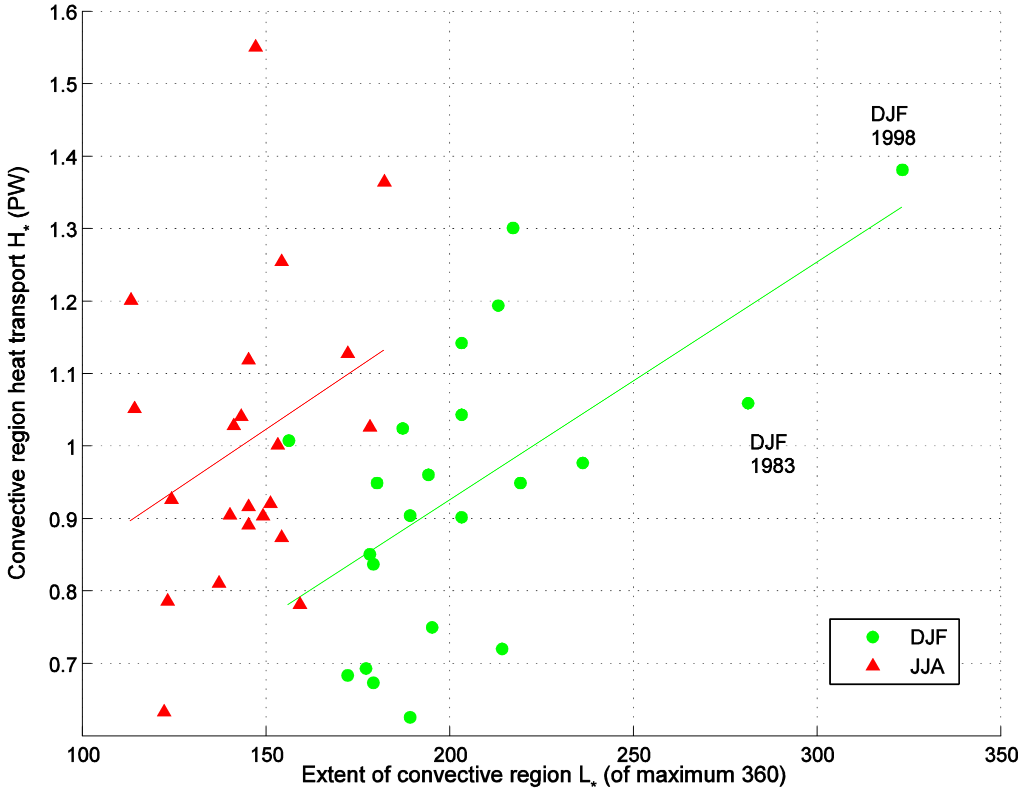

Figure 3.6. Poleward heat transport by the convective region H_* in PW and the extent of the convective region L_* represented by the number of degrees longitude at the equator which are classed as convective, out of a maximum 360 degrees. A linear fit has been added to the data for each season. Each point represents a year from 1980 to 2001, seasons are: DJF (green circles) and JJA (red triangles).

There is a significant linear increase in H_* with increased L_* during DJF, and the convective region heat transport increases by 3.3 Terawatts (10^{12} Watts) for every degree of longitude increase of equatorial region which is classed as convective. This is an indication that the strength of the convective region cross equatorial heat transport increases as high SSTs become more extensive in the tropics during this season. The correlation is relatively high in DJF (0.6), but weaker in JJA, (the correlation between H_* and L_* is 0.30 at a P value of 0.17). The similar increase in H_* with L_* for each season (slope) implies that the relationship will hold for very small or large convective regions. Table 3.2 demonstrates the increase in H_* which occurs with an increase in L_* for the solsticial seasons. It should be remembered that we are only looking at data points along the equator in this chapter, which do not necessarily coincide with the regions with maximum SST during solsticial seasons.

b) Mass transport and heat transport

In order to investigate the mechanisms which determine how H_* is controlled, we investigated the mass transport ψ_* and the gross moist static stability Δh_* in the convective region. There is a positive correlation between poleward mass transport ψ_* and heat transport H_* in the convective region during DJF and JJA (Figure 3.7). A best fit line has been added, and the gradient of the slope gives an approximate estimate of Δh_*. A discussion on the variability of Δh_* is presented in section 3.4.4.

The positive relationship between the mass transport and heat transport in the convective region in both DJF ($R = 0.72$, $P < 0.001$) and JJA ($R = 0.67$, $P < 0.001$; Figure 3.7) means that the variability in mass transport explains at least two thirds of the variability of the heat transport in the convective region in solsticial seasons. In section 3.4 we further investigate the variability of gross moist static stability. Since we expect the gross moist static stability to be fairly uniform throughout the convective region (section 2.4), now we can say that the overturning circulation plays a large role in setting the heat transport in the convective region, even with small variations in Δh_*.

In section 3.3.2 so far, results have concerned investigating the role of the convective region extent (section 3.3.2a) and mass transport (3.3.2b) on convective heat transport using the method outlined in section 3.2. In sections 3.3.2c) to f), we present further results using a modified method, whereby the baroclinic component of the meridional wind is calculated differently, in order to more accurately estimate mass transport and gross moist stability. The motivation behind using the alternative method to calculate the baroclinic component of the meridional wind is addressed at the start of the next section, and the details of the method can be found in the appendix (section A.1).

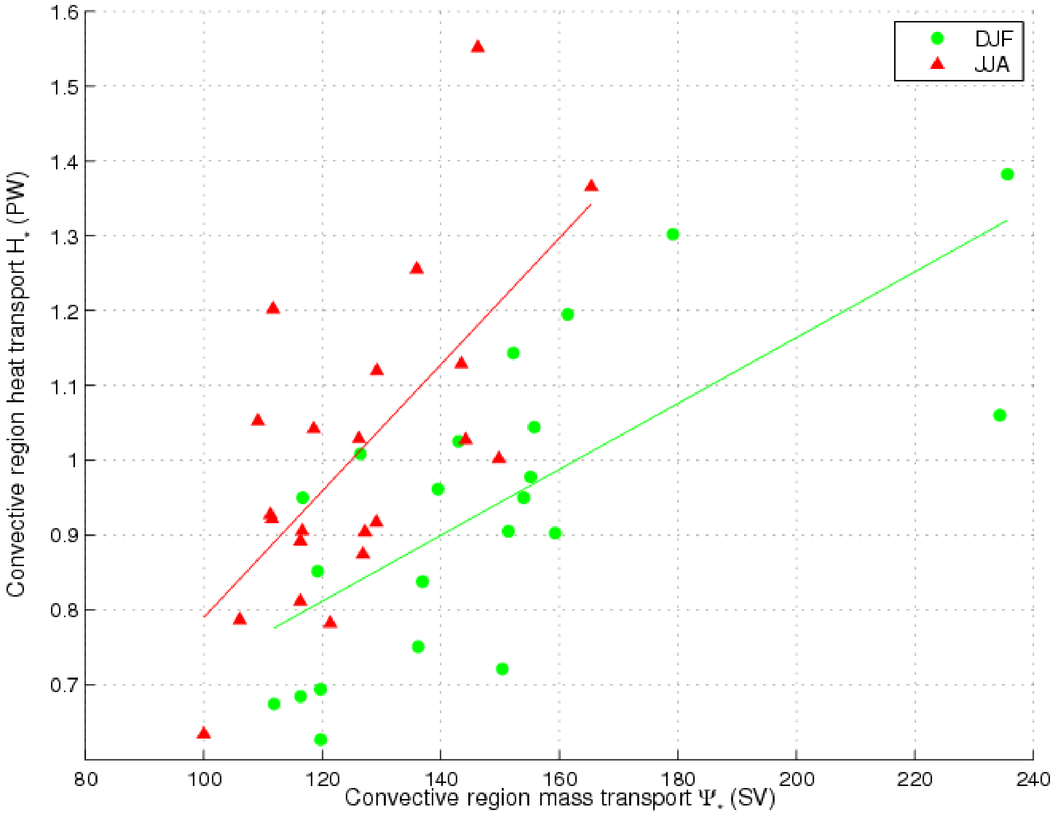

Figure 3.7. Seasonal cross equatorial convective region mass transport ψ_* in Sverdrups (where 1 Sv = 1 × 10^9 kg s^{-1}) and convective region heat transport H_* in PW. Each point represents a year from 1980 to 2001, seasons are: DJF (green circles) and JJA (red triangles).

c) Variability of meridional wind strength and convective region extent

Previously, we calculated the overturning heat transport in the convective regions, H_*, by removing the vertical mean meridional wind from the total wind field (section 3.2). Following this, the results for the rest of section 3.3.2 from now on are based on a different method of calculating the overturning component of the meridional wind. We use a framework to predict the meridional wind based on the convective region temperature profile, rather than the method of removing the vertical mean meridional wind from the total.

The model predicts the shape of the overturning circulation in the convective regions and gives a meridional structure with all mass transport below a fixed zero crossing point at around 500 hPa to have the opposite sign to the mass transport above the crossing point, and integrating to zero over the whole depth. Since the mass transport below a fixed crossing point is constrained to be equal and opposite to that above the point, it is easy to calculate the mass transport by the overturning circulation by integrating between the surface and the mid-point. Since we go on to look into variations in mass transport and gross moist stability, this means that the model lends itself well. For the estimates in the variability in gross moist stability, we use a 2 layer model of the atmosphere, which again fits well with the idea of the fixed crossing point where the meridional wind profile goes to zero.

The method behind the framework is described in the appendix (section A.1) and also a comparison of convective heat transport using each method of calculating meridional wind (section A.2) shows that the results are comparable. For the rest of section 3.3.2, we now use the meridional wind calculated using the framework described in the appendix, and denote it as v_{ovr}, and the corresponding heat and mass transport as H_{ovr} and ψ_{ovr}. Although the method is slightly different, the results are essentially similar (A.2).

We saw in section 3.3.2 that there is a positive relationship between poleward mass transport ψ_* and heat transport H_* in the convective region (Figure 3.7). H_* is largely controlled by ψ_*, whereas variations in Δh_* are smaller and contribute less. We therefore concentrate on ψ_* here and postpone a discussion of the smaller variation of Δh_* until section 3.4.4.

Here we use the baroclinic model described in the appendix, so the convective region mass transport ψ_{ovr} is determined using the overturning wind profile v_{ovr} over the convective region and the horizontal extent of this region L_*:

$$\psi_{ovr} = L_* \int_{P_{mid}}^{P_{sfc}} v_{ovr} \frac{dP}{g} \tag{3.8}$$

By calculating the variation of these two terms (L_* and v_{ovr}), we can determine their relative importance in controlling ψ_{ovr} since, neglecting variations in P_{mid} and P_{sfc} in equation (3.8),

$$\frac{d\psi_{ovr}}{\psi_{ovr}} \approx \frac{dL_*}{L_*} + \frac{dv_{ovr}}{v_{ovr}} \tag{3.9}$$

Both terms on the right hand side of equation (3.9) are shown in Figure 3.8 as a function of $d\psi_{ovr}/\psi_{ovr}$ for each of the solsticial seasons (where values of mass transport are larger than for the equinoctial seasons) for the 22 year period.

For DJF and JJA, 95% of the data lies within ±0.4 of the mean of ψ_{ovr}. There are 2 outlying points for each data set plotted, where the deviations are +0.6 and +0.7 of the mean for ψ_{ovr}. These values represent DJF in 1983 and 1998 respectively, where strong El Niño conditions led to extensive convection and increased convective region heat transport (McPhaden 1999; Trenberth *et al.* 2002). Apart from the two outliers for each set of data, which show large positive deviations from the mean L_*, the data points for both v_{ovr} and L_* all lie within ±0.3 of their respective means.

The extent of the convective region L_* is increased by almost 40% and 60% of the mean during the two El Niño seasons, although the convective region wind profile is only increased by just under 10% and 20% of the mean during the same seasons (El Niño is discussed in more detail in section 3.2.4e). Further analysis indicates that there is little correlation between L_* and v_{ovr}, the correlation coefficient for DJF is 0.3, and for JJA it is -0.2, which means that it is not necessarily the case that larger convective regions give rise to enhanced meridional winds. The similar amplitude in the variability of L_* and v_{ovr} indicates that both terms are important in terms of setting the cross equatorial convective region mass transport.

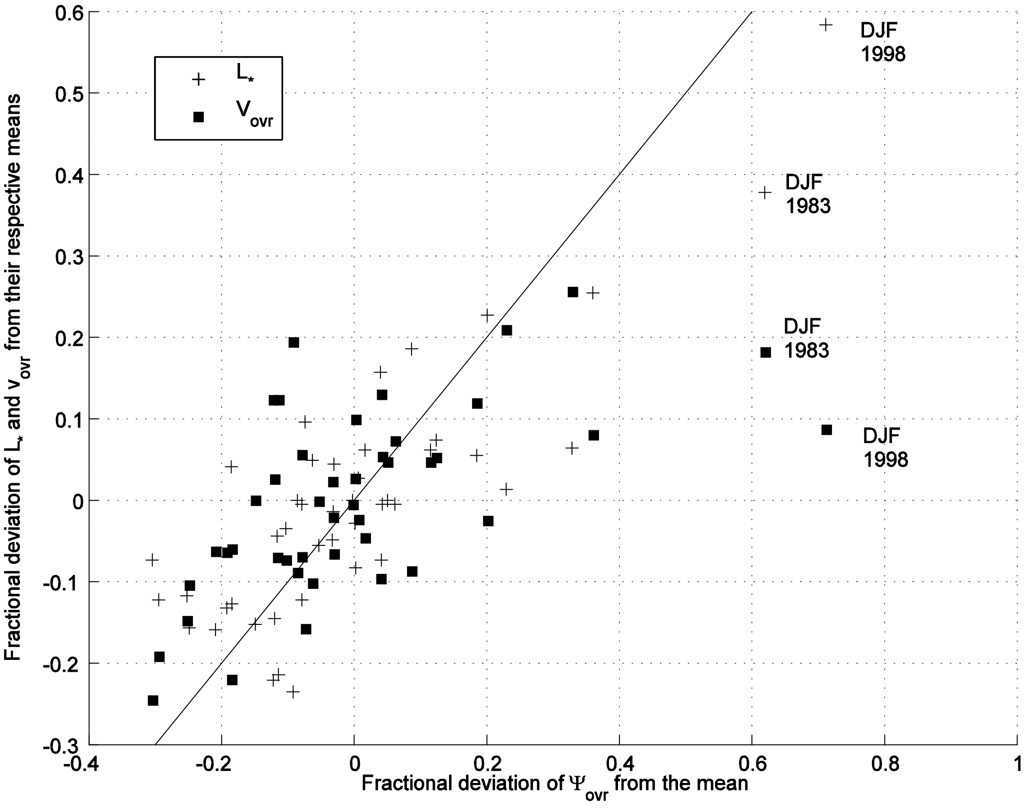

Figure 3.8. Deviation of convective region mass transport from the mean $d\psi_{ovr}/\psi_{ovr}$ against the fractional deviation of convective region extent from the mean dL_*/L_* (crosses) and fractional deviation of mean overturning wind below P_{mid} from the mean dv_{ovr}/v_{ovr} (squares). Each point represents a deviation from the long term mean for either a DJF or JJA in the 22 year period. The line represents a 1:1 ratio between the axes.

In summary, changes in H_{ovr} are primarily driven by changes in the overturning circulation strength, with a lesser role played by gross moist static stability changes (section 3.3.2b). The convective mass transport ψ_{ovr} is itself controlled approximately equally by L_* and the strength of the overturning wind, v_{ovr} (Figure 3.8).

d) Seasonal variability of gross moist static stability

In this section we again use the predicted wind profile, v_{ovr} (see appendix) as a basis for investigating gross moist static stability variations in the convective regions. Gross moist static stability does not vary greatly throughout the convective region and interannual variations are around 5.5% depending on season. However, there is some seasonal variability in Δh_* which we discuss now. Variations in moist static energy are often of interest in studies investigating energy transports in possible future climate scenarios

(Held & Soden 2006; Frierson *et al.* 2007). We can use the overturning wind profile to calculate the gross moist static stability in the convective region Δh_{ovr} as follows:

$$\Delta h_{ovr} = \frac{L_* \int_{P_{100}}^{P_s} v_{ovr} h_* \frac{dP}{g}}{L_* \int_{P_{100}}^{P_s} v_{ovr} \frac{dP}{g}} \tag{3.10}$$

The darkest shaded bar in Figure 3.9 represents the seasonal value of Δh_{ovr} calculated in this way, minus the annual mean. The value of Δh_{ovr} is close to the annual mean of 7.53 K during DJF and SON and the seasonal variation is largest during MAM (-0.74 K from the mean) and JJA (+0.87 K from the mean). Thus, Δh_{ovr} changes by about 10% seasonally. The largest gross moist static stability occurs in JJA due to strong SST gradients in the tropics during this season, and the smallest in MAM where SST gradients are weakest.

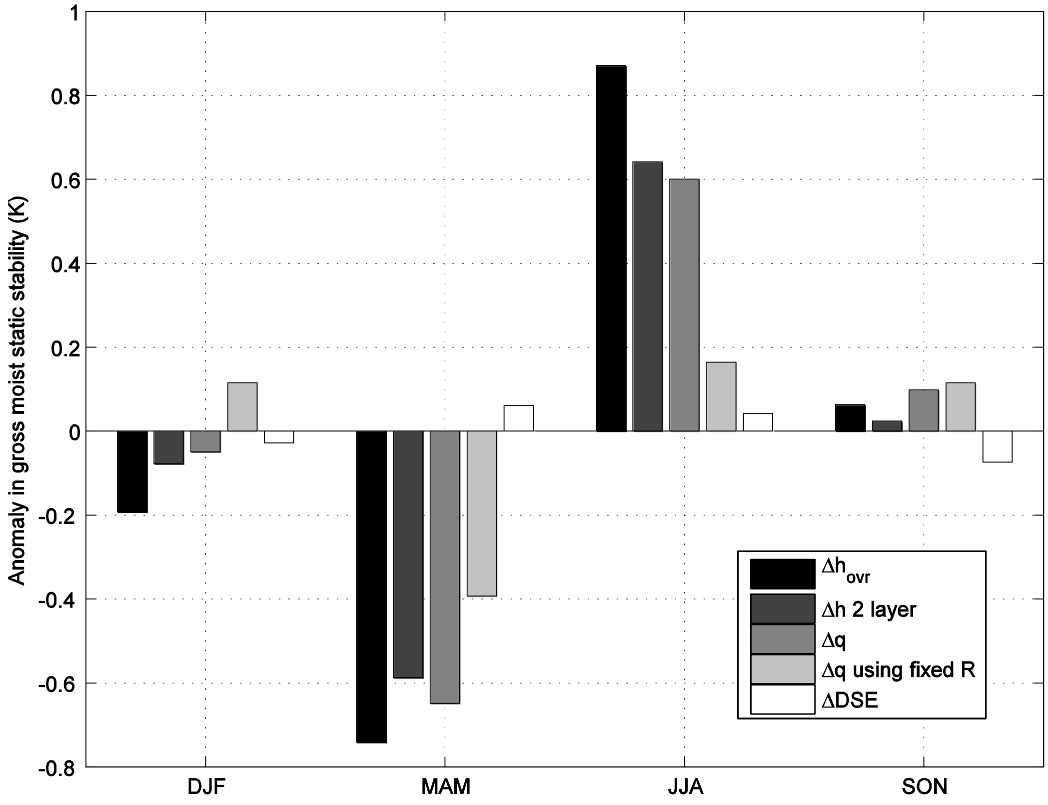

Figure 3.9. Seasonal variation of gross moist static stability *Δh* from annual mean. Δh_{ovr} was calculated using H_{ovr}/M_{ovr}, and *Δh 2 layer* was calculated using the difference between *h* averaged over an upper layer and *h* averaged over a lower layer. *Δq* is the contribution to *Δh* from humidity using the 2 layer model, *Δq using fixed R* used a fixed annual mean value of relative humidity, and *ΔDSE* (dry static energy) is the contribution to the gross moist static stability anomaly from temperature and geopotential terms only. See text for details of calculations.

In order to investigate the seasonal variation in gross moist static stability and how it is controlled, a simplification was made to the calculation of Δh_{ovr} as follows. A 2-layer model was constructed whereby Δh_{ovr} was calculated using the difference between the mean value of the upper and lower layers of the mean moist static energy profile over the convective region ($\bar{h}_{upper}$ and $\bar{h}_{lower}$) and denoted $\Delta h_{2\ layer}$. The interface between upper and lower layers was at P_{mid}. Calculating $\Delta h_{2\ layer}$ in this way gives a reasonable approximation to Δh_{ovr} (Figure 3.9, back versus darkest grey bars) and means we can separate the components of the gross moist static stability into the contribution from the dry static energy and the contribution from moisture (1.16) by using mean profiles of temperature, humidity and geopotential over the convective region.

The contribution to seasonal variations in $\Delta h_{2\ layer}$ from moisture (Δq) in degrees Kelvin is calculated using the same 2 layer model as for $\Delta h_{2\ layer}$, but using the specific humidity profile: $\Delta q = L_v(\bar{q}_{upper} - \bar{q}_{lower})/C_p$ where $\bar{q}_{upper}$ and $\bar{q}_{lower}$ represent the mean values of the upper and lower layers of the mean specific humidity profile in the convective region, and finding the seasonal difference from the annual mean value. The contribution to $\Delta h_{2\ layer}$ from the dry static energy (the geopotential and temperature terms in equation 2) was calculated using $\Delta DSE = \left(C_p\left(\bar{T}_{upper} - \bar{T}_{lower}\right) + (\bar{\Phi}_{upper} - \bar{\Phi}_{lower})\right)/C_p$, and the mean temperature and geopotential profiles over the convective region. The sum of the contributions from ΔDSE and Δq make up the total $\Delta h_{2\ layer}$ calculated using the 2 layer model. Seasonal variations in Δq and ΔDSE are plotted in Figure 3.9, along with $\Delta h_{2\ layer}$ all using the 2 layer model. It is clear that the variation of dry static energy from the annual mean is small in all seasons, whereas there is more variation in specific humidity from the annual mean, especially during MAM and JJA.

Thus there is little seasonal compensation between dry static energy and latent energy, and the main controller of Δh is Δq (Figure 3.9). Since water vapour content falls off rapidly with height, variations in Δq are mainly driven by low level fluctuations. With increased q at low level, Δq (specific humidity at upper level minus that at lower level) is made more negative. This change in Δq decreases the total Δh since the moist static energy is higher at upper levels. During JJA, the conditions on the equator at lower levels are on average colder and drier than during MAM (Figure 3.9), which leads to Δq becoming less negative, and increased Δh. We have investigated what controls the seasonal variations in Δq by keeping the relative humidity constant at the annual mean value and using the seasonal temperature profiles to calculate Δq. This means we can quantify how much of the variation in Δq can be explained by temperature variations, and how much is due to changes in relative humidity between seasons. In this way, *Δq using fixed R* was calculated for each season using the 2 layer model with the seasonal temperature profile, but using the annual mean relative humidity (Figure 3.9). The partitioning of relative humidity and temperature effects on Δq show that in JJA, the relative humidity effects play a greater role than temperature effects in setting the total Δh larger than the annual mean. During MAM, temperature and relative humidity play more of an equal role in setting Δh at a value smaller than the annual mean.

e) El Niño conditions

We saw in section 2.4.3 that El Niño conditions lead to an increase in the extent of the convective region, and as an example, we now look in detail at the convective heat transport in a single season, DJF 1998, using the baroclinic framework described in the appendix.

The winter of 1998 coincided with strong El Niño conditions where high SSTs were extensive in the tropics (McPhaden 1999). The convective region extent L_* in DJF 1998 was larger than any other season during the data period we have used (3 standard deviations larger than the mean for DJF) and 90% of the equatorial data points were classed as convective. We found previously (in section 3.3.2a) that increased L_* generally leads to increased H_* in DJF and in this particular season, H_{ovr} was enhanced, at 1.4 PW, which was an increase of almost 50% on the mean DJF value. It was also true that ψ_{ovr} was enhanced in DJF 1998 by more than 70% of the mean DJF value. Both H_{ovr} and ψ_{ovr} in DJF 1998 were more than 2 standard deviations from the mean values for DJF. In contrast to the significant increases in L_*, H_{ovr} and ψ_{ovr} there was a decrease in Δh_{ovr} in this season, although much smaller, which is consistent with the discussion in section 3.3.2d, where it is noted that variations in gross moist static stability within seasons are small. In DJF 1998, Δh_{ovr} was slightly decreased (just over 5% less than the mean) and was the 6th lowest Δh_{ovr} of the 22 DJFs in the time period used. The lowest DJF Δh_{ovr} of this 22 year period occurred in DJF 1983, which was also an El Niño year, and it was lower than the mean by just over 20%. We would expect reduced gross moist static stability during El Niño conditions, since the increased warm and moist conditions at low levels reduces the vertical Δh_{ovr} (section 2.4.3). We saw in section 3.3.2d that Δq was the main controller of the seasonal variations in Δh_{ovr}. For the particular season of DJF 1998, it is also true that Δq plays the key role, since the increased q at lower levels makes Δq more negative by over 7%, which leads to a decrease in Δh_{ovr}, whilst the ΔDSE (the contribution to Δh_{ovr} from the temperature and geopotential height terms) changes only very slightly, with a 1% increase. Year to year variations in Δh_{ovr} for particular seasons are modest, and the deviation in DJF 1998 from the mean DJF is smaller than variations between seasons.

In summary, the 1998 El Niño showed an increase in H_{ovr} in DJF, primarily as a result of a more extensive convective region. No compensation between latent and dry static energy was found (consistent with section 3.3.2d for the seasonal cycle) and the reduction in gross moist static stability could not significantly offset the increase in heat transport associated with the change in L_*.

3.5. Summary and conclusions

We have presented an investigation into the mechanisms controlling the convective region heat transport H_* and its contribution to the cross-equatorial atmospheric heat transport H_A. We used reanalysis data to define regions of the tropics which were classified as convective, based on a vertical mean relative humidity threshold, and calculated the associated heat transport. Next, we performed a baroclinic decomposition of the meridional wind profile in the convective region to introduce a simple model to investigate the mechanisms controlling the convective region heat transport H_{ovr}. The analysis has highlighted several key points:

- The convective region contributes significantly to the total zonally averaged cross – equatorial heat transport, especially during the solsticial seasons (approximately three quarters and half of the total during DJF and JJA respectively).
- Variations in convective region heat transport H_* are mainly driven by variations in the mass transport ψ_*. Also, the extent of the convective region is positively correlated with the convective region heat transport in the solsticial seasons.
- Gross moist static stability Δh is approximately constant within the convective region, with only small seasonal variations and even smaller inter-annual variations (half the size of seasonal variations). The small fluctuations do not

result from compensation between dry static energy and latent energy; rather they appear to be entirely driven by small changes in Δq.

- The north-south asymmetry which is present in the total cross – equatorial atmospheric heat transport did not feature in the convective region heat transport. This indicates that mechanisms other than the convective region heat transport are responsible for the net southward heat transport in the atmosphere across the equator. Calculations using the reanalysis data (not shown here) indicate that the seasonally reversing monsoon circulation drives the asymmetrical atmospheric heat transport and is especially important during JJA, when the monsoon circulation in the Indian Ocean region is greatly enhanced.

The contribution of the convective region to the total heat transport presented in section 3.3 and concluded here clearly depends on the choice of RH threshold used to define the convective region. A discussion on and justification for the choice of RH threshold was presented in section 3.3.1. Increasing the threshold has the effect of limiting data points in some seasons, and reducing it can mean that part of the monsoon circulation is included in the convective heat transport. The lack of north-south asymmetry in convective region heat transport when using a threshold of 60% is a good indication of its suitability, since the convective heat transport is separated from the asymmetric monsoon component, which tends to occur over slightly reduced SST.

Overall, our results suggest the presence of a ‘true’ overturning cell in the convective region is instrumental in explaining why the Hadley Cell is dominant to H_A. There are still areas with open discussion, relating to the possible compensation mechanisms between ocean and atmosphere heat transport. For example, with increased convective region extent, and associated increase in atmospheric heat transport, does the ocean compensate by advecting more cold water and reducing the convective region extent? Such a coupling scenario can be investigated using ocean-reanalysis data, and also by analysing idealized simulations with coupled ocean atmosphere general circulation models (OAGCM), and in the next chapter we use an OAGCM to look at the coupling of ocean and atmosphere heat transport.

Chapter 4 The coupling of ocean and atmosphere heat transport in the FORTE aquaplanet coupled model

This chapter presents an analysis of output from a version of the FORTE (Fast Ocean, Rapid Troposphere Experiment) model developed at Southampton Oceanography Centre (Sinha & Smith 2002). The model is a fully coupled ocean-atmosphere GCM but run in an idealized geometry.

The analysis presented here focuses on the interaction between ocean and atmosphere heat transport in the tropics. We test the theory that annual variations in the ocean and atmosphere heat transport are positively correlated in the tropics and that it is difficult to change the ratio of the poleward energy transport between atmosphere and ocean in the tropics (Held 2001), (see section 1.4).

We find there is a strong relationship between variations in the heat budget of the tropical ocean and the Ekman component of the ocean heat transport, indicating a strong relationship between the trade winds and ocean heat transport out of the tropics. There is a similar relationship in the atmosphere, although with a smaller correlation, highlighting the important role of atmosphere eddies in the aquaplanet model in the tropics.

4.1 Using an aquaplanet coupled model to study heat transport

The analysis presented in this chapter combines the use of a highly idealized model setup – using a planet without land and with an ocean with constant fixed depth – with a fully coupled ocean and atmosphere Global Circulation Model (OAGCM). The atmosphere part is an Intermediate Complexity GCM (ICGCM), IGCM3 (Forster *et al.* 2000), and the ocean model is called the Modular Ocean Model Array (MOMA) (Webb 1996). More details on the model are outlined in section 4.2.

The idea behind the aquaplanet model is not to simulate a realistic climate but to investigate fundamental processes in a world without some of the complications introduced by the presence of land. The aquaplanet is ideal for testing the ideas of Held (2001) since the absence of land means the wind stress on the ocean surface occurs all around the planet and all the heat transport is Ekman or diffusive since the lack of latitudinal barriers means there is no meridional geostrophic ocean heat transport. We use the waterworld geometry, although this is often used as a control run for other coupled simulations such as ridges and channels, for example, Smith *et al*. (2006), (Figure 4.1).

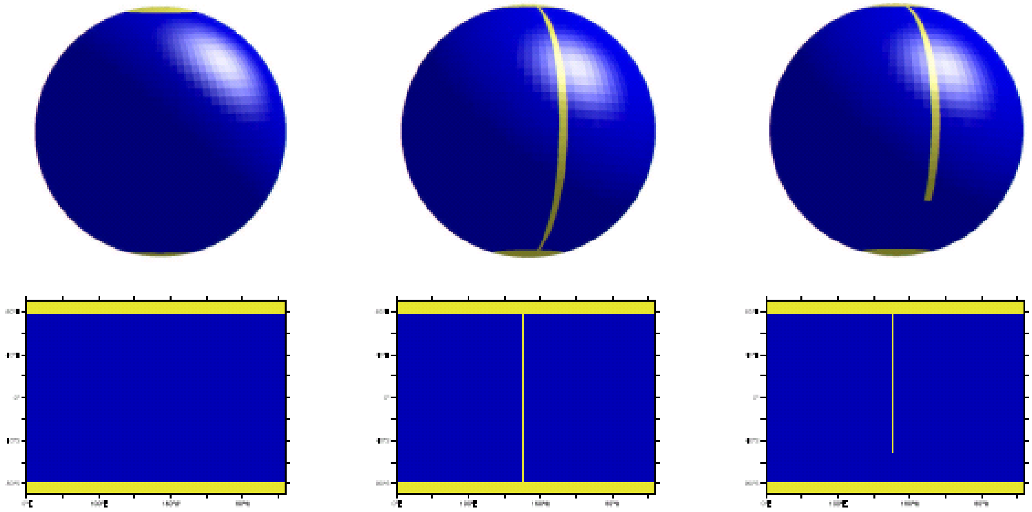

Figure 4.1. The aquaplanet geographies used by Smith *et al.* (2006): left: WaterWorld, middle: RidgeWorld, and right: DrakeWorld. From Smith (2004).

As computing power becomes more readily available, climate modellers are able to model the complex nature of the earth's system with increasing accuracy, for example, the high resolution Earth Simulator (Sumi *et al.* 2004). The wide range of spatial and temporal scales of processes and feedbacks on our planet means that the complex GCMs become very expensive to run in terms of computer time, and often the model runs are limited to investigate limited climate configurations. Simpler, more idealized investigations are also carried out using less complex models, such as Intermediate Complexity GCMs, which have simpler radiative and convection schemes. The reduced complexity of FORTE means that integrations can be run more rapidly, or with less computing power than is required for more realistic models (Sinha & Smith 2002).

In a complex system, such as that of the ocean and atmosphere, the simplicity of the aquaplanet setup can be an advantage. By excluding some processes it may become easier to understand the factors under investigation without having to account for unwanted interactions elsewhere. For example, there is no thermohaline circulation in waterworld and buoyancy forced ocean circulation is weak. The aquaplanet scenario has been used in previous atmospheric studies, but not often with a fully coupled dynamical ocean. For example Hess *et al.* (1993) prescribed the SSTs in the slab ocean of their aquaplanet model in order to investigate factors affecting the location and dynamics of the ITCZ. Another example is an aquaplanet with a dynamical ocean and a 1D energy balance type atmosphere such as the UVic Earth System Climate Model (Weaver *et al.* 2001). Sometimes a slab ocean or 1D atmosphere in an aquaplanet is appropriate, for example, to study the changes in atmospheric energy transport based on variations in moisture which might be expected in a global warming scenario, a fixed ocean suffices (Frierson *et al.* 2007). The Aqua-Planet Experiment (APE) was an experiment which was developed to provide a benchmark of current model behaviour and test various AGCMs using prescribed SSTs as a basis (Neale & Hoskins 2000).

Recently, oceanographers have started adding a full dynamical ocean to the aquaplanet models. In 1995, an investigation into equilibria in the ocean-atmosphere system based on the state of the thermohaline circulation, was carried out using a coupled model with a 2 layer atmosphere and simplified geometry (Saravanan & McWilliams 1995). The coupled model was used to investigate meridional heat transport for different equilibrium solutions (Figure 4.2). This work highlighted that the atmosphere compensates well for the changes in ocean heat transport in the coupled model. It is particularly noticeable in the total heat transport (right panel), where the atmosphere compensates almost completely for the variations in ocean heat transport between the solutions. This is consistent with the result from Stone (1978) where the distribution of the total heat transport does not depend on ocean-atmosphere dynamics.

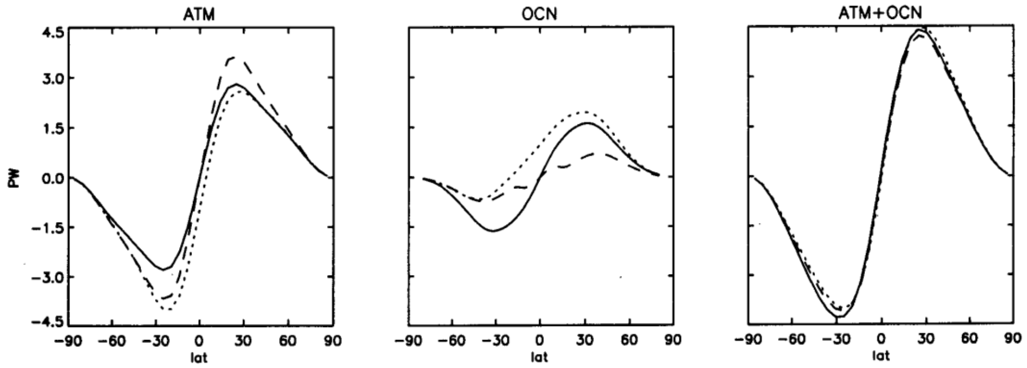

Figure 4.2. Annual mean zonally averaged meridional heat transport in PW for 3 coupled equilibria. Hemispherically symmetric solution based on thermal buoyancy (solid), asymmetric pole to pole forcing (dotted) and symmetric solution based on freshwater forcing (dashed). Panels represent atmosphere component, ocean component and total atmosphere plus ocean component. From Saravanan & McWilliams (1995).

An example of one of the first studies to use a coupled aquaplanet with a dynamic ocean and intermediately complex atmosphere is that of Smith *et al.* (2006). This work used different simple land configurations, such as narrow meridional ridges, to investigate the associated changes in ocean circulation, as well as the waterworld setup as used in this chapter (Figure 4.1). The model had 15 ocean layers and 22 atmospheric layers. The model used by Smith *et al.* (2006) was also a version of FORTE, although at a reduced horizontal resolution to that used here. The reduced resolution of this early version of FORTE led to significant differences between the representation of heat transports in the real world and the FORTE world (Smith 2004).

Czaja & Marshall (2006) used an aquaplanet with a five layer simplified atmosphere (Molteni 2003) coupled to the MIT ocean model (Marshall *et al.* 2004) to study the robustness of the partitioning of heat transport with a change in continents. They found a large similarity in the relative contributions of ocean and atmosphere heat transport between the aquaplanet and reanalysis data, which reinforces the applicability of the use of an aquaplanet when investigating poleward heat transport (Figure 4.3).

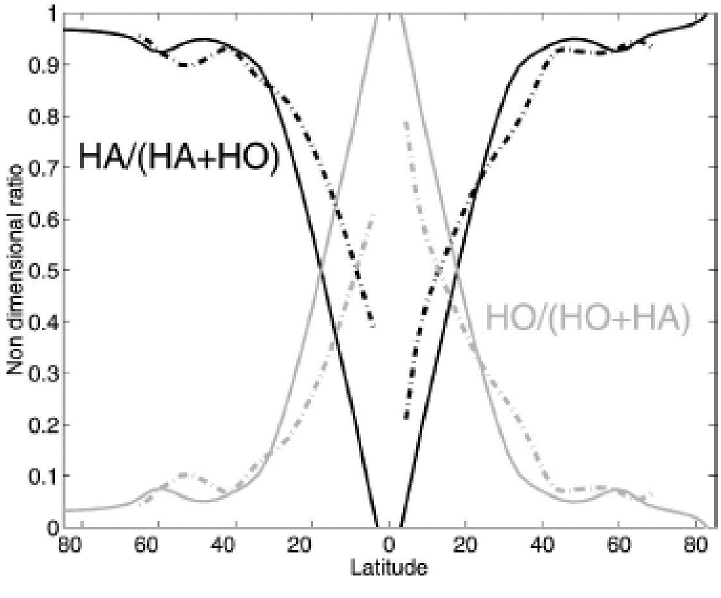

Figure 4.3. Relative contribution of ocean (grey) and atmosphere (black) to the total energy transport for an aquaplanet (continuous curves), and observed ratios using NCEP and ECMWF heat transports (broken curves). From Czaja & Marshall (2006).

More recently, the same MIT aquaplanet was used to study mean climate variability (Marshall *et al.* 2007). It was found that the atmospheric climate was similar to our own present climate, and again, the partitioning of heat transport between ocean and atmosphere was similar to that found in Czaja & Marshall (2006), but the ocean circulation in a world without meridional barriers was quite different. Marshall *et al.* (2007) found that weak stratification in the mid to high latitudes led to inefficient poleward heat transport and substantial polar ice caps. In the tropics, mixing of strongly stratified water produced more efficient heat transport, in an analogy of the heat transported by the subtropical gyres in the real planet (Marshall *et al.* 2007). Differences in the ocean circulation between the studies of Smith *et al.* (2006) and Marshall *et al.* (2007) could be due to differences in the ocean model formulation, which highlights the importance of the development of the ocean part of the model and sets the requirement for further studies using fully coupled aquaplanets. In fact the work contained in this chapter presents results which differ from those of Smith *et al.* (2006) when using the same model, just with increased resolution.

4.1.1 Testing theories of ocean-atmosphere interaction using FORTE

The idea behind the analysis in this chapter is to test the theory of compensation between the tropical ocean and atmosphere in an idealized, coupled climate model. Historically, studies have been carried out to investigate the partitioning between ocean and atmosphere heat transport (section 1.2), and with increased observational coverage, estimates are beginning to diverge on the relative contributions of ocean and atmosphere (Trenberth & Caron 2001). The idea of compensation between the heat transport in ocean and atmosphere is a further subject for investigation, since changes in heat transport in one medium affect the other.

Bjerknes Compensation is the term commonly used to describe the theory that if the top of atmosphere radiative fluxes and heat storage do not vary greatly, then the total energy transport would not vary greatly either, over long time periods (Bjerknes 1964), and this was detailed in section 1.2.3. In 2001, Held concentrated on the tropics and suggested that here, the ocean and atmosphere are strongly coupled and mass transport in both is a result of by the surface wind, and this is detailed in section 1.4. Held argued that it is difficult to change the partitioning of poleward heat transport between atmosphere and ocean as the partitioning depends only on physical constants of the system, and weakly on surface temperatures. This theory rules out the idea of compensation in the tropics, and suggested heat transport in the ocean and atmosphere varies together here. Hazeleger *et al*. (2004) highlighted the fact that there is compensation between the poleward heat transport and equatorward heat transport in the wind driven ocean circulation and suggest the partitioning of ocean and atmosphere heat transport is not as strongly fixed as Held suggested.

Shaffrey and Sutton (2006) used a coupled model to test Bjerknes Compensation theory over decadal timescales (Figure 4.4). They found that the compensation between ocean and atmosphere heat transport applied in the mid latitudes, consistent with Bjerknes (1964). They did not find compensation in the tropics, which is consistent with Held (2001). In this chapter, we concentrate on the tropics and investigate the relationship between ocean and atmosphere heat transport out of the tropical band between 20°N and 20°S in order to see if Held's theory can be realized in an aquaplanet model. We use the FORTE aquaplanet as a tool to test the ocean and atmosphere interaction, since the model is fully coupled and simplified, with wind stress acting all over the whole surface and no continents, which is similar to the idealized set up put forward by Held (2001).

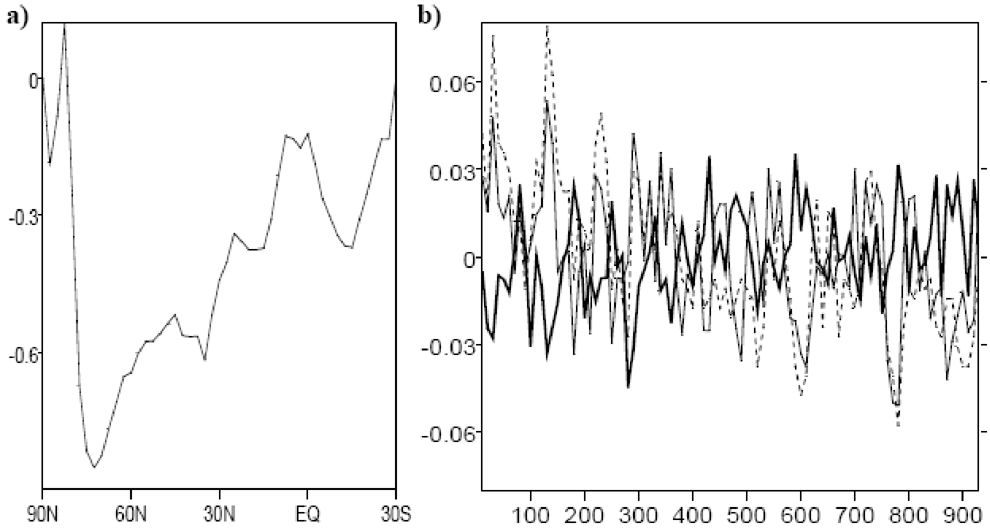

Figure 4.4. a) Correlation of decadal atmospheric and Atlantic Ocean energy transports and b) Time series of decadal anomalies in extratropical atmospheric energy transport (bold), Atlantic energy transport (solid) and Atlantic Meridional Overturning Index (dashed). Units in b) are PW (left) and Sverdrups (right) and time in years (x axis). From Shaffrey & Sutton (2006).

4.2 Components and details of the FORTE model

The FORTE model is a fully coupled, ocean-atmosphere model. It consists of an ocean part named MOMA, the Modular Ocean Model Array (Webb 1996) which is based on code developed at the Geophysical Fluid Dynamics Laboratory (GFDL) at Princeton University (Pacanowski *et al.* 1991) and is a fully dynamic ocean. The mixing in the ocean is based on an isopycnic scheme (Gent & McWilliams 1990; Gent *et al.* 1995), and a sea ice scheme ensures the poles are not at sub-zero temperatures.

The atmospheric part of the model comes from Reading University and is the Intermediate General Circulation Model (IGCM3) (Forster *et al.* 2000) which is based on earlier model dynamics (Hoskins & Simmons 1975). A multiband radiation scheme includes the effects of water (interactive), and carbon dioxide and ozone (prescribed), and the convective adjustment scheme is that of Betts (1986). The clouds are based on a simplified version of that described in Slingo (1987).

The ocean and atmosphere components are coupled using the Ocean Atmosphere Sea Ice Soil (OASIS) coupler (Terray *et al.* 1999) developed in the Centre Europeen et de Formation Avancée en Calcul Scientifique (CERFACS) in Toulouse, France. The coupler performs calculations to interpolate spatially between the different grids used in the ocean and atmosphere parts of the model, and exchanges information between the ocean and atmosphere (Sinha & Smith 2002). The ocean model has 15 vertical levels with increasing thickness with increased ocean depth, and a 2^{o} resolution in the horizontal. The atmosphere has 15 sigma levels in the vertical and a spectral T42 resolution in the horizontal. The integration was run over approximately 1000 years which is consistent with periods used in previous aquaplanet studies (Smith *et al.* 2006) and (Marshall *et al.* 2007).

The data used in this analysis is taken from the monthly mean model output from the later years in the model run. The monthly mean values for each year were averaged to give annual means. Due to slow diffusion processes in the ocean part, the output from the simulation included here has not reached a true equilibrium, although conditions are asymptotically adjusting and close to a steady state during this time period (Smith *et al.* 2006). The global ocean temperature trend is on the order of 0.01 K per decade during the final 40 years of the output, 980-1020, and the TOA global imbalance is 0.08 W m^{-2}.

4.3 Climate of the FORTE aquaplanet

The waterworld geometry used here is the simplest FORTE configuration and means that the only continents on the planet are small polar islands which reach to 80 degrees and the ocean bed is at flat and at a depth of 5.3 km. The polar islands are included to minimize computational complexity at the poles where meridian lines converge. The absence of barriers to zonal flow means that meridional geostrophic flow does not occur in the ocean. This means that the methods of ocean heat transport are limited to diffusive transport or wind-driven Ekman transport and there are no ocean gyres. Zonal winds and ocean currents are shown in Figure 4.5 along with potential temperature. In the atmosphere, westerly winds occur at around 40° and easterlies occur in the tropics, as in the real world. Ocean currents are largely zonal in waterworld, and reflect the position of the overlying surface winds.

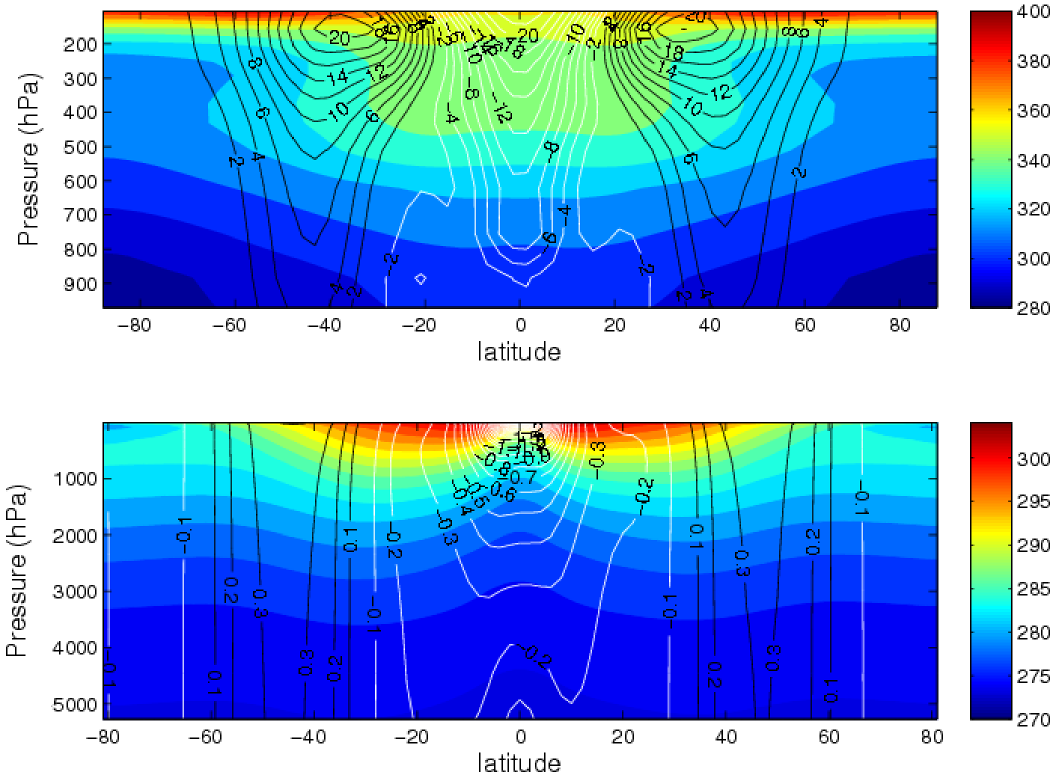

Figure 4.5. Potential temperature (colours) and zonal wind (contours) for atmosphere (upper) and theta (colours) and zonal current (contours) for ocean (lower). Black contours show eastward flow and white contours show westward flow. Units are K for potential temperature and meridional velocity contour interval is 2 m s^{-1} (upper) and 0.1 m s^{-1} (lower) for zonal flow.

At the equator of waterworld, there is a cold tongue, which is reflected in the atmospheric surface temperature (Figure 4.6). This is due to the upwelling of cold water to replace the warm surface water as it gets advected poleward by the effect of Ekman transport driven by the trade winds, known as Ekman suction (section 1.3), (Gill 1982). This is an example of the effect of using a dynamical ocean in the aquaplanet model, and would not occur if the ocean had prescribed SSTs. The ocean section of potential temperature (Figure 4.5) shows the cold tongue at the surface along the equator, where temperatures are around 4° Celsius lower at 0° than at 10° of latitude, and the upwelling of colder, deep water can be seen near the equator.

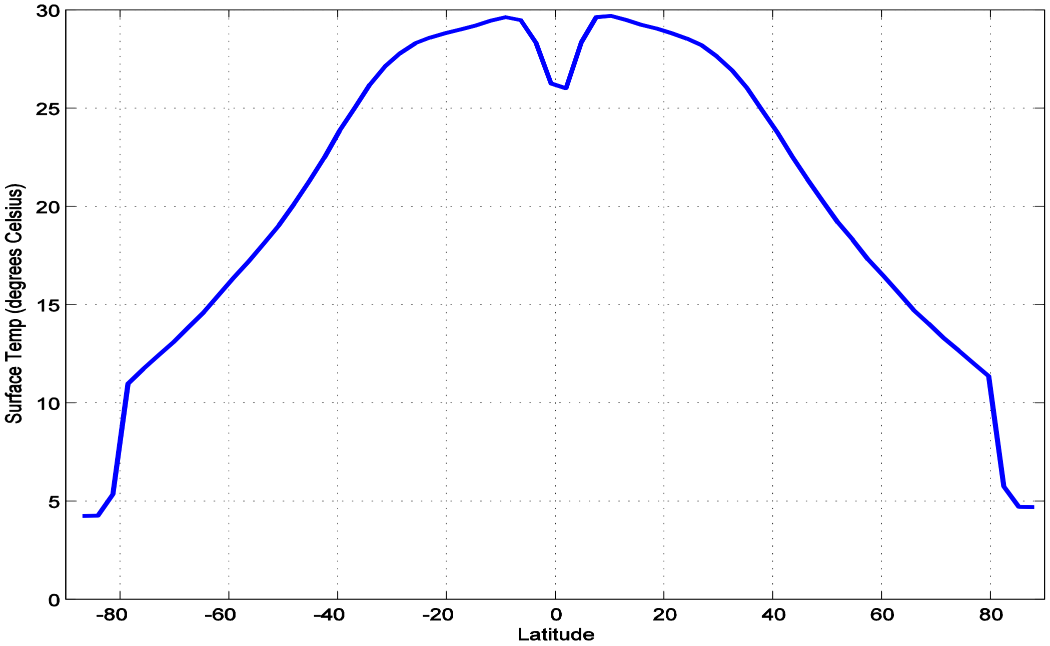

Figure 4.6. Atmospheric surface temperature in °C, against latitude, mean for years 980-1020.

On annual mean timescales, there are ITCZs at around 10° north and south. These are reflected in the distribution of precipitation (Figure 4.7). The precipitation plot also shows the position of the storm tracks in mid latitudes, and a minimum at the equator, coinciding with subsiding air.

Since there are two regions of high relative humidity and convection, one each side of the equatorial cold tongue, the circulation in the atmosphere acts to transport heat from the ITCZs towards the colder equator. This results in a pair of deep Hadley cells acting in the reverse direction to normal in the deep tropics, as well as the expected Hadley cell circulation just poleward of these cells, described in section 1.3.1, (Held & Hou 1980). The meridional atmospheric circulation is illustrated in Figure 4.8. The deep overturning cell is visible (colours) with equatorward transport at around 200 hPa and poleward transport at the surface and at 750 hPa between the equator and 10°N and 10°S (Figure 4.8).

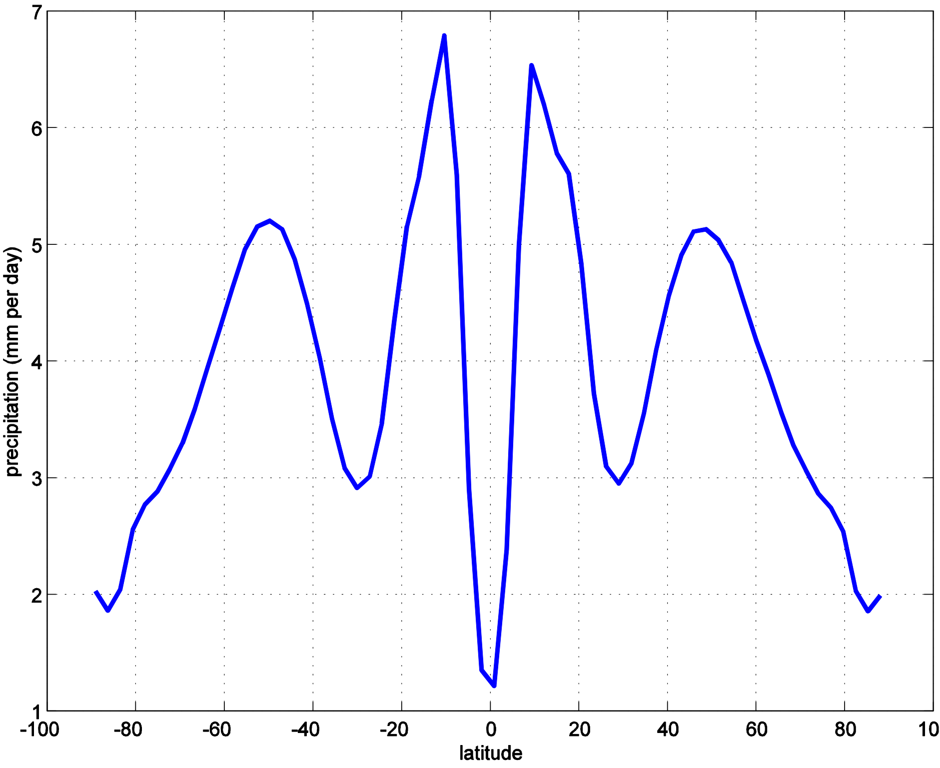

Figure 4.7. Zonal mean precipitation in mm day^{-1} for waterworld. Mean for years 980 - 1020.

The direction of this overturning cell means that heat is transported equatorward at this point, since the upper branch has more energy than the poleward flowing surface branch. The more realistic Hadley Cell is visible at around 20° with low level equatorward flow, and upper troposphere (150 hPa) flow poleward, which acts to transport heat out of the tropics, to the extratropics. Arrows show the direction of the circulation.

The mean atmospheric surface temperature for waterworld is around 24°C. This is warm compared to the real world, and reflects the radiative effects of increased moisture in the atmosphere, the lowered albedo of water compared to most land types and the absence of land surface, reducing high altitude cold air (Smith 2004).

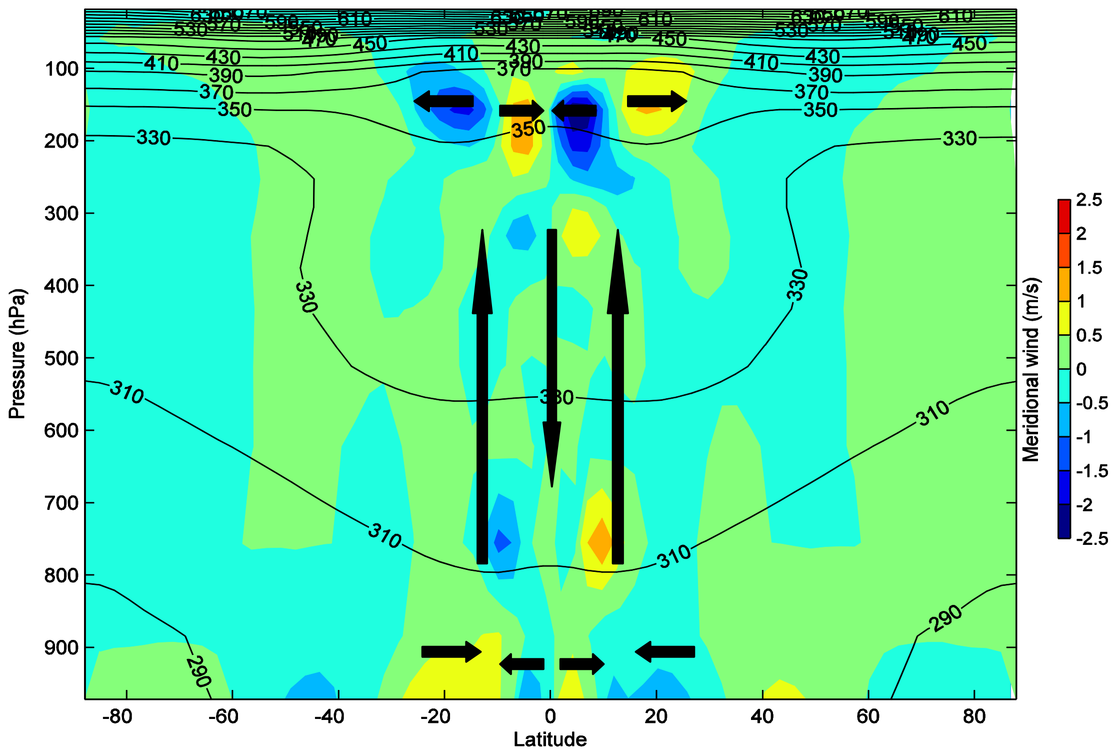

Figure 4.8. Zonal mean meridional wind in ms^{-1} (colours) and potential temperature in Kelvin (contours) versus latitude, annual mean for years 980-1020. Arrows show direction of circulation.

4.4 Heat transport calculations

4.4.1 Heat transport calculated from radiative fluxes

The latitudinal distribution of the top of atmosphere (TOA) radiative flux, F_t and the flux into the surface of the ocean, F_s are plotted in Figure 4.9. F_t is calculated using

$$F_t = SW_{\downarrow}^{TOA} - SW_{\uparrow}^{TOA} - LW_{\uparrow}^{TOA} \tag{4.1}$$

where *SW* and *LW* represent longwave and shortwave fluxes at the TOA and the arrow is the direction of radiation, down represents towards the earth and up is away from the earth. F_s is calculated as follows:

$$F_s = SW_{net}^{sfc} + LW_{net}^{sfc} - LH - SH \tag{4.2}$$

where the *SW* and *LW* fluxes are taken at the surface and represent the net radiative fluxes. *LH* and *SH* are the latent heat and sensible heat terms. There is net positive incoming heat flux from the top of atmosphere in the tropics equatorward of about 40°

of latitude and negative heat flux poleward of that. Heating of the ocean is confined to the deep tropics and extends to about 10° north and south (Figure 4.9). Discontinuities at 80° are due to the presence of land from here to the poles.

From F_t and F_s , we have calculated the total northward heat transport in the ocean and atmosphere from years 980 to 1020 of the model output (Figure 4.10). The total heat transport (ocean plus atmosphere) was calculated by integrating the net radiation at the top of the atmosphere, F_t, over latitude and removing the global imbalance (amounting to 0.08 W m^{-2}), and to calculate the ocean component of the heat transport, we integrated the flux into the ocean surface, F_s (see section 1.2.1). The atmospheric heat transport component was calculated as the residual of the total heat transport and the ocean component. The FORTE northward heat transport estimations can be compared to estimates using data presented by Trenberth & Caron (2001), Figure 1.16, Chapter 1.

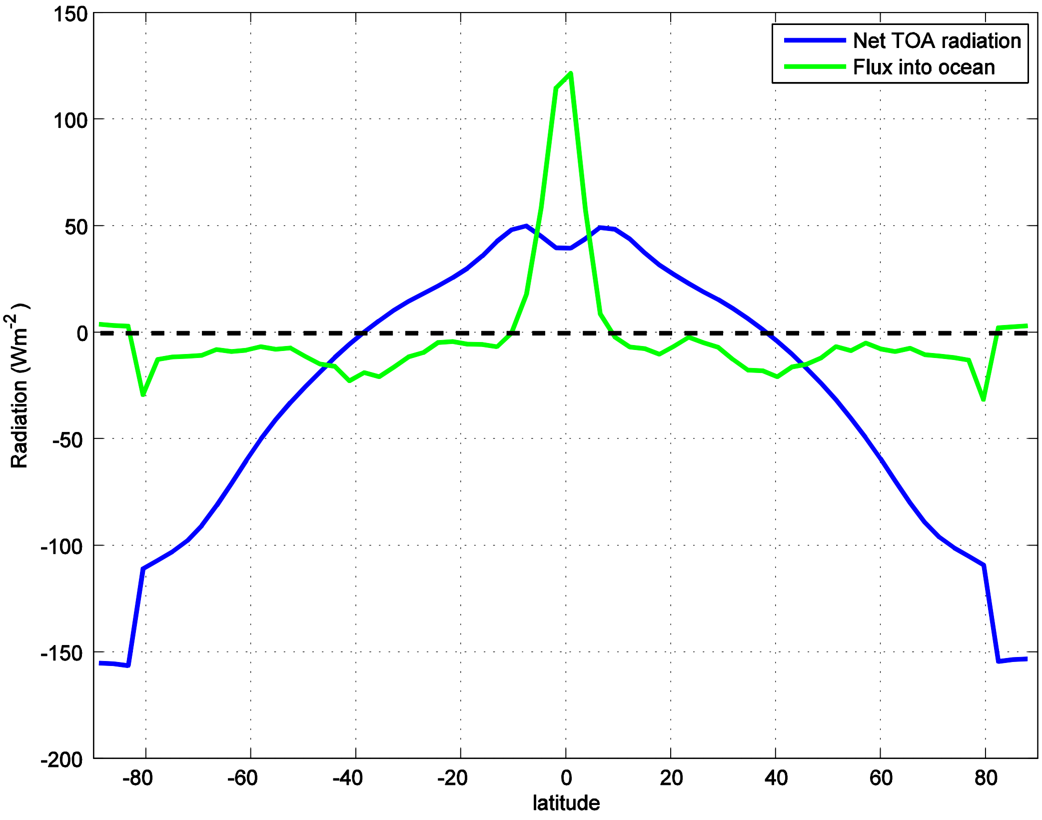

Figure 4.9. Zonal mean net TOA radiation (blue) and surface heat flux into the ocean (green) in Wm^{-2} versus latitude, mean for years 980-1020 of the FORTE model waterworld run.

The implied total heat transport in the FORTE aquaplanet model (Figure 4.10) peaks at a similar value to that calculated using the data from Trenberth & Caron (2001) Figure

1.16; around 5.5 PW for Trenberth and Caron, and around 4.8 PW for the FORTE world. There is some equatorward heat transport in the atmosphere in the deep tropics in FORTE, consistent with the deep reverse Hadley Cells (Figure 4.8) and the poleward ocean heat transport in the deep tropics is greater than the total heat transport in order to compensate for this equatorward atmospheric transport. The latitude where ocean and atmosphere heat transport are similar in size is at 20° in the northern hemisphere and 25° in the southern hemisphere (Figure 4.10). At these latitudes, the surface wind stress is also at a maximum in the tropics so it is conceivable that the heat transport associated with surface wind stress is significant around 20° north and south. In the next section we focus on the heat transport associated in both the ocean and atmosphere at these latitudes.

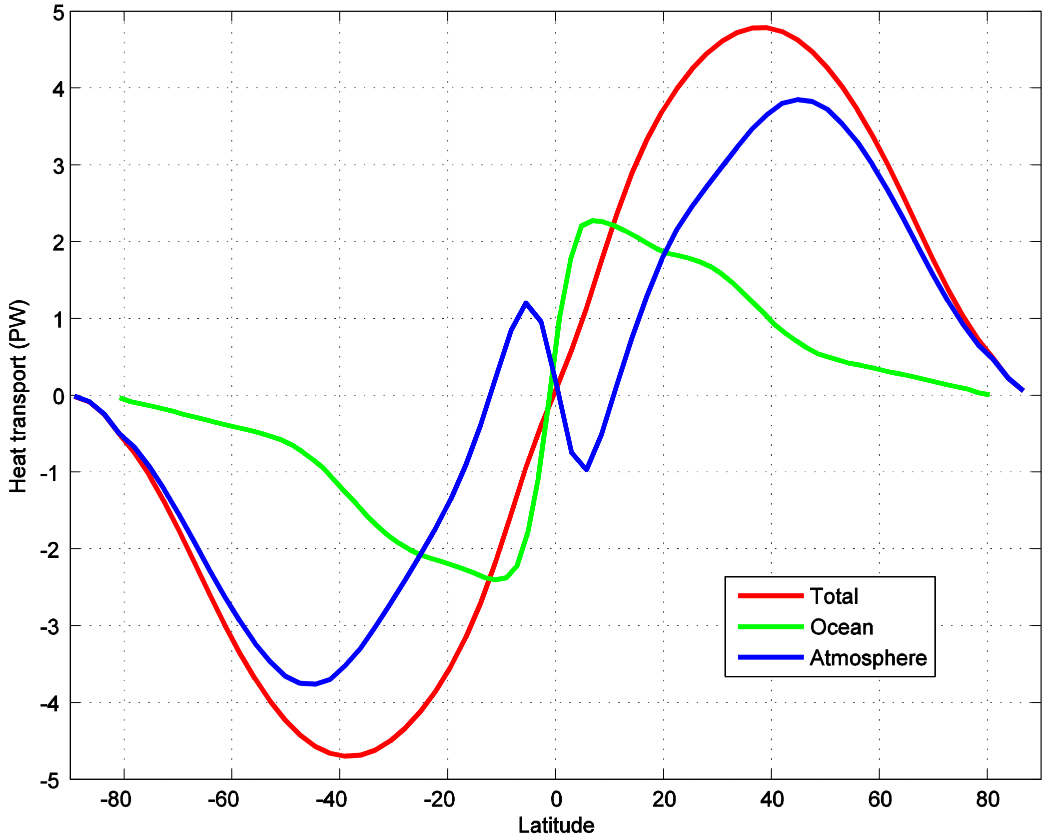

Figure 4.10. Total northward heat transport (red), ocean heat transport (green) and atmospheric heat transport (blue), in petawatts, mean for years 980-1020.

4.4.2 Heat transport out of the tropics

At around 20° north and south, the values of ocean and atmosphere heat transport are approximately equal in FORTE (Figure 4.10). In the real world, ocean and atmosphere heat transport are also approximately equal at 20°N (Figure 1.16). Since we are looking at the coupling of heat transport, it makes sense to concentrate on a region where ocean and atmosphere heat transport are roughly comparable. This regions also coincides with the maximum mass flux of the Hadley Cell for FORTE (Figure 4.8). Similarly in Held (2001), the emphasis is the deep tropics, where the Hadley Cell has the maximum mass flux (Figure 1.6). We calculated the energy budget within a band of latitude stretching from 20° north and south in the ocean and atmosphere by using estimates of energy fluxes and ocean heat storage.

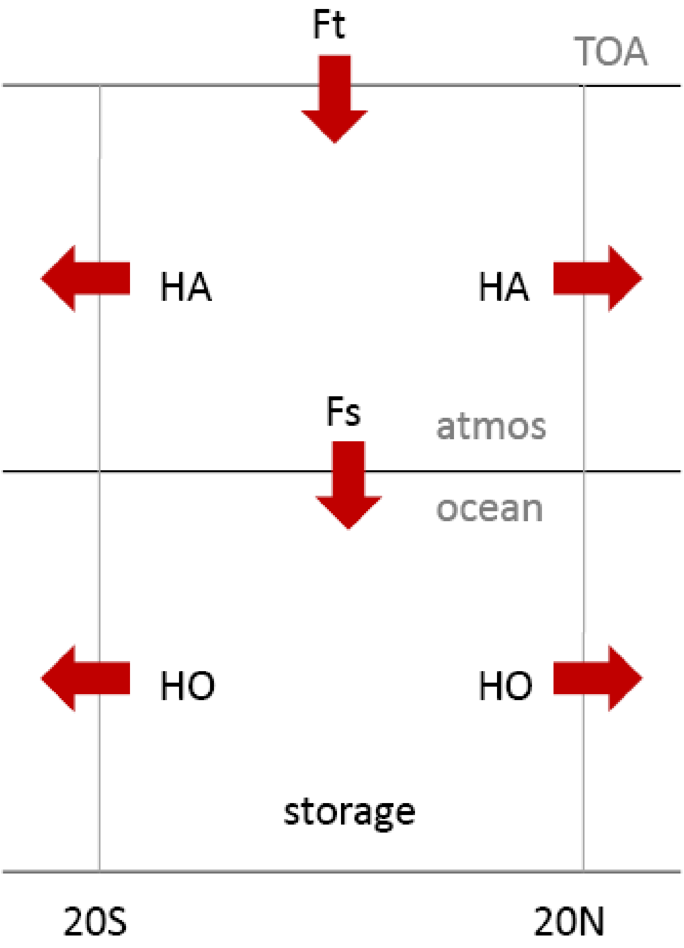

Figure 4.11. Schematic showing direction of energy fluxes in the ocean and atmosphere in a 20° latitude band. Vertical red arrows represent heat fluxes from the TOA and flux between atmosphere and ocean, and horizontal arrows show heat transport out of the latitude band by the ocean and atmosphere. There is storage of heat in the ocean, but this is assumed to be negligible in the atmosphere.

In order to investigate the coupling of ocean and atmosphere heat transport in the tropics, we focus on the latitude band from 20°N to 20°S throughout this chapter and calculate the amount of poleward energy transport in both the ocean and atmosphere out of this band to represent poleward heat transport in the tropics. All heat transport calculations refer to the amount of heat transported out of this latitude band, both in the ocean and atmosphere.

Figure 4.11 is a schematic of the fluxes of energy in the ocean-atmosphere system. The upper box represents the atmosphere between 20°N and 20°S, and the lower box represents the ocean in the same region. The upper line represents the top of atmosphere, the middle line is the interface between ocean and atmosphere and the lowest line is the ocean bed. The red arrows represent fluxes of energy. F_t is the TOA flux, calculated from equation (4.1), and applied to the region bounded by 20°N and 20°S. In order to calculate the ocean heat transport out of the latitude band 20° south to 20° north, we use

$$HO = F_s - storage \tag{4.3}$$

where F_s is the total heat flux into the ocean surface between 20° north and south, calculated from equation (4.2). The ocean heat storage term, *storage*, is calculated using

$$storage = \frac{\partial}{\partial t}\left[\iiint \rho_o C_p \theta \; dxdydz\right] \tag{4.4}$$

Where ρ_o is the density of seawater (taken as a constant 1025 kgm^{-3}), C_p is the specific heat capacity of the ocean (3850 $\text{J kg}^{-1}\,\text{K}^{-1}$) and θ is the potential temperature of the ocean. To estimate the annual heat storage, we used the change in θ from January to December from the monthly mean output integrated over the 20 degree latitude band and the depth of the ocean.

The atmospheric heat transport out of the 20° tropical band is simply

$$HA = F_t - F_s \tag{4.5}$$

where F_t and F_s are summed over the 20° band, and we assume that atmospheric heat storage is negligible.

Figure 4.12 shows a scatterplot of atmospheric heat transport, *HA*, versus oceanic heat transport, *HO*, out of the 20° band. One of the first things to notice is that the range of

HO is much larger than *HA*, (3 PW versus 0.5 PW), although the mean values of *HA* and *HO* are similar at 3.4 PW and 3.5 PW, respectively. This is due to very small variations in F_t and F_s with time, whereas the large fluctuations in ocean heat storage contribute to the larger variations in *HO*. There is no significant correlation between *HA* and *HO* out of the 20^{o} degree band, which suggests Held's idea of the coupling of ocean and atmosphere heat transport does not hold in the tropics of the aquaplanet FORTE model at this particular latitude.

The relative magnitudes and variations of the major heat transport components are highlighted in a timeseries (Figure 4.13). The large variability of *HO* and *storage* compared to the other terms is particularly clear. The relatively large variations in *HO* compared with *HA* are due to the variability in ocean heat storage, and the range of *storage* and *HO* is very similar. *HO* is anticorrelated with ocean heat storage, so the ocean warms when the ocean heat transport out of the tropical band is reduced, and when *HO* increases, heat is removed from the tropical band, the tropical ocean is cooled and heat storage reduced (Figure 4.14). This is consistent with previous results which found that fluctuations in ocean heat transport were balanced by changes in ocean heat content on annual timescales (Shaffrey & Sutton 2006).

We have seen that there is no correlation between *HA* and *HO* out of the 20 degree band (Figure 4.12). There also does not seem to be compensation occurring between *HA* and *HO* in the tropics. Although the mean values are similar, the variability of *HO* is much larger than that of *HA*. The Held model we are testing assumed the mass transport in the ocean and atmosphere was equal and opposite in the tropics and a result of the trade winds, so next we look specifically at wind driven heat transport in the ocean and atmosphere and the relationship between these.

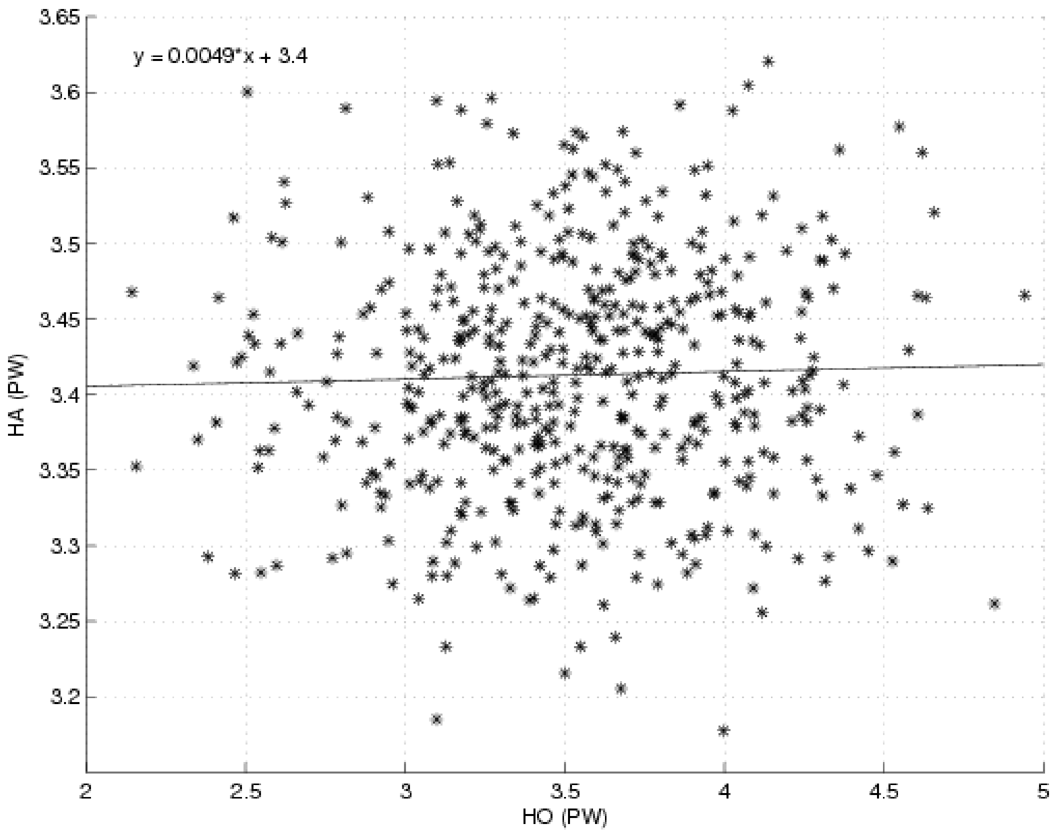

Figure 4.12. Ocean heat transport (*HO*) and atmospheric heat transport (*HA*) out of 20° band in PW, for years 500-1020, calculated from TOA and surface fluxes and ocean heat storage.

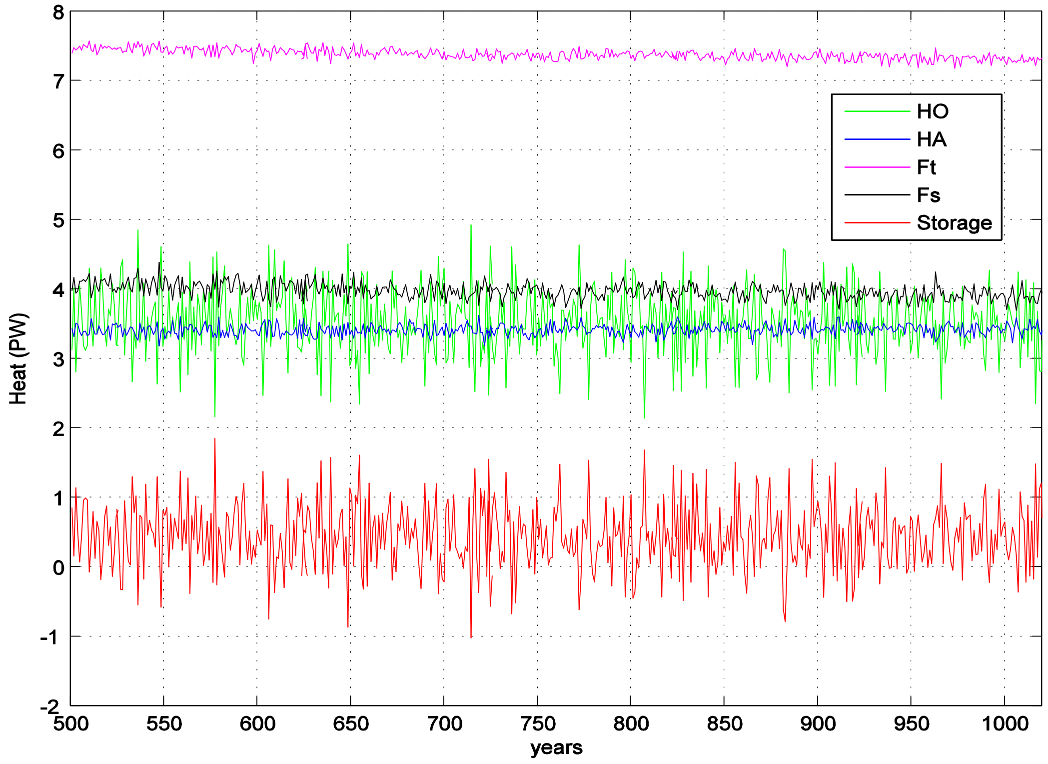

Figure 4.13. Timeseries of annual mean *HA*, *HO*, F_t, F_s and *storage* for years 500 to 1020, in PW.

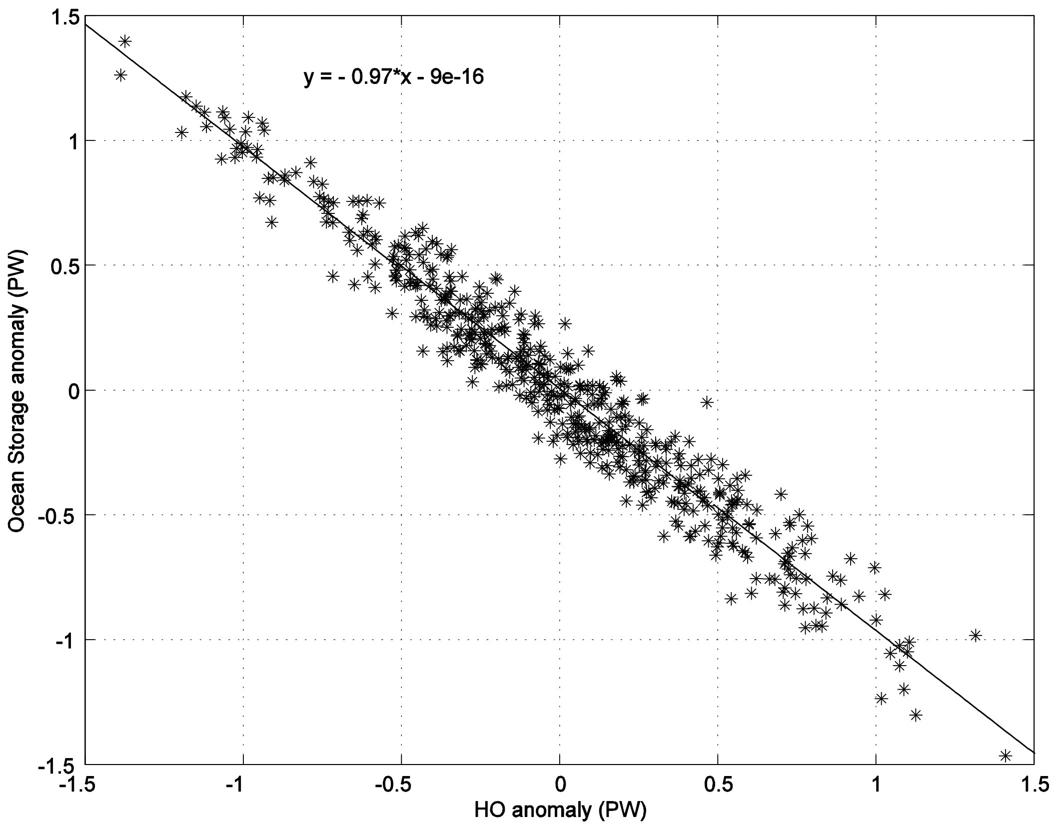

Figure 4.14. Difference from mean *HO* and difference from mean *storage* for annual means, from year 500 to 1020, in PW.

4.5 Heat transport associated with surface winds

4.5.1 Wind stress calculations

In this chapter we are concerned with the coupling of heat transport in the ocean and atmosphere, and the surface wind stress plays a key role in our analysis. It is associated with a significant amount of heat transport out of the tropics by Ekman transport since there is no meridional geostrophic ocean heat transport in an aquaplanet. The flat ocean bottom means that there are no ridges to support geostrophic flow at depth. Here, we investigate how the calculation of surface wind stress based on surface wind output from daily and monthly means from FORTE varies with latitude. We then compare them to the surface wind stress (τ_x) output from FORTE, which uses data output several times each day.

The zonal mean, annual mean surface wind stress, τ_x, for the years 980-1020 yrs and the same data for just the tropics as output from the model, is plotted in Figure 4.15, left and right panels respectively. The trade easterlies can be seen reaching a maximum at around 20°, and the mid latitude westerlies can be seen at around 50° N and S. There is considerable variation in τ_x from year to year, for example in some years the trade winds at 20° are half the strength they are in other years (Figure 4.15, right panel). There is also some north-south asymmetry, for instance the wind stress associated with the trade winds is larger in the southern hemisphere than the northern, due to the eccentricity of the earth's orbit and some asymmetry in ozone and cloud cover which was introduced inadvertently at early stages of the model development.

Surface wind stress is calculated as follows:

$$\tau_x = C_D \rho_{air} \left(\sqrt{u^2 + v^2} + 3 \right) u \tag{4.6}$$

where *u* and *v* are the zonal and meridional surface winds respectively and the 3 ms^{-1} is there to account for gustiness and maintain realistic transfers at low wind speeds, and C_D is a drag coefficient (Forster *et al.* 2000).

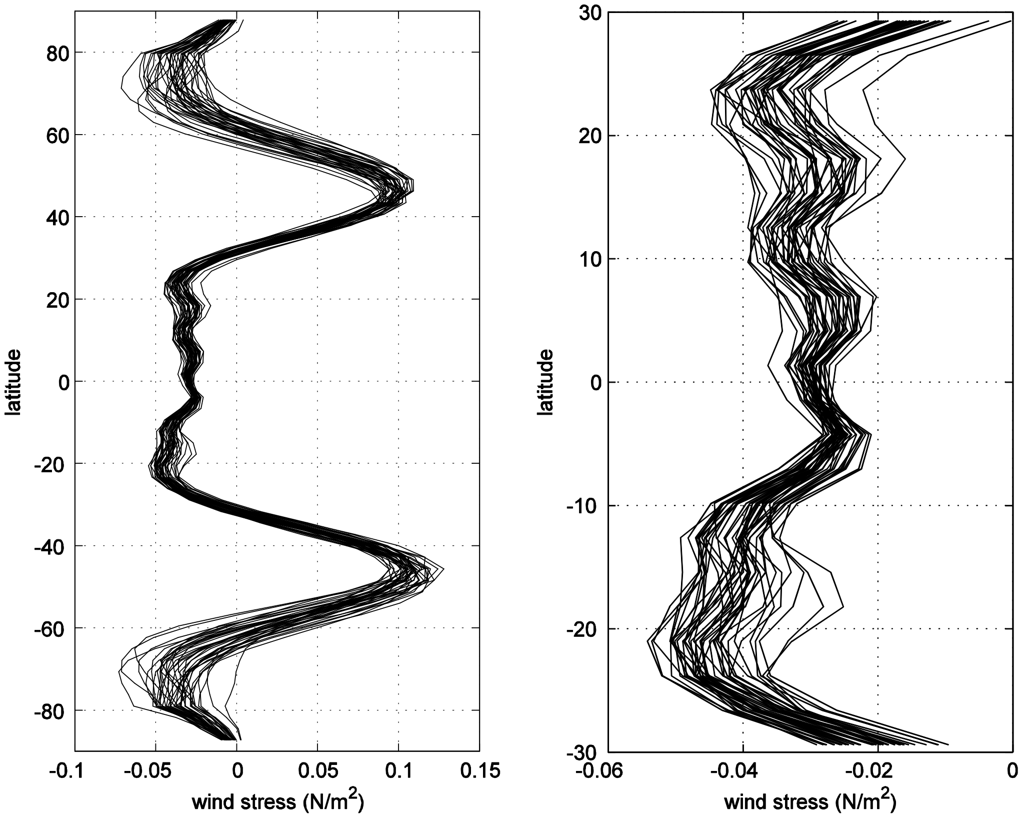

Figure 4.15. Zonal mean wind stress 40 annual means (left), years 980 to 1020 and zonal mean wind stress in the tropics (right) in Nm^{-2}

The windstress output in FORTE is calculated using daily values of surface winds (Sinha & Smith 2002). Because of the squared terms in equation (4.6), small fluctuations in u and v have a significant effect on τ_x. Windstress varies on short timescales, so by using annual means we miss some variation on shorter timescales. Next we investigate how τ_x varies at different latitudes depending on whether we use monthly or daily u and v. We used (4.6) to calculate the wind stress from u and v in the lowest atmospheric layer. First, we calculated the wind stress from the annual mean calculated from monthly mean u and v and compared this to the annual mean windstress from the model output, which we will call τ_x (blue solid line and black solid line respectively, Figure 4.16).

The estimate of windstress calculated from the monthly mean atmospheric wind does not take into account the fluctuations on timescales of less than a month, however the two estimates are very similar in the tropics and the mean difference between them (blue dashed line, Figure 4.16) shows only small discrepancies. The difference is larger in the midlatitudes, indicating that fluctuations in windstress at these latitudes, happens on shorter timescales than in the tropics.

The shortest timescale the FORTE data is available on is daily data, and the windstress calculated from daily u and v is plotted in Figure 4.16 (red solid line). The windstress calculated from daily u and v is much closer to τ_x than the calculation from the monthly values, which is expected since this calculation includes daily fluctuations. This analysis of wind stress using monthly and daily data highlights that the fluctuations in surface wind on timescales of less than a month are more significant in the extratropics than in the tropics. At the latitude we are concentrating on (20^o), the short term fluctuations are much smaller. The similarity between the monthly calculation of windstress using u and v and the model output of τ_x in the tropics, and particularly around 20^o, provides some justification for the use of monthly mean variables when carrying out the analysis presented in this chapter. For the rest of the chapter, we use the monthly mean surface wind stress output from FORTE, τ_x, which is based on data taken several times each day.

Next we concentrate on the heat transport out of the tropics by the ocean and atmosphere, specifically the heat transported out of the band of latitude coinciding with 20^oN to 20^oS.

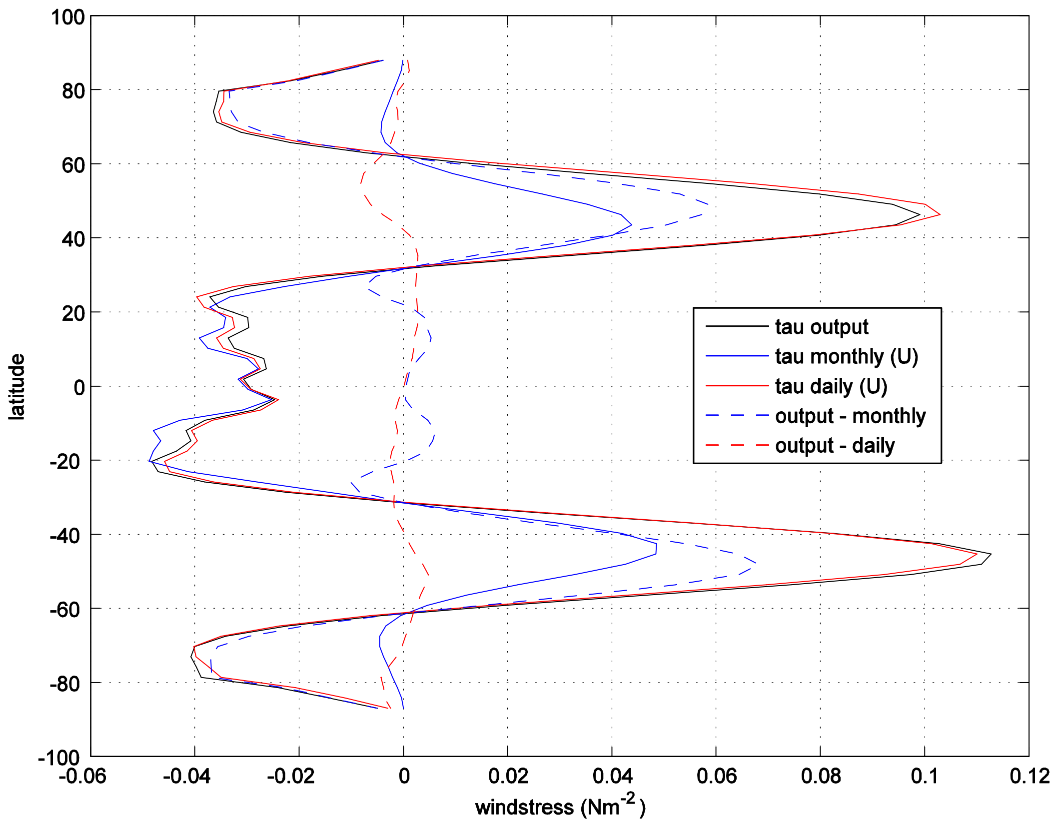

Figure 4.16. zonal mean wind stress from model output windstress field, τ_x (black), windstress calculated using low level atmospheric wind for monthly output (blue) and daily output (red) using equation (4.6). Differences between τ_x and the monthly calculation (blue dashed) and τ_x and the daily field (red dashed) are included.

4.5.2 Ekman mass transport

In investigating Ekman mass transport, here we focus again on the latitude band between 20^o north and south, and base the calculation on the amount of Ekman transport at the boundaries of this latitude band, which represents the transport from this tropical band toward the poles.

It has been suggested that the mass transport in the tropical ocean and atmosphere can be reasonably approximated as the Ekman transport as a result of the trade winds (section 1.3), (Held 2001). For this reason, the mass transport in the tropical ocean should be equal and opposite to that of the atmosphere. The easterly trade winds present at 20^{o}N and 20^{o}S drive poleward surface currents and result in an Ekman mass transport as follows:

$$M_{Ek} = \frac{\tau_x L_x}{f} \tag{4.7}$$

where τ_x is the wind stress at the ocean surface over the extent of the latitude circle, L_x and f is the coriolis force (Gill 1982). Calculated in this way, M_{Ek} represents the overturning mass transport in kg s^{-1} in the ocean and atmosphere at 20^o north and south. In order to calculate the heat transport associated with the wind driven overturning, we need to consider the energy contrasts between the poleward and equatorward flowing branches of the circulation in both the ocean and atmosphere in turn.

4.5.3 Ekman heat transport in the ocean

The heat transport in the ocean associated with Ekman transport is calculated thus:

$$HO_{Ek} = M_{Ek} C_p \, \Delta\theta \tag{4.8}$$

where C_p is the specific heat capacity of the ocean and $\Delta\theta$ is the difference in potential temperature between the two branches of the overturning circulation, that is, the poleward water flowing at the surface and the return flow of water beneath the surface layer.

To calculate $\Delta\theta$ in this case, the surface layer was taken as the weighted mean θ in the top 2 ocean layers ($\theta1$), representing a depth of around 70 metres, and the return layer beneath this was the weighted mean θ over the lowest 13 ocean layers ($\theta2$), representing the remaining ocean. Then $\Delta\theta$ was calculated using $\theta1 - \theta2$. These layers were chosen because the meridional ocean current in the top 2 ocean layers is positively correlated with the ocean heat transport, *HO*, and the lower 13 layers are negatively correlated with *HO* (not shown). This indicates that the direction of the meridional current changes direction between layers 2 and 3 in the ocean, with warm surface water travelling poleward and all the deeper layers returning equatorward.

Figure 4.17 shows that there is a good correlation between HO_{Ek}, calculated using equation (4.8) and *HO*, the ocean heat transport out of the 20^o latitude band calculated using equation (4.3). This data is represented in Figure 4.17 by blue markers; each marker represents one annual mean for the 520 year period 500-1020 yrs . The correlation coefficient for HO_{Ek} and *HO* is R = 0.93, at a significance value of P<0.0001.

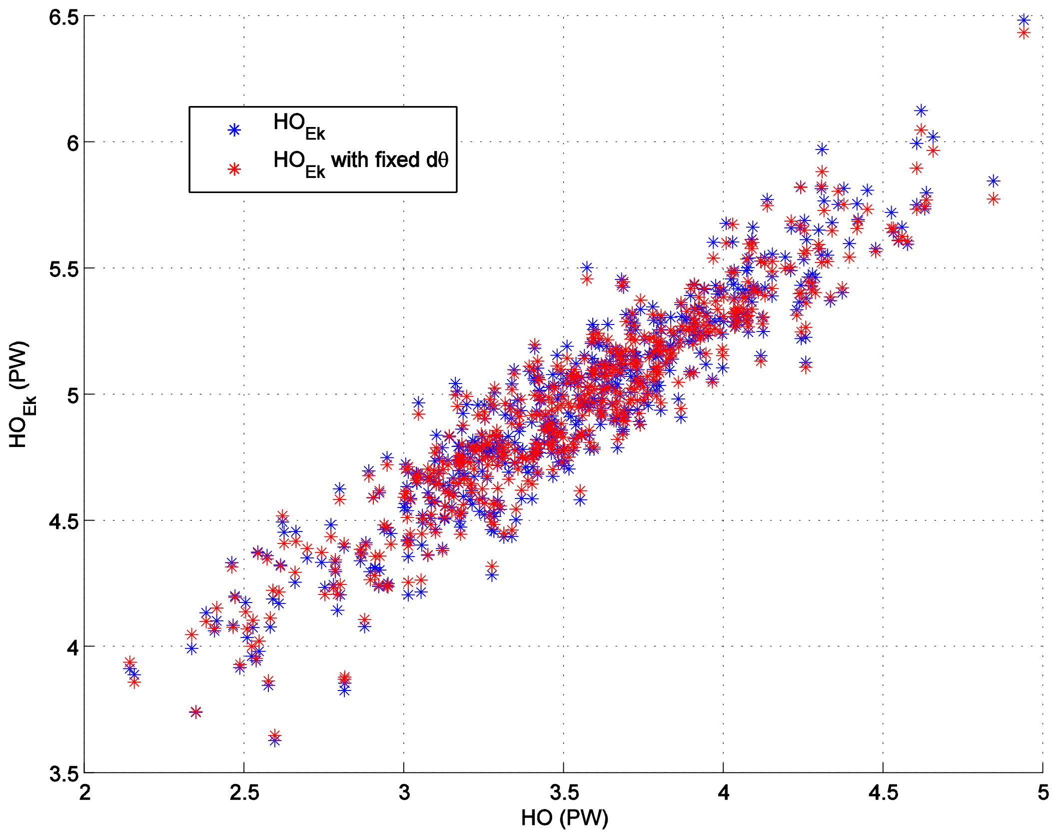

Figure 4.17. Ocean heat transport out of 20 degree latitude band (*HO*) and the Ekman heat transport in the ocean (HO_{Ek}) in petawatts shown with blue markers. HO_{Ek} calculated using fixed Δθ is shown with red markers.

Variations in the Ekman heat transport in the ocean are mainly controlled by the Ekman mass transport, rather than variations in Δθ, and this is illustrated in Figure 4.17 by the use of red markers. Values of *HO* represented using the red markers were calculated using (4.3), the same as for the blue markers. However HO_{Ek} represented by the red markers is calculated using (4.8) but with the same fixed value of Δθ for every year. The value of Δθ for the red markers was taken as the mean Δθ over the 520 year period, which was around 21 K.

There is an offset between HO_{EK} and *HO*, which reflects the lack of a diffusion term included in the calculation for ocean heat transport. The upwelling of cold water at the equator sets up a temperature gradient which leads to diffusion of heat towards the equator. For example, the meridional heat transport term associated with this diffusion (along isopyncals) can be denoted by

$$H_{Diff} = \iint \rho C_P \, \kappa \frac{\partial \theta}{\partial y} dxdz \qquad (4.9)$$

where κ represents a diffusion coefficient. There is also a bolus advection term from the ocean mixing scheme (Gent & McWilliams 1990). In addition, ocean heat storage may be slightly underestimated, since monthly mean values of θ in January and December were used to calculate the yearly change instead of daily values.

The close relationship between the red and blue markers indicates that fixing Δθ does little to change the Ekman heat transport by the ocean, and points towards a scenario which is consistent with ideas of Held (2001), whereby the ocean heat transport in the tropics is controlled by the Ekman transport driven by surface winds.

4.5.4 Axisymmetric atmospheric heat transport (HA_{axisym})

In order to calculate the corresponding atmospheric Ekman heat transport out of the 20° latitude band, HA_{EK}, it follows that we should start by using the Ekman mass transport, M_{Ek} as calculated above from (4.7), but instead of potential temperature, we use the moist static energy, *h* in the atmosphere as the energy quantity:

$$HA_{Ek} = M_{Ek} \Delta h \qquad (4.10)$$

where Δ*h* is the same as was defined in section 1.3.2, and is discussed in more detail in Chapter 2. In order to calculate Δ*h*, we used *T* and *q* from the model output and calculated geopotential, ϕ using the hydrostatic equation:

$$\frac{\partial \phi}{\partial P} = -\alpha \qquad (4.11)$$

where ϕ is geopotential height and α is specific volume. Integrating over pressure gives

$$\phi(P_s) - \phi(P) = \int_P^{P_S} \alpha \, dP \qquad (4.12)$$

Geopotential at the surface is zero, and $\alpha = RT/P$ where *R* is the universal gas constant. Latitude-pressure sections of the terms contributing to *h* (temperature, humidity and geopotential) and their sum are shown in Figure 4.18, in units of Kelvin. The colder equatorial region can be seen in panels a, b and d.

Zonal mean moist static energy profiles at various latitudes are shown in Figure 4.19. The profiles taken at 10°N and 20°N have higher moist static energy than those at 1°N and 30°N, especially nearer to the surface, which reflects the position of the ITCZ, since surface *h* is higher than at the equator and poleward sides of the ITCZ. Moist static energy in the upper troposphere increases rapidly at all latitudes, in agreement with conditions in the real world (see chapter 2). Unlike our world, however, there is a region of relatively low *h* at around 300 hPa.

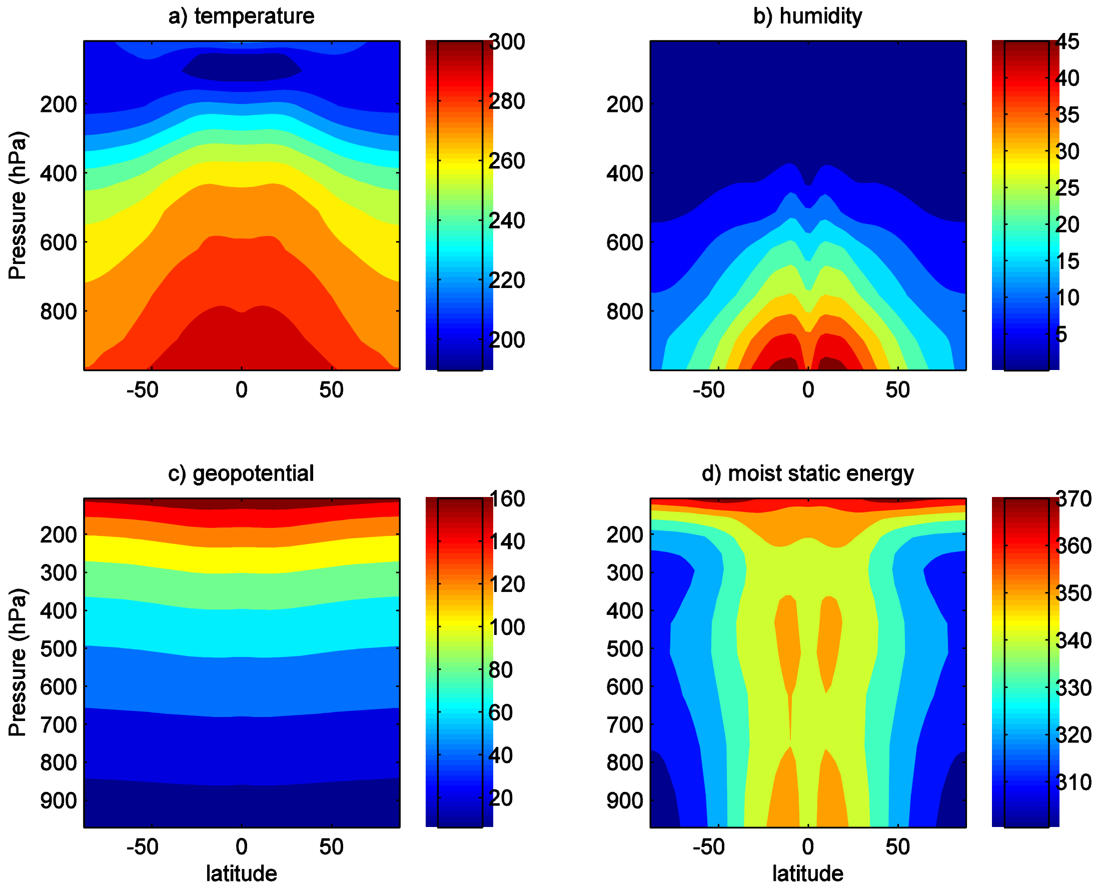

Figure 4.18. Contribution to moist static energy of (a) internal energy, (b) latent heat, (c) geopotential and (d) their total, in Kelvin.

In order to calculate Δ*h*, we require the difference between *h* of the poleward flow and equatorward flow. We previously used a simple 2 layer model to calculate Δ*h* (see chapter 3, section 3.3.2d), where we took the mean *h* in the upper half of the troposphere and subtracted it from the mean *h* in the lower half of the troposphere, and here we apply the same method. The midpoint of the atmosphere was around 500 hPa, and the mean *h* in the upper and lower troposphere was weighted by pressure. Using this method of calculating Δ*h*, the typical value of $\Delta h/C_P$ was around 5 K. This is a smaller value than observations of the real world, where it is typically around 8 K (see section 3.3.2d).

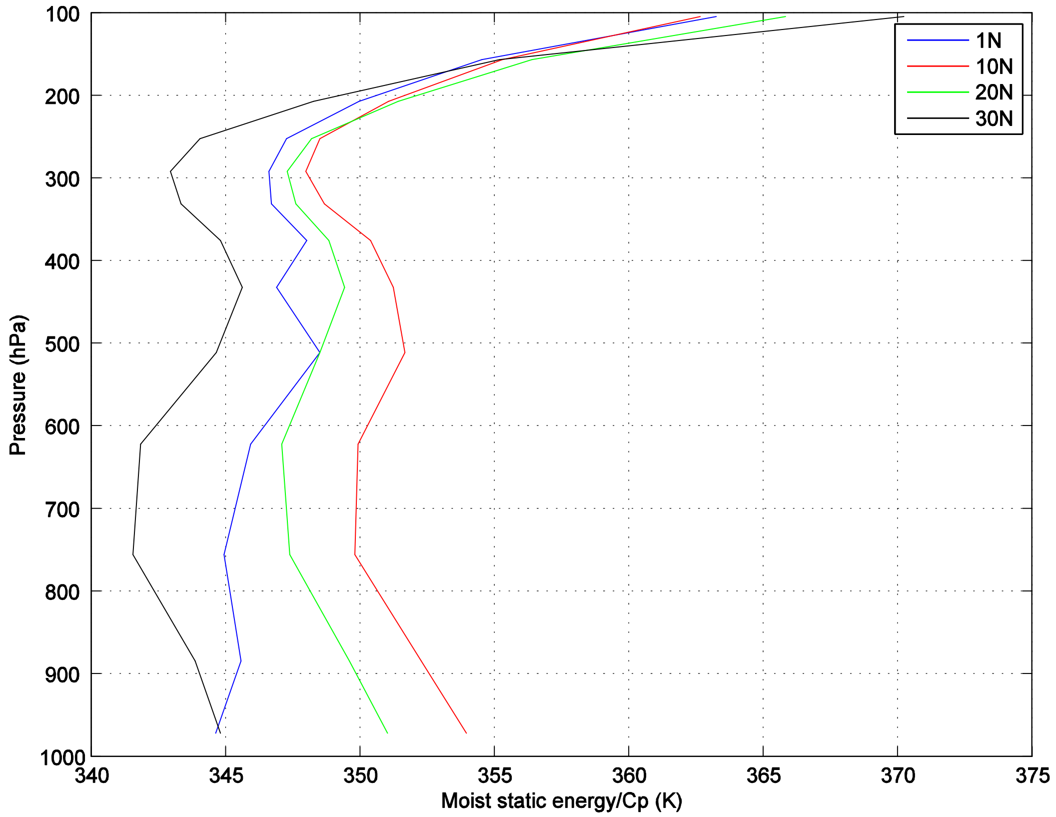

Figure 4.19. Zonal mean moist static energy profiles at various latitudes (divided by C_p to give units in Kelvin). Mean for years 980-1020.

One reason that Δh may be underestimated using the simple 2 layer model is due to the region of relatively high h in the middle troposphere (around 450 hPa) where there is little mass transport. The meridional wind profiles shown in Figure 4.20 illustrate that the poleward wind at 20°N and 20°S is mostly confined to a region between 100 – 200 hPa, where the corresponding moist static energy is relatively high. The equatorward wind is confined to the surface, up to about 800 hPa, where moist static energy is lower.

Also note that the meridional wind profiles at the equator (Figure 4.20, right panel) show much more variability in this colder, region of descending air compared to the profiles on the left hand side. This is consistent with the idea discussed in chapter 3 where the structure of the atmosphere in moist regions (ITCZs) demonstrates a positive-negative structure compared to those in drier regions. Since the meridional wind is confined to certain pressure levels, in this case, the 2 layer method for calculating Δ*h* may not be appropriate, and may be leading to an underestimation of Δ*h* at 20° latitude.

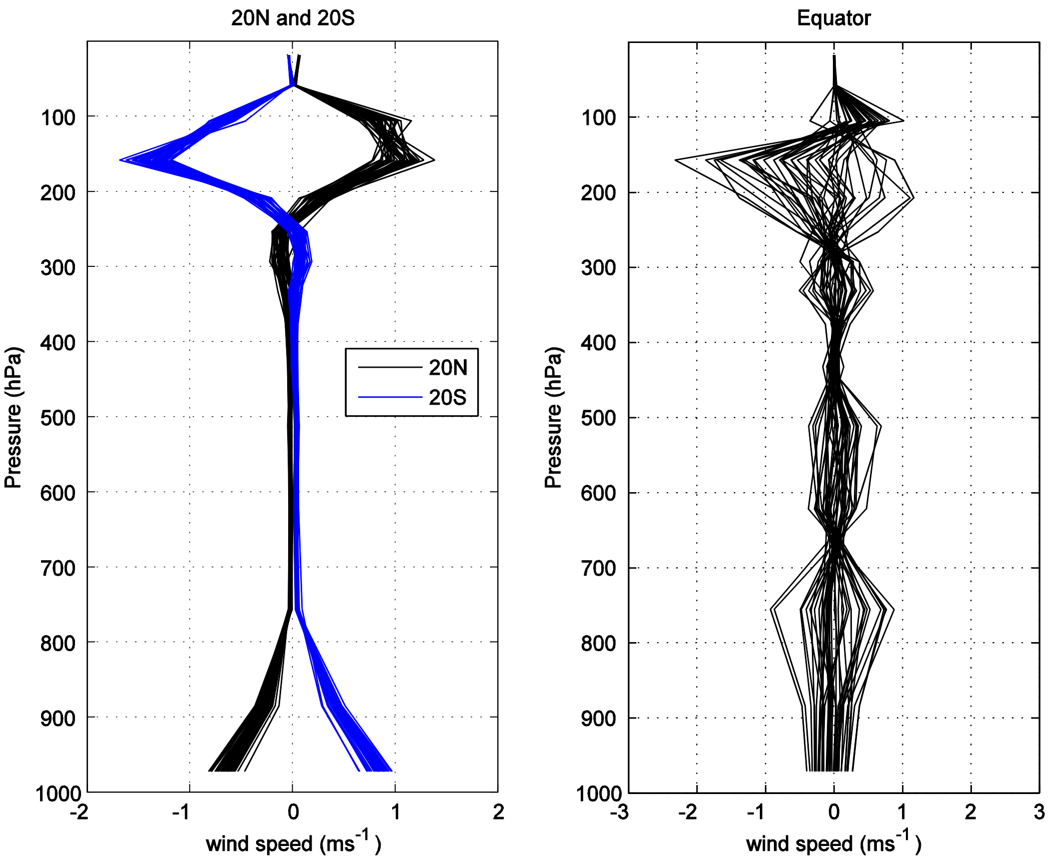

Figure 4.20. Meridional wind profiles for 40 years of annual means (980-1020yrs of the model run) at 20°N, 20°S (left) and the equator (right), in ms^{-1}

Another way to calculate Δ*h* is similar to that described in 3.2.4 b) equation (3.6), where heat transport is divided by mass transport to calculate gross moist static stability. In this case, we use the heat transport by the axisymmetric overturning circulation in the atmosphere (numerator) and the Ekman mass transport based on the surface wind stress (denominator):

$$\Delta h = \frac{\int \bar{v}\bar{h}\frac{dP}{g}}{M_{Ek}} \tag{4.13}$$

where the overbar represents a zonal mean. The axisymmetric overturning heat transport in the atmosphere is:

$$HA_{axisym} = \int \bar{v}\bar{h}\frac{dP}{g} \tag{4.14}$$

Calculating Δh using (4.13) gives a value of around 15 K, which is more representative of the difference in moist static energy between the region with poleward wind and the equatorward wind (Figure 4.19, Figure 4.20). Since we have seen that this method of calculating Δh gives an accurate value, we can now use (4.14) to approximate the wind driven heat transport, HA_{axisym}, which is the atmospheric equivalent of HO_{Ek}. From now on, we use HA_{axisym} to represent the wind driven atmospheric heat transport, and HO_{Ek} to represent the wind driven oceanic heat transport.

The relationship between HA and HA_{axisym} is shown in Figure 4.21. The correlation coefficient, R, is 0.2 for a significance value of $P < 0.0001$. The correlation between HO and HO_{Ek} is much tighter than that between HA and HA_{axisym}: R = 0.93, at the same significance level (Figure 4.17). This is an indication that the ocean heat transport is well approximated by Ekman heat transport, in line with the theory put forward by Held (2001). In the atmosphere, there is still a correlation between HA and HA_{axisym}, although it is much smaller, indicating that the atmospheric heat transport at 20^{o}N and 20^{o}S is not well represented by the axisymmetric heat transport. We next tested whether it was variations in v or h which were mostly responsible for controlling variations in HA_{axisym} and found that anomalies in v were more important in controlling HA_{axisym} than h, which is consistent with results in chapter 3, where it was found that mass transport was more of a control on convective region heat transport than variations in gross moist static stability. The fact that HA_{axisym} is much smaller than HA implies that there must be other important components of poleward heat transport and implies that eddies play a key role in heat transport around 20^{o} in FORTE (more on eddies in section 4.6).

Figure 4.22 shows the relationship between HO_{Ek} and HA_{axisym}, both of which represent the heat transport associated with the surface winds. We have previously seen that there is a strong dependency of ocean heat transport on wind stress (Figure 4.17). Figure 4.22 shows that there is some correlation between HO_{Ek} and HA_{axisym}: the correlation coefficient is R = 0.28 at $P < 0.0001$. The size of the axisymmetric heat transport in the atmosphere is much smaller than for the ocean. At 20 degrees, typical values of $\Delta\theta$ in the ocean are of the order of 25 K, due to a highly stratified ocean, and C_p for the ocean is 3850 J kg^{-1} K^{-1}. In the atmosphere, Δh is on the order of 15 K and C_p is 1004 J kg^{-1} K^{-1}. This means the wind-driven ocean heat transport dominates over the atmospheric heat transport at 20 degrees. This is consistent with previous results (Czaja & Marshall 2006; Vallis & Farneti 2008a), although the latitude where ocean heat transport dominates for those studies was deeper into the tropics than the latitude of 20^{o} used here. This means that we can understand that the ocean heat transport dominates over the atmospheric heat transport at 20 degrees, but it is unclear as to why the correlation between HO_{Ek} and HA_{axisym} is not larger, since we expect both to be controlled by the same surface wind stress, and therefore strongly correlated with each other. Timeseries of the heat transport terms calculated in this chapter are shown in Figure 4.23.

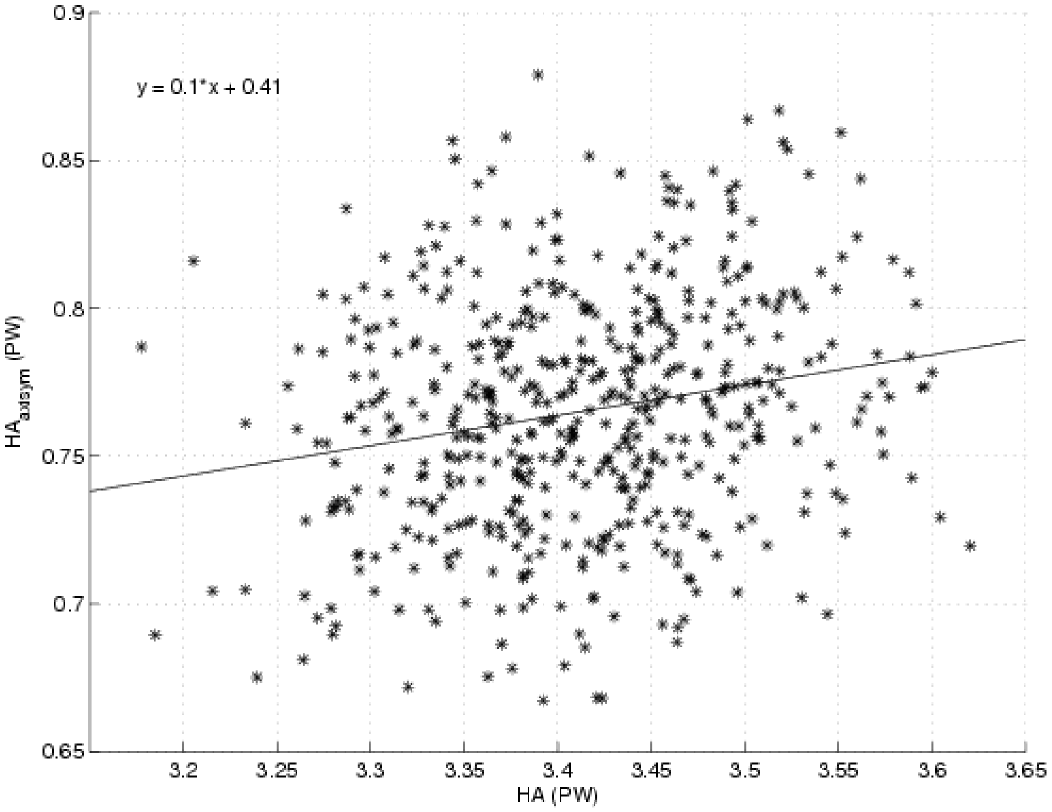

Figure 4.21. Atmospheric heat transport from radiative fluxes, *HA*, and axisymmetric atmospheric heat transport, HA_{axisym} in PW at 20^{o} latitude.

Figure 4.23 illustrates the relative magnitude of the heat transport terms and gives an idea of their variability. Note the similar sizes of *HO* and *HA* (green and blue) but the larger variability of *HO*. The atmospheric axisymmetric heat transport, HA_{axisym} (yellow) is a small term compared to the ocean Ekman heat transport, HO_{Ek}, (cyan).

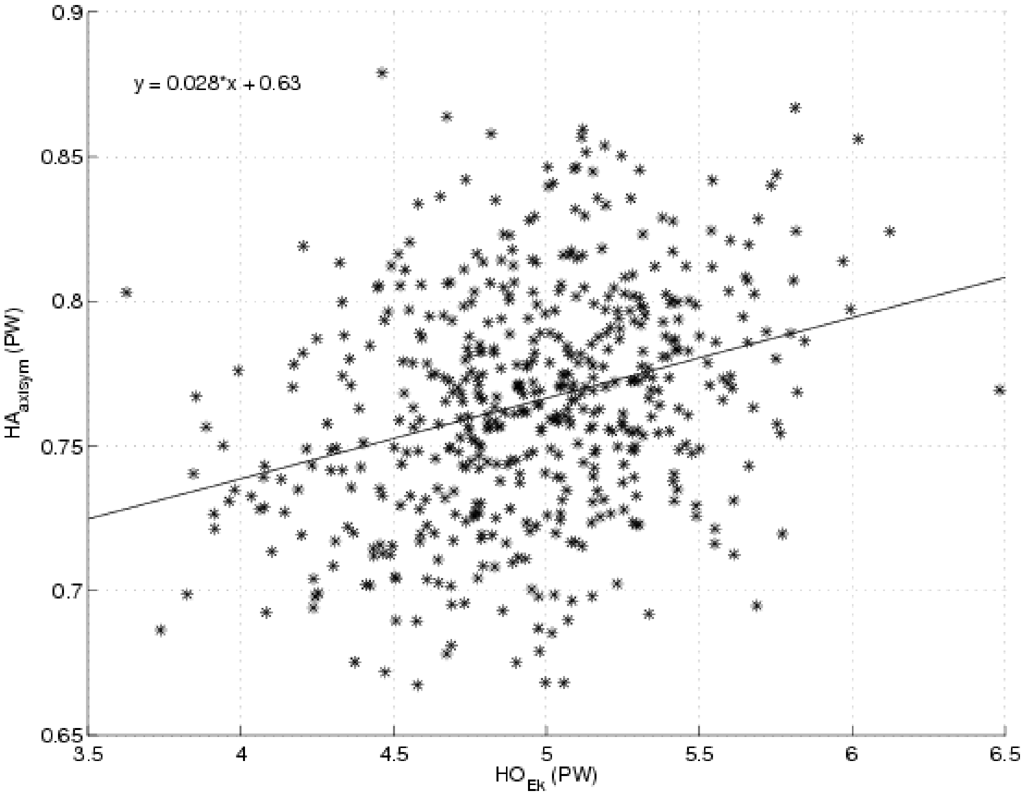

Figure 4.22. Ekman heat transport in the ocean, *HO_{Ek}*, and axisymmetric heat transport in the atmosphere, *HA_{axisym}* in PW.

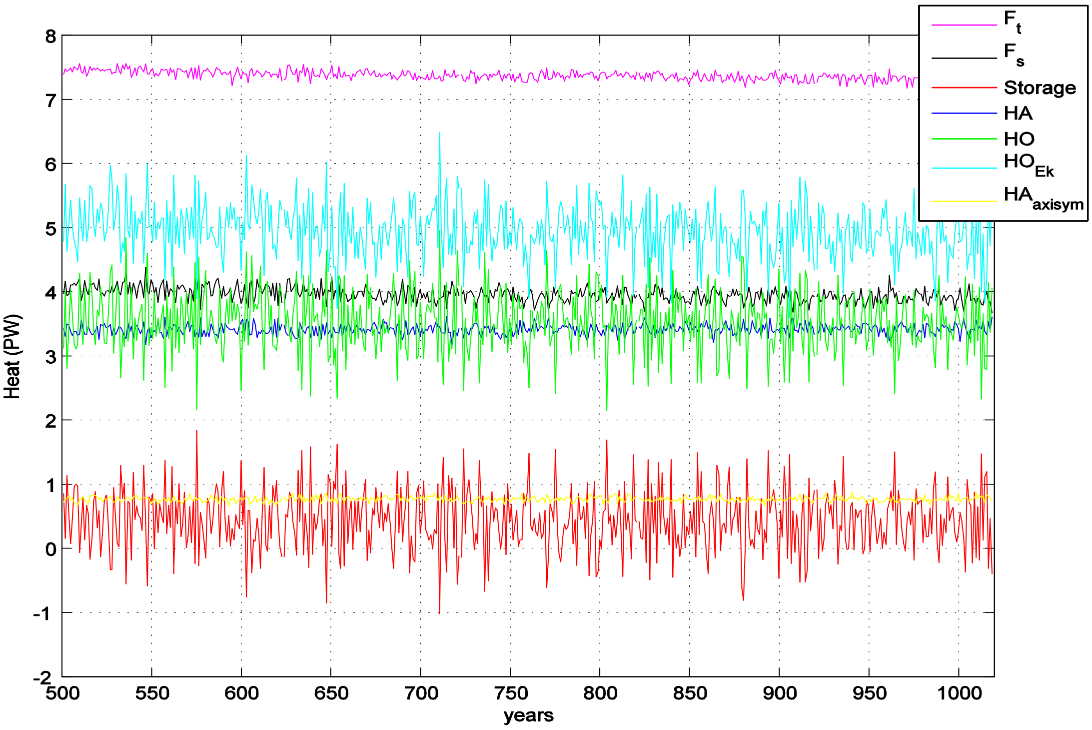

Figure 4.23. Timeseries of main components of heat transport for years 500 to 1020 in PW. See text for explanation.

4.6 Atmospheric Eddy heat transport in FORTE

In section 4.4, we saw that the mean heat transport from the tropical atmosphere in the FORTE model, *HA*, was 3.4 PW and in section 4.5.2, the mean axisymmetric overturning atmospheric heat transport, HA_{axisym} was only 0.8 PW (the sum of both hemispheres, i.e. poleward transport at 20°N added to that at 20°S). This implies that there must be a large atmospheric eddy heat flux contribution at around 20° in the model. We calculated the sensible eddy heat flux as a function of latitude as follows:

$$eddy_{sensible}(\phi) = L_x(\phi)C_p \int \overline{v'T'} \frac{dP}{g} \tag{4.15}$$

And the latent eddy heat flux was:

$$eddy_{latent}(\phi) = L_x(\phi)L_v \int \overline{v'q'} \frac{dP}{g} \tag{4.16}$$

where the primes represent the deviation from the time mean. The latitudinal distributions of sensible eddy heat flux and the latent eddy heat flux are plotted in Figure 4.24.

At 20°, the contribution of eddy heat flux is 1 PW in each hemisphere making a total of 2 PW (Figure 4.24), which is a substantial amount, at more than twice the axisymmetric overturning contribution. The assumption in Held (2001), was that eddies were negligible in the tropics and could be ignored. Here we find that the eddy term is large, however we are concentrating on 20° latitudes, which is not usually considered to be in the deep tropics. It is also interesting to note that the latent eddy heat flux is nearly entirely responsible for the eddy heat flux equatorward of 20°. In fact, the latent eddy heat flux dominates at all latitudes. Colman *et al*. (1994) performed an investigation into meridional energy flux, comparing the control run of a GCM with data calculated by Oort & Peixoto (1983). They noted that the total eddy heat flux was dominated by sensible heat at high latitudes, and latent heat at low latitudes, (Figure 4.25) largely because of the high specific humidity in the tropics and low baroclinicity compared to the mid latitudes (Colman *et al.* 1994).

It was also noted that latent and sensible eddy heat flux is approximately equal in the midlatitudes (Trenberth & Stepaniak 2003). The latent eddy heat flux dominates between 50°N and S in FORTE. This large latent eddy heat flux in the waterworld model may be due to the increased temperature and humidity of the atmosphere compared to the real world (Smith 2004).

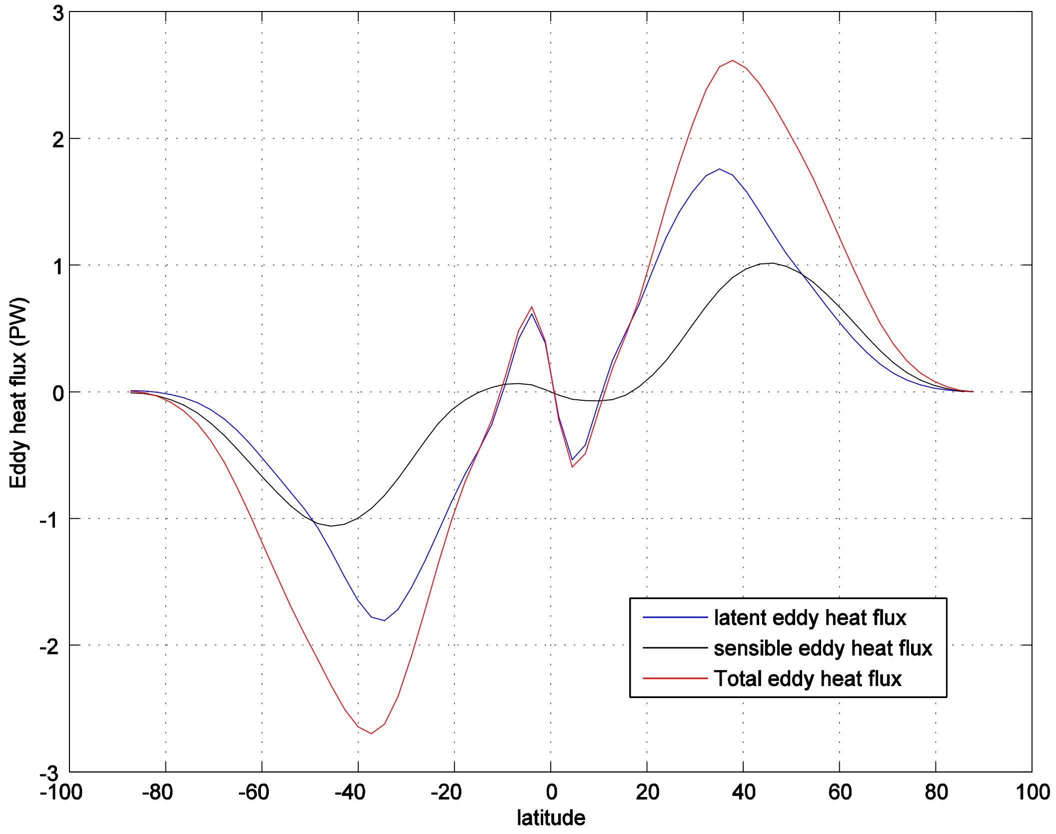

Figure 4.24. Eddy heat flux versus latitude for years 585 to 600. (Data kindly donated by Jacob Cheung, Imperial College.)

The total eddy heat flux is clearly an important contribution to the total atmospheric heat transport at 20^o in FORTE. The northward atmospheric energy flux, separated into the mean meridional circulation and the eddy heat flux for the northern hemisphere in the real world is shown in Figure 4.26. It is striking that the total eddy heat flux takes over as the main contributor of northward heat transport from the MMC equatorward of 15^o. At around 20^{o}N, the mean meridional circulation accounts for less than 0.5 PW of the total heat transport, and this represents about a third of the total (Figure 4.26).

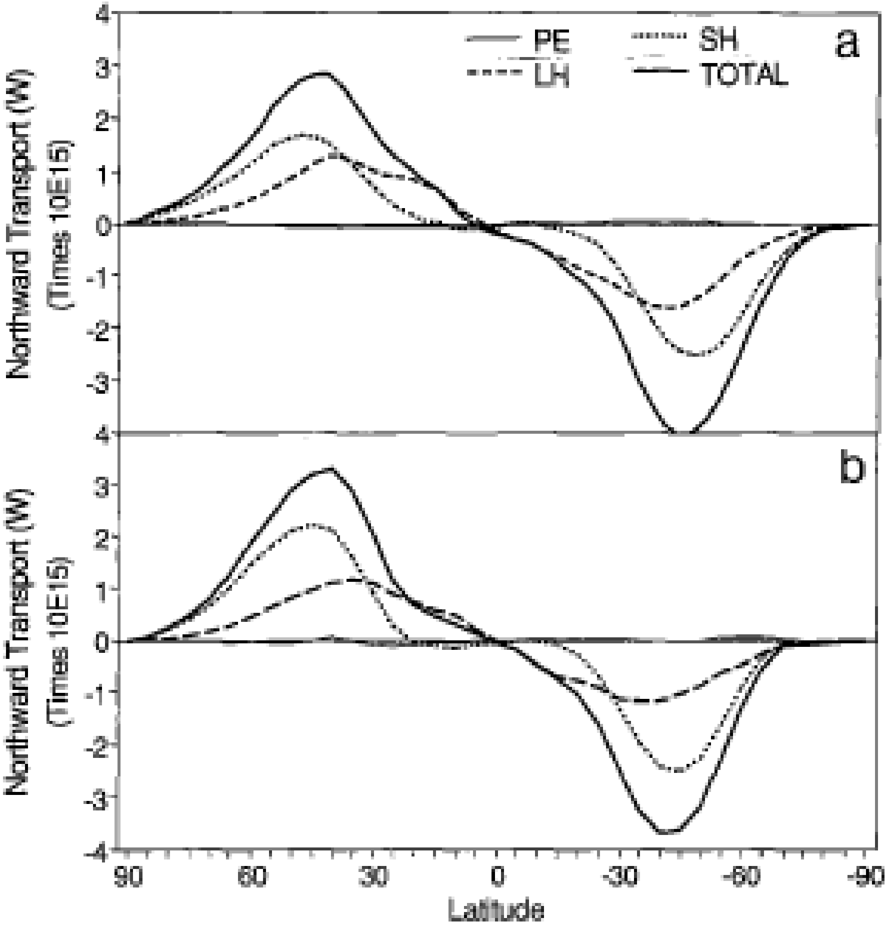

Figure 4.25. The transient eddies showing the contributions to the total of latent heat, sensible heat and potential energy for a) model results and b) observations (Oort & Peixoto 1983). From Colman *et al*. (1994).

According to the data used in producing Figure 4.26, at 20^{o}N in the real world, the total atmospheric poleward heat transport is around 1.5 PW (Oort 1971). In FORTE, the corresponding value at 20^{o}N is around 1.8 PW. At 20^{o}S in FORTE, the total is very close to the estimate by Oort (1971), also around 1.5 PW. The axisymmetric overturning, HA_{axisym} value at 20^{o} in FORTE is around 0.8 PW (including both hemispheres), which agrees well with the estimate by Oort (Figure 4.26).

From these approximate calculations, there is a mean meridional circulation (MMC) component of atmospheric poleward heat transport at 20^{o} in FORTE which accounts for around 0.8 PW from both hemispheres, and sensible and latent eddies account for around 2 PW, leaving a deficit from the total atmospheric heat transport of approximately 0.5 PW.

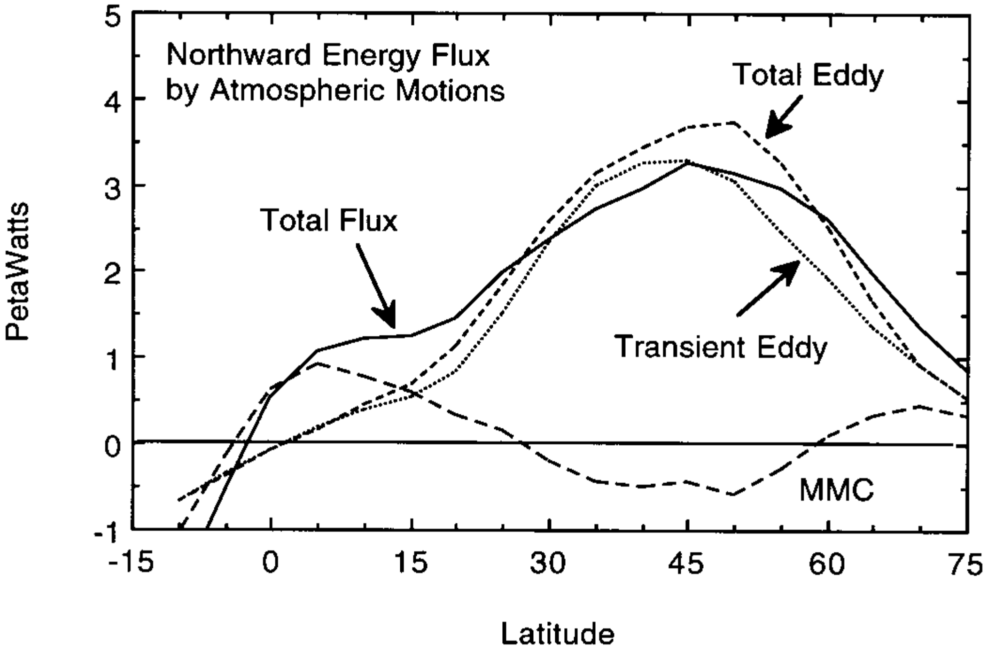

Figure 4.26. Annual average northward energy flux versus latitude in Northern Hemisphere for real world. MMC indicates mean meridional circulation. Data from Oort (1971), figure from Hartmann (1994).

The similarity between the FORTE heat transport calculations (sections 4.4 and 4.5) and the estimates by Oort (1971), Figure 4.26, indicate that the eddy heat flux is a significant component of the total atmospheric heat transport at around 20°. Similar values of eddy heat flux and mean meridional heat flux at these latitudes are found in Peixoto & Oort (1992). In the analysis carried out in chapter 3, we concentrated on the cross equatorial heat transport where the mass transport of the Hadley Cell was generally at a maximum during solsticial seasons. When studying the axisymmetric overturning at 20° in this chapter, we are at the edge of the Hadley cell, where the mean meridional mass transport is smaller, meaning eddy heat flux is larger than it is at the equator (Figure 4.27). This is true in the real world, and it also seems to hold in the FORTE model in terms of estimates of heat transport.

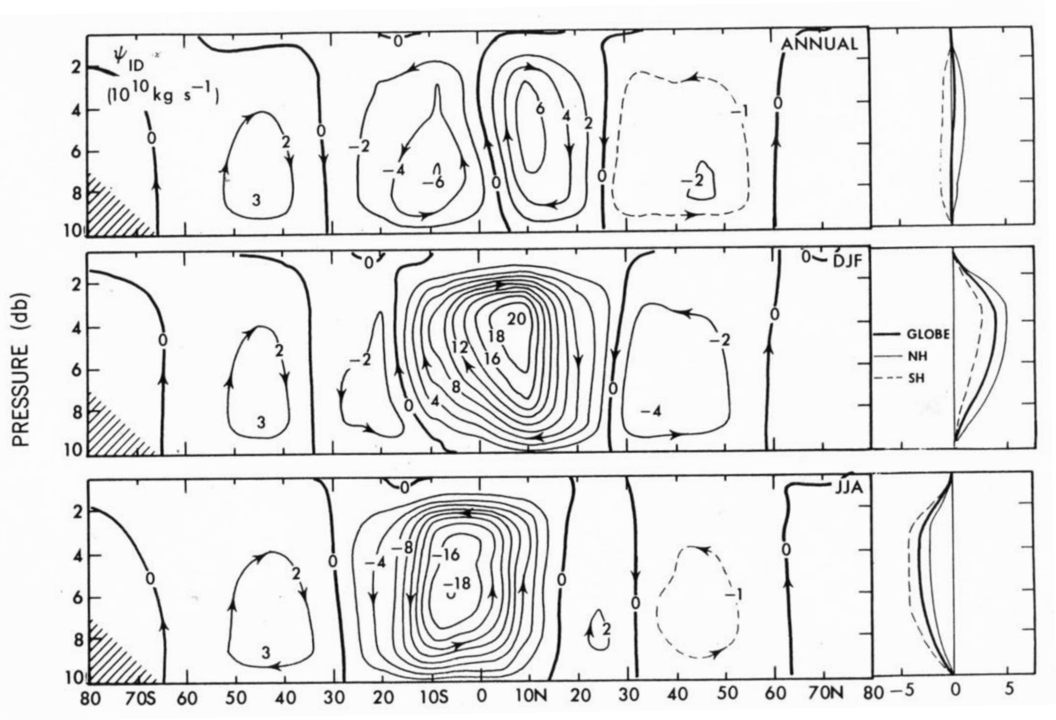

Figure 4.27. Zonal-mean cross sections of the mass stream function in 10^{10} kg s^{-1} for annual, DJF and JJA mean conditions. Vertical profiles of the hemispheric and global mean values are shown on the right. From Peixoto & Oort (1992).

From the results in this chapter we can conclude that the Held model of the dominance of heat transport associated with the trade winds works well in the tropical ocean in the FORTE waterworld run and in fact, wind stress controls the ocean heat transport out of the 20^{o} latitude band. In the atmosphere in the waterworld set up, at 20^{o}N and 20^{o}S, atmospheric eddies play a key role in transporting heat polewards, and hence the axisymmetric overturning heat transport in the atmosphere is a much smaller contribution to the total heat transport. There is some correlation between HA_{axisym} and HO_{Ek} at 20^{o} of latitude (Figure 4.22), but generally the Held model does not apply as well at this latitude in the atmosphere of the FORTE waterworld run as in the ocean.

4.7 Timeseries analysis

In order to investigate longer term trends in the data, timeseries of *HA*, *HO*, F_t, and *storage* with long-term linear trends removed have been produced along with 10, 20 and 50 year running means (Figure 4.28).

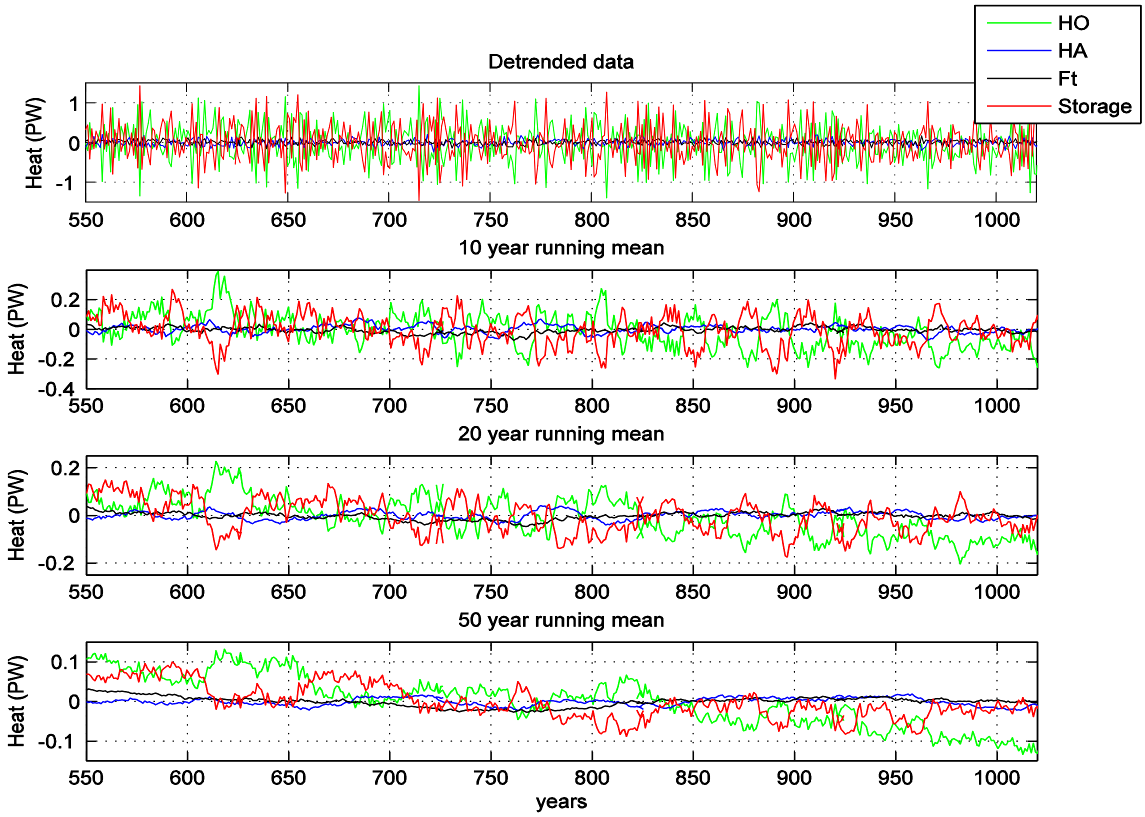

Figure 4.28. Detrended timeseries of *HO*, *HA*, F_t and *storage* (top), and 10, 20 and 50 year running means (2nd, 3rd and 4th panels).

The relatively large variability of *HO* and *storage* compared to *HA* and F_t is clear to see in Figure 4.28, as is the anticorrelation between *HO* and *storage*. We performed an analysis of the timeseries of the main terms in the heat transport calculations, and the resulting power spectrum is shown in Figure 4.29.

The power spectra were produced using a power spectral density estimate using the Thomson multitaper method (MTM), (Percival & Walden 1993). The power represents the power per year of the last 470 year period of the model run. Figure 4.29 shows that the radiative flux at the top of the atmosphere, F_t, and the atmospheric heat transport, *HA* are essentially white noise spectra, with no dominance at any particular frequency. The power values for *HA* and F_t are also noticeably around a factor of 10 smaller than the other spectra, indicating relatively small fluctuations. Also, HA_{axisym} appears as a white noise spectrum with similar power values.

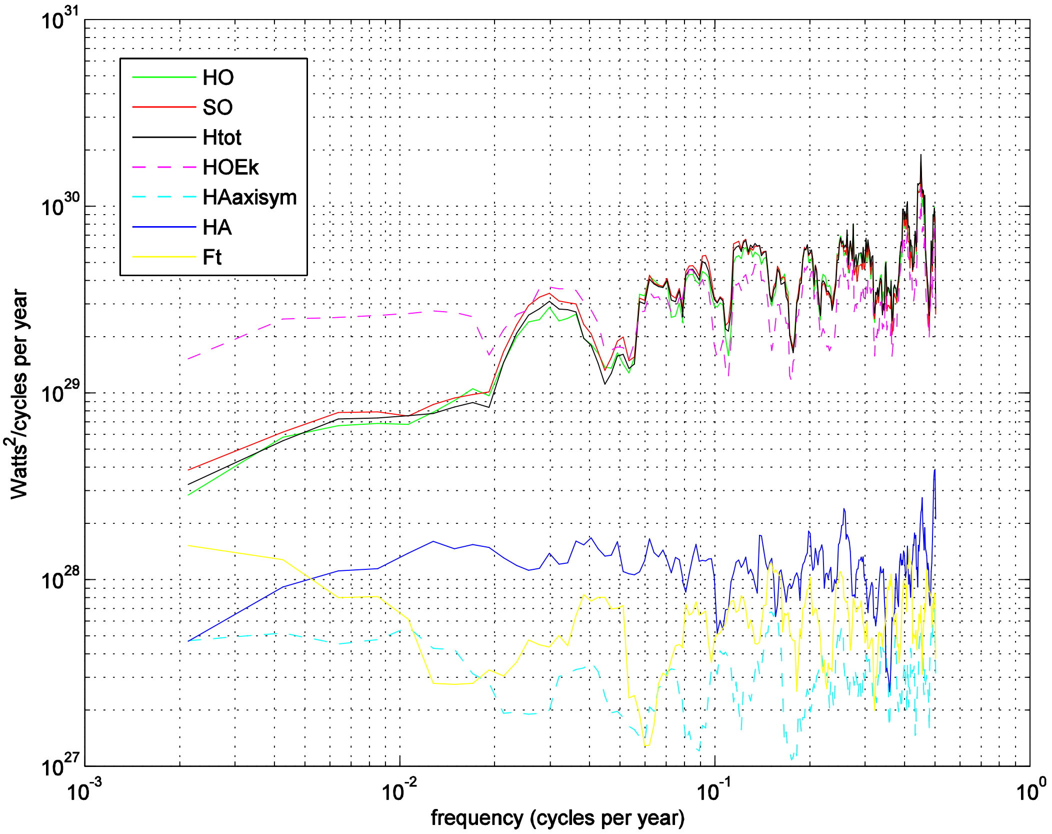

Figure 4.29. Power spectra for *HO*, *HA*, F_t, *SO*, H_t, HO_{Ek} and HA_{axisym} using Thomson multitaper method.

As for the spectra for ocean heat storage, *SO*, and oceanic heat transport, *HO*, they show more of a blue spectrum, meaning that power is increased at shorter timescales. The power at low frequency is decreased, indicating less variation at long timescales than short. In the real world, we might expect more decadal variability of heat transport in the ocean than is illustrated in Figure 4.29. For example, Shaffrey & Sutton (2006) studied the decadal variability in a coupled model and found significant decadal variability of heat transport in the ocean. They found that most of the decadal variability in the extra-tropics was associated with the north Atlantic, but in the tropical ocean, it occurred mostly in the Indo-Pacific Ocean (Shaffrey & Sutton 2006). In their model, the presence of land may have played a large role in contributing to the thermohaline circulation decadal variability in this region and may be connected with phenomena such as ENSO. In FORTE, without continents, the decadal variability of heat transport in the ocean is not obvious.

The spectra of SO and *HO* are closely related, since they are strongly anticorrelated (Figure 4.14), with heat transport in the ocean acting to cool the tropical ocean. As seen previously in section 4.4, there is little coupling of ocean and atmosphere heat transport in the 20 degree latitude band and this is apparent in the power spectra of *HA* and *HO* in Figure 4.29. The spectrum of HO_{Ek} shows similar variability as *SO* and *HO* and closely resembles them, although it is more of a white noise spectrum, again showing no dominance at any particular frequency. At long timescales, however, HO_{Ek} is larger than *HO* and *SO*, and this must be due to the diffusion term (4.9) and the ocean mixing term (Gent & McWilliams 1990) which balances HO_{Ek}.

4.8 Summary and conclusions

Essentially, the purpose of this chapter was to test Held's theory of ocean-atmosphere coupling on a coupled aquaplanet model. The model contained the assumption that tropical heat transport is mainly wind driven and that the ocean and atmosphere are strongly coupled, and as such, the heat transport varies similarly in each. By using the aquaplanet set up of FORTE, the wind stress on the ocean is not disrupted by continents which makes it useful for testing Held's theoretical model (Held 2001). The FORTE model is a simple model which lacks complicated feedbacks related to continents, which is advantageous for our analysis. However the FORTE model does not represent the real world so this was a theoretical, idealized test. We chose to focus on a latitude of 20^{o}, since this is where ocean and atmosphere heat transport are fairly similar (Figure 4.10) at the heart of the Hadley Cells (Figure 4.15). The following points came from the analysis:

- There is no correlation between variations in ocean and atmosphere heat transport, *HO* and *HA*, at 20 degrees calculated using ocean heat storage, surface and TOA fluxes.
- The ocean heat transport, *HO*, is well approximated by the ocean Ekman heat transport, HO_{Ek}, which confirms Held's theory that ocean heat transport in the tropics is largely driven by the trade winds. There was also a close inverse relationship between *HO* and ocean heat storage, indicating that the wind driven heat transport was effective at removing heat from the tropical ocean in FORTE.

- There is some correlation between HA and HA_{axisym}, indicating that the atmospheric heat transport is partly controlled by the trade winds, as it is in the ocean. However, the axisymmetric atmospheric heat transport is a small term compared to HA, which indicates that wind driven atmospheric heat transport is less significant in the tropics of the FORTE model than in our world.
- There was also some correlation between HA_{axisym} and HO_{Ek}, showing that the wind driven heat transport is coupled between ocean and atmosphere in the tropics to some extent, although it was not as marked as suggested by the model of Held (2001).
- Atmospheric eddies play a large role in the tropical atmosphere of FORTE at 20^o, and account for around 75% of the total atmospheric heat transport.

In summary, Held's heat transport partition model works well in the tropical ocean in FORTE at 20^o in that the ocean heat transport is well approximated by HO. However, for the atmosphere, at this latitude, eddy heat fluxes play a significant role in poleward heat transport, which means that we cannot consider that the Held model is a good approximation of the FORTE atmosphere. We have used latitudes of 20^o since this was just poleward of the ITCZs and the heat transport was in the same direction as the real world here (polewards). Equatorward of 20^o, the atmospheric heat transport is toward the equator, due to the cold tongue which extends around the planet. 20^o is also the latitude where ocean and atmosphere play an equal role in transporting heat. However, we can only suggest that Held's model does not apply to the atmosphere at this particular latitude and further investigation at different latitudes is necessary.

Chapter 5 Summary and conclusions

The first chapter of this thesis began with an overview of the climate of the tropics, discussing features such as ENSO, the Walker and Hadley Circulations and the monsoons as an introduction. These features highlighted the fact that although we often use zonal mean data when looking at the tropics (in particular when calculating heat transport), there is a certain amount of spatial variability in properties such as SST, relative humidity and atmospheric circulation throughout the tropics. This motivated investigations into the distribution of moist static energy and mass transport in the tropics (chapter 2) and the calculation of heat transport in convective regions of the tropics (chapter 3). The idea of strong coupling between the ocean and atmosphere in the tropics led to the study of ocean and atmosphere heat transport using a coupled aquaplanet model (chapter 4). In this chapter we provide a short summary of the findings of each of the 3 chapters.

The motivation for chapter 2 came from studying the simple heat transport model of Held (2001) which assumed that mass transport in the tropical ocean and atmosphere is a result of the trade winds and therefore equal in magnitude and opposite in sign. Held postulated that the ratio of atmospheric to oceanic heat transport in the tropics could be given by:

$$\frac{H_A}{H_O} = \frac{\psi_A}{\psi_O}\frac{\Delta h_A}{\Delta h_O} \simeq \frac{\Delta h_A}{\Delta h_O} \tag{5.1}$$

where ψ represents an overturning circulation, Δh is gross stability, and the O and A subscripts represent ocean and atmosphere. This motivated an investigation into the horizontal variations in moist static energy and atmospheric mass transport. A key figure from chapter 2 repeated below (Figure 5.1), highlights the relationship between low level moist static energy and atmospheric mass transport for JJA. Some key results from chapter 2 can be summarized as follows:

- Moist static energy in the tropics is strongly influenced by SST (section 2.3).
- Horizontal variations in moist static energy at the surface (h_{sfc}) are of the same order as vertical ones (around 10 K), (section 2.4).

- Atmospheric mass transport in regions associated with high h_{sfc} and high relative humidity, which is a feature of deep convection, has a dipolar structure, which was illustrated by the framework described in section 2.5 (Figure 5.1).
- In regions with low h_{sfc} the atmospheric mass transport is more complex, and relative humidity is lower, indicating there is descent of air in these regions and a lack of deep convection (Figure 5.1).
- We identified the Somali Jet during JJA, which consists of a strong low level flow over the western Indian Ocean with little return flow directly above (section 2.6.1).

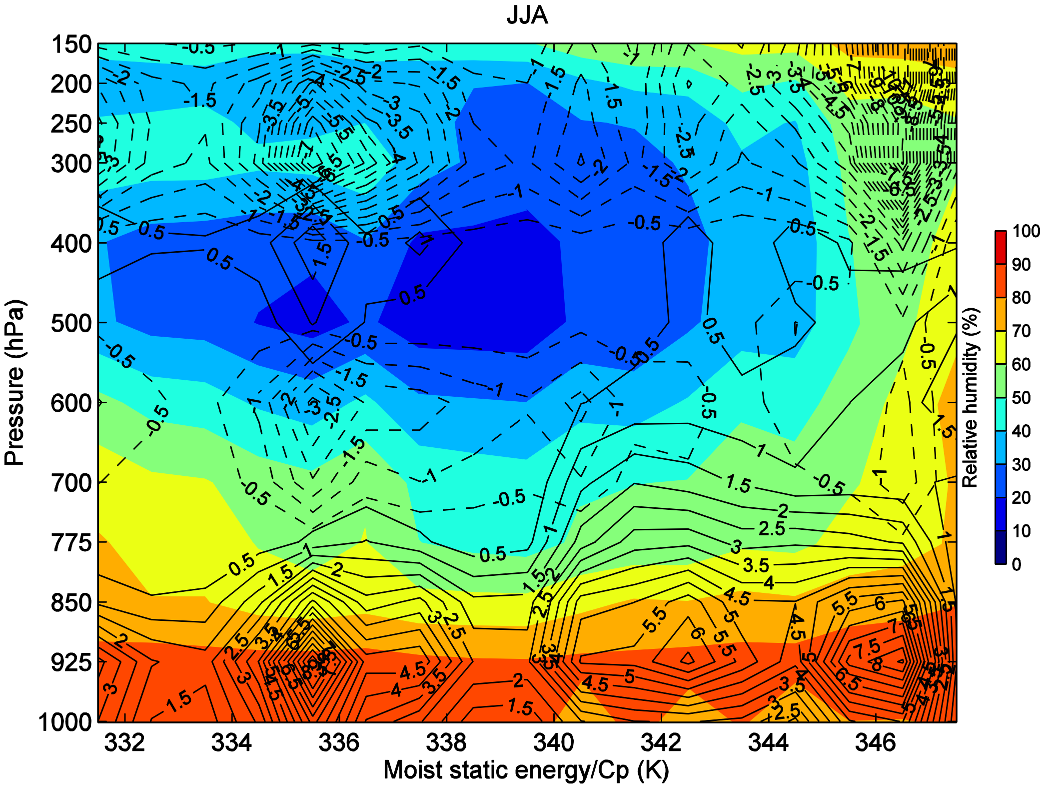

Figure 5.1. Mass transport as a function of surface moist static energy for JJA. Colours represent relative humidity and contours are mass transport, solid northward and dashed southward. On the right hand side, high relative humidity represents the convective regions, where heat transport takes a dipolar form. The low-level Somali jet is visible centred around 342 K, with little return flow at upper levels. Below 336 K is the region associated with low relative humidity and low surface moist static energy, where the mass transport is more complicated. Figure repeated from section 2.5.3.

Following the identification of different circulatory regimes in regions of tropics associated with different surface conditions, chapter 3 focused on the convective regions in particular. Hadley Cell heat transport can be approximated as

$$H_A = \psi_A \Delta h \qquad (5.2)$$

where Δh is the difference in moist static energy between upper and lower level flows (Held 2001). The total heat transport in the tropics can be approximated using zonal mean values (Peixoto & Oort 1992), and (5.2), which implies that an overturning circulation dominates the heat transport in the tropics. In chapter 3, we used a criterion based on relative humidity to identify the regions of the tropics which are characterized by convection and have a dipolar meridional structure. A key figure from chapter 3 illustrates the contribution of the convective region to the total heat transport, and is repeated below (Figure 5.2).

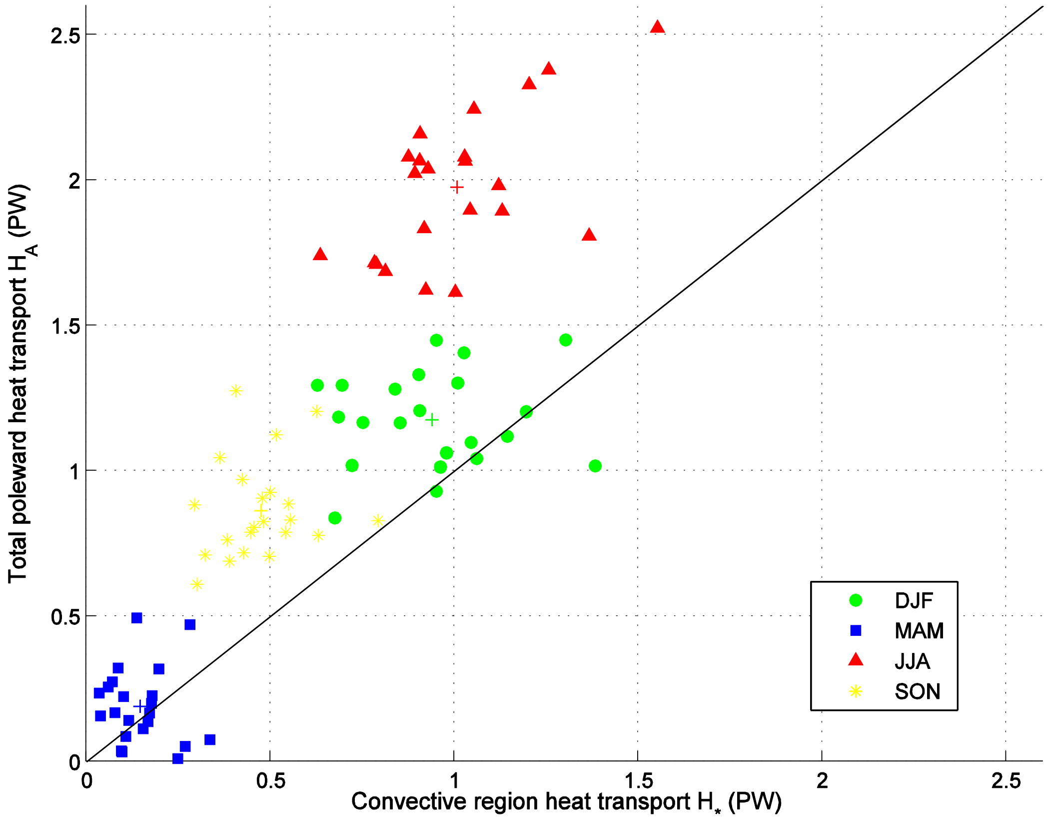

Figure 5.2. Convective region heat transport and total poleward heat transport at the equator, showing that the convective region contributes significantly to the total heat transport. Figure repeated from section 3.3.1.

Key results from Chapter 3 are summarized as follows:

- The Hadley Cell in the convective regions accounts for 51% and 80% of the total cross equatorial heat transport in JJA and DJF respectively (section 3.3.1).

- We also noted that the net southward flow of the atmosphere across the equator on annual timescales was not explained by the convective region, and that other mechanisms, such as the monsoon circulation were responsible for this asymmetry.
- Mass transport is the main controlling factor in the variability of heat transport in the convective regions of the tropics, and Δh plays a smaller role (section 3.3.2b).
- Furthermore, the size of the convective region and the strength of the meridional wind each played a similar role in determining the mass transport of the Hadley Cell (section 3.3.2c).
- During an El Niño season (DJF 1998), convective region extent was greatly increased, as was the convective mass transport and heat transport. There was a small decrease in gross moist static stability which did not offset the increase in heat transport associated with the increase in convective region extent (section 3.3.2e).

In chapter 4, we used a coupled aquaplanet model (FORTE) in order to investigate the extent of the coupling of heat transport in the tropical ocean and atmosphere, following predictions made by Held (2001) about the close coupling of heat transport in his model. The aquaplanet was useful to test Held's model since the absence of land meant the heat transport in the ocean was mainly wind driven. A key figure from chapter 4 is shown below (Figure 5.3), and key results are detailed as follows:

- The analysis of the FORTE aquaplanet output showed that there was no correlation between HO and HA (heat transport in ocean and atmosphere based on radiative fluxes) at 20° in the model.
- However, there was some correlation between the wind driven heat transport in ocean and atmosphere, calculated using Ekman mass transport based on wind stresses.
- In particular, HO is well approximated by the oceanic Ekman heat transport at 20°, indicating that, as predicted by Held (2001), the ocean heat transport was mainly Ekman.
- In the atmosphere, there is a correlation between HA and the wind driven atmospheric heat transport, HA_{axisym}, although HA_{axisym} is only a small component

of *HA*. This observation indicated that in FORTE, atmospheric eddies play a role in heat transport at 20° latitudes.

- Hence, Held's model can not be said to accurately represent the heat transport in the atmosphere at this particular latitude in FORTE, but is more applicable in FORTE's ocean.

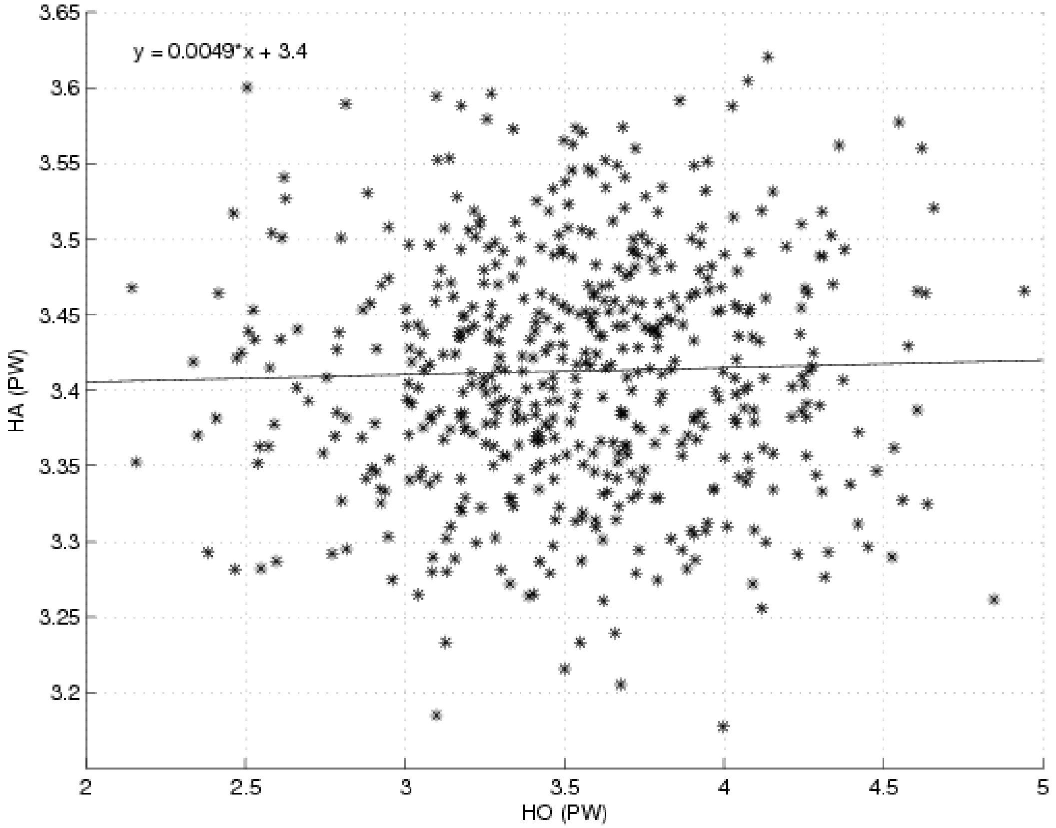

Figure 5.3. The relation between atmospheric and oceanic heat transport out of the tropics in the FORTE aquaplanet calculated using radiative fluxes and ocean heat storage. The figure shows there is no correlation between *HO* and *HA* at 20° in FORTE. Figure repeated from section 4.4.2.

5.1 Future work

In chapter 2, we identified the complicated structure of the atmosphere over the parts of ocean with relatively low SST in the tropics. This structure, and particularly the low level return flow, was noted by Zhang *et al.* (2004) in observations taken over the eastern Pacific. A good understanding of this shallow circulation is required for accurate modelling of the atmosphere, and further work could involve more investigation into the the role of the circulation over cooler SSTs in terms of heat transport. It would be good to quantify the heat transported by the complex circulation to see if it added to or opposed the heat transport by the convective regions.

In chapter 3 we identified and quantified the heat transport associated with convective regions of the tropics. Future work could involve similar analyses on non-convective regions and regions associated with the monsoon circulation to investigate the amount of mass and heat transport in each. The use of oceanic reanalysis data could be used to perform similar estimates of heat transport in the ocean, such as ENACT, which is the European Union-funded project entitled "ENhAnced ocean data assimilation and ClimaTe prediction” (ENACT 2005).

During the Pliocene (3-5 million years ago), it is thought that conditions in the tropics were much warmer than the present day, and there is evidence of a ‘permanent El Niño’ (Barreiro *et al.* 2006; Fedorov *et al.* 2006). It has been suggested that the Pliocene warm interval closely resembles conditions we might expect under increased greenhouse gas emissions and climate change scenarios (Solomon *et al.* 2007). We saw in chapter 3 that heat transport by the Hadley Cell is increased during El Niño seasons. There is also evidence to suggest that an enhanced tropical warmpool results in a weakening and poleward expansion of the Hadley Cell, since the warmest SSTs migrate poleward, reducing the meridional gradient in SST (Brierley *et al.* 2009). If indeed future climate conditions on earth are likely to resemble those during the Pliocene, it is important to understand the connection between Hadley Cell heat transport and variations in the extent of the warm pool so we can predict the expected response to atmospheric heat transport and circulation, and this is a clear example of future work relating to that of chapter 3.

Following the work on the FORTE model, an obvious choice for further work would include an investigation into the extent of ocean-atmosphere coupling at other latitudes in the tropics, in order to investigate whether the model used in Held (2001) can be applied for both ocean and atmosphere at other latitudes of the aquaplanet, for example, nearer to the equator. More investigation should also be carried out to look into the axisymmetric atmospheric heat transport and to discover why it is not entirely explained by Ekman transport, and at which latitudes, if any, does it become more of an approximation of Ekman transport. More realistic heat transport scenarios would be realized with the use of ocean basins, so adding ridges to the FORTE model could be an area worth investigating.

Appendix – Isolating the convective region heat transport using a baroclinic framework

A.1 Description of the model

Within convective regions of the atmosphere, the circulation takes the form of a true overturning, and we can calculate the heat transport based on the overturning wind speed and the gross moist static stability (section 3.2.2). Indeed, considering that in the convective regions of the tropics, deep convection acts to maintain a moist adiabatic temperature profile with constant saturation moist entropy (S_{sat}) from the boundary layer to the upper troposphere, the so-called statistical equilibrium assumption (Emanuel *et al.* 1994), it is possible to predict the overturning meridional wind in the convective region given the temperature profile as follows.

Specific volume, α, can be can be represented by $\alpha = \bar{\alpha} + \alpha'$, where the bar represents a reference state, and the prime represents a perturbation. In this case, the prime represents a seasonal perturbation. The seasonal perturbation α' is related to the perturbation S_{sat}' on a constant pressure level by

$$\alpha' \simeq \left(\frac{\partial \bar{\alpha}}{\partial S_{sat}}\right)_P S'_{sat} \tag{A.1}$$

where P is pressure. Using Maxwell's relation:

$$\left(\frac{\partial \bar{\alpha}}{\partial S_{sat}}\right)_P = \left(\frac{\partial \bar{T}}{\partial P}\right)_{S_{sat}} \tag{A.2}$$

and assuming hydrostatic balance:

$$\frac{\partial \phi'}{\partial P} = -\alpha' \tag{A.3}$$

the following expression can be obtained:

$$\phi' = \int_P^{P_s} \left(\frac{\partial \bar{T}}{\partial P}\right)_{S_{sat}} S'_{sat}\, dP \tag{A.4}$$

Integrating with respect to pressure from the surface, assuming S'_{sat} is constant with height and perturbations are much smaller than the mean state (in other words, perturbations still follow a moist adiabat), we can obtain the following expression for geopotential height perturbations:

$$\phi' = S'_{sat}[\bar{T}(P_s) - \bar{T}(P)] \quad \text{(A.5)}$$

where P_s is the surface pressure. The geopotential height can be further written as the sum of a barotropic, (vertically averaged) component ϕ'_{bt} and a deviation from it (baroclinic) component ϕ'_{bc},

$$\phi' = \phi'_{bt} + \phi'_{bc} \quad \text{(A.6)}$$

The vertical mean of (A.5) gives the barotropic component ϕ'_{bt}:

$$\phi'_{bt} = S'_{sat}[\bar{T}(P_s) - \bar{T}_{bt}] \quad \text{(A.7)}$$

where $\overline{T}_{bt}$ is the vertically averaged mean temperature profile $\overline{T}$. Therefore, the baroclinic component is:

$$\phi'_{bc} = \phi' - \phi'_{bt} = S'_{sat}[\bar{T}_{bt} - \bar{T}(P)] \quad \text{(A.8)}$$

By using the mean temperature profile over the convective region, we have determined the geopotential perturbation. This is useful since geopotential height perturbations and wind perturbations have the same vertical structure which can be seen by considering a form of the momentum equation (1.22) where we neglect pressure gradients as they are small compared to the mean state:

$$\frac{\partial u'}{\partial t} - fv' = -\frac{\partial \phi'}{\partial x} \quad \text{(A.9)}$$

$$\frac{\partial v'}{\partial t} - fu' = -\frac{\partial \phi'}{\partial y} \quad \text{(A.10)}$$

which indicates that v', u' and ϕ' have the same vertical structure.

As mentioned previously, the barotropic component represents circulations which do not sum to zero when mass transport is vertically integrated and the shape of the baroclinic component is based on the meridional wind profile minus the vertical mean wind profile. There is just one zero crossing at mid levels, and the baroclinic component represents a closed overturning circulation, where mass transport at upper levels is equal and opposite to that at lower levels.

The prediction for the overturning component, v_{pred} is thus calculated using the mean temperature profile in the convective region, $T(P)$, and the vertical average of this, T_{bt}:

$$v_{pred} \propto (T_{bt} - T(P)) \tag{A.12}$$

By projecting the meridional wind in the convective region onto the predicted profile, it is possible to isolate the overturning component, v_{ovr}. This can then be used to calculate the heat transport associated with the overturning circulation of the Hadley Cell in the convective regions of the atmosphere. We define v_{ovr} from the reanalysis data, computed by projecting the mean meridional wind velocity profile, v, onto a normalised v_{pred} as follows:

$$\vec{v}_{ovr} = (\vec{v} \cdot \vec{v}_{pred})\vec{v}_{pred} \tag{A.13}$$

where the arrows represent pressure level vectors. We do not perform decomposition for timescales of less than a season, in line with work which highlights that statistical equilibrium is not reached on timescales of less than one month (Brown & Bretherton 1997).

Figure A.1 shows meridional wind profiles over the convective region for DJF and JJA, and these profiles projected onto the predicted profile, which are v_{ovr}. Included for information are mean meridional wind profiles over the non-convective region of the tropics (where vertical mean RH < 60%). Overall, Figure A.1 shows a satisfactory fit between v_{ovr} and the profile in the convective region v_{conv}, as the profiles have a similar shape and the crossing point at v=0 is well predicted by v_{ovr}. In contrast to the convective region profile, the non-convective region wind profile changes sign more than once in both seasons. This is expected, since in these regions, large scale descent leads to vertical contrasts in S_{sat} and violates the statistical equilibrium assumption (Emanuel *et al.* 1994), and as a result, we will not further perform the baroclinic decomposition in non-convective regions. The fit between v_{ovr} and v_{conv}, is better below the crossing point than above. We experimented with removing the upper layers of data when calculating heat transport, but there was little difference in the heat transport calculations. The difference between the predicted and actual meridional wind profiles is illustrated in more detail in Figure A.2, which shows the mean meridional wind speed for the lower half of the profile, from the surface to the point where $v_{ovr} = 0$ for JJA and DJF for each of the 22 years of data.

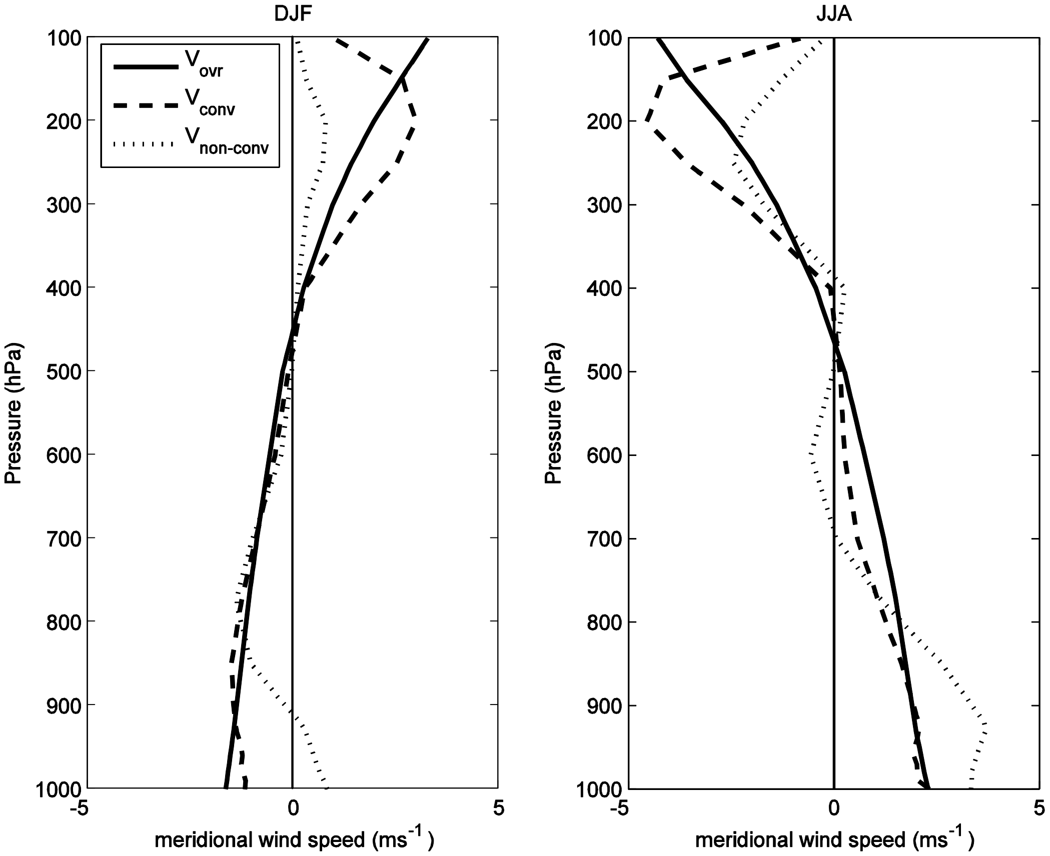

Figure A.1. Profiles of the mean meridional wind within the convective region v_{conv} (dashed), non-convective region $v_{non\text{-}conv}$ (dotted) and the predicted overturning wind profile v_{ovr} (solid) for DJF (left) and JJA (right).

The upper panels show significant correlation in the convective region ($r = 0.64$ at $p = 0.001$ for JJA and $r = 0.86$ at $p < 0.0001$ for DJF), and the lower panels show the absence of correlation for the dry region and a greater spread of data. During DJF in the convective region, v_{ovr} and v_{conv} are very similar, and there is a small offset in the JJA convective region between v_{ovr} and v_{conv} which is visible in Figure A.1 as the area between the solid and dashed line on the lower half of the right hand panel.

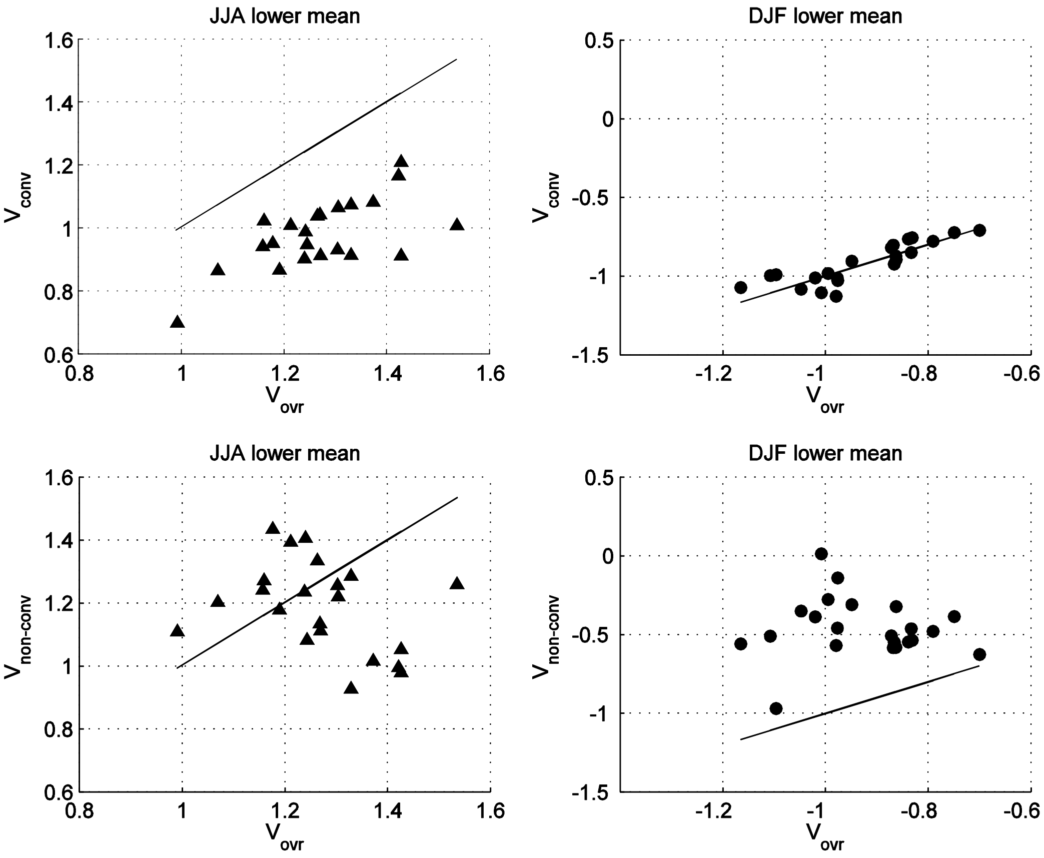

Figure A.2. For each of the 22 years of data, the mean meridional windspeed in ms^{-1} for the lower layer (Surface to where $v_{ovr} = 0$) for the convective region v_{conv} and corresponding predicted overturning windspeed v_{ovr} (upper panels) and non-convective region wind speeds $v_{non\text{-}conv}$ against v_{ovr} (lower panels). Left hand panels are JJA and right hand panels are DJF and the straight lines represent x = y in each panel.

Since there is one meridional wind profile for each convective region per season, we can adapt (3.3) in section 3.2.4b to calculate the overturning heat transport based on the dynamical framework as follows:

$$H_{ovr} = L_* \int_{P_{100}}^{P_S} v_{ovr} h_* \frac{dP}{g} \tag{A.14}$$

A.2 Validation of baroclinic decomposition model against previous results

After calculating the convective region heat transport, H_* simply by removing the barotropic component of the wind profile in regions of RH > 60% according to (3.3) and based on the method outlined in section 3.2.4, we next redid the calculation replacing v_*

with v_{ovr} which was calculated using the framework described in section A.1 and equation (A.14). Calculations of H_* and H_{ovr} are plotted together in Figure A.3.

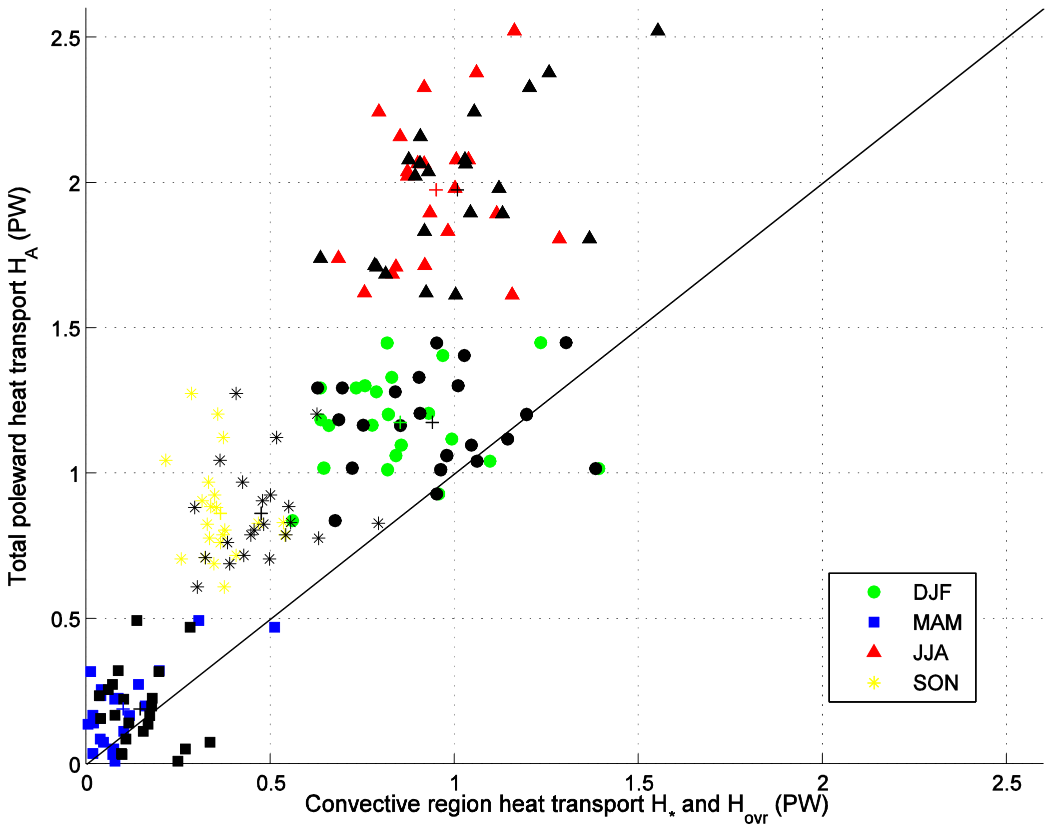

Figure A.3. Total zonally integrated poleward heat transport and the contribution from the convective region in Petawatts for seasonal data. Black markers show *H_**, the same data as in Figure 3.5, colours show *H_{ovr}*, calculated using the dynamical framework described in section A.1. The diagonal line represents a 1:1 ratio of convective region heat transport to total heat transport. Each point represents a season from 1980 to 2001. Seasons are DJF (green, circles), MAM (blue, squares), JJA (red, squares), SON (yellow, stars) and mean values for each season are represented by crosses.

There is a good agreement between the convective region heat transport calculated using each of the different methods (Figure A.3). For the solsticial seasons, the difference between the mean H_{ovr} and mean H_* is under 0.1 PW. The range of convective region heat transport is also similar for each method used in all seasons. This implies that the baroclinic model for predicting the wind profile is a good indicator of the overturning wind profile and can be used to look into gross moist static stability variability, which is the focus of sections 3.3.2c to e. From now on, when using the baroclinic framework to calculate convective heat transport, we use the subscript *ovr*, so that convective region heat transport calculated using (A.14) is H_{ovr}.

Bibliography

Back LE, Bretherton CS. 2006. Geographic variability in the export of moist static energy and vertical motion profiles in the tropical Pacific. *Geophysical Research Letters*, **33,** L17810.

Barreiro M, Philander G, Pacanowski R, Fedorov A. 2006. Simulations of warm tropical conditions with application to middle Pliocene atmospheres. *Climate Dynamics*, **26,** 349-365.

Bess TD, Smith GL. 1993. Earth Radiation Budget: Results of outgoing longwave radiation from Nimbus-7, NOAA-9, and ERBS Satellites. *Journal of Applied Meteorology*, **32,** 813-824.

Betts A. 1986. A new convective adjustment scheme. 1. Observational and theoretical basis. *Quarterly Journal of the Royal Meteorological Society*, **112,** 667-691.

Bjerknes J. 1964. Atlantic air-sea interaction. *Advances in Geophysics*, **10,** 1-82.

Bjerknes J. 1969. Atmospheric teleconnections from the equatorial Pacific. *Monthly Weather Review*, **97,** 163-172.

Bohren CF, Albrecht BA. 1998. *Atmospheric Thermodynamics*. Oxford University Press.

Bony S, Colman R, Kattsov VM, Allan RP, Bretherton CS, Dufresne JL, Hall A, Hallegatte S, Holland MM, Ingram W, Randall DA, Soden BJ, Tselioudis G, Webb MJ. 2006. How well do we understand and evaluate climate change feedback processes? *Journal of Climate*, **19,** 3445-3482.

Bony S, Dufresne JL, Le Treut H, Morcrette JJ, Senior C. 2004. On dynamic and thermodynamic components of cloud changes. *Climate Dynamics*, **22,** 71-86.

Brierley CM, Fedorov A, Liu Z, Herbert TD, Lawrence KT, LaRiviere JP. 2009. Greatly expanded tropical warm pool and weakened Hadley circulation in the early Pliocene. *Science*, **323,** 1714-1718.

Britannica. 2008. Encyclopaedia Britannica. [Available online at http://www.britannica.com/EBchecked/topic/41463/atmospheric-circulation].

Brown RG, Bretherton CS. 1997. A test of the strict quasi-equilibrium theory on long time and space scales. *Journal of the Atmospheric Sciences*, **54,** 624-638.

Bryan K, Lewis LJ. 1979. A water mass model of the world ocean. *Journal of Geophysical Research*, **81,** 25032517.

Carissimo BC, Oort AH, Vonderhaar TH. 1985. Estimating the meridional energy transports in the atmosphere and ocean. *Journal of Physical Oceanography*, **15,** 82-91.

Colman RA, McAvaney BJ, Fraser JR, Power SB. 1994. Annual mean meridional energy-transport modeled by a General-Circulation Model for present and 2-X-Co2 equilibrium climates. *Climate Dynamics*, **10,** 221-229.

Czaja A, Marshall J. 2006. Partitioning of poleward heat transport between the atmosphere and ocean. *Journal of the Atmospheric Sciences*, **63,** 1498-1511.

Dima IM, Wallace JM. 2003. On the seasonality of the Hadley cell. *Journal of the Atmospheric Sciences*, **60,** 1522-1527.

Ekman VW. 1905. On the influence of the Earth's rotation on ocean currents. *Arkiv for Matematik, Astronomi och Fysik*, **2,** 1-52.

Emanuel KA, Neelin JD, Bretherton CS. 1994. On large-scale circulations in convecting atmospheres. *Quarterly Journal of the Royal Meteorological Society*, **120,** 1111-1143.

ENACT. 2005. Enhanced Ocean Data Assimilation and Climate Prediction. A European Commission Framework 5 Project. Met Office.

Fang M, Tung KK. 1999. Time-dependent nonlinear Hadley circulation. *Journal of the Atmospheric Sciences*, **56,** 1797-1807.

Fedorov AV, Dekens PS, McCarthy M, Ravelo AC, deMenocal PB, Barreiro M, Pacanowski RC, Philander SG. 2006. The Pliocene paradox (mechanisms for a permanent El Nino). *Science*, **312,** 1485-1489.

Forster PM, Blackburn M, Glover R, Shine KP. 2000. An examination of climate sensitivity for idealised climate change experiments in an intermediate general circulation model. *Climate Dynamics*, **16,** 833-849.

Frierson DMW, Held IM, Zurita-Gotor P. 2007. A gray-radiation aquaplanet moist GCM. Part II: Energy transports in altered climates. *Journal of the Atmospheric Sciences*, **64,** 1680-1693.

Fuglister FC. 1960. *Atlantic Ocean atlas of temperature and salinity profiles and data from the International Geophysical Year of 1957-1958.*: pp 141-143, Woods Hole Oceanographic Institution, Woods Hole, MA.

Ganachaud A, Wunsch C. 2003. Large-scale ocean heat and freshwater transports during the World Ocean Circulation Experiment. *Journal of Climate*, **16,** 696-705.

Gent P, McWilliams J. 1990. Isopycnal mixing in ocean circulation models. *Journal of Physical Oceanography*, **20,** 150-155.

Gent P, Willebrand J, McDougall T, McWilliams J. 1995. Parameterizing eddy-induced transports in ocean circulation models. *Journal of Physical Oceanography*, **25,** 463-474.

Gill AE. 1982. *Atmosphere-Ocean Dynamics*. Academic Press, 1st edition.

Hadley G. 1735. Concerning the cause of the general trade winds. *Philosophical Transactions of the Royal Society of London*, **39,** 58-62.

Hall MM, Bryden HL. 1982. Direct estimates and mechanisms of ocean heat-transport. *Deep-Sea Research Part a-Oceanographic Research Papers*, **29,** 339-359.

Halley E. 1686. An historical account of the trade winds, and monsoons, observable in the seas between and near the tropicks, with an attempt to assign the physical cause of the said winds. *Transactions of the Royal Society of London*, **16,** 153-168.

Hartmann DL. 1994. *Global Physical Climatology*. California: Academic Press.

Hartmann DL, Michelsen ML. 1993. Large-scale effects on the regulation of tropical sea-surface temperature. *Journal of Climate*, **6,** 2049-2062.

Hastenrath S. 1982. On meridional heat transport in the world ocean. *Journal of Physical Oceanography*, **12,** 922-927.

Hastenrath S. 1985. *Climate and Circulation of the Tropics*. Holland, D. Reidel Publishing Company.

Hazeleger W, Seager R, Cane MA, Naik NH. 2004. How can tropical Pacific Ocean heat transport vary? *Journal of Physical Oceanography*, **34,** 320-333.

Held IM. 2001. The partitioning of the poleward energy transport between the tropical ocean and atmosphere. *Journal of the Atmospheric Sciences*, **58,** 943-948.

Held IM, Hou AY. 1980. Non-linear axially-symmetric circulations in a nearly inviscid atmosphere. *Journal of the Atmospheric Sciences*, **37,** 515-533.

Held IM, Schneider T. 1999. The surface branch of the zonally averaged mass transport circulation in the troposphere. *Journal of the Atmospheric Sciences*, **56,** 1688-1697.

Held IM, Soden BJ. 2006. Robust responses of the hydrological cycle to global warming. *Journal of Climate*, **19,** 5686-5699.

Hess PG, Battisti DS, Rasch PJ. 1993. Maintenance of the Intertropical Convergence Zones and the large-scale tropical circulation on a water-covered Earth. *Journal of the Atmospheric Sciences*, **50,** 691-713.

Holton JR. 2004. *An Introduction to Dynamic Meteorology*. Academic Press.

Hoskins BJ, Simmons AJ. 1975. Multilayer spectral model and semi-implicit method. *Quarterly Journal of the Royal Meteorological Society*, **101,** 637-655.

Houghton HG. 1954. On the annual heat balance of the northern hemisphere. *Journal of Meteorology*, **11,** 1-9.

James IN. 1994. *Introduction to Circulating Atmospheres*. Cambridge University Press, 1st edition.

James IN. 2003. Hadley Circulation. In: *Encyclopedia of Atmospheric Sciences* (Ed. by Holton, JR), pp. 2334-2338: Academic Press.

Jayne SR, Marotzke J. 2001. The dynamics of ocean heat transport variability. *Reviews of Geophysics*, **39,** 385-411.

Kalnay E, Kanamitsu M, Kistler R, Collins W, Deaven D, Gandin L, Iredell M, Saha S, White G, Woollen J, Zhu Y, Chelliah M, Ebisuzaki W, Higgins W, Janowiak J, Mo KC, Ropelewski C, Wang J, Leetmaa A, Reynolds R, Jenne R, Joseph D. 1996. The NCEP/NCAR 40-year reanalysis project. *Bulletin of the American Meteorological Society*, **77,** 437-471.

Klinger BA, Marotzke J. 2000. Meridional heat transport by the subtropical cell. *Journal of Physical Oceanography*, **30,** 696-705.

Kumar MRR, Schlussel P. 1998. Air-sea interaction over the Indian Ocean during the two contrasting monsoon years 1987 and 1988 studied with satellite data. *Theoretical and Applied Climatology*, **60,** 219-231.

Lindzen RS, Hou AY. 1988. Hadley Circulations for zonally averaged heating centered off the equator. *Journal of the Atmospheric Sciences*, **45,** 2416-2427.

Lorenz EN. 1967. *The nature and theory of the general circulation of the atmosphere*. World Meteorological Organization, No 218, 161 pp.

Manabe S, Bryan K, Spelman MJ. 1975. Global ocean-atmosphere climate model .1. Atmospheric circulation. *Journal of Physical Oceanography*, **5,** 3-29.

Manabe S, Smagorinsky J, Strickler RF. 1965. Simulated climatology of a general circulation model with a hydrologic cycle. *Monthly Weather Review*, **93,** 769-798.

Manabe S, Terpstra TB. 1974. Effects of mountains on general circulation of atmosphere as identified by numerical experiments. *Journal of the Atmospheric Sciences*, **31,** 3-42.

Marshall J, Adcroft A, Campin JM, Hill C, White A. 2004. Atmosphere-ocean modeling exploiting fluid isomorphisms. *Monthly Weather Review*, **132,** 2882-2894.

Marshall J, Ferreira D, Campin JM, Enderton D. 2007. Mean climate and variability of the atmosphere and ocean on an aquaplanet. *Journal of the Atmospheric Sciences*, **64,** 4270-4286.

McPhaden MJ. 1999. Climate Oscillations - Genesis and Evolution of the 1997-98 El Nino. *Science*, **283,** 950-954.

Meehl GA, Washington WM, Semtner Jr AJ. 1982. Experiments with a global ocean model driven by observed atmospheric forcing. *Journal of Physical Oceanography*, **12,** 301-312.

Mitchell TP, Wallace JM. 1992. The annual cycle in equatorial convection and sea-surface temperature. *Journal of Climate*, **5,** 1140-1156.

Molteni F. 2003. Atmospheric simulations using a GCM with simplified physical parametrizations. I: model climatology and variability in multi-decadal experiments. *Climate Dynamics*, **20,** 175-191.

NASA. 2006. Earth Observatory [availabile online from http://earthobservatory.nasa.gov/IOTD/view.php?id=6308].

Neale R, Hoskins B. 2000. A standard test for AGCMs including their physical parametrizations. II: Results for the Met. Office model. *Atmospheric Science Letters*, **1,** 108-114.

Neelin JD, Held IM. 1987. Modeling tropical convergence based on the moist static energy budget. *Monthly Weather Review*, **115,** 3-12.

Newell RE, Kidson JW, Vincent DG, Boer GJ. 1972. *The General Circulation of the Tropical Atmosphere, Vol. 1.*: The MIT Press.

NOAA. 2009. El Nino theme page. [Available online from http://www.pmel.noaa.gov/tao/elnino/nino-home.html].

Oort AH. 1971. Observed annual cycle in meridional transport of atmospheric energy. *Journal of the Atmospheric Sciences*, **28,** 325-339.

Oort AH, Peixoto JP. 1983. Global angular-momentum and energy-balance requirements from observations. *Advances in Geophysics*, **25,** 355-490.

Oort AH, Vonder Haar TH. 1976. Observed annual cycle in ocean-atmosphere heat balance over Northern Hemisphere. *Journal of Physical Oceanography*, **6,** 781-800.

Oort AH, Yienger JJ. 1996. Observed interannual variability in the Hadley circulation and its connection to ENSO. *Journal of Climate,* **9,** 2751-2767.

Pacanowski RC, Dixon K, Rosati A. 1991. The GFDL modular ocean model users guide: Version 1.0. Tech. Rep. 2, NOAA/Geophysical Fluid Dynamics Laboratory, Princeton University, 44 pp.

Pauluis O, Czaja A, Korty R. 2008. The global atmospheric circulation on moist isentropes. *Science*, **321,** 1075-1078.

Peixoto JP, Oort AH. 1992. *Physics of Climate*. New York, American Institute of Physics.

Percival DB, Walden AT. 1993. *Spectral Analysis for Physical Applications: Multitaper and Conventional Univariate Techniques*. Cambridge: Cambridge University Press.

Philander SG. 1990. *El Nino, La Nina and the Southern Oscillation*. Academic Press.

Philander SG, Fedorov AV. 2003. Role of tropics in changing the response to Milankovich forcing some three million years ago. *Paleoceanography*, **18,** 1045-1057.

Philander SGH, Gu D, Halpern D, Lambert G, Lau NC, Li T, Pacanowski RC. 1996. Why the ITCZ is mostly north of the equator. *Journal of Climate*, **9,** 2958-2972.

Pierrehumbert RT. 1995. Thermostats, radiator fins, and the local runaway greenhouse. *Journal of the Atmospheric Sciences*, **52,** 1784-1806.

Ramanathan V, Collins W. 1991. Thermodynamic regulation of ocean warming by cirrus clouds deduced from observations of the 1987 El-Nino. *Nature*, **351,** 27-32.

Ramanathan V, Collins W. 1992. Thermostat and global warming. *Nature*, **357,** 649-649.

Raymond DJ, Bretherton CS, Molinari J. 2006. Dynamics of the intertropical convergence zone of the east Pacific. *Journal of the Atmospheric Sciences*, **63,** 582-597.

Saravanan R, McWilliams JC. 1995. Multiple equilibria, natural variability, and climate transitions in an idealized ocean-atmosphere model. *Journal of Climate*, **8,** 2296-2323.

Schulman LL. 1973. Summer hemisphere Hadley Cell. *Quarterly Journal of the Royal Meteorological Society*, **99,** 197-201.

Shaffrey L, Sutton R. 2006. Bjerknes compensation and the decadal variability of the energy transports in a coupled climate model. *Journal of Climate,* **19,** 1167-1181.

Sinha BS, Smith RS. 2002. Development of a fast coupled general circulation model (FORTE) for climate studies, implemented using the OASIS coupler. Tech. Rep. 81, National Oceanography Centre, Southampton, U.K., 67 pp.

Slingo JM. 1987. The development and verification of a cloud prediction scheme for the ECMWF model. *Quarterly Journal of the Royal Meteorological Society*, **113,** 899-927.

Smith RS. 2004. *Ocean circulation and climate dynamics under idealised continental configurations in a coupled ocean-atmosphere model*. PhD thesis. University of Southampton.

Smith RS, Dubois C, Marotzke J. 2006. Global climate and ocean circulation on an aquaplanet ocean-atmosphere general circulation model. *Journal of Climate*, **19,** 4719-4737.

Solomon S, Qin D, Manning M, Chen Z, Marquis M, Averyt KB, Tignor M, Miller HL. 2007. IPCC, 2007: Summary for Policymakers. In: *Climate Change 2007: The Physical Science Basis. Contribution of Working Group*

I to the Fourth Assessment Report of the Intergovernmental Panel on Climate Change. Cambridge University Press, Cambridge, United Kingdom and New York, NY, USA.

Stone PH. 1978. Constraints on dynamical transports of energy on a spherical planet. *Dynamics of Atmospheres and Oceans*, **2,** 123-139.

Sumi A, Kimoto M, Emori S, Nozawa M, Hasumi H. 2004. Model development for the global warming prediction by using the earth simulator. *Seventh International Conference on High Performance Computing and Grid in Asia Pacific Region, Proceedings***,** 480-486.

Sun DZ, Liu ZY. 1996. Dynamic ocean-atmosphere coupling: A thermostat for the tropics. *Science*, **272,** 1148-1150.

Sverdrup HU. 1957. Transport of heat by the currents of the North Atlantic and North Pacific Oceans. Festskrift til Professor Bjorn Helland-Hansen. *Naturen,* pp. 226-236. Bergen, Norway, 1957.

Terray L, Valcke S, Piacentini A. 1999. OASIS 2.3 user's guide. Tech. Rep. TR/CGMC/99-37, CERFACS, Toulouse, France, 82 pp.

Tomas RA, Webster PJ. 2003. Tropical Meteorology. In: *Encyclopedia of Atmospheric Sciences* (Ed. by Holton, JR), pp. 2306-2345: Academic Press.

Trenberth KE. 1979. Mean annual poleward energy transports by oceans in the Southern Hemisphere. *Dynamics of Atmospheres and Oceans*, **4,** 57-64.

Trenberth KE, Caron JM. 2001. Estimates of meridional atmosphere and ocean heat transports. *Journal of Climate*, **14,** 3433-3443.

Trenberth KE, Caron JM, Stepaniak DP, Worley S. 2002. Evolution of El Nino-Southern Oscillation and global atmospheric surface temperatures. *Journal of Geophysical Research-Atmospheres*, **107,** 4065-4087.

Trenberth KE, Stepaniak DP. 2003. Seamless poleward atmospheric energy transports and implications for the Hadley circulation. *Journal of Climate*, **16,** 3706-3722.

Trenberth KE, Stepaniak DP, Hurrell JW, Fiorino M. 2001. Quality of reanalyses in the Tropics. *Journal of Climate*, **14,** 1499-1510.

Uppala SM, Kallberg PW, Simmons AJ, Andrae U, Bechtold VD, Fiorino M, Gibson JK, Haseler J, Hernandez A, Kelly GA, Li X, Onogi K, Saarinen S, Sokka N, Allan RP, Andersson E, Arpe K, Balmaseda MA, Beljaars ACM, Van De Berg L, Bidlot J, Bormann N, Caires S, Chevallier F, Dethof A, Dragosavac M, Fisher M, Fuentes M, Hagemann S, Holm E, Hoskins BJ, Isaksen L, Janssen P, Jenne R, McNally AP, Mahfouf JF, Morcrette JJ, Rayner NA, Saunders RW, Simon P, Sterl A, Trenberth KE, Untch A, Vasiljevic D, Viterbo P, Woollen J. 2005. The ERA-40 re-analysis. **131,** 2961-3012.

Vallis GK. 2006. *Atmospheric and Oceanic Fluid Dynamics*. Cambridge: Cambridge University Press.

Vallis GK, Farneti R. 2008a. Meridional energy transport in the atmosphere-ocean system. Part I: Theory and an idealized model. Submitted to. *Quarterly Journal of the Royal Meteorological Society*.

Vallis GK, Farneti R. 2008b. Meridional energy transport in the atmosphere-ocean system. Part II: Numerical experiments. Submitted to. *Quarterly Journal of the Royal Meteorological Society*.

Walker CC, Schneider T. 2005. Response of idealized Hadley circulations to seasonally varying heating. *Geophysical Research Letters*, **32,** L06813.

Wallace JM. 1992. Effect of deep convection on the regulation of tropical sea-surface temperature. *Nature*, **357,** 230-231.

Weaver AJ, Eby M, Wiebe EC, Bitz CM, Duffy PB, Ewen TL, Fanning AF, Holland MM, MacFadyen A, Matthews HD, Meissner KJ, Saenko O, Schmittner A, Wang HX, Yoshimori M. 2001. The UVic Earth System Climate Model: Model description, climatology, and applications to past, present and future climates. *Atmosphere-Ocean*, **39,** 361-428.

Webb DJ. 1996. An ocean model code for array processor computers. *Computers & Geosciences*, **22,** 569-578.

WOCE. 2003. International Project Office. *WOCE observations 1990-1998; a summary of the WOCE global data resource*. WOCE International Project Office, WOCE Report No. 179/02., Southampton, UK.

Wunsch C. 1997. The vertical partition of oceanic horizontal kinetic energy. *Journal of Physical Oceanography*, **27,** 1770-1794.

Wunsch C. 2005. The total meridional heat flux and its oceanic and atmospheric partition. *Journal of Climate*, **18,** 4374-4380.

Zhang CD, McGauley M, Bond NA. 2004. Shallow meridional circulation in the tropical eastern Pacific. *Journal of Climate*, **17,** 133-139.